# Solution Processed Kesterite Light Absorber on Titania Electron Conductor for Photovoltaic Application

**Zhuoran Wang**

Department of Mining and Materials Engineering
McGill University, Montreal

July 2017

A thesis submitted to McGill University in partial fulfillment of the
requirements of the degree of Doctor of Philosophy in Engineering

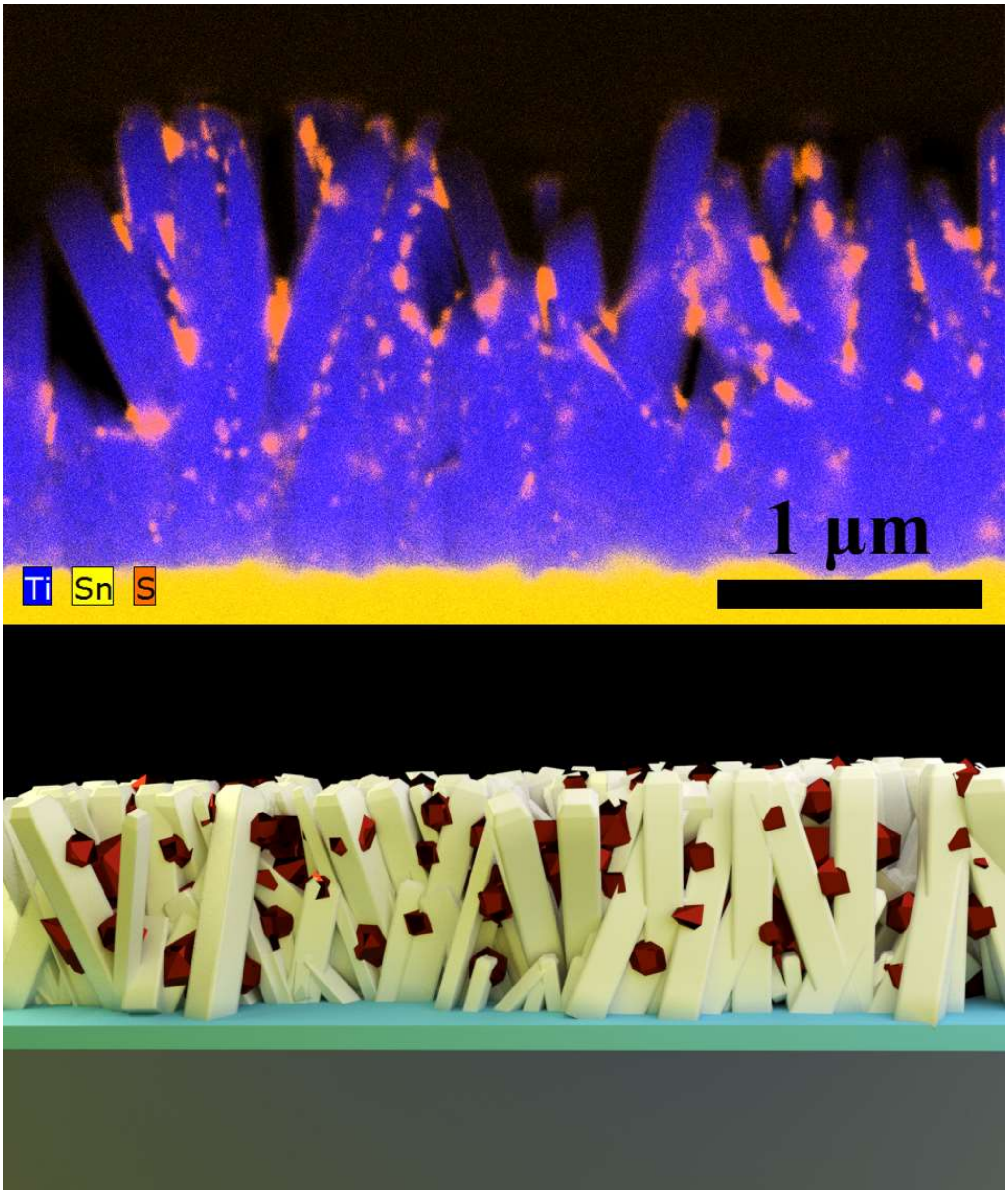

The structure of CZTS nanocrystallites (light absorber) on $TiO_2$ nanorod arrays (electron conductor): EDS mixed map (upper) and schematic depiction (lower).

*This thesis is dedicated to my grandfather*

*Zimin Wang (1925-2010)*

# ABSTRACT

$Cu_2ZnSnS_4$ (CZTS) in its kesterite crystal phase, a semiconductor with earth-abundant, non-toxic composition, is a promising candidate for new generation photovoltaics to power a sustainable energy future. However, the issue of impurities and defects that form during CZTS crystallization has retarded the development of standard CZTS thin film solar cells as those of CIGS and CdTe. In this work, CZTS is investigated in an alternative solar cell type that is known from recent emerging photovoltaic technologies - dye-, quantum dots-, and perovskite- sensitized solar cells – to have high tolerance to imperfection of photo-absorbing crystals. More specifically, the thesis evaluates CZTS as nanoscale light absorber coated on a charge conductor structure (in this case $TiO_2$) and assembled in liquid junction or solid state hole-transport incorporating photoelectrochemical cells. The work involved varying the $TiO_2$ substrate and method of CZTS deposition, in-depth study of annealing, and comprehensive nanoscale and optical property characterization of photoanodes and devices

To fabricate this light absorber-conductor nanostructure, firstly, CZTS was deposited as binary metal sulfide precursor on a pre-sintered $TiO_2$ mesoporous film via an aqueous solution successive-ionic-layer-adsorption-reaction (SILAR) method followed by annealing to induce its crystallization. Composition control was realized by the step-by-step solution deposition-exchange sequence and homogeneity was improved by employing a post-annealing hydrochloric acid etching step. Optical measurements confirmed the light absorbing functionality of the nanostructured $TiO_2$@CZTS film. Subsequently, the focus was directed in understanding the CZTS crystal phase formation during annealing of CZTS-$TiO_2$ film via the employment of in-situ Raman spectroscopy. It was found that annealing at 400 °C is sufficient for stabilizing the kesterite phase, but it is only at 500 °C that complete reactive crystallization takes place leading to elimination of the undesirable copper tin sulfide (CTS) impurity phase. More importantly, this in-situ study revealed the real-time dependence of Raman peak intensity enhancement, shift and broadening for CZTS at 500 °C that is critical in the further development of CZTS sensitized devices.

In parallel to the $TiO_2$ mesoporous electron conductor structure, a hydrothermally synthesized rutile $TiO_2$ nanorod-structured film grown on FTO glass was used to form the absorber-conductor structure with SILAR processed CZTS nanoscrystallites. Of the two $TiO_2$ sub-structures was the latter that yielded photovoltaic response, proving the feasibility of the electron injection/collection of the CZTS/$TiO_2$ photoelectrode and was retained for further investigation. The initial proof-of-concept photoelectrochemical cell featuring rutile nanorod (NR) arrays covered with CZTS nanocrystallites yielded a rather modest efficiency of 0.25 %. It was concluded that the amount of CZTS nanocrystal loading on the rutile nanorod sub-structure should be increased and interfacial CZTS/$TiO_2$ recombination suppressed by modifying the solution deposition approach. To this end a water/ethanol direct solution coating method was developed to deposit CZTS on $TiO_2$ NRs resulting in improved kesterite quality film as characterized via high resolution (HR) SEM, TEM, XPS, optical and electrochemical (impedance spectroscopy) techniques. Eventually a solid-state $TiO_2$NR@CZTS sensitized solar cell, featuring spiro-OMeTAD as hole-transporting medium and CdS as buffer layer, was successfully assembled delivering a 10 fold improvement in power conversion efficiency (2 %), opening the avenue for further developments in alternative CZTS-$TiO_2$ optoelectronic applications.

# RÉSUMÉ

$Cu_2ZnSnS_4$ (CZTS) sous sa phase kësterite crystalline est un semiconducteur constitué d'élément abondant, non-toxique,et un candidat prometteur pour la nouvelle génération de cellules photovoltaïques afin de promouvoir un futur basé sur des énergies renouvelables. Pourtant, tout comme les CIGS and CdTe, les impuretés et les défauts engendré lors de la cristallisation retarde le développement des cellules photovoltaïque CZTS. Dans cette thèse, CZTS est étudié comme un type alternatif de cellules solaires reconnu par les récentes technologies photovoltaïques émergentes comme les cellules solaires à colorant, à boîte quantique, à base de pérovskite qui a par ailleurs la plus grande tolérance contre les défautscristallins des cristaux photo-absorbants. Plus précisément, cette thèse étudie le CZTS comme absorbeur de lumière nanométrique qui est enduits sur une structure de conducteur de charges (dans ce cas $TiO_2$). Par la suite, la cellule photovoltaïque est créée en ajoutant une jonction liquide photoélectrochimique ou une jonction solide de conducteurs de trous. La thèse étudiera aussi les effets apportés par d'autre type de substrat de $TiO_2$, le changement de la méthode de déposition du CZTS et élaborera une étude approfondie du recuit en utilisant des techniques de caractérisations sur la propriété nanométrique et optique des photos anodes et des dispositifs.

Pour fabriquer une nanostructure absorbant-conducteur, le CZTS a été déposé sous forme de précurseur de sulfure bimétallique sur une couche de $TiO_2$ mésoporeuse pré-fritté via des réactions successives d'adsorption-couche-ionique (SILAR) en milieu aqueux qui est suivie par un recuit pour initier une cristallisation. La composition chimique de la couche est contrôlée par la séquence de déposition-échange choisi, et l'homogénéité est améliorée par l'addition d'une étape de gravure de l'acide chlorhydrique après le recuit. Les tests optiques confirment la fonctionnalité de la couche nanostructuré de $TiO_2$@CZTS et les subséquents travaux ont été dirigé vers la compréhension de la formation de la phase cristalline de CZTS durant le processus du recuit de couche CZTS-$TiO_2$ en utilisant de la spectroscopie Raman in situ. Les tests ont montréqu'un recuit à 400 °C est suffisant pour stabiliser la phase kësterite, mais seulement à 500 °C qu'une cristallisation réactive complète menant à une élimination de la phase de sulfure de cuivre et d'étain (CTS) indésirable est observée. Le plus important, les études in situ à démontrerune dépendancedans le temps lors d'un recuit à 500 °Cpar l'augmentation de l'intensité maximale, le décalage, l'élargissement du spectre Raman de CZTS. Cette propriété est indispensable pour le développement futur des dispositifs sensibilisés au CZTS.

Parallèlement, la variation du conducteur d'électron a étéétudié en synthétisanthydro thermiquement sur des verres FTO des nanobâtons (NR) comme substitue de la couche mésoporeuse de $TiO_2$. De ces deux substructures de $TiO_2$ c'était la dernière qui a montré la performance photovoltaïque la plus forte. Prouvant ainsi, la confirmation de l'hypothèse d'injection collection d'électron pour la photodiode de $CZTS/TiO_2$ et a donc été retenue pour la suite de l'étude. Les prototypes de cellules photoélectrochimiques utilisant des nanobâtons de $TiO_2$ ont démontré une efficacité relativement modeste de 0.25 %. Il a été conclu qu'il faut augmenter la quantité de nanocristal de CZTS déposé sur la substructure de nanobâton rutile et diminuer la recombinaison interfaciale de $CZTS/TiO_2$ en modifiant l'approche de la technique de déposition en solution. Par conséquent une méthode revêtement utilisant un mélange d'eau/éthanol comme solvant a été développé pour déposer le CZTS sur NRs de $TiO_2$ qui aboutis à une meilleure qualité de couche de këstерite confirmée par une caractérisation via des techniques de SEM de haute résolution (HR), de TEM, de XPS, optique et électrochimique (spectroscopie d'impédance). Finalement une cellule solaire solide sensibilisée de $TiO_2$NR@CZTS, avec spiro-OMeTAD comme le médium de transport de trous et CdS comme le couche de tampon, a été assemblé avec succès qui a montré une augmentation 10 fois supérieur en efficacité de conversion de puissance (2 %), et il ouvre le chemin à un développement d'application optoélectronique alternative de CZTS-$TiO_2$.

# FOREWORD

This thesis has been compiled using manuscript-based format, as prescribed by McGill University thesis preparation guidelines. The following research articles have been included as chapters 3, 4, 5, and 6 in this thesis respectively.

1. Zhuoran Wang, and George P. Demopoulos, 2016, Nanoscale Photo-Absorbing Kesterite Grown on Anatase Mesoscopic Films by Sequential Binary Chalcogenide Solution Deposition-Exchange, Annealing, and Etching, *Cryst. Growth Des.*, 16 (7), 3618–3630.
2. Zhuoran Wang, Samir Elouatik, and George P. Demopoulos, 2016, Understanding the Phase Formation Kinetics of Nano-Crystalline Kesterite Deposited on Mesoscopic Scaffold via In-Situ Multi-Wavelength Raman-Monitored Annealing, *Phys. Chem. Chem. Phys.*, 18, 29435-29446
3. Zhuoran Wang, and George P. Demopoulos, 2015, Growth of $Cu_2ZnSnS_4$ Nanocrystallites on $TiO_2$ Nanorod Arrays as Novel Extremely Thin Absorber Solar Cell Structure via the Successive-Ion-Layer-Adsorption-Reaction Method, *ACS Appl. Mater. Interfaces*, 7 (41), 22888–22897.
4. Zhuoran Wang, Raynald Gauvin, and George P. Demopoulos, 2017, Nanostructural and Photo-electrochemical Properties of Water-Ethanol Clear Solution Spin-coated $Cu_2ZnSnS_4$-$TiO_2$ Nanorod Forest Films with Improved Photovoltaic Performance. *Nanoscale*, 9 (22), 7650-7665

Dr. Samir Elouatik assisted in the set-up of in-situ Raman characterization and analysis. Prof. Raynald Gauvin helped us with nanoscale morphology characterization using electron microscope SU8230. All experimental work, analyses, and writing of the manuscripts were carried out by the author. Prof. George P. Demopoulos provided overall guidance for the research work and assistance with the writing of the manuscripts.

The accuracy of the contribution of authors is attested by the author's supervisor

Professor George P. Demopoulos
Mining and Materials Engineering
McGill University
Montreal, QC, Canada

# ACKNOWLEDGEMENTS

The journey of doctoral study is a mix of joys and bitterness, which could not be accomplished without the persistence in oneself and more importantly the support from the others. I am fortunate to have many people accompanied though this journey of intellectual training. First of all, I would like to send my sincerest gratitude to Professor George P. Demopoulos for providing me the opportunity to embark upon this great adventure, and the unremitting support throughout the whole time. I am greatly thankful for his trust and confidence in me even during the hardest, unfruitful period of the project, which is the major power that has stimulated me to overcome difficulties and make breakthrough eventually. I am especially thankful for his guidance though my manuscripts writing and his advices during each meeting, from which I have improved a lot. I believe all his influences on me will be precious assets for my future research career.

The next person I would like to thank is my wife Sihan Ran, who quitted her job and accompanied me to Montreal two years ago. She has been supporting me not only by sparing the burden of daily life so that I can be more concentrated on research, but also she listens to my troubles and her suggestions have helped me overcome many difficulties in research. It is impossible for me to go through all these without her by my side. Every bit of my achievement is also hers. Also, I can never thank my parents enough for their unconditional supports in both emotional and financial ways all the time. They give so much but only ask for so little, for which I am deeply and sincerely grateful.

During these years I am lucky to have met many good people and made friends of life. I want to thank all of them for listening to my troubles and sharing my joys. Dr. Xia Lu, a former post-doc fellow in our group, has helped me a lot with my research. His passion, persistence and rigorous attitude in scientific research has profoundly influenced me, which has greatly stimulated my interests and motivations. Dr. Hsien-chieh Chiu, who is like a big brother to us all in the HydroMET group, to whom I could like to thank a lot for all the technical supports for the lab. Then I would like to thank all the other past and present

members of group, especially, Fuqiang, Belete, Ravi, Christine, Han, Helen, Marianna, Konstantina, Majid, Andrea, Thomas, Nima, Nathan, Amrita. I am particularly grateful to Mr. William Courchesne, a very talent young researcher, who has single-handedly developed an effective production line of perovskite solar cell and unconditionally shared all his experience with me. And I still benefit a lot from the method he developed for preparing Spiro-OMeTAD. I will not forget the last batch of devices we made together which achieved surprisingly high efficiency of 15%. Also, I thank him very much for helping me with the abstract translation and French practicing.

I would like to thank my non-research related friends Dr. Duo Zhang and Dr. Binhan Sun for all the help and company during these years, and for many new insights they brought from their field of study which were also beneficial to my research. And also the friends from McGill: Yu Cao, Qijun Tang, Xiao Zhou, Baoqi Guo, Weizhen Wang, Xin Chu, to whom I am grateful for their help in both my research and personal life. Special thanks to Mrs. Francoise Guindon and Mr. Chris Michel for helping me fit in the local culture and life during my first two years in Montreal.

I am very thankful for all the technical help I received for my research. I appreciate the help with SEM and EDS by Nicolas Brodusch and Professor Raynald Gauvin, and the assistance with TEM operation by Dr. Xuedong Liu. I also would like to thank Dr. Samir Elouatik for his assistance with Raman, Dr. Lihong Shang for the training and help with XPS, Mr. Ranjan Roy and Andrew Golzstajn for the help with ICP-OES, and all the staff members of the Microfab lab especially Jun Li, Zhao Lu, Alireza Mesgar, and Sasa Ristic for the help with equipment training. Also I would like to thank Dr. Hendrix Demers very much for the help with the proof-read and correction of my French abstract.

Last but not the least I very humbly acknowledge the financial assistance by NSERC (Natural Science and Engineering Research Council of Canada) MEDA (McGill Engineering Doctoral Award), the Department of Materials Engineering, and the support from Targray Technology International, 5N Plus, and CIS Scientific.

# TABLE OF CONTENTS

# LIST OF FIGURES

# LIST OF TABLES

# CHAPTER 1

–

# INTRODUCTION

## 1.1 Motivations

### 1.1.1 Photovoltaic Technology

Photovoltaic (PV) technology has greatly advanced since French scientist Edmond Becquerel discovered the photon-to-electron conversion effect.[1] Capturing natural sunlight to generate electricity for the masses, especially when facing the increasing pressure from energy shortage and environmental pollution in recent years is one of humanity's great hopes. However, the cost and pollution problems associated with classical PV fabrication technology have largely limited its wide adoption. With the development of new PV technologies in recent years, the solar power generated electricity price now is much lower than before. But still highly-efficient low-cost modules made of abundant elements are needed to meet the increasing global energy demand. More importantly, the negative environmental impact of conventional solar panel production has been highlighted.[2] Hence there is an interest for more environmentally friendly solar energy technologies to be developed.

Crystalline silicon solar cells (mono- and polycrystalline silicon) - constituting the first generation - have dominated the market since they are the most developed technology with their high efficiency for single junction solar cells being 25%.[3] Thin film solar cells are regarded as the second generation using very thin layer (a few micrometers) of active materials with high optical absorption coefficient to capture sufficient solar energy. Among them, Copper-indium-gallium-selenide (CIGS) and cadmium telluride (CdTe) solar cells are the dominant technologies. The efficiency of thin film solar cells have approached the level of silicon cells after years of improvement (over 20%). However, the expensive or toxic elements contained in their composition (indium, cadmium, and tellurium) make them less sustainable options over the long term. Meanwhile, the vacuum-processed fabrication method used like sputtering, evaporation and so on inevitably raise the cost. The new generation of the emerging technologies within a couple decades like organic PV[4], quantum-dot[5] and dye-sensitized cells[1] promise significantly lower fabrication cost due to their amenability to solution processing. However, they tend to yield lower efficiencies than the other PV types not to mention other problems like stability for long service life. Very recently, a new type of light absorber – hybrid organic-inorganic lead halide perovskite - has arisen to prominence with solid state solar cell efficiency of ~ 20%[6] bringing low-cost high-efficient PV closer to becoming a reality. However, the organic-inorganic lead based perovskite absorber is highly humidity-sensitive not to mention that it contains toxic lead (Pb), hence there is need to continue the search for an alternative non-toxic and stable inorganic sensitizer.

### 1.1.2 $Cu_2ZnSnS_4$ Solar Cells

$Cu_2ZnSnS_4$ (CZTS) is a competitive candidate due to its optimal optical properties and the abundant and low cost elements it is made of.[7] However its full potential is still to be materialized because of the difficulties in controlling its quaternary composition and phase crystallinity. Among the various fabrication methods, hydrazine based solution-processing has achieved the best control towards phase crystalinity, enabling the building of thin film solar cells (similar to CIGS) with certified efficiency of 12.6 %.[8] However, the highly toxic and reactive hydrazine solvent that is used greatly limits the further development/commercialization. Though alternatives have been investigated in this regard,[9] aqueous or water/ethanol mixture solutions as opposed to highly toxic organic solvents, may offer versatility, low-cost, and more environmentally-friendly approach to this challenge. Moreover, the traditional thin film solar cell structure requires CZTS to function simultaneously as both light absorber and charge conductor, which compromises its excellent light absorbing property due to its usually high defect/impurity density.

### 1.1.3 Light Absorber- Conductor Nanostructure

In parallel to the thin film p-n junction solar cell configuration, light absorber-charge conductor structure[10] has been widely investigated in recent years. Examples like dye-sensitized solar cells,[11] perovskite solar cell,[6a] quantum dots[12] and inorganic semiconductor sensitized solar cells[13] are featuring a thin layer of light absorbing materials (i.e. dye, perovskite, quantum dots, inorganic semiconductor nanoparticles, etc.) attached to wide bandgap semiconductors as charge conductors (i.e. $TiO_2$, ZnO, etc.). In this device configuration, the light absorbing process can be isolated from the charge transferring/collecting process which is fulfilled solely by the charge conductors.[10] In most cases, the charge conductors are applied in the form of nanoparticle-built mesoscopic films,[13] nanorod arrays,[14] nanotubes,[15] etc. These three-dimensional nanostructures have large light interaction volume as well as reasonable absorber loading density, hence can harvest sufficient fraction of incident photons. With its inherent separated light absorbing and charge conducting functionalities, the absorber-conductor nanostructure should be a good platform to exploit the light-absorbing advantages of CZTS for photovoltaic application. This is indeed the scope of this thesis that explores the potential of the CZTS light absorber- $TiO_2$ electron conductor device configuration, aiming at developing a new alternative to the traditional thin film CZTS solar cell structure.

## 1.2 Research Objectives

The research described in this thesis is focusing on the fabrication, characterization and PV analysis of CZTS based light absorber-$TiO_2$ charge conductor photoanodes. The specific objectives are:

- To develop aqueous solution based methods for in-situ deposition of CZTS on electron conductor $TiO_2$ sub-structure;
- To realize the composition/phase control of CZTS directly on $TiO_2$ sub-structure and study the annealing-induced crystallization of CZTS kesterite phase;
- To verify the feasibility of electron injection from CZTS to $TiO_2$ by fabricating preliminary solar cell devices using CZTS/$TiO_2$ composite electrode (“photoanode”);

- To optimize the device photovoltaic performance by altering the synthesis/annealing conditions, conducting nanoscale characterization and photo-electrochemical analysis, and performing interface engineering.

## 1.3 Thesis Layout

This thesis follows manuscript-based structure. Chapter 1 introduces the motivation and objectives of the proposed research. Chapter 2 provides extensive literature review of $Cu_2ZnSnS_4$ (CZTS) thin film solar cells, light absorber-charge conductor structured solar cells as well as a specific review of CZTS sensitized solar cell research. Chapter 3 details the in-situ growth of nanoscale light absorber CZTS (kesterite phase) with uniform composition on a sintered anatase mesoscopic film via sequential binary chalcogenide solution deposition, ion-exchange, annealing and etching; and its preliminary optical property evaluation. The following Chapter 4 introduces the in-situ Raman spectroscopy monitored annealing method to investigate the phase formation of kesterite built on the anatase mesoporous scaffold. Chapter 5 describes the aqueous solution deposition of CZTS nanocrystallites on a different $TiO_2$ sub-structure, namely rutile nanorod arrays; and demonstrates early stage photovoltaic response, serving as “proof-of-concept” of the new absorber-conductor CZTS/$TiO_2$ solar cell. Chapter 6 describes the optimization of the CZTS/$TiO_2$ photoanode and device by investigating further the CZTS solution coating method, the growth of the $TiO_2$ rutile nanorods, the device interface structure including the use of solid hole-transfer electrolyte. Lastly, Chapter 7 provides a summary with major conclusions, original contributions to knowledge, and an outlook for future work.

## 1.4 References

1. Gratzel, M., Photoelectrochemical Cells. *Nature* **2001,** *414* (6861), 338-344.

2. Hernandez, R. R.; Easter, S. B.; Murphy-Mariscal, M. L.; Maestre, F. T.; Tavassoli, M.; Allen, E. B.; Barrows, C. W.; Belnap, J.; Ochoa-Hueso, R.; Ravi, S.; Allen, M. F., Environmental Impacts of Utility-Scale Solar Energy. *Renewable and Sustainable Energy Reviews* **2014,** *29*, 766-779.

3. Green, M. A.; Emery, K.; Hishikawa, Y.; Warta, W.; Dunlop, E. D., Solar Cell Efficiency Tables (Version 48). *Progress in Photovoltaics: Research and Applications* **2016,** *24* (7), 905-913.

4. Gasparini, N.; Lucera, L.; Salvador, M.; Prosa, M.; Spyropoulos, G. D.; Kubis, P.; Egelhaaf, H.-J.; Brabec, C. J.; Ameri, T., High-Performance Ternary Organic Solar Cells with Thick Active Layer Exceeding 11% Efficiency. *Energy & Environmental Science* **2017**.

5. Lan, X.; Masala, S.; Sargent, E. H., Charge-Extraction Strategies for Colloidal Quantum Dot Photovoltaics. *Nature Materials* **2014,** *13* (3), 233-240.

6. (a) Snaith, H. J., Perovskites: The Emergence of a New Era for Low-Cost, High-Efficiency Solar Cells. *Journal of Physical Chemistry Letters* **2013,** *4* (21), 3623-3630; (b) Yang, W. S.; Noh, J. H.; Jeon, N. J.; Kim, Y. C.; Ryu, S.; Seo, J.; Seok, S. I., High-Performance Photovoltaic Perovskite Layers Fabricated through Intramolecular Exchange. *Science* **2015,** *348* (6240), 1234-1237.

7. Mitzi, D. B.; Gunawan, O.; Todorov, T. K.; Barkhouse, D. A. R., Prospects and Performance Limitations for Cu-Zn-Sn-S-Se Photovoltaic Technology. *Philosophical Transactions of the Royal Society a-Mathematical Physical and Engineering Sciences* **2013,** *371* (1996).

8. Wang, W.; Winkler, M. T.; Gunawan, O.; Gokmen, T.; Todorov, T. K.; Zhu, Y.; Mitzi, D. B., Device Characteristics of CZTSSe Thin-Film Solar Cells with 12.6% Efficiency. *Advanced Energy Materials* **2013**, 1301465.

9. Romanyuk, Y. E.; Fella, C. M.; Uhl, A. R.; Werner, M.; Tiwari, A. N.; Schnabel, T.; Ahlswede, E., Recent Trends in Direct Solution Coating of Kesterite Absorber Layers in Solar Cells. *Solar Energy Materials and Solar Cells* **2013,** *119* (0), 181-189.

10. (a) Roelofs, K. E.; Brennan, T. P.; Bent, S. F., Interface Engineering in Inorganic-Absorber Nanostructured Solar Cells. *The Journal of Physical Chemistry Letters* **2014,** *5* (2), 348-360; (b) Hodes, G.; Cahen, D., All-Solid-State, Semiconductor-Sensitized Nanoporous Solar Cells. *Accounts of Chemical Research* **2012,** *45* (5), 705-713.

11. Kay, A.; Grätzel, M., Dye-Sensitized Core−Shell Nanocrystals: Improved Efficiency of Mesoporous Tin Oxide Electrodes Coated with a Thin Layer of an Insulating Oxide. *Chem Mater* **2002,** *14* (7), 2930-2935.

12. Kim, M. R.; Ma, D., Quantum-Dot-Based Solar Cells: Recent Advances, Strategies, and Challenges. *The Journal of Physical Chemistry Letters* **2015,** *6* (1), 85-99.

13. Choi, Y. C.; Lee, D. U.; Noh, J. H.; Kim, E. K.; Seok, S. I., Highly Improved $Sb_2S_3$ Sensitized-Inorganic–Organic Heterojunction Solar Cells and Quantification of Traps by Deep-Level Transient Spectroscopy. *Advanced Functional Materials* **2014,** *24* (23), 3587-3592.

14. Dongwook, L.; Kijung, Y., Solution-Processed $Cu_2ZnSnS_4$ Superstrate Solar Cell Using Vertically Aligned ZnO Nanorods. *Nanotechnology* **2014,** *25* (6), 065401.

15. Roy, P.; Kim, D.; Lee, K.; Spiecker, E.; Schmuki, P., $TiO_2$ Nanotubes and their Application in Dye-Sensitized Solar Cells. *Nanoscale* **2010,** *2* (1), 45-59.

# CHAPTER 2

–

# LITERATURE REVIEW

## 2.1 Overview

This chapter provides introductory information and a survey of research studies undertaken previously related to the research presented in this thesis. It contains three main sections: 1. copper zinc tin sulfide (CZTS) and the current research status of CZTS thin film photovoltaics; 2. the absorber-conductor solar cell device structure in comparison to the thin film configuration and its research status; 3. CZTS sensitized nanostructured solar cells. In each section, general introduction and up-to-date technological/research progress are provided.

## 2.2 Copper Zinc Tin Sulfide (CZTS)

Thin film photovoltaic cells featuring direct band gap light absorbing materials such as copper indium (gallium) diselenide (CIGS) and cadmium telluride (CdTe) have reached the commercialization stage with highest reported conversion efficiency of over 21% in lab and over 15% for module production.[1] Copper zinc tin sulfide (CZTS) has a great resemblance to CIGS in terms of optoelectronic and crystallographic properties that due to its earth abundant and environmentally benign compositional nature, has been the subject of interest since the late 2000s as a promising candidate for solar cell applications.[2] The class of related materials includes other $I_2$-II-IV-$VI_4$ such as copper zinc tin selenide (CZTSe) and the sulfur-selenium alloy CZTSSe. So far, a record efficiency of 12.6% was made in laboratory,[3] but still it is far below the Shockley–Queisser limit (around 30%).[4] There is still plenty of room for optimization towards a higher efficiency device. Also, further work is still needed to realize the commercialization of the CZTS thin film solar cells.

### 2.2.1 General properties of CZTS

Generally accepted, CZTS has three principal crystal structures known as kesterite, stannite and wurtzite as shown in Figure 2.1.[5] Kesterite is the most common crystalline phase of CZTS and also the most widely investigated one in solar cell research as is highly related to the chalcopyrite crystal phase of CIGS. The anions and cations in a kesterite CZTS crystal are located in a tetrahedral bonding environment which is similar to zinc blende (the crystal structure of ZnO and ZnS)[6]. Stannite is another important crystal structure of CZTS. The difference between kesterite CZTS crystal and stannite CZTS crystal lies in a different order in the cation sub-lattice. The wurtzite structure can be formed by replacing Zn(II) with Cu(I), Zn(II) and Sn(IV) in wurtzite ZnS with each sulfur atom equally coordinating with two Cu(I), one Zn(II), and one Sn(IV).[7]

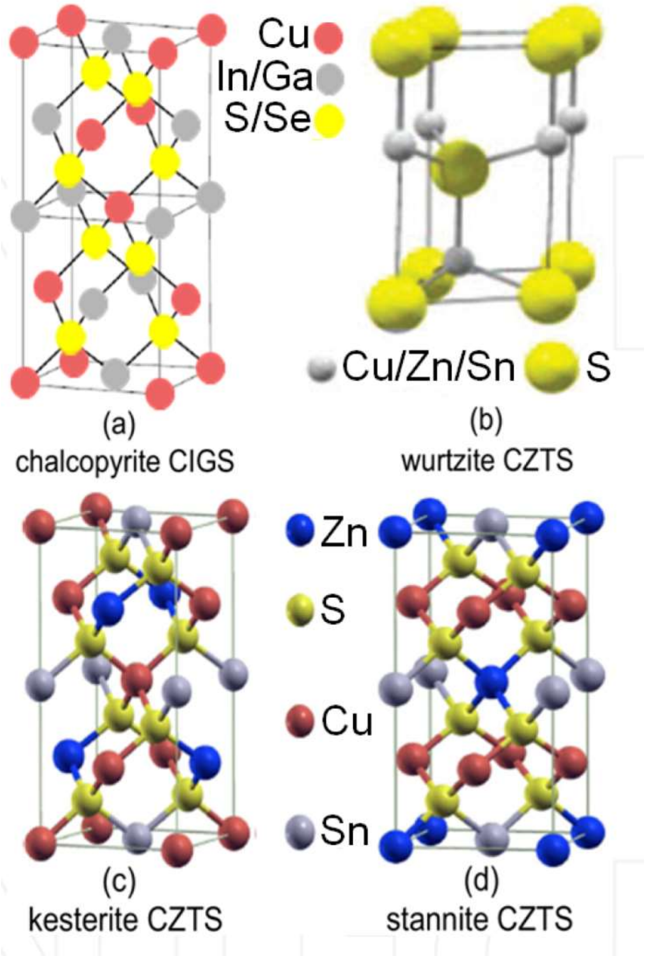

(a) chalcopyrite CIGS
(b) wurtzite CZTS
(c) kesterite CZTS
(d) stannite CZTS

Figure 2.1 Crystal structures of CIGS and CZTS.[5]

CZTS and its selenide alloy CZTSSe has a tunable band gap from 1.0 eV to 1.5 eV,[8] which is the optimal direct bandgap for photovoltaic application considering the competition between light absorption and charge recombination. As a direct bandgap semiconductor, it has a visible light absorption coefficient as high as $10^4$ $cm^{-1}$, with a resistivity ranging from $10^{-3}$ Ω·cm to $10^3$ Ω·cm.[5, 9] Therefore, CZTS holds the potential to enable the development of low-cost high-performance solar cells. However, the carrier mobility in CZTS, according to Hall effect measurements, is in the range of less than 1 to 10 $cm^2V^{-1}S^{-1}$,[9, 10] depending on the synthesis procedure, a relatively low value that limits the maximum thickness of CZTS thin film. Issues such as impurities (ZnS, $Cu_2S$, $Cu_2SnS_3$, $Cu_3SnS_4$) and defects (antisites, intermediate band)[11] have prevented CZTS from fully materializing its excellent light absorbing property when applied to thin film solar cell application.

## 2.2.2 CZTS thin film solar cells

### 2.2.2.1 Device structure

Solar cells can convert light into electricity based on the built-in electric field by p-n junction. Unlike silicon solar cells, which are intentionally doped with either atoms of phosphorus or boron to form n-type and p-type materials, respectively, CZTS is self-doped due to intrinsic defects, and in most cases it is a p-type semiconductor. Since the direct bandgap semiconductor has relatively higher light absorption coefficient, only a thin layer of material (few micrometers) can lead to maximum utilization of solar energy, hence it can enable thin film photovoltaic applications. Conventionally, like CIGS and CdTe, CZTS can be deposited as a thin layer onto substrate followed by incorporation of a n-type material to fabricate standard type thin film solar cells. Figure 2.2 shows a typical CZTS thin film device structure fabricated layer-by-layer in comparison to CIGS.[12] Briefly, molybdenum thin film with thickness of 500~700 nm is sputtering-deposited on glass substrate as back contact. The absorber layer, p-type CZTS thin film with thickness ranging from 1.0 to 2.0 μm is then coated on Mo thin film. To form p-n junction with the p-type CZTS, 50~100 nm n-type CdS thin film is deposited on the absorber layer usually by chemical bath deposition. The surface of CZTS thin film is usually difficult to be fully covered with CdS. To prevent current leakage because of this poor coverage, 50~90 nm intrinsic ZnO (i-ZnO) thin film is usually sputtered on CdS before 500~1000 nm transparent conducting oxide (TCO) thin film is deposited by sputtering as the front contact layer of the cell. Finally, to electrically measure the J-V property of the CZTS solar cell, Ni/Al grid is separately deposited on both TCO and Mo layer.

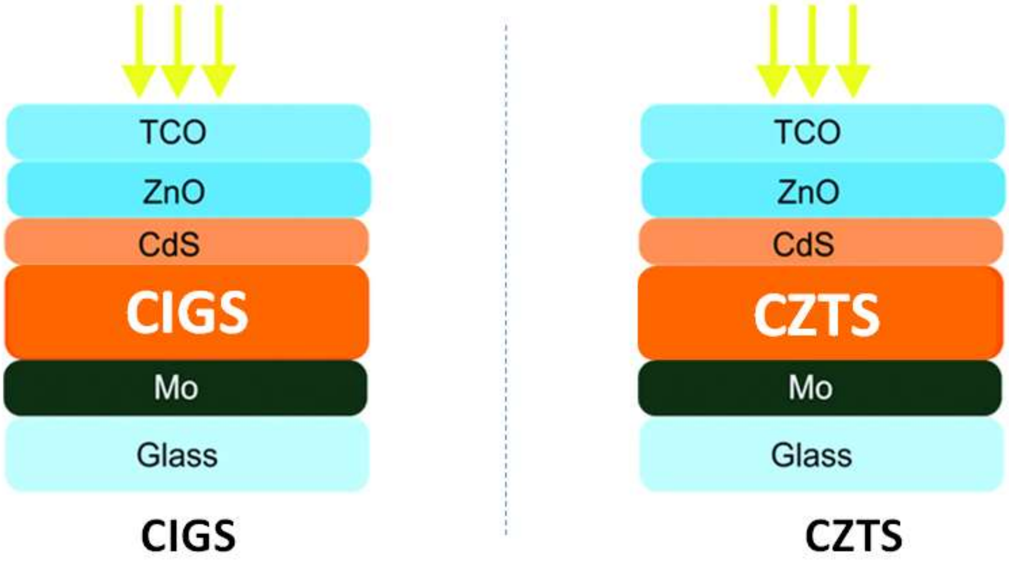

Figure 2.2 Device structure of CIGS and CZTS thin film solar cells.[12]

### 2.2.2.2 Fabrication of CZTS thin films

2.2.2.2.1 Vacuum based deposition

2.2.2.2.1.1 Sputtering deposition

Vacuum based deposition, due to its controllable operating environment, has been widely applied for high quality semiconductor fabrication. Sputtering and evaporation are the two most popular vacuum based methods being used for thin film deposition, which have been proven effective in thin film photovoltaic field including CIGS and CZTS.

Sputtering deposition was introduced as the first approach for CZTS thin film device fabrication by Ito et al. in 1988.[10a] Sputtering is a popular physical vapor deposition (PVD) method involving ejecting particles from a solid target material - due to bombardment of the target by energetic particles (e.g. gas ions), and depositing them on a substrate (Mo glass in this case). Generally, CZTS(Se) is obtained by first stacking or co-sputtering the precursor elements then followed by high temperature annealing to induce crystallization/phase formation.[13] Katagiri et al.[14] have studied the influence of the composition ratio on co-sputtering deposited CZTS-based thin film solar cells, wherein the important CZTS film material property of copper-poor zinc-rich optimal stoichiometric ratio has been discovered. By sputtering deposition, pure sulfide CZTS has reached the efficiency of 7.9 %[15] and over 9 % efficiency has been reported after introducing selenium.[16]

#### 2.2.2.2.1.2 Thermal co-evaporation

Co-evaporation is another popular vacuum deposition method that has been proven effective in the commercialization of CIGS thin film photovoltaics.[17] For a typical evaporation process, various source materials (targets) are heated by means of electron beam or resistive heating to volatilize them and then deposit them on a substrate by condensation to form a uniform thin film layer. However, for CZTS, this thermal evaporation approach has encountered significant challenges, especially in maintaining the substrate at high temperature while delivering precisely controlled elemental fluxes.[18] Optimization of the co-evaporation deposition/annealing process conducted by IBM researchers has resulted in 8.4 % efficiency for a pure sulfide CZTS thin film solar cell.[19] Later via a combination of electron-beam and RF sputtering methods the efficiency was raised to 9.4 %.[20] An even higher efficiency of 11.6 % has been achieved with a pure selenide CZTSe solar cell.[21] Besides, there are other vacuum methods like pulsed laser deposition (PLD),[22] atomic layer deposition (ALD)[23] etc. that have been investigated for CZTS thin film fabrication but these techniques did not achieve satisfactory composition control, while at the same time they seem to suffer from low yield, low raw material utilization and relatively high cost.[24] These difficulties with the vacuum-based methods have prompted investigations into solution based non-vacuum approaches.

### 2.2.2.2.2 Non-vacuum based deposition

#### 2.2.2.2.2.1 Solution direct coating

The highest efficiency (12.6 %) with a CZTS,Se thin film solar cell has been reached with the non-vacuum solution based approach developed by Wang et al. of IBM.[3] Solution processes may involve dissolved precursor salts or slurries of precursor particles. The pure solution approach based on soluble zinc salts in selenium-containing hydrazine[25] was found to give higher efficiency (12.6 %) than the slurry approach that made use of zinc hydrazinate particles, which yielded 11.1 % efficiency.[26] The two process options are described in Figure 2.3. In the case of the pure solution process option the prepared solution was spin-coated on the substrate to form thin film precursor, followed by 500℃ annealing in the presence of elemental S or $H_2S$.

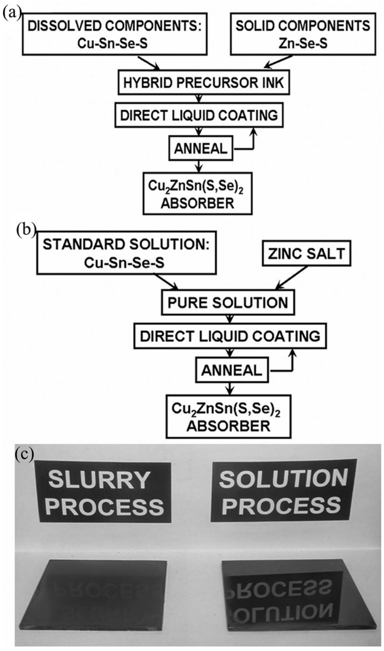

Figure 2.3. Flowcharts for (a) slurry and (b) pure solution-based processes. (c) Image showing better optical reflectivity of solution-processed precursors.[25]

Therefore, the non-vacuum solution coating method is a promising method which offers advantages like the possibility to use low-cost and high yield process equipment, low raw material waste and high uniformity over large area. In this regard, preparing a suitable coating solution is the key to a uniform precursor film of CZTS, and the solvent is one of the most critical components, which is often used to name a particular approach in the scientific community ,i.e. “hydrazine route” or “DMSO route”.[27] A good solvent must have high solubility of Cu, Zn, Sn and S containing compounds to form homogeneous solution, and also should be amenable to complete decomposition without leaving any detrimental carbonaceous residual after annealing. Hydrazine, as a strong reducing agent with high solubility of metal salts and elemental chalcogens (S, Se), has been proven the ideal solvent for non-vacuum solution coating of CZTS,Se as demonstrated with the 12.6 % record efficiency device developed by IBM. However, the highly toxic and explosive nature of hydrazine limits the further development/commercialization of this approach.

Water is the best solvent choice for sure in terms of cost and toxicity. However, no work involves using pure water as solvent to prepare CZTS thin film can be found. It was concluded by Romanyuk et al.[27] that many salts of Cu and Sn readily hydrolyze in water and thus induce high solution acidity ($pH<2$) that can corrode the molybdenum-coated substrate. Also the high surface tension of water makes hard to induce good wetting on the flat substrate surface and oxidation is difficult to avoid. This has led researchers choosing ethanol to replace part of water and use as mixed solvent. This approach led to achieving a device efficiency of over 5% in the case of pure CZTS thin film solar cell.[28] Meanwhile, other solvents including mixtures of alcohols,[29] ethylene glycol,[30] 2-methoxyethanol,[31] pyridine,[32] N,N-dimethyl formamide (DMF)[33] and dimethyl sulfoxide (DMSO)[34] have been widely studied in this regard.

#### 2.2.2.2.2.2 Nanocrystal ink coating

In parallel to the homogeneous solution direct coating technique, formation of semiconductor thin films from nanocrystal (NC) inks is emerging as a very important technology for thin film photovoltaics of CdTe and CIGS. This technique has also been adopted to CZTS and a record efficiency was achieved close to 11 % by Larramona et al.,[35] making it very promising in fabricating highly efficient CZTS,Se solar cells.

The first step of this approach is to prepare the CZTS nanocrystal colloidal “ink”, and a batch reaction method called “hot injection” is the most widely used technique in this regard. Typically, the raw materials are separated into metal salts (“cations”) and chalcogens (“anions”) and dissolved in organic solvents such as oleylamine (OLA). The two solutions are heated up to a relatively high temperature (~250℃) and then one is injected to the other.

The entire process is performed under protection of inert atmosphere, where usually a Schlenk line is involved to provide the required vacuum/inert environment.[36] Afterwards, the formed CZTS nanocrystals are extracted and dispersed in a suitable solvent to prepare the "ink". Various coating techniques such as spin-coating, doctor blading are applied to guarantee a good coverage of Mo glass. Selenization is important for this technique to get highly efficient CZTS,Se devices. This is realized by high temperature annealing/sintering in the presence of elemental selenium. A schematic depiction of this technique is shown in Figure 2.4.[37]

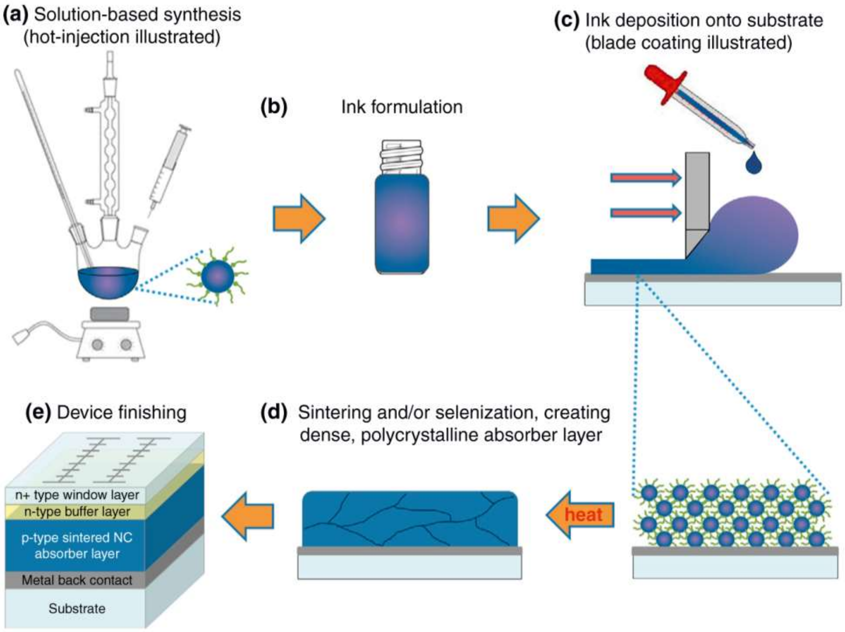

Figure 2.4. Nanocrystal-ink coating for CZTS solar cell fabrication.[37]

The superiority of this technique is: instead of coating the precursor solution, highly crystalline CZTS nanoparticles are being coated, which improves the homogeneity of the entire film and provides opportunity for low temperature processed CZTS solar cells. Nevertheless, high annealing temperature is still inevitable for the purpose of creating dense, polycrystalline, selenized CZTS,Se solar cells. However, the strict requirement of the inert environment for the "hot injection" method is complicating its scale-up, while residual organic solvents/surfactants are very likely to leave impurities in the film after annealing hence lowering its performance.

#### 2.2.2.2.2.3 Other non-vacuum solution based methods

There are several other methods for CZTS thin film deposition, including electrodepositon (ED), spray pyrolysis deposition (SPD), chemical bath deposition (CBD), successive ionic layer adsorption and reaction (SILAR), etc.

Among these, electrodeposition was reported to have achieved CZTS thin film solar cell efficiency of ~ 8 %.[38] The process involves first electrodeposition of metal stacks of either Cu/Zn/Sn or Cu/Sn/Zn onto the substrate followed subsequently by annealing in sulfur vapor atmosphere to get pure crystalline CZTS. Spray pyrolysis (SPD) deposition is another popular method for thin film formation due to its simplicity. In the SPD process, the substrates (as target) are usually heated to a certain temperature while the prepared solution(s) containing the dissolved metal elements and sulfur source is sprayed either altogether or separately to the hot substrate to form CZTS in-situ.[39]

Chemical bath deposition (CBD) and successive ionic layer adsorption and reaction (SILAR) are also important solution based thin film deposition methods. As the name suggests, for the chemical bath deposition method, the substrate is immersed in an aqueous solution containing all precursor elements to effect nucleation and growth of a solid phase film. SILAR is a modified CBD method, in which instead of immersion into a single solution containing both cationic and anionic species, the substrates are immersed sequentially into cationic and anionic solutions for several cycles to induce reaction of the adsorbed ions that leads to film nucleation and growth. Although these methods are quite popular in preparing thin films with simple composition like CdS, CdSe, ZnS, etc., much less work has been reported regarding CZTS, a more complex quaternary compound. But still there are some studies that prove their feasibility. Bent et al. from Stanford University prepared, by chemical bath deposition (CBD) and ion exchange, chalcogenide thin films that upon subsequent sulfurization/heat treatment were successfully converted into CZTS thin films.[40] Figure 2.5 describes schematically the thin film formation sequence. Firstly, ZnS and SnS were deposited on Mo using CBD followed by ion-exchange of part of deposited ZnS with $Cu^{2+}$ in a second solution to form the precursor binary sulfide (CuS/ZnS/SnS) mixture. After annealing under $H_2S$ gas atmosphere, CZTS film was uniformly grown. Additional CBD deposition routes have been investigated.[41]

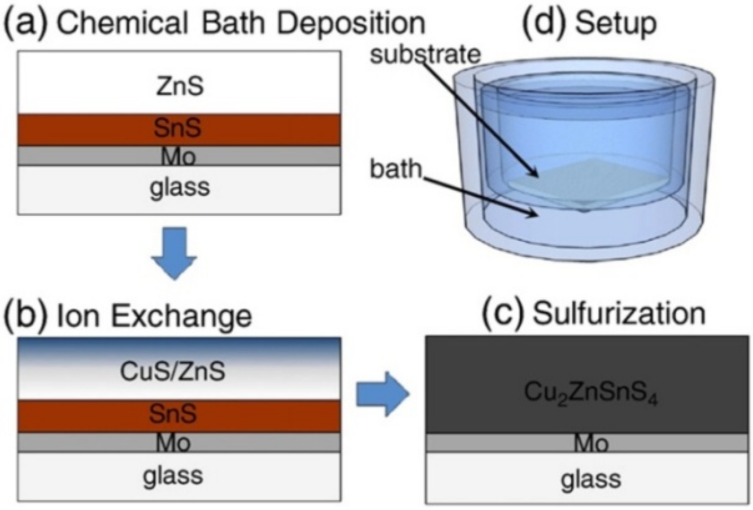

Figure 2.5. Illustration of CZTS film formation with CBD.[40]

Also, there are a few studies involving SILAR processed CZTS thin film deposition. Mali et al. were the first to prepare CZTS thin films using the SILAR method back in 2012.[42] In a typical synthesis sequence, a cationic solution containing all three metal salts and an anionic solution containing $Na_2S$ were used. CZTS was deposited on FTO glass by dipping into those two solutions successively for different number of SILAR cycles. Further, a modified approach was developed by depositing Cu, Sn first and Zn after, which allowed for better controlled composition.[43,44] However, the SILAR method is not particularly suited for deposition on flat substrate as it relies on adsorption for surface reaction to occur. It would be by far more appropriate for application on large surface area porous substrates like mesoscopic films as it is investigated in this thesis.

#### 2.2.2.2.3 Annealing/crystallization of CZTS thin films

Annealing is the final step to induce crystallization of CZTS film as well as removing the entrained part of organic component from the solvent. Nearly all the studies that report functioning CZTS thin film devices involve annealing of the thin film under the protection of inert gas, and more importantly, with the presence of excess sulfur, $H_2S$ for sulfurizaiton or selenium for selenization.[27] The presence of excess S/Se serves to suppress loss of these chalcogens from the film due to volatilization. Additional elemental Sn, SnS or SnSe have also been proven effective in suppressing the decomposition of CZTS,Se during annealing.[45] Annealing temperature is another important factor. Most of the efficient devices were annealed in the range of 500 °C~580 °C,[3, 25-26, 36, 38b, 46] indicating an optimal CZTS,Se crystallization temperature range.

### 2.2.3 Prospects and limits for CZTS,Se thin film photovoltaic technology

The first vacuum-deposited CZTS solar cell was reported by Katagiri et al. with an efficiency of 0.66 % in 1997[47] and the current 12.6 % record holding cell was reported in 2013 by IBM using a solution based method.[3] Although there is a great improvement of efficiency during the past two decades, further performance boosting is required to reach the level of CIGS as well as the current “hot” perovsikte[48] solar cells so CZTS cells become attractive enough for commercialization. Table 2.1 shows a list of selective high performance devices based on CZTS,Se absorber along all their photovoltaic parameters.

Table 2.1 Technological status of CZTS,Se thin film solar cells

| **Absorber** | **Technique** | **Efficiency (%)** | **FF (%)** | **$J_{sc}$ ($mA/cm^2$)** | **$V_{oc}$ (mV)** | **$E_g$ (eV)** |
|---|---|---|---|---|---|---|
| **CZTSSe**[3] | hydrazine solution | 12.6 | 69.8 | 35.2 | 513.4 | 1.13 |
| **CZTSSe**[49] | hydrazine solution | 12.3 | 70.3 | 37.1 | 471 | 1.07 |
| **CZTSSe**[50] | sol-gel | 8.25 | 57.7 | 31.7 | 451 | 1.09 |
| **CZTSSe**[35] | nanocrystal ink | 10.8 | 65 | 32.5 | 510 | 1.18 |
| **CZTS**[19] | co-evaporation | 8.4 | 65.8 | 19.5 | 661 | 1.45 |
| **CZTS**[20] | electron beam and RF sputtering | 9.4 | 63 | 21.3 | 700 | 1.4 |
| **CZTS**[38a] | electrodeposition | 7.99 | 62.8 | 17.7 | 719 | 1.5 |
| **CZTSe**[21] | co-evaporation | 11.6 | 67.3 | 40.6 | 423 | 1 |
| **CZTSe**[51] | DC sputtering | 9.7 | 61.4 | 38.9 | 408 | 1 |
| **CZTGSe**[52] | hydrazine slurry | 9.14 | 60.4 | 31.8 | 476 | 1.15 |
| **CZTGSe**[53] | DMSO solution | 11.0 | 55.9 | 33.6 | 583 | 1.13 |

Generally, the pure sulfide CZTS has the largest bandgap ~1.5 eV and hence the highest Voc value among all the CZTS,Se members, but it suffers from much lower photocurrent value. Selenization is found to be effective to convert CZTS nanoparticles into large CZTS,Se grains while minimizing the number of grain boundaries, thereby largely increasing the cell efficiency by reducing interface recombination.[54] The highest efficiency of CZTS,Se solar cell was achieved by partially selenized CZTS,Se thin film solar cell by IBM with a hydrazine solution coating route.[3] CZTSe though has the advantage of selenium induced larger grain size, its much lower bandgap (~1 eV) has a negative effect on the open circuit voltage of the device as well as the overall power conversion efficiency. As an effective alloying strategy of mixing S and Se to adjust bandgap from 1eV to 1.5eV, the partially selenized CZTS,Se achieves better performance by balancing the light absorption and band-to-band recombination kinetics.

When comparing a high efficient CZTS,Se device to a CIGS solar cell, a larger $V_{oc}$ deficit is seen to plague the CZTS,Se device.[18] The formation of secondary phases, vacancies, antisites and self-compensating defect-complexes in CZTS,Se along with carrier recombination at different interfaces affects device efficiency and may be the main reason for the significantly reduced carrier lifetime.[11] The narrow phase stability and the complexity of the quaternary system complicates the crystallization of CZTS because of competing binary ($Cu_2S$, ZnS, SnS, and $SnS_2$) and ternary phases ($Cu_2SnS_3$), a situation that is further complicated when Se is also introduced. Among all the possible parasitic secondary phases, ZnS is a wide bandgap semiconductor (3.5 eV) considered an insulator that causes a reduced active PV area. $Cu_2S$ is highly conductive in nature on the other hand and may short the solar cell. Moreover, tin sulfides including $SnS_2$, SnS and $Sn_2S_3$ have different properties due to variety of bandgap values, and as such may form recombination centers or barriers for charge collection. The copper-tin-sulfide phase ($Cu_2SnS_3$ or $Cu_3SnS_4$) (CTS) though is considered a light absorber material in itself, recent studies reveal that this material is much less efficient than CZTS thin film hence its formation should be avoided.[55] This is the reason that copper-rich CZTS is undesirable as it is associated with co-formation of CTS. Therefore, for highly efficient CZTS cells any of these secondary phases should be carefully monitored and eliminated.

In addition to the secondary phases, a variety of other defects have been observed in CZTS including vacancies, antisites etc.[11] These defects and defect-complexes form at different energy states within the band gap of CZTS absorbing material. Hence the induced band tail and additional mid-band states tend to lower the effective bandgap while increasing recombination; these defects could be one of the reasons for the large $V_{oc}$ deficit of CZTS in comparison to CIGS as shown in Figure 2.6.[56]

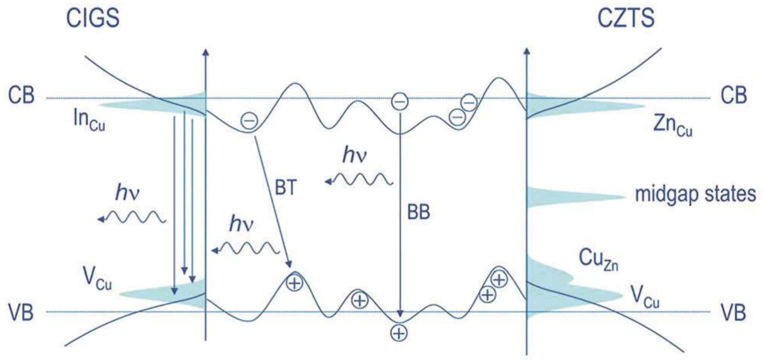

Figure 2.6 The schematic band diagrams of CIGS and CZTS.[56]

In comparison to the traditional X-ray diffraction method which exhibits significant pattern overlapping between CZTS and Cu-Sn-S (CTS) and ZnS phases,[57] Raman spectroscopy is by-far the most common method employed to characterize/identify kesterite as it exhibits reasonably well resolved characteristic vibration modes: bulk CZTS (338 cm$^{-1}$), $Cu_3SnS_4$ (318 cm$^{-1}$), $Cu_2SnS_3$ (298 cm$^{-1}$), and $Cu_{2-x}S$ (475 cm$^{-1}$).[57-58] Different Raman spectroscopy techniques including multi-wavelength Raman spectroscopy,[59] surface-enhanced Raman spectroscopy (SERS),[60] in-depth resolved Raman spectroscopy,[57] etc. have been applied to differentiate CZTS,Se from secondary phases.[61] As a solution to the presence of impurity phases in CZTS films, chemical etching with KCN,[62] HCl[63] or $(NH_4)_2S$[64] have been applied to effectively eliminate Cu-, Zn-, and Sn- chalcogenide secondary phases, respectively, and in this way enhance device performance. Further, sodium is reported to effectively passivate the grain boundary defects hence prolonging the carrier life time.[65] An intermediate layer of Ag[66] or TiN[67] was also applied between CZTS and Mo substrate for a modified interface. All these approaches have been proven useful in minimizing the formation of secondary phases towards improved power conversion efficiency. It would be valuable to understand more clearly the phase formation kinetics of kesterite and its secondary phases, the mechanism by which bulk and crystal defects form, hence contributing to higher-performing CZTS solar cells.

In thin film solar cells with p-n junction configuration, the active materials need to function simultaneously as light absorber and charge carrier, so purity and defect level is as important as its light absorbing ability. However, the complex nature of CZTS as discussed above makes it very difficult to achieve the goal of impurity- and defect- free thin films. As a result the realization of the full potential of CZTS in traditional thin film configuration as achieved with CIGS remains unfulfilled despite otherwise their equivalent optoelectronic properties.

## 2.3 Light Absorber- Conductor Nanostructured Solar Cells

Apart from the conventional bulk p-n junction thin film solar cell configuration which requires the light absorber to transfer charges, the absorber-conductor structure based on a thin layer of light absorbing material on a nanostructured charge conductor is an attractive one. This is so because this structure design may enable the functioning of even "poor quality" absorber compound crystals/molecules as it separates the light absorbing process from the charge transfer one that is carried out by another large bandgap semiconductor ($TiO_2$, ZnO, etc.). A typical example of this type of solar cell is the dye-sensitized solar cell, which is based on the organometallic dye adsorbed on a $TiO_2$ mesoporous film, featuring the dye as light absorber and $TiO_2$ as electron conductor.[68] Currently, most the research attention has been shifted from dye-sensitized solar cells towards perovskite solar cells featuring methylammonium lead halides as light absorber materials, as the latter has shown an impressive conversion efficiency (> 20%) within only a few years.[48] Interestingly, perovskite has proven equally efficient in both cell configurations, i.e. in an absorber-conductor structure (also labeled as sensitized), [69] as well as in a thin film structure[70]. In parallel to the organic dye and organo-metallic perovskite sensitized solar cells, inorganic semiconductors have also been studied in this regard because of their inherent stability. One such group of inorganic semiconductor sensitizers is quantum dots featuring size-dependent light-absorbing small nanocrystals (a few nanometers only) like CdS, CdSe, PbS, PbSe, $CuInSe_2$ etc. and wide bandgap semiconductor as electron conductor; quantum-dot solar cells have reached over 11% efficiency after appropriate surface passivation to quench charge recombination.[71] Meanwhile, other inorganic semiconductors most notably $Sb_2S_3$, which do not fall into the size range of quantum confinement, have been investigated in a similar absorber-conductor structure known as extremely thin absorber (ETA) solar cell,[72] showing significant potential in solar energy conversion application due to their inherent simplicity.

### 2.3.1 Charge extraction strategies

For a solar cell to function properly, the first condition is for the semiconductor to absorb enough photons to generate electron-hole pairs, in other words it is critical to be a good light absorber. However, without a properly designed device structure, the photogenerated charges will immediately be recombined before they are being eventually collected. Therefore, charge extraction is the other key condition for a well functioning PV device to achieve effective separation and collection of the generated electrons and holes.

In thin film solar cells known as the second generation PV technology featuring very thin layer of active materials (such as CIGS or CdTe) the charge extraction is realized by the built-in-electric film within the p-n junction similar to the first generation crystalline silicon solar cells. In this configuration (refer to simplified schematic in Figure 2.7a), the p type or n type junction is formed by either intentionally doping (silicon) or self doping through the formation of intrinsic defects (thin film compounds). After the junction is formed, the diffusion of electrons and holes due to their respective concentration gradients leads to the formation of a charge depleted region where a built-in electric field forms. When the light illuminates on the semiconductor, the generated electrons and holes are separated and driven apart by this internal electric field within the junction region, thus the photocurrent can be collected at the contact. P-n junction is the most widely used structure in optoelectronic devices and has been proven to be an effective charge extraction strategy to achieve a very high efficiency, e.g. ~28.8% for a thin film GaAs solar cell.[73] However, the working mechanism involves simultaneously absorbing light and transferring charges by the active materials, as a result, the semiconductor is imperative to have excellent charge conducting property. Any impurities and unwanted defects in the active material become barriers to charge transfer, and thus significantly affect charge collection efficiency. Therefore, this structure is suitable strictly for very high-purity low-defect semiconductors such as crystalline silicon, III-V group compounds, CdTe, CIGS, etc. but also the recently reported high efficient planar-type perovskite films.[70] This requirement renders light absorbing semiconductors such as quantum dots and other inorganic nanocrystals,[72a, 74] which tend to have short carrier lifetime due to complex composition nature, high defect density, and small grain not suitable for adoption in thin film cell structure despite their excellent light absorbing properties otherwise.

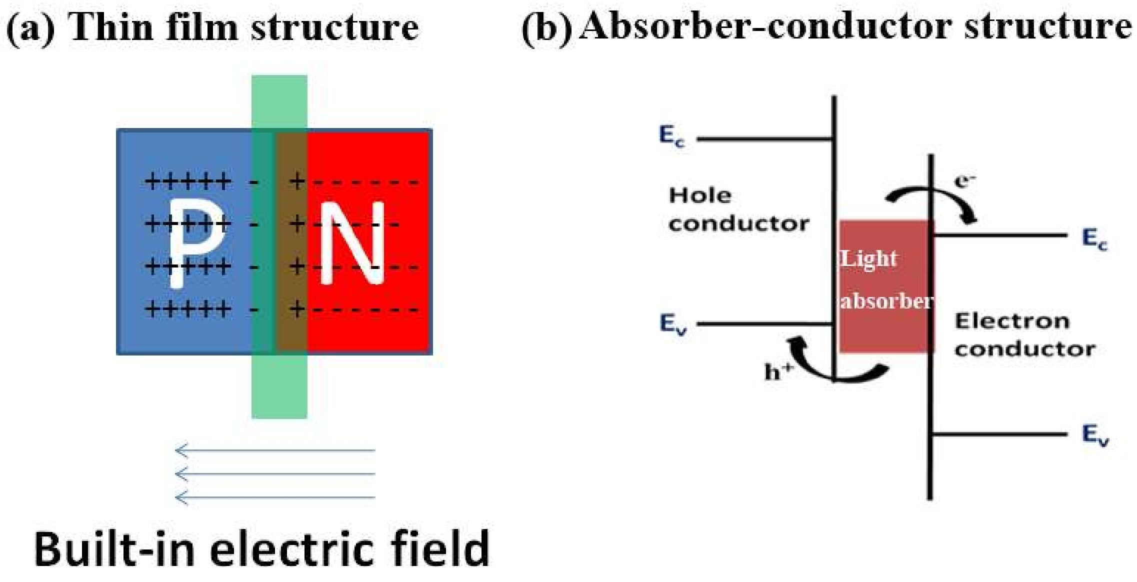
(a) Thin film structure

(b) Absorber-conductor structure

Figure 2.7 Schematics of two charge extraction strategies.

In contrast to the classical thin film structure, the absorber-charge conductor device architecture i.e. dye-sensitized solar cells,[75] quantum dots sensitized solar cells,[76] etc. is characterized by different mechanism of charge collection as shown in Figure 2.7b. Here the light absorber –as a very thin layer (around its charge diffusion length)- is positioned between an electron conductor (a large bandgap semiconductor such as $TiO_2$ or ZnO) and a hole conductor. Charge separation is realized due to the overpotential of the aligned energy band of absorber and conductor materials. Hence the light absorbing and charge transferring process are separated and performed by two different materials, having as result a higher tolerance for impurities and defects in the absorber.[72a] Since only a very thin layer of absorber material can be applied between the hole and electron conductor to ensure efficient charge collection, nanostructures of high porosity/surface area have been used to enhance the overall light absorber loading density (i.e. mesosporous $TiO_2$ films[72b, 77] or ZnO nanorod arrays[78]). The hole transfer materials (HTM) can be either liquid electrolyte with redox species or solid state material like CuSCN,[79] spiro-OMeTAD,[69] P3HT,[80] etc. However, except for the mesoporous based perovskite solar cell which has an efficiency of over 20 %[81], the general efficiency of this type of nanostructured devices is relatively low (~10-12%) mainly due to poor crystal quality and significantly enlarged interface. As a result, these cell technologies have not yet been commercialized despite their promise of low cost manufacturing via solution processing. Significant interface engineering research is the key to realize higher performance PV devices based on the absorber-conductor structure.

### 2.3.2 Dye-sensitized solar cells

The introduction of dye sensitized solar cells (DSSC) in 1991 by O'Regan and Grätzel has attracted great attention since then. The general working mechanism of dye-sensitized solar cells is illustrated in Fig. 2.8.[75] There are three main parts composing a DSSC device: photoanode, counter electrode and electrolyte. The photoanode is fabricated by depositing a layer of mesoporous wide-bandgap semiconductor (usually $TiO_2$) thin film sensitized in dye solution; when sunlight illuminates on it, the excited dye molecules generate electrons that can be directly injected to the conduction band of $TiO_2$. Meanwhile, the mediator (redox couple in electrolyte) is oxidized by reducing the excited state of dye molecule, which is also regenerated by receiving electrons from counter electrode (Pt or C). Thus current can flow in the external circuit. The DSSC device is the typical light absorber (dye)-charge conductor ($TiO_2$ for electron conductor and electrolyte for HTM) structure, which has reached a record efficiency of 12.3 %.[82] However, DSSCs face difficulties in achieving strong broadband absorption with dye species alone on one hand, while on the other the liquid electrolyte compromises their long operational life, hence other materials with better light absorbing property in all-solid state device configuration become very attractive in this regard.

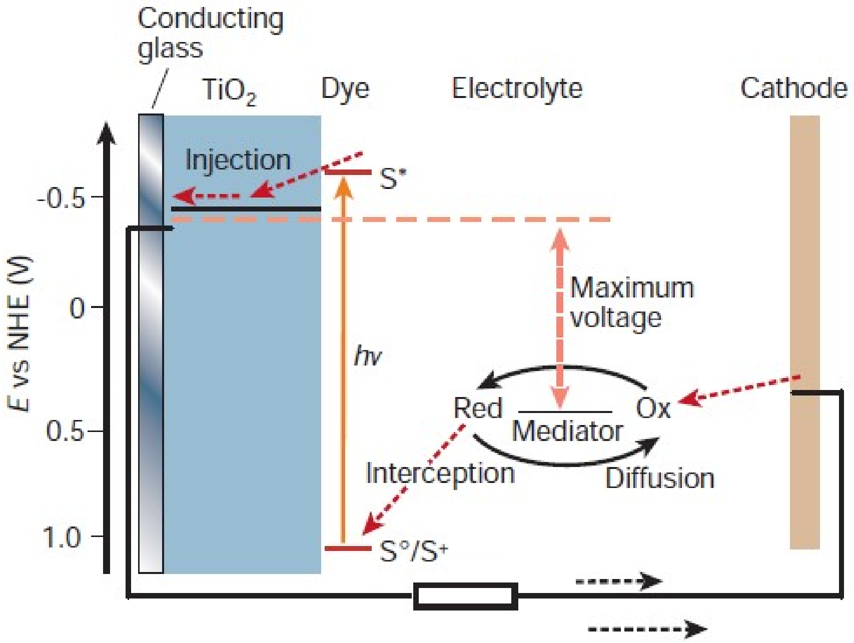

Figure 2.8 Schematic of operation of the dye-sensitized electrochemical photovoltaic cell.[75]

### 2.3.3 Perovskite solar cells

Perovskite solar cells is the most active PV research topic currently with efficiencies having increased dramatically from 3.8% in 2009[83] to 22.1% in early 2016[73], making this the fastest-advancing solar technology ever.[84] The most commonly studied absorber material is methylammonium lead trihalide ($CH_3NH_3PbX_3$, where X is a halogen atom such as iodine, bromine or chlorine), which adopts the $ABX_3$ crystal structure and hence the device is named perovskite solar cell. The optical bandgap varies between 1.5 and 2.3 eV depending on halide content. Two device structures are currently applied as shown in Figure 2.9.[85] Figure 2.9a depicts a perovskite sensitized solar cell configuration where the perovskite material is coated onto a charge-conducting mesoporous scaffold (most commonly $TiO_2$) as light-absorber, which is similar to a dye-sensitized solar cell structure except that the HTM is solid state spiro-OMeTAD instead of liquid electrolyte. Also, the perovskite was found to have high charge mobility for both electrons and holes, hence a planar p-i-n (or inversed) structure was found effective to fabricate solar cell as shown in Figure 2.9b. The current barrier for commercialization of peroskite solar cell is the stability of the absorber material due to its water-sensitivity of the organic constituent. Also, the toxicity of lead has been a potential concern. Intensive studies have been carried out in this aspect. Though the efficiency boosting of perovskite solar cell is breathtaking, light absorber materials with high stability and low toxicity are still needed for practical optoelectronic applications, thus there is a lot of interest in the development of inorganic semiconductor sensitized solar cells.

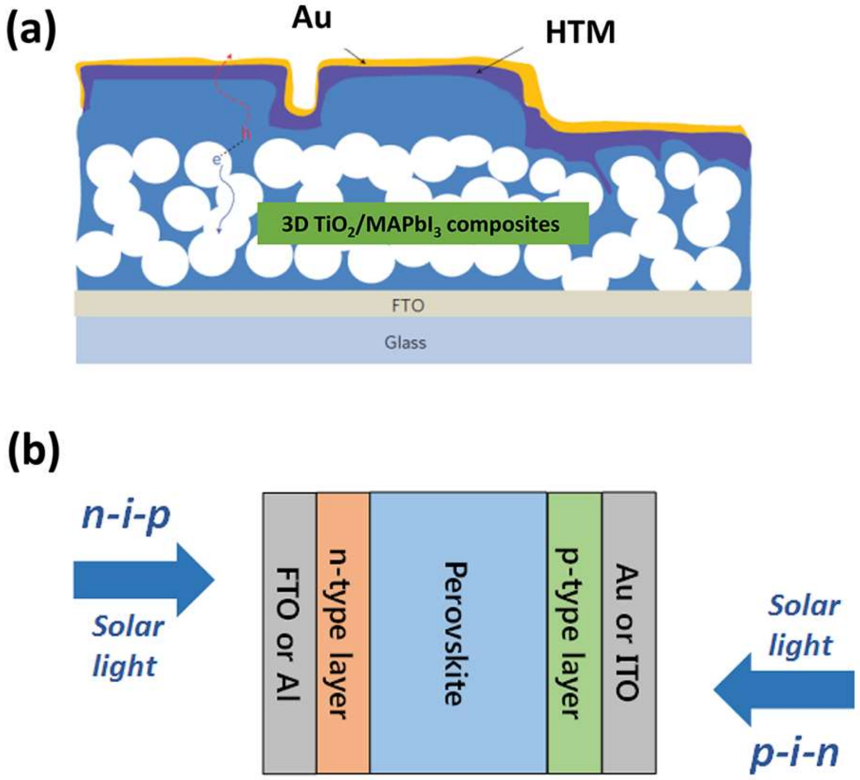

Figure 2.9 a) Sensitized solar cell structure and b) planar thin film structure of perovskite solar cell.[85]

### 2.3.4 Inorganic semiconductor sensitized solar cells

Due to their broad light absorption range in comparison to dye molecules and polymers, inorganic semiconductor absorbers are an attractive alternative for sensitized solar cell application. Moreover, they offer the potential of stable devices not susceptible to light/moisture induced degradation, which is a concern with organic dyes or perovskites. Intensive research has been made in this regard by investigating different inorganic light absorber materials including CdS, CdSe, PbS, PbSe, etc.[77, 86] quantum dots and $Sb_2S_3$ nanocrystals.[72b, 79] An impressive efficiency of 11.6% has been achieved by Du et.al with Zn-Cu-In-Se quantum dots sensitized solar cells,[71b] which is comparable to high efficiency dye-sensitized solar cell devices.[82] For those semiconductors of particle size not small enough to fall into the quantum dot size range, the term "extremely thin absorber solar cells (ETASCs)" is used to refer to inorganic light absorber sensitized solar cells. One such example is $Sb_2S_3$ nanocrystals that have been used to sensitize $TiO_2$ and achieved a device efficiency of over 7%.[72b]

#### 2.3.4.1 Quantum dot sensitized solar cells (QDSSCs)

Quantum dots (QD) are the semiconducting particles with size below the Exciton Bohr radius and hence show special optical and electronic properties such as tunable bandgap,[87] multiple exciton generation (MEG) effects,[88] etc., which offer a possibility beyond the Shockley–Queisser limit.[4] Different device structures have been reported including QD-sensitized solar cells (QDSSCs), QD heterojunction solar cells and QD schottky solar cells.[89] Among them, QD-sensitized solar cells have achieved the highest power conversion efficiency of ~11.6% after a series of interface engineering measures to minimize surface recombination.[71b]

Three methods are currently used to sensitize the electron conductor scaffold (i.e. $TiO_2$, ZnO): 1. coating of pre-synthesized colloidal QD via hot injection;[71] 2. chemical bath deposition (CBD);[90] 3. successive ionic layer adsorption reaction (SILAR).[86b, 87] Among them, the first method is the most widely used in all quantum dot based research as it offers better size/uniformity control of quantum dots via a well controlled synthesis environment, especially for the high efficiency devices. CBD and SILAR are both aqueous solution based methods, which have been demonstrated to be effective in nanocrystal size/composition control and fabricating functioning devices.

To fabricate QDSSCs, pre-synthesized colloidal QDs could either be directly attached onto the nanostructured metal oxides or through bifunctional molecular linkers, such as thioglycolic acid (TGA) and 3-mercaptopropionic acid (MPA).[91] The hole transfer materials (HTM) can be either the liquid polysufide electrolyte[76] or solid state HTM such as CuSCN,[92] P3HT,[93] Spiro-OMeTAD,[94] etc. In addition, copper(I) sulfide ($Cu_2S$) counter electrode is commonly used as catalyst to promote the regeneration of the redox species. Due to the significant surface traps of bare quantum dot-sensitized electrodes, interface engineering becomes equally important as the quality of light absorber materials for improving device functionality. To this end, several passivation methods have been applied including using large-bandgap semiconductors (ZnS, ZnSe, CdS, etc.),[76, 78, 95] metal oxides ($Al_2O_3$, $TiO_2$, $SiO_2$, etc.)[74, 96] and organic molecules,[97] which have proven to effectively reduce charge recombination at interfaces.

#### 2.3.4.2 Extremely thin absorber solar cells (ETASCs)

The term “extremely thin absorber” or “ETA” as reviewed by Hodes, et al. has been used to describe a very thin (mostly <50 nm) semiconductor absorber, deposited on a transparent porous electron conductor, which is then infiltrated with a non light absorbing solid hole conductor.[72a] Both quantum dot sensitized solar cells (QDSSCs) and extremely thin absorber solar cells (ETASCs) fall into the broader category of semiconductor-sensitized solar cells, where the main difference is, as described by Roelofs, et al., whether it exhibits the quantum size effect (i.e. QDSSCs) or not.[74] $Sb_2S_3$ is one of the most efficient absorber materials for ETASCs, having delivered 7.5% record efficiency in 2014 by Choi, et al. upon incorporation of an additional step of thioacetamide (TA) assisted sulfurization. Similar to the QDSSCs, interface engineering is also very important to get efficient devices by suppressing the interfacial recombination. [79, 98]

The ETASC device structure is considered to have higher tolerance for defects and impurities due to the separated light absorbing and charge transfer process, hence it offers opportunities to better enable the optical properties of certain group of materials. For example, CZTS as a quaternary semiconducting compound can be applied to this structure instead of thin film structure. As already discussed previously, thin film CZTS is facing serious difficulties such as composition, impurity and defect control, which leads to a significantly reduced carrier diffusion length. With the absorber-conductor structure, CZTS only needs be used for light absorption and photoelectron generation, while the electron/hole conductors be used for efficient charge transfer, and as such this cell structure offers better chance to realize the low cost, and environmentally friendly advantage of CZTS photovoltaic technology. The exciton Bohr radius for CZTS nanocrystals was estimated to be around 3.4–2.5 nm,[99] which makes it very difficult to make high quality CZTS quantum dots with the common synthesis methods. Therefore, by default the CZTS sensitized solar cells fall into the group of extremely thin absorber solar cells.

## 2.4 CZTS Sensitized Nanostructured Solar Cells

### 2.4.1 Device structure

Similar to the dye/quantum dot sensitized solar cells, the CZTS nanocrystals can be either pre-synthesized or in-situ grown on the electron conductor substrate to prepare the sensitized photoelectrode. More specifically, two types of nanostructured electron conductors are being used which give two different device structures of CZTS sensitized solar cells as shown in Figure 2.10. Similar to dye/quantum dot sensitized solar cells, $TiO_2$ mesoporous films are used in most cases as electron conductor for CZTS sensitized solar cells (Figure 2.10a).[100] Meanwhile, a few studies have explored the potential of a different structure featuring the directly grown nanorods (ZnO or $TiO_2$) as shown in Figure 2.10b.[78, 101] Due to the reduced electron pathway and less grain boundaries to cross, this “one dimensional” nanostructure is considered to have improved charge transfer/collection properties, which hence could serve as good electron conductor for CZTS sensitized solar cells.

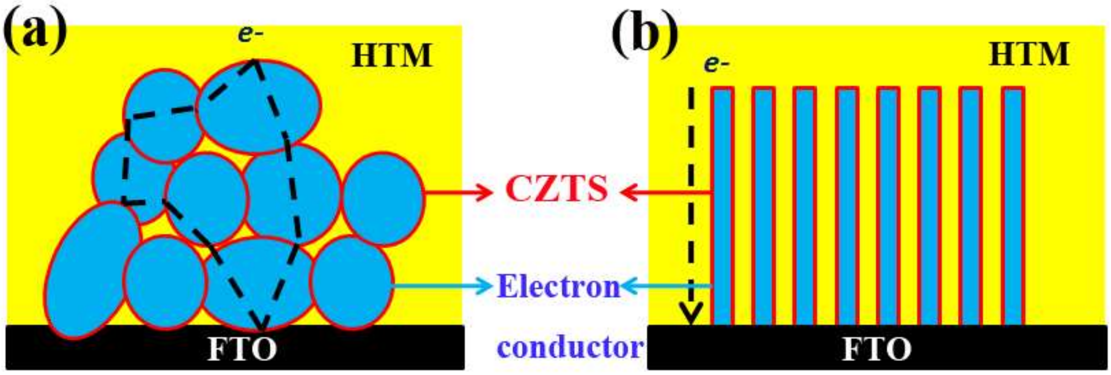

Figure 2.10 a) Nanoparticle-based mesoporous and b) vertically grown nanorod arrays structured electron conductor applied to CZTS sensitized solar cells.

### 2.4.2 Development of CZTS sensitized solar cells

The first fundamental study to replace dye by CZTS to prepare a CZTS sensitized solar cell was performed by Wang et al. in 2013,[100b] where CZTS sensitizer was pre-synthesized via a solid state reaction then dispersed into ethanol to prepare an “ink”. However, after immersing the $TiO_2$ mesoporous film in the CZTS suspension overnight, only a layer of CZTS was found on the surface of $TiO_2$ instead of filling the pores. The lack of sensitizer infiltrating the electron conductor framework was concluded a main reason for the only 0.71 $mA/cm^2$ short circuit current density and 0.29 % power conversion efficiency. The working principle of a CZTS sensitized solar cell with liquid electrolyte is schematically described in Figure 2.11. Due to suitable energy band alignment, when the light illuminates on the device, CZTS generates electrons and holes, the photoelectrons inject to the conduction band of $TiO_2$ and the left holes are removed by the redox triiodide/iodide ($I_3^-/I^-$) species of the electrolyte. A similar device structure was also investigated by Dai et al.[102] and apparently again because of their similar powder suspension sensitizing procedure, lack of good contact between CZTS and $TiO_2$ rendered the device ineffective.

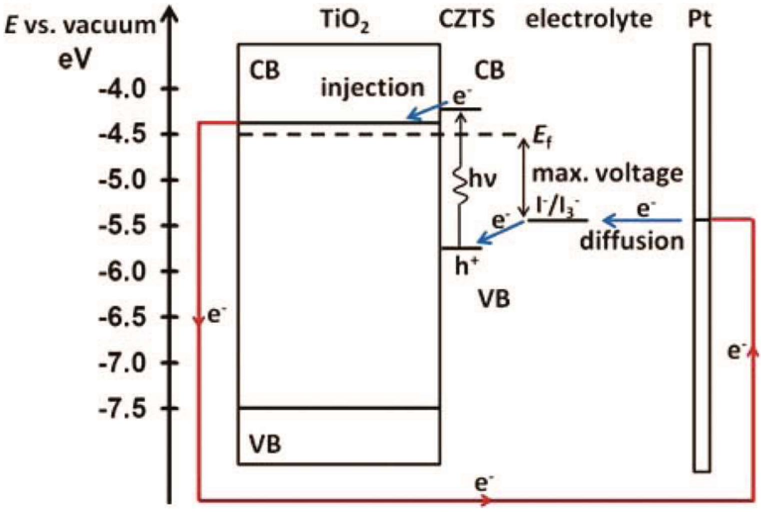

Figure 2.11 Operation principle of a CZTS sensitized solar cell[100b]

Other than good CZTS coating/infiltration of the $TiO_2$ scaffold, another important factor that should be taken into account is interfacial charge recombination caused by the poor quality of CZTS nanocrystals. Hot injection has been used to prepare nanocrystal colloidal "ink" for quantum dot sensitized solar cells,[71b] and also high efficient CZTS(Se) thin film devices,[46b] indicating the superiority of this method to get good quality nanocrystals in terms of morphological and compositional uniformity. By coating the pre-synthesized CZTS nanocrystal "ink" on mesoporous $TiO_2$ scaffold, Bai et al.[100a] have developed an optimized synthesis route that included surface passivation and ligand exchange of nanocrystals that led to an impressive efficiency of 4.7% with the assistance of CdSe, demonstrating the potential for developing highly efficient CZTS sensitized solar cells.

In another development, vertically aligned ZnO nanorod arrays fabricated from low temperature aqueous reaction have been investigated as the sub-structure in CZTS nanostructured solar cells. Lee et al. described a ZnO nanorod arrays based nanostructured CZTS thin film solar cell with efficiency of 1.2%.[101b] This result was further improved by coating a layer of Spiro-OMeTAD as hole transfer material (HTM), and the efficiency was increased from 1.5% (without HTM) to 2.8% (with HTM).[103] Meanwhile, Aftab Akram et al. have investigated a similar structure but with a liquid polysulfide electrolyte instead of the solid state HTM.[78] By performing interface passivation via forming a ZnSe "shell" on the ZnO nanorod core, an efficiency of 2.2% was achieved with the CZTS sensitized photoelectrochemial cell.[78] Besides, $TiO_2$ rutile nanorod arrays have been used as sub-structure to deposit CZTS on a pre-coated CdS buffer layer by Ho et al.,[101a] however, this structure was investigated as a photocatalyst for hydrogen generation but not tested as photoanode in a sensitized solar cell configuration.

### 2.4.3 Limits and prospects

The inorganic semiconductor sensitized solar cell or ETA solar cell, adopting the absorber-conductor charge extraction strategy, offers the opportunity to enable better functioned solar cells with less rigid requirements of the absorber crystal quality, which is especially important for quaternary compounds like CZTS. However, there are challenges that have prevented the development of efficient devices.

The major difficulties in the field of thin film CZTS solar cells is the control of grain size, composition, phase purity and defects, which all impact the charge transfer properties of the active materials. As for a light absorber-conductor structure in the sensitized solar cell, the requirement of high charge mobility for the light absorber is lowered, however, certain control of the composition, phase and defects is still necessary. In comparison to the bulk/thin film single phase materials, the CZTS absorber infiltrated electron conductor imposes much more difficulties in characterizing the composite electrode. Also, the physical contact between the absorber and electron conductor (i.e. $TiO_2$ and ZnO) is usually weak when the ink deposition method is employed, so in-situ deposition of CZTS from solution directly onto the electron conductor sub-structure would be more preferable. But due to the interference of the major background of $TiO_2$ or ZnO, the composition, phase and defect control of the quaternary CZTS becomes even more challenging. To date, no or little work has been devoted to this avenue. Hence, further in-depth study to investigate this absorber-conductor based CZTS solar cell structure is important. Also, the CZTS sensitized device configuration has been mostly realized by hot-injection prepared nanocrystals, which is a relatively low-yield, vacuum and toxic organic solvent based synthesis. In contrast, aqueous or water/ethanol mixture solution based direct formation of CZTS could offer a more attractive synthesis route for potential large scale application, which deserves further efforts.

More importantly, interface engineering is essential in this ultra-fine absorber sensitized solar cell, because the much reduced grain size and significantly enlarged interface will certainly induce high density of surface traps for charge carriers. Herein, a properly pursued strategy for passivated interface is deemed a key in achieving high efficiency CZTS semiconductor sensitized solar cells as the control of quaternary compound composition is more challenging than the binary or ternary quantum dot systems. Several passivating techniques have been reported to reduce the charge recombination of CZTS sensitized solar cells as discussed in the former context. A careful verification and selection of the effective method would be necessary, meanwhile, new effective techniques are to be developed.

In summary, the electron conductor - CZTS absorber layer nanostructure has the advantage of guaranteed optical interaction volume as well as separated light absorption and electron transfer process, hence of interest given the potential for abundant and non-toxic material – based PV cells. It is indeed the scope of this research thesis to investigate the $TiO_2$-CZTS structure and contribute towards the development of all-solid state inorganic PV devices via understanding and controlling solution deposition, annealing, and interface engineering.

## 2.5 References

1. Green, M. A.; Emery, K.; Hishikawa, Y.; Warta, W.; Dunlop, E. D., Solar Cell Efficiency Tables (Version 47). *Progress in Photovoltaics: Research and Applications* **2016,** *24* (1), 3-11.

2. Katagiri, H.; Jimbo, K.; Maw, W. S.; Oishi, K.; Yamazaki, M.; Araki, H.; Takeuchi, A., Development of CZTS-Based Thin Film Solar Cells. *Thin Solid Films* **2009,** *517* (7), 2455-2460.

3. Wang, W.; Winkler, M. T.; Gunawan, O.; Gokmen, T.; Todorov, T. K.; Zhu, Y.; Mitzi, D. B., Device Characteristics of CZTSSe Thin-Film Solar Cells with 12.6% Efficiency. *Advanced Energy Materials* **2013**, 1301465.

4. Shockley, W.; Queisser, H. J., Detailed Balance Limit of Efficiency of P ‐ N Junction Solar Cells. *Journal of Applied Physics* **1961,** *32* (3), 510-519.

5. Jiang, M.; Yan, X., $Cu_2ZnSnS_4$ Thin Film Solar Cells: Present Status and Future Prospects. *Solar Cells- ‑Research and Application Pro- ‑spectives* **2013**, 107-143.

6. Paier, J.; Asahi, R.; Nagoya, A.; Kresse, G., $Cu_2ZnSnS_4$ as a Potential Photovoltaic Material: A Hybrid Hartree-Fock Density Functional Theory Study. *Physical Review B* **2009,** *79* (11), 115126.

7. Lu, X.; Zhuang, Z.; Peng, Q.; Li, Y., Wurtzite $Cu_2ZnSnS_4$ Nanocrystals: a Novel Quaternary Semiconductor. *Chemical Communications* **2011,** *47* (11), 3141-3143.

8. Zhou, H. P.; Hsu, W. C.; Duan, H. S.; Bob, B.; Yang, W. B.; Song, T. B.; Hsu, C. J.; Yang, Y., CZTS Nanocrystals: A Promising Approach for Next Generation Thin Film Photovoltaics. *Energy & Environmental Science* **2013,** *6* (10), 2822-2838.

9. Tai, K. F.; Gunawan, O.; Kuwahara, M.; Chen, S.; Mhaisalkar, S. G.; Huan, C. H. A.; Mitzi, D. B., Fill Factor Losses in $Cu_2ZnSn(S_xSe_{1-x})_4$ Solar Cells: Insights from Physical and Electrical Characterization of Devices and Exfoliated Films. *Advanced Energy Materials* **2016,** *6* (3), 1501609.

10. (a) Ito, K.; Nakazawa, T., Electrical and Optical Properties of Stannite-Type Quaternary Semiconductor Thin Films. *Japanese Journal of Applied Physics* **1988,** *27* (11R), 2094; (b) Tanaka, T.; Nagatomo, T.; Kawasaki, D.; Nishio, M.; Guo, Q.; Wakahara, A.; Yoshida, A.; Ogawa, H., Preparation of $Cu_2ZnSnS_4$ Thin Films by Hybrid Sputtering. *Journal of Physics and Chemistry of Solids* **2005,** *66* (11), 1978-1981.

11. Kumar, M.; Dubey, A.; Adhikari, N.; Venkatesan, S.; Qiao, Q., Strategic Review of Secondary Phases, Defects and Defect-Complexes in Kesterite CZTS-Se Solar Cells. *Energy & Environmental Science* **2015,** *8* (11), 3134-3159.

12. Azimi, H.; Hou, Y.; Brabec, C. J., Towards Low-Cost, Environmentally Friendly Printed Chalcopyrite and Kesterite solar cells. *Energy & Environmental Science* **2014,** *7* (6), 1829-1849.

13. (a) Jimbo, K.; Kimura, R.; Kamimura, T.; Yamada, S.; Maw, W. S.; Araki, H.; Oishi, K.; Katagiri, H., $Cu_2ZnSnS_4$-Type Thin Film Solar Cells Using Abundant Materials. *Thin Solid Films* **2007,** *515* (15), 5997-5999; (b) Hironori, K.; Kazuo, J.; Satoru, Y.; Tsuyoshi, K.; Win

Shwe, M.; Tatsuo, F.; Tadashi, I.; Tomoyoshi, M., Enhanced Conversion Efficiencies of $Cu_2ZnSnS_4$ -Based Thin Film Solar Cells by Using Preferential Etching Technique. *Applied Physics Express* **2008,** *1* (4), 041201.

14. Katagiri, H.; Jimbo, K.; Tahara, M.; Araki, H.; Oishi, K., The Influence of the Composition Ratio on CZTS-Based Thin Film Solar Cells. *MRS Proceedings* **2011,** *1165.*

15. Scragg, J. J.; Kubart, T.; Watjen, J. T.; Ericson, T.; Linnarsson, M. K.; Platzer-Bjorkman, C., Effects of Back Contact Instability on $Cu_2ZnSnS_4$ Devices and Processes. *Chemistry of Materials* **2013,** *25* (15), 3162-3171.

16. Chawla, V.; Clemens, B., Effect of Composition on High Efficiency CZTSSe Devices Fabricated Using Co-sputtering of Compound Targets. *2012 38th Ieee Photovoltaic Specialists Conference (Pvsc)* **2012**, 2990-2992.

17. Wolden, C. A.; Kurtin, J.; Baxter, J. B.; Repins, I.; Shaheen, S. E.; Torvik, J. T.; Rockett, A. A.; Fthenakis, V. M.; Aydil, E. S., Photovoltaic Manufacturing: Present Status, Future Prospects, and Research Needs. *Journal of Vacuum Science & Technology A* **2011,** *29* (3), 030801.

18. Mitzi, D. B.; Gunawan, O.; Todorov, T. K.; Barkhouse, D. A. R., Prospects and Performance Limitations for Cu-Zn-Sn-S-Se Photovoltaic Technology. *Philosophical Transactions of the Royal Society a-Mathematical Physical and Engineering Sciences* **2013,** *371* (1996).

19. Shin, B.; Gunawan, O.; Zhu, Y.; Bojarczuk, N. A.; Chey, S. J.; Guha, S., Thin Film Solar Cell with 8.4% Power Conversion Efficiency Using an Earth-Abundant $Cu_2ZnSnS_4$ Absorber. *Progress in Photovoltaics* **2013,** *21* (1), 72-76.

20. Tajima, S.; Umehara, M.; Hasegawa, M.; Mise, T.; Itoh, T., $Cu_2ZnSnS_4$ Photovoltaic Cell with Improved Efficiency Fabricated by High-Temperature Annealing after CdS Buffer-Layer Deposition. *Progress in Photovoltaics: Research and Applications* **2017,** *25* (1), 14-22.

21. Lee, Y. S.; Gershon, T.; Gunawan, O.; Todorov, T. K.; Gokmen, T.; Virgus, Y.; Guha, S., $Cu_2ZnSnSe_4$ Thin-Film Solar Cells by Thermal Co-evaporation with 11.6% Efficiency and

Improved Minority Carrier Diffusion Length. *Advanced Energy Materials* **2015,** *5* (7), 1401372.

22. Vanalakar, S. A.; Agawane, G. L.; Shin, S. W.; Suryawanshi, M. P.; Gurav, K. V.; Jeon, K. S.; Patil, P. S.; Jeong, C. W.; Kim, J. Y.; Kim, J. H., A Review on Pulsed Laser Deposited CZTS Thin Films for Solar Cell Applications. *Journal of Alloys and Compounds* **2015,** *619*, 109-121.

23. Thimsen, E.; Riha, S. C.; Baryshev, S. V.; Martinson, A. B. F.; Elam, J. W.; Pellin, M. J., Atomic Layer Deposition of the Quaternary Chalcogenide $Cu_2ZnSnS_4$. *Chemistry of Materials* **2012,** *24* (16), 3188-3196.

24. Suryawanshi, M. P.; Agawane, G. L.; Bhosale, S. M.; Shin, S. W.; Patil, P. S.; Kim, J. H.; Moholkar, A. V., CZTS Based Thin Film Solar Cells: a status review. *Materials Technology* **2013,** *28* (1-2), 98-109.

25. Todorov, T.; Sugimoto, H.; Gunawan, O.; Gokmen, T.; Mitzi, D. B., High-Efficiency Devices With Pure Solution-Processed $Cu_2ZnSn(S,Se)_4$ Absorbers. *Ieee Journal of Photovoltaics* **2014,** *4* (1), 483-485.

26. Todorov, T. K.; Tang, J.; Bag, S.; Gunawan, O.; Gokmen, T.; Zhu, Y.; Mitzi, D. B., Beyond 11% Efficiency: Characteristics of State-of-the-Art $Cu_2ZnSn(S,Se)_4$ Solar Cells. *Advanced Energy Materials* **2013,** *3* (1), 34-38.

27. Romanyuk, Y. E.; Fella, C. M.; Uhl, A. R.; Werner, M.; Tiwari, A. N.; Schnabel, T.; Ahlswede, E., Recent Trends in Direct Solution Coating of Kesterite Absorber Layers in Solar Cells. *Solar Energy Materials and Solar Cells* **2013,** *119* (0), 181-189.

28. (a) Yeh, M. Y.; Lee, C. C.; Wuu, D. S., Influences of Synthesizing Temperatures on the Properties of $Cu_2ZnSnS_4$ Prepared by Sol–Gel Spin-Coated Deposition. *Journal of Sol-Gel Science and Technology* **2009,** *52* (1), 65-68; (b) Park, S.-N.; Sung, S.-J.; Sim, J.-H.; Yang, K.-J.; Hwang, D.-K.; Kim, J.; Kim, G. Y.; Jo, W.; Kim, D.-H.; Kang, J.-K., Nanostructured P-Type CZTS Thin Films Prepared by a Facile Solution Process for 3D P-N Junction Solar Cells. *Nanoscale* **2015,** *7* (25), 11182-11189.

29. Fella, C. M.; Uhl, A. R.; Romanyuk, Y. E.; Tiwari, A. N., $Cu_2ZnSnSe_4$ Absorbers Processed from Solution Deposited Metal Salt Precursors under Different Selenization Conditions. *Physica Status Solidi (a)* **2012,** *209* (6), 1043-1048.

30. Sun, Y.; Zong, K.; Zheng, H.; Wang, H.; Liu, J.; Yan, H.; Zhu, M., Ethylene Glycol-Based Dip Coating Route for the Synthesis of $Cu_2ZnSnS_4$ Thin Film. *Materials Letters* **2013,** *92*, 195-197.

31. (a) Tanaka, K.; Oonuki, M.; Moritake, N.; Uchiki, H., Thin Film Solar Cells Prepared by Non-Vacuum Processing. *Solar Energy Materials and Solar Cells* **2009,** *93* (5), 583-587; (b) Maeda, K.; Tanaka, K.; Fukui, Y.; Uchiki, H., Influence of $H_2S$ Concentration on the Properties of $Cu_2ZnSnS_4$ Thin Films and Solar Cells Prepared by Sol–Gel Sulfurization. *Solar Energy Materials and Solar Cells* **2011,** *95* (10), 2855-2860; (c) Kazuya, M.; Kunihiko, T.; Yuya, N.; Hisao, U., Annealing Temperature Dependence of Properties of $Cu_2ZnSnS_4$ Thin Films Prepared by Sol–Gel Sulfurization Method. *Japanese Journal of Applied Physics* **2011,** *50* (5S2), 05FB08; (d) Ilari, G. M.; Fella, C. M.; Ziegler, C.; Uhl, A. R.; Romanyuk, Y. E.; Tiwari, A. N., Solar Cell Absorbers Spin-Coated from Amine-Containing Ether Solutions. *Solar Energy Materials and Solar Cells* **2012,** *104*, 125-130.

32. Fischereder, A.; Rath, T.; Haas, W.; Amenitsch, H.; Albering, J.; Meischler, D.; Larissegger, S.; Edler, M.; Saf, R.; Hofer, F.; Trimmel, G., Investigation of $Cu_2ZnSnS_4$ Formation from Metal Salts and Thioacetamide. *Chemistry of Materials* **2010,** *22* (11), 3399-3406.

33. Masato, K.; Kunihiko, T.; Katsuhiko, M.; Hisao, U., Fabrication of Three-Dimensional-Structure Solar Cell with $Cu_2ZnSnS_4$. *Japanese Journal of Applied Physics* **2012,** *51* (10S), 10NC33.

34. (a) Ki, W.; Hillhouse, H. W., Earth-Abundant Element Photovoltaics Directly from Soluble Precursors with High Yield Using a Non-Toxic Solvent. *Advanced Energy Materials* **2011,** *1* (5), 732-735; (b) Hou, Y.; Azimi, H.; Gasparini, N.; Salvador, M.; Chen, W.; Khanzada, L. S.; Brandl, M.; Hock, R.; Brabec, C. J., Low-Temperature Solution-Processed

Kesterite Solar Cell Based on in Situ Deposition of Ultrathin Absorber Layer. *ACS Applied Materitals and Interfaces* **2015,** *7* (38), 21100-21106.

35. Larramona, G.; Levcenko, S.; Bourdais, S.; Jacob, A.; Choné, C.; Delatouche, B.; Moisan, C.; Just, J.; Unold, T.; Dennler, G., Fine-Tuning the Sn Content in CZTSSe Thin Films to Achieve 10.8% Solar Cell Efficiency from Spray-Deposited Water–Ethanol-Based Colloidal Inks. *Advanced Energy Materials* **2015,** *5* (24), 1501404.

36. Miskin, C. K.; Yang, W.-C.; Hages, C. J.; Carter, N. J.; Joglekar, C. S.; Stach, E. A.; Agrawal, R., 9.0% Efficient $Cu_2ZnSn(S,Se)_4$ Solar Cells from Selenized Nanoparticle Inks. *Progress in Photovoltaics: Research and Applications* **2015,** *23* (5), 654-659.

37. Bucherl, C. N.; Oleson, K. R.; Hillhouse, H. W., Thin Film Solar Cells from Sintered Nanocrystals. *Current Opinion in Chemical Engineering* **2013,** *2* (2), 168-177.

38. (a) Jiang, F.; Ikeda, S.; Harada, T.; Matsumura, M., Pure Sulfide $Cu_2ZnSnS_4$ Thin Film Solar Cells Fabricated by Preheating an Electrodeposited Metallic Stack. *Advanced Energy Materials* **2014,** *4* (7), 1301381; (b) Ahmed, S.; Reuter, K. B.; Gunawan, O.; Guo, L.; Romankiw, L. T.; Deligianni, H., A High Efficiency Electrodeposited $Cu_2ZnSnS_4$ Solar Cell. *Advanced Energy Materials* **2012,** *2* (2), 253-259.

39. Kamoun, N.; Bouzouita, H.; Rezig, B., Fabrication and Characterization of $Cu_2ZnSnS_4$ Thin Films Deposited by Spray Pyrolysis Technique. *Thin Solid Films* **2007,** *515* (15), 5949-5952.

40. Wangperawong, A.; King, J. S.; Herron, S. M.; Tran, B. P.; Pangan-Okimoto, K.; Bent, S. F., Aqueous Bath Process for Deposition of $Cu_2ZnSnS_4$ Photovoltaic Absorbers. *Thin Solid Films* **2011,** *519* (8), 2488-2492.

41. (a) Kumar, A. V.; Park, N.-K.; Kim, E.-T., A Simple Chemical Approach for the Deposition of $Cu_2ZnSnS_4$ Thin Films. *physica status solidi (a)* **2014,** *211* (8), 1857-1859; (b) Tiwari, D.; Chaudhuri, T. K.; Ray, A.; Tiwari, K. D., $Cu_2ZnSnS_4$ Thin Films by Simple Replacement Reaction Route for Solar Photovoltaic Application. *Thin Solid Films* **2014,** *551* (0), 42-45.

42. (a) Mali, S. S.; Patil, B. M.; Betty, C. A.; Bhosale, P. N.; Oh, Y. W.; Jadkar, S. R.; Devan, R. S.; Ma, Y.-R.; Patil, P. S., Novel Synthesis of Kesterite $Cu_2ZnSnS_4$ Nanoflakes by Successive Ionic Layer Adsorption and Reaction Technique: Characterization and Application. *Electrochimica Acta* **2012,** *66* (0), 216-221; (b) Mali, S. S.; Shinde, P. S.; Betty, C. A.; Bhosale, P. N.; Oh, Y. W.; Patil, P. S., Synthesis and Characterization of $Cu_2ZnSnS_4$ Thin Films by SILAR Method. *Journal of Physics and Chemistry of Solids* **2012,** *73* (6), 735-740.

43. Suryawanshi, M. P.; Patil, P. S.; Shin, S. W.; Gurav, K. V.; Agawane, G. L.; Gang, M. G.; Kim, J. H.; Moholkar, A. V., The Synergistic Influence of Anionic Bath Immersion Time on the Photoelectrochemical Performance of CZTS Thin Films Prepared by a Modified SILAR Sequence. *RSC Advances* **2014,** *4* (36), 18537-18540.

44. Suryawanshi, M. P.; Shin, S. W.; Ghorpade, U. V.; Gurav, K. V.; Hong, C. W.; Agawane, G. L.; Vanalakar, S. A.; Moon, J. H.; Yun, J. H.; Patil, P. S.; Kim, J. H.; Moholkar, A. V., Improved Photoelectrochemical Performance of $Cu_2ZnSnS_4$ (CZTS) Thin Films Prepared Using Modified Successive Ionic Layer Adsorption and Reaction (SILAR) Sequence. *Electrochimica Acta* **2014,** *150*, 136-145.

45. Redinger, A.; Berg, D. M.; Dale, P. J.; Siebentritt, S., The Consequences of Kesterite Equilibria for Efficient Solar Cells. *Journal of the American Chemical Society* **2011,** *133* (10), 3320-3323.

46. (a) Chawla, V.; Clemens, B.; Ieee, Effect of Composition on High Efficiency CZTSSe Devices Fabricated Using Co-sputtering of Compound Targets. *2012 38th Ieee Photovoltaic Specialists Conference (PVSC)* **2012**, 2990-2992; (b) Larramona, G.; Levcenko, S.; Bourdais, S.; Jacob, A.; Choné, C.; Delatouche, B.; Moisan, C.; Just, J.; Unold, T.; Dennler, G., Thin Film Solar Cells: Fine-Tuning the Sn Content in CZTSSe Thin Films to Achieve 10.8% Solar Cell Efficiency from Spray-Deposited Water–Ethanol-Based Colloidal Inks. *Advanced Energy Materials* **2015,** *5* (24), 1501404; (c) Xin, H.; Hillhouse, H. W. In *8.3%* Efficient Copper Zinc Tin Sulfoselenide Solar Cells Processed from Environmentally Benign Solvent, *2013 39th Photovoltaic Specialists Conference (PVSC)*, **2013**, 0441-0443.

47. Katagiri, H.; Sasaguchi, N.; Hando, S.; Hoshino, S.; Ohashi, J.; Yokota, T., Preparation and Evaluation of $Cu_2ZnSnS_4$ Thin Films by Sulfurization of E-B Evaporated Precursors. *Solar Energy Materials and Solar Cells* **1997,** *49* (1), 407-414.

48. Snaith, H. J., Perovskites: The Emergence of a New Era for Low-Cost, High-Efficiency Solar Cells. *Journal of Physical Chemistry Letters* **2013,** *4* (21), 3623-3630.

49. Kim, J.; Hiroi, H.; Todorov, T. K.; Gunawan, O.; Kuwahara, M.; Gokmen, T.; Nair, D.; Hopstaken, M.; Shin, B.; Lee, Y. S.; Wang, W.; Sugimoto, H.; Mitzi, D. B., High Efficiency $Cu_2ZnSn(S,Se)_4$ Solar Cells by Applying a Double $In_2S_3$/CdS Emitter. *Advanced Materials* **2014,** *26* (44), 7427-7431.

50. Liu, F.; Zeng, F.; Song, N.; Jiang, L.; Han, Z.; Su, Z.; Yan, C.; Wen, X.; Hao, X.; Liu, Y., Kesterite $Cu_2ZnSn(S,Se)_4$ Solar Cells with beyond 8% Efficiency by a Sol–Gel and Selenization Process. *ACS Applied Materials and Interfaces* **2015,** *7* (26), 14376-14383.

51. Brammertz, G.; Buffière, M.; Oueslati, S.; ElAnzeery, H.; Ben Messaoud, K.; Sahayaraj, S.; Köble, C.; Meuris, M.; Poortmans, J., Characterization of Defects in 9.7% Efficient $Cu_2ZnSnSe_4$-CdS-ZnO Solar Cells. *Applied Physics Letters* **2013,** *103* (16), 163904.

52. Bag, S.; Gunawan, O.; Gokmen, T.; Zhu, Y.; Mitzi, D. B., Hydrazine-Processed Ge-Substituted CZTSe Solar Cells. *Chemistry of Materials* **2012,** *24* (23), 4588-4593.

53. Collord, A. D.; Hillhouse, H. W., Germanium Alloyed Kesterite Solar Cells with Low Voltage Deficits. *Chemistry of Materials* **2016,** *28* (7), 2067-2073.

54. Qu, Y.; Zoppi, G.; Beattie, N. S., Selenization Kinetics in $Cu_2ZnSn(S,Se)_4$ Solar Cells Prepared from Nanoparticle Inks. *Solar Energy Materials and Solar Cells*.

55. Vanalakar, S. A.; Agawane, G. L.; Kamble, A. S.; Hong, C. W.; Patil, P. S.; Kim, J. H., Fabrication of $Cu_2SnS_3$ Thin Film Solar Cells Using Pulsed Laser Deposition Technique. *Solar Energy Materials and Solar Cells* **2015,** *138*, 1-8.

56. Romero, M. J.; Du, H.; Teeter, G.; Yan, Y.; Al-Jassim, M. M., Comparative Study of the Luminescence and Intrinsic Point Defects in the Kesterite $Cu_2ZnSnS_4$ and Chalcopyrite $Cu(In,Ga)Se_2$ Thin Films Used in Photovoltaic Applications. *Physical Review B* **2011,** *84* (16), 165324.

57. Fontané, X.; Calvo-Barrio, L.; Izquierdo-Roca, V.; Saucedo, E.; Pérez-Rodriguez, A.; Morante, J. R.; Berg, D. M.; Dale, P. J.; Siebentritt, S., In-Depth Resolved Raman Scattering Analysis for the Identification of Secondary Phases: Characterization of $Cu_2ZnSnS_4$ Layers for Solar Cell Applications. *Applied Physics Letters* **2011,** *98* (18), 181905.

58. (a) Lin, X.; Kavalakkatt, J.; Kornhuber, K.; Levcenko, S.; Lux-Steiner, M. C.; Ennaoui, A., Structural and Optical Properties of $Cu_2ZnSnS_4$ Thin Film Absorbers from ZnS and $Cu_3SnS_4$ Nanoparticle Precursors. *Thin Solid Films* **2013,** *535* (0), 10-13; (b) Berg, D. M.; Djemour, R.; Gütay, L.; Siebentritt, S.; Dale, P. J.; Fontane, X.; Izquierdo-Roca, V.; Pérez-Rodriguez, A., Raman Analysis of Monoclinic $Cu_2SnS_3$ Thin Films. *Applied Physics Letters* **2012,** *100* (19), 192103.

59. Dimitrievska, M.; Fairbrother, A.; Fontané, X.; Jawhari, T.; Izquierdo-Roca, V.; Saucedo, E.; Pérez-Rodríguez, A., Multiwavelength Excitation Raman Scattering Study of Polycrystalline Kesterite $Cu_2ZnSnS_4$ Thin Films. *Applied Physics Letters* **2014,** *104* (2), 021901.

60. Tan, J. M. R.; Lee, Y. H.; Pedireddy, S.; Baikie, T.; Ling, X. Y.; Wong, L. H., Understanding the Synthetic Pathway of a Single-Phase Quarternary Semiconductor Using Surface-Enhanced Raman Scattering: A Case of Wurtzite $Cu_2ZnSnS_4$ Nanoparticles. *Journal of the American Chemical Society* **2014,** *136* (18), 6684-6692.

61. Dimitrievska, M.; Fairbrother, A.; Saucedo, E.; Pérez-Rodríguez, A.; Izquierdo-Roca, V., Influence of Compositionally Induced Defects on the Vibrational Properties of Device Grade $Cu_2ZnSnSe_4$ Absorbers for Kesterite Based Solar Cells. *Applied Physics Letters* **2015,** *106* (7), 073903.

62. Tanaka, T.; Sueishi, T.; Saito, K.; Guo, Q.; Nishio, M.; Yu, K. M.; Walukiewicz, W., Existence and Removal of $Cu_2Se$ Second Phase in Coevaporated $Cu_2ZnSnSe_4$ Thin Films. *Journal of Applied Physics* **2012,** *111* (5), 053522.

63. Fairbrother, A.; García-Hemme, E.; Izquierdo-Roca, V.; Fontané, X.; Pulgarín-Agudelo, F. A.; Vigil-Galán, O.; Pérez-Rodríguez, A.; Saucedo, E., Development of a Selective

Chemical Etch To Improve the Conversion Efficiency of Zn-Rich $Cu_2ZnSnS_4$ Solar Cells. *Journal of the American Chemical Society* **2012,** *134* (19), 8018-8021.

64. Xie, H.; Sánchez, Y.; López-Marino, S.; Espíndola-Rodríguez, M.; Neuschitzer, M.; Sylla, D.; Fairbrother, A.; Izquierdo-Roca, V.; Pérez-Rodríguez, A.; Saucedo, E., Impact of Sn(S,Se) Secondary Phases in $Cu_2ZnSn(S,Se)_4$ Solar Cells: a Chemical Route for Their Selective Removal and Absorber Surface Passivation. *ACS Applied Materials and Interfaces* **2014,** *6* (15), 12744-12751.

65. Zhou, H.; Song, T.-B.; Hsu, W.-C.; Luo, S.; Ye, S.; Duan, H.-S.; Hsu, C.-J.; Yang, W.; Yang, Y., Rational Defect Passivation of $Cu_2ZnSn(S,Se)_4$ Photovoltaics with Solution-Processed $Cu_2ZnSnS_4$:Na Nanocrystals. *Journal of the American Chemical Society* **2013,** *135* (43), 15998-16001.

66. Cui, H.; Liu, X.; Liu, F.; Hao, X.; Song, N.; Yan, C., Boosting $Cu_2ZnSnS_4$ Solar Cells Efficiency by a Thin Ag Intermediate Layer between Absorber and Back Contact. *Applied Physics Letters* **2014,** *104* (4), 041115.

67. Scragg, J. J.; Kubart, T.; Wätjen, J. T.; Ericson, T.; Linnarsson, M. K.; Platzer-Björkman, C., Effects of Back Contact Instability on $Cu_2ZnSnS_4$ Devices and Processes. *Chemistry of Materials* **2013,** *25* (15), 3162-3171.

68. O'Regan, B.; Gratzel, M., A Low-Cost, High-Efficiency Solar Cell Based on Dye-Sensitized Colloidal $TiO_2$ Films. *Nature* **1991,** *353* (6346), 737-740.

69. Burschka, J.; Pellet, N.; Moon, S.-J.; Humphry-Baker, R.; Gao, P.; Nazeeruddin, M. K.; Gratzel, M., Sequential Deposition as a Route to High-Performance Perovskite-Sensitized Solar Cells. *Nature* **2013,** *499* (7458), 316-319.

70. Yoon, H.; Kang, S. M.; Lee, J.-K.; Choi, M., Hysteresis-Free Low-Temperature-Processed Planar Perovskite Solar Cells with 19.1% Efficiency. *Energy & Environmental Science* **2016,** *9* (7), 2262-2266.

71. (a) Ren, Z.; Wang, J.; Pan, Z.; Zhao, K.; Zhang, H.; Li, Y.; Zhao, Y.; Mora-Sero, I.; Bisquert, J.; Zhong, X., Amorphous $TiO_2$ Buffer Layer Boosts Efficiency of Quantum Dot Sensitized Solar Cells to over 9%. *Chemistry of Materials* **2015,** *27* (24), 8398-8405; (b) Du,

J.; Du, Z.; Hu, J.-S.; Pan, Z.; Shen, Q.; Sun, J.; Long, D.; Dong, H.; Sun, L.; Zhong, X.; Wan, L.-J., Zn–Cu–In–Se Quantum Dot Solar Cells with a Certified Power Conversion Efficiency of 11.6%. *Journal of the American Chemical Society* **2016,** *138* (12), 4201-4209.

72. (a) Hodes, G.; Cahen, D., All-Solid-State, Semiconductor-Sensitized Nanoporous Solar Cells. *Accounts of Chemical Research* **2012,** *45* (5), 705-713; (b) Choi, Y. C.; Lee, D. U.; Noh, J. H.; Kim, E. K.; Seok, S. I., Highly Improved $Sb_2S_3$ Sensitized-Inorganic–Organic Heterojunction Solar Cells and Quantification of Traps by Deep-Level Transient Spectroscopy. *Advanced Functional Materials* **2014,** *24* (23), 3587-3592.

73. Green, M. A.; Emery, K.; Hishikawa, Y.; Warta, W.; Dunlop, E. D., Solar Cell Efficiency Tables (Version 48). *Progress in Photovoltaics: Research and Applications* **2016,** *24* (7), 905-913.

74. Roelofs, K. E.; Brennan, T. P.; Bent, S. F., Interface Engineering in Inorganic-Absorber Nanostructured Solar Cells. *The Journal of Physical Chemistry Letters* **2014,** *5* (2), 348-360.

75. Gratzel, M., Photoelectrochemical cells. *Nature* **2001,** *414* (6861), 338-344.

76. Zhao, K.; Pan, Z.; Mora-Seró, I.; Cánovas, E.; Wang, H.; Song, Y.; Gong, X.; Wang, J.; Bonn, M.; Bisquert, J.; Zhong, X., Boosting Power Conversion Efficiencies of Quantum-Dot-Sensitized Solar Cells Beyond 8% by Recombination Control. *Journal of the American Chemical Society* **2015,** *137* (16), 5602-5609.

77. Ren, Z.; Wang, Z.; Wang, R.; Pan, Z.; Gong, X.; Zhong, X., Effects of Metal Oxyhydroxide Coatings on Photoanode in Quantum Dot Sensitized Solar Cells. *Chemistry of Materials* **2016,** *28* (7), 2323-2330.

78. Aftab Akram, M.; Javed, S.; Islam, M.; Mujahid, M.; Safdar, A., Arrays of CZTS Sensitized ZnO/ZnS and ZnO/ZnSe Core/Shell Nanorods for Liquid Junction Nanowire Solar Cells. *Solar Energy Materials and Solar Cells* **2016,** *146*, 121-128.

79. Tsujimoto, K.; Nguyen, D.-C.; Ito, S.; Nishino, H.; Matsuyoshi, H.; Konno, A.; Kumara, G. R. A.; Tennakone, K., $TiO_2$ Surface Treatment Effects by $Mg^{2+}$, $Ba^{2+}$, and $Al^{3+}$ on $Sb_2S_3$ Extremely Thin Absorber Solar Cells. *The Journal of Physical Chemistry C* **2012,** *116* (25), 13465-13471.

80. Guo, W.; Shen, Y.; Wu, M.; Ma, T., Highly Efficient Inorganic-Organic Heterojunction Solar Cells Based on SnS-Sensitized Spherical $TiO_2$ Electrodes. *Chemical Communications* **2012,** *48* (49), 6133-6135.

81. Yang, W. S.; Noh, J. H.; Jeon, N. J.; Kim, Y. C.; Ryu, S.; Seo, J.; Seok, S. I., High-Performance Photovoltaic Perovskite Layers Fabricated through Intramolecular Exchange. *Science* **2015,** *348* (6240), 1234-1237.

82. Yella, A.; Lee, H. W.; Tsao, H. N.; Yi, C. Y.; Chandiran, A. K.; Nazeeruddin, M. K.; Diau, E. W. G.; Yeh, C. Y.; Zakeeruddin, S. M.; Gratzel, M., Porphyrin-Sensitized Solar Cells with Cobalt (II/III)-Based Redox Electrolyte Exceed 12 Percent Efficiency. *Science* **2011,** *334* (6056), 629-634.

83. Kojima, A.; Teshima, K.; Shirai, Y.; Miyasaka, T., Organometal Halide Perovskites as Visible-Light Sensitizers for Photovoltaic Cells. *Journal of the American Chemical Society* **2009,** *131* (17), 6050-6051.

84. Collavini, S.; Völker, S. F.; Delgado, J. L., Understanding the Outstanding Power Conversion Efficiency of Perovskite-Based Solar Cells. *Angewandte Chemie International Edition* **2015,** *54* (34), 9757-9759.

85. Seo, J.; Noh, J. H.; Seok, S. I., Rational Strategies for Efficient Perovskite Solar Cells. *Accounts of Chemical Research* **2016,** *49* (3), 562-572.

86. (a) Zhang, H.; Cheng, K.; Hou, Y. M.; Fang, Z.; Pan, Z. X.; Wu, W. J.; Hua, J. L.; Zhong, X. H., Efficient CdSe Quantum Dot-Sensitized Solar Cells Prepared by a Postsynthesis Assembly Approach. *Chemical Communications* **2012,** *48* (91), 11235-11237; (b) Becker, M. A.; Radich, J. G.; Bunker, B. A.; Kamat, P. V., How Does a SILAR CdSe Film Grow? Tuning the Deposition Steps to Suppress Interfacial Charge Recombination in Solar Cells. *The Journal of Physical Chemistry Letters* **2014,** *5* (9), 1575-1582; (c) Kim, M. R.; Ma, D., Quantum-Dot-Based Solar Cells: Recent Advances, Strategies, and Challenges. *The Journal of Physical Chemistry Letters* **2015,** *6* (1), 85-99.

87. Kongkanand, A.; Tvrdy, K.; Takechi, K.; Kuno, M.; Kamat, P. V., Quantum Dot Solar Cells. Tuning Photoresponse through Size and Shape Control of CdSe−$TiO_2$ Architecture. *Journal of the American Chemical Society* **2008,** *130* (12), 4007-4015.

88. Sukhovatkin, V.; Hinds, S.; Brzozowski, L.; Sargent, E. H., Colloidal Quantum-Dot Photodetectors Exploiting Multiexciton Generation. *Science* **2009,** *324* (5934), 1542-1544.

89. Lan, X.; Masala, S.; Sargent, E. H., Charge-Extraction Strategies for Colloidal Quantum Dot Photovoltaics. *Nature Materials* **2014,** *13* (3), 233-240.

90. Chang, C.-H.; Lee, Y.-L., Chemical Bath Deposition of CdS Quantum Dots onto Mesoscopic $TiO_2$ Films for Application in Quantum-Dot-Sensitized Solar Cells. *Applied Physics Letters* **2007,** *91* (5), 053503.

91. Shen, C.; Fichou, D.; Wang, Q., Interfacial Engineering for Quantum-Dot-Sensitized Solar Cells. *Chemistry – An Asian Journal* **2016,** *11* (8), 1183-1193.

92. Boix, P. P.; Larramona, G.; Jacob, A.; Delatouche, B.; Mora-Seró, I.; Bisquert, J., Hole Transport and Recombination in All-Solid $Sb_2S_3$-Sensitized $TiO_2$ Solar Cells Using CuSCN As Hole Transporter. *The Journal of Physical Chemistry C* **2012,** *116* (1), 1579-1587.

93. Hao, Y.; Pei, J.; Wei, Y.; Cao, Y.; Jiao, S.; Zhu, F.; Li, J.; Xu, D., Efficient Semiconductor-Sensitized Solar Cells Based on Poly(3-hexylthiophene)@CdSe@ZnO Core−Shell Nanorod Arrays. *The Journal of Physical Chemistry C* **2010,** *114* (18), 8622-8625.

94. Jumabekov, A. N.; Siegler, T. D.; Cordes, N.; Medina, D. D.; Böhm, D.; Garbus, P.; Meroni, S.; Peter, L. M.; Bein, T., Comparison of Solid-State Quantum-Dot-Sensitized Solar Cells with ex Situ and in Situ Grown PbS Quantum Dots. *The Journal of Physical Chemistry C* **2014,** *118* (45), 25853-25862.

95. Li, T.-L.; Lee, Y.-L.; Teng, H., High-Performance Quantum Dot-Sensitized Solar Cells Based on Sensitization with $CuInS_2$ Quantum Dots/CdS Heterostructure. *Energy & Environmental Science* **2012,** *5* (1), 5315-5324.

96. Roelofs, K. E.; Brennan, T. P.; Dominguez, J. C.; Bailie, C. D.; Margulis, G. Y.; Hoke, E. T.; McGehee, M. D.; Bent, S. F., Effect of $Al_2O_3$ Recombination Barrier Layers Deposited by

Atomic Layer Deposition in Solid-State CdS Quantum Dot-Sensitized Solar Cells. *The Journal of Physical Chemistry C* **2013,** *117* (11), 5584-5592.

97. (a) Rühle, S.; Greenshtein, M.; Chen, S. G.; Merson, A.; Pizem, H.; Sukenik, C. S.; Cahen, D.; Zaban, A., Molecular Adjustment of the Electronic Properties of Nanoporous Electrodes in Dye-Sensitized Solar Cells. *The Journal of Physical Chemistry B* **2005,** *109* (40), 18907-18913; (b) Shalom, M.; Rühle, S.; Hod, I.; Yahav, S.; Zaban, A., Energy Level Alignment in CdS Quantum Dot Sensitized Solar Cells Using Molecular Dipoles. *Journal of the American Chemical Society* **2009,** *131* (29), 9876-9877; (c) Shen, C.; Wang, X.; Jiang, X.-F.; Zhu, H.; Li, F.; Yang, J.; Xu, Q.-H.; Wang, Q., Fast Charge Separation at Semiconductor Sensitizer–Molecular Relay Interface Leads to Significantly Enhanced Solar Cell Performance. *The Journal of Physical Chemistry C* **2015,** *119* (18), 9774-9781.

98. Chang, J. A.; Rhee, J. H.; Im, S. H.; Lee, Y. H.; Kim, H.-j.; Seok, S. I.; Nazeeruddin, M. K.; Gratzel, M., High-Performance Nanostructured Inorganic−Organic Heterojunction Solar Cells. *Nano Letters* **2010,** *10* (7), 2609-2612.

99. Liu, W. C.; Guo, B. L.; Wu, X. S.; Zhang, F. M.; Mak, C. L.; Wong, K. H., Facile Hydrothermal Synthesis of Hydrotropic $Cu_2ZnSnS_4$ Nanocrystal Quantum Dots: Band-Gap Engineering and Phonon Confinement Effect. *Journal of Materials Chemistry A* **2013,** *1* (9), 3182-3186.

100. (a) Bai, B.; Kou, D.; Zhou, W.; Zhou, Z.; Tian, Q.; Meng, Y.; Wu, S., Quaternary $Cu_2ZnSnS_4$ Quantum Dot-Sensitized Solar Cells: Synthesis, Passivation and Ligand Exchange. *Journal of Power Sources* **2016,** *318*, 35-40; (b) Wang, Y.; Li, C. X.; Yin, X. J.; Wang, H.; Gong, H., $Cu_2ZnSnS_4$ (CZTS) Application in $TiO_2$ Solar Cell as Dye. *ECS Journal of Solid State Science and Technology* **2013,** *2* (7), Q95-Q98.

101. (a) Ho, T.-Y.; Chen, L.-Y., The Study of $Cu_2ZnSnS_4$ Nanocrystal/$TiO_2$ Nanorod Heterojuction Photoelectrochemical Cell for Hydrogen Generation. *Energy Procedia* **2014,** *61* (Complete), 2050-2053; (b) Dongwook, L.; Kijung, Y., Solution-Processed $Cu_2ZnSnS_4$ Superstrate Solar Cell Using Vertically Aligned ZnO Nanorods. *Nanotechnology* **2014,** *25* (6), 065401.

102. Dai, P.; Shen, X.; Lin, Z.; Feng, Z.; Xu, H.; Zhan, J., Band-Gap Tunable $(Cu_2Sn)_{x/3}Zn_{1-x}S$ Nanoparticles for Solar Cells. *Chemical Communications* **2010,** *46* (31), 5749-5751.

103. Jiang, M.; Wu, J.; Di, G.; Li, G., Nanostructured Solar Cell Based on Solution Processed $Cu_2ZnSnS_4$ Nanoparticles and Vertically Aligned ZnO Nanorod Array. *Physica Status Solidi (RRL) – Rapid Research Letters* **2014,** *8* (12), 971-975.

# CHAPTER 3

–

# NANOSCALE PHOTO-ABSORBING KESTERITE GROWN ON ANATASE MESOSCOPIC FILMS BY SEQUENTIAL BINARY CHALCOGENIDE SOLUTION DEPOSITION-EXCHANGE, ANNEALING, AND ETCHING

This thesis proposes an absorber-conductor structure featuring CZTS as light absorber and a large bandgap semiconductor (i.e. $TiO_2$) as electron conductor. This chapter focuses on building the CZTS/$TiO_2$ heterostructure on an anatase ($TiO_2$) mesoporous sintered film via sequential aqueous solution deposition of CZTS precursor, followed by annealing to induce crystallization of CZTS kesterite phase, and performing preliminary optical characterization. This chapter has been published as: Z. Wang and G. P. Demopoulos, *Crystal Growth & Design*, 2016, *16*, pp. 3618–3630. In Appendix A, the Supporting Information of the paper is provided.

## 3.1 Abstract

In this paper-chapter, the nanoscale coating of CZTS on anatase mesoscopic films is studied to build an absorber (kesterite)-conductor (anatase) photoanode structure with high composition uniformity - a challenge for complex absorbers like quaternary CZTS. To this end, a three-step binary chalcogenide solution deposition-exchange sequence is developed for precursor preparation that is followed by in-depth analysis of the deposit-forming chemical reactions and characterization of elemental distribution and composition control. Then, crystallization is induced by annealing at 500 °C for 1 h, followed by an additional hydrochloric acid etching step to remove secondary binary phases and surface imperfections

leading to improved composition of a CZTS/$TiO_2$ film as a candidate for use in kesterite-sensitized solar cells.

## 3.2 Introduction

Because of the quaternary composition of CZTS that easily leads to secondary phase coformation or crystal inhomogeneities, it is very difficult to obtain high purity, perfectly ordered kesterite crystalline material,[1] having as a result to delay the development of competitive CZTS photovoltaic devices. Great efforts have been taken to better characterize secondary phases using near resonant Raman spectroscopy[1b, 2] and X-ray absorption near edge structure analysis.[3] In the meantime, researchers resort to highly toxic and explosive solvents like hydrazine to facilitate the formation of high quality CZTS(Se) films.[4] In this context, it is worth exploring CZTS photovoltaics by evaluating the absorber (CZTS)-conductor ($TiO_2$) structure as done in sensitized solar cells and extremely thin absorber (ETA) solar cell configurations.[5]

The concept of using CZTS as a sensitizer was first introduced by Wang et al.;[6] however, only very low efficiency has been achieved when a layer of CZTS particles was coated on top of a $TiO_2$ film as a photoelectrode by dip-immersion. Poor contact between the absorber and conductor caused by the lack of CZTS particle penetration/insertion inside the mesoporous film was a major problem. Therefore, instead of ex situ preparing a CZTS suspension and applying it, in situ solution deposition of CZTS directly onto the $TiO_2$ scaffold could lead to a better interfaced composite structure. Successive ionic layer adsorption and reaction,[7] or SILAR, based on aqueous solution has been used to deposit metal chalcogenide layers on substrates and also employed to coat extremely fine semiconductors like CdS, ZnS, and CdSe on $TiO_2$ mesoscopic films.[8] Also, CZTS deposition via SILAR method on planar substrates has been attempted.[9] However, a thorough study is still lacking that can lead to spatial and chemical composition control given the complexity of depositing a quaternary absorber compound (CZTS) into a 3D mesoporous ($TiO_2$) film. Herein, a three-step solution deposition-exchange sequence has been developed for nanoscale precursor CZTS coating on $TiO_2$ that is followed by in-depth analysis of the deposit-forming chemical reactions and film characterization. Crystallization of the precursor film is induced by annealing at 500 °C. Hydrochloric acid etching was finally developed to remove secondary impurity binary phases. This study is of interest not only from the standpoint of developing CZTS solar cells[10] or other absorber-conductor optoelectronic devices[11] but also in terms of developing nanoscale composition control strategies for quaternary compound crystallization and thin film deposition systems in general.

## 3.3 Experimental Section

### 3.3.1 Materials and chemicals

The materials and chemicals used were transparent $TiO_2$ paste (NR-18T, Dyesol), copper(II) chloride dihydrate (99%, Alfa Aesar), tin(II) chloride dihydrate (98%, SigmaAldrich), zinc chloride anhydrous (99.99%, Sigma-Aldrich), sodium sulfide nonahydrate (Sigma-Aldrich), concentrated hydrochloric acid (36.5% by weight, Fisher Scientific), fluorine-doped tin oxide (FTO) glass (Sigma-Aldrich), tin(II) sulfide (96%, Sigma-Aldrich), zinc sulfide (99.99%, Sigma-Aldrich), and copper(II) sulfide (99%, Sigma-Aldrich).

### 3.3.2 Materials synthesis

#### 3.3.2.1 Preparation of $TiO_2$ mesoscopic film

A $TiO_2$ mesoscopic film was prepared by doctor-blading of commercially available anatase paste (Dyesol 18NR-T) on cleaned FTO glass, which was then slowly heated to 450 °C and kept for 30 min to form the porous mesoscopic film as per dye-sensitized solar cell fabrication protocols.[12]

#### 3.3.2.2 In situ deposition of CZTS precursor consisting of Cu, Zn, Sn, and S

As shown in Figures A.1-A.3, there are three steps for the quaternary precursor to be in situ deposited and coated onto the mesoscopic $TiO_2$ film: (1) 100 mL of 0.02 M $SnCl_2$ (pH ~2) and 0.16 M $Na_2S$ (pH ~12) aqueous solution were prepared separately in two containers. Then, the as-prepared $TiO_2$ film on FTO glass was immersed into aqueous cationic solution containing $Sn^{2+}$ and aqueous anionic solution containing excess $S^{2-}$ successively with 1 min interval time; the process was repeated 5−20 times as per successive ion layer adsorption reaction (SILAR) methodology[13] to form a $SnS_x$ coating on the walls of the $TiO_2$ mesopores.

(2) Similarly, ZnS was in situ deposited with another SILAR round, instead of $SnCl_2$, 100 mL of 0.1 M $ZnCl_2$ (pH ~5) aqueous solution was used as the cationic ion source. The cycles for deposition varied from 1 to 15. (3) For the precursor preparation to be completed, copper was incorporated by an additional ion-exchange step. Briefly, 100 mL of 0.02 M copper(II) chloride aqueous solution (pH ~4) was prepared; then, the ternary sulfide (Sn−Zn−S)-coated $TiO_2$ film was immersed into the Cu solution and kept for a variable amount of time (1−35 min). At the end of this immersion stage, the color of the film changed from redbrown to black, indicating that ion-exchange had led to the CZTS precursor being coated onto the $TiO_2$ mesoporous film. Finally, the films were washed with deionized water before being subjected to characterization and annealing.

#### 3.3.2.3 Annealing

Annealing was performed in a hot plate (Linkam hot/ cold stage) with a sealed chamber filled with continuously flowing $N_2$ to prevent oxidation of CZTS. The CZTS precursor-coated $TiO_2$ film deposited on FTO glass was annealed at 500 °C for 1 h without using excess sulfur. The heating/cooling rate was 30 °C/min.

#### 3.3.2.4 Characterization

A D8 Discover Bruker copper source X-ray diffractometer (XRD) was used for phase characterization; Thermo Scientific K-Alpha X-ray photoelectron spectroscopy (XPS) was used for chemical state and element depth profile analysis. For the depth profile, film etching was performed using Ar ion gun sputtering at 3 keV and high current for achieving a maximum etching rate; A Hitachi SU3500 scanning electron microscope (SEM) was used for thin film or particle morphology investigation and for compositional analysis by EDS. Inductively coupled-plasma optical emission spectrometry (ICP-OES) was used for composition analysis after dissolving CZTS precursor in aqua-regia, and hydrochloric acid was used for the byproduct etching study. A Thermo Scientific Dektak profilometer was used for film thickness measurements. Raman spectroscopy was performed using a Renishaw inVia Raman spectrometer equipped with a LEICA optical microscope. Four lasers with wavelength of 488, 514, 633, and 785 nm were used as excitation light source; transmission electron microscopes (FEI Tecnai G2 F20 200 kV and Cryo-STEM equipped with EDAX Genesis EDS) were used to investigate the morphology of CZTS nanocrystals coated on $TiO_2$ as well as the film uniformity at nanoscale. IPCE/EQE system (PVM Inc.) was used for optical transmittance measurements of the thin film. Steady-state photoluminescence (PL) was characterized at room temperature by the inVia photoluminescence spectrometer equipped with a LEICA optical microscope with 514 nm laser excitation. Time-resolved photoluminescence (TR-PL) measurements were performed using a Horiba DynaMyc system equipped with a time-correlated single photon counting (TCSPC) system. A pulsed 375 nm diode laser was used as the excitation source. The signal was detected by a TBX picosecond detection module after a long pass filter (>500 nm).

## 3.4 Results and Discussion

### 3.4.1 In situ deposition of CZTS precursor on $TiO_2$ mesoscopic film

For coating CZTS onto $TiO_2$ preconstructed mesoporous films, precursor binary sulfides were deposited from aqueous solution in a sequential manner making use of SILAR protocols and ion-exchange reaction followed by annealing. Aqueous-based organic-free solution processing has significant cost and environmental advantages over other fabrication technologies. The successive ion layer adsorption reaction (SILAR) methodology is employed as it is known to provide uniform semiconductor sensitizer infiltration into a mesoporous $TiO_2$ scaffold.[5a, 14] However, the challenge here is that a quaternary as opposed to binary chalcogenide semiconductor needs to be deposited having uniform composition. During preliminary testing, the common SILAR approach of alternating between a cationic and an anionic solution did not prove effective in producing good CZTS deposits as it was noticed that predeposition reactions among the cations led to composition inhomogeneities and impurity byproduct phases. The problem was overcome by adopting a sequential binary chalcogenide deposition sequence.

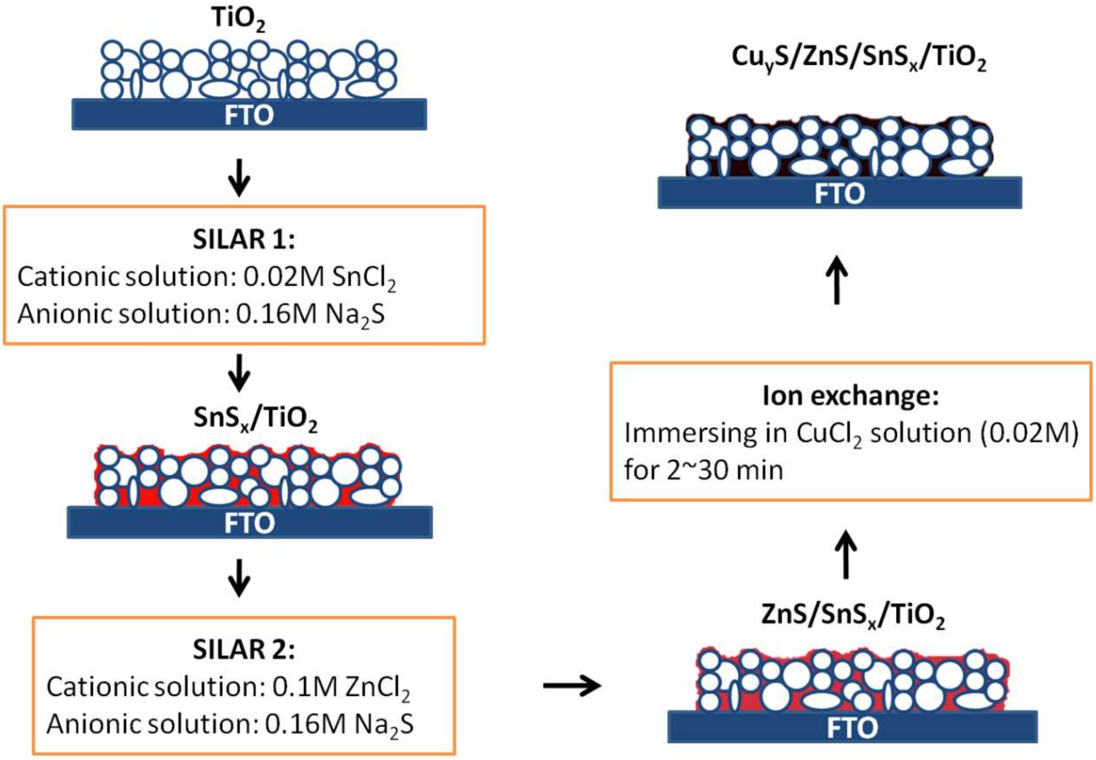

Figure 3.1 Schematic process diagram for the in-situ deposition of CZTS precursor binary sulfides on $TiO_2$ mesoscopic film.

### 3.4.1.1 SnS and ZnS deposition

The adopted 3-step sequential deposition sequence is illustrated in Figure 3.1. In steps 1 and 2 SILAR deposition of $SnS_x$ and ZnS was practiced followed by a cation exchange step for Cu incorporation. CuS is by far the binary sulfide with the highest thermodynamic stability among the three; hence, it is selected last to deposit via cation exchange. The first step, or SILAR 1, was performed by immersing the as-prepared $TiO_2$/FTO film first into $SnCl_2$ (0.02M) solution and then into $Na_2S$ (0.16M) aqueous solution (cycle 1), and this is repeated over several cycles. This led to deposition of tin sulfide - see reaction stoichiometry 1 - as evident by significant color change and confirmed by performing XPS depth profile analysis with high energy Ar gun surface etching.

$$Sn^{2+}{}_{(aq)} + S^{2-}{}_{(aq)} \rightarrow SnS_{(@TiO2\ surface)} \qquad (1)$$

Figure A.4 shows the depth profile of the tin sulfide-coated $TiO_2$ film after 5, 10, and 20 cycles of SILAR 1. In general, the concentration of Sn content is lower near the surface, slightly increases with depth, and eventually remains constant. At the same time, the concentration of S is almost the same (1:1 stoichiometry: SnS) with that of Sn near the surface but increases above the 1:1 stoichiometric ratio with increasing film depth: $SnS_x$, where $1 < x < 2$. The excess S is deemed beneficial to the ultimate CZTS coating as during annealing at 500 °C some S will volatilize given that the boiling point of S lies at 445 °C. The XPS depth profile results indicate that $SnS_x$ is distributed uniformly inside the $TiO_2$ film, which proves the superiority of the SILAR deposition method. For the growth rate of $SnS_x$ to be quantified, the Sn-to-Ti ratio is calculated and plotted in Figure 3.2. Because the absolute titanium content is constant, the composition of the film can be represented on a % basis of each element with reference to Ti. As can be seen in Figure 3.2, the % Sn content not only increases as a function of film thickness but also increases with increasing number of cycles, namely, from approximately 5, 8, and 12% tin (to Ti) after 5, 10, and 20 SILAR cycles of deposition, respectively.

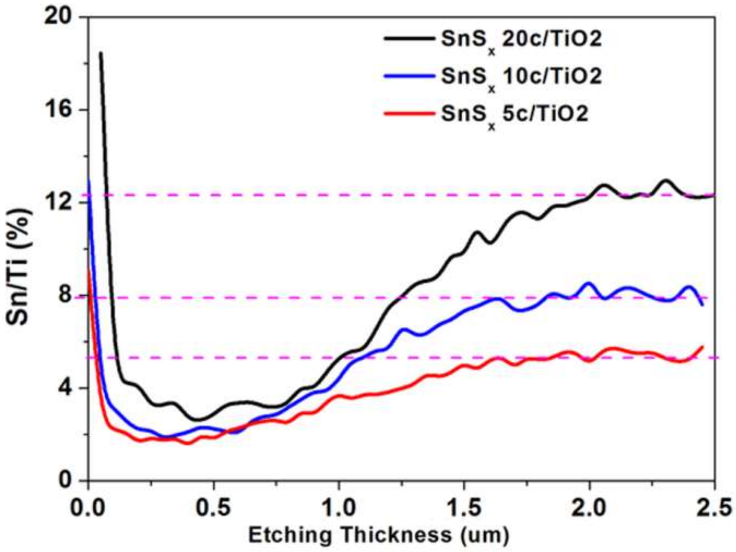

Figure 3.2 The ratio of Sn to Ti as function of depth for the films obtained with different number of SILAR cycles.

In the next step, zinc sulfide was deposited via a similar SILAR protocol. However, the amount of Zn deposited was deliberately in excess of that dictated by the CZTS formula to satisfy the subsequent step of copper incorporation via ion-exchange. For the rate of zinc deposition to be controlled precisely, predeposited Sn was used as a reference, and ICP-OES was used to monitor the Zn-Sn atomic fractions as shown in Figure 3.3a. In this case, 10

SILAR cycles of $SnS_x$ was applied first on $TiO_2$ (~8% Sn/Ti); then different numbers of cycles (1−15) of ZnS deposition followed onto the as-prepared $SnS_x$ coated $TiO_2$ mesoporous film.

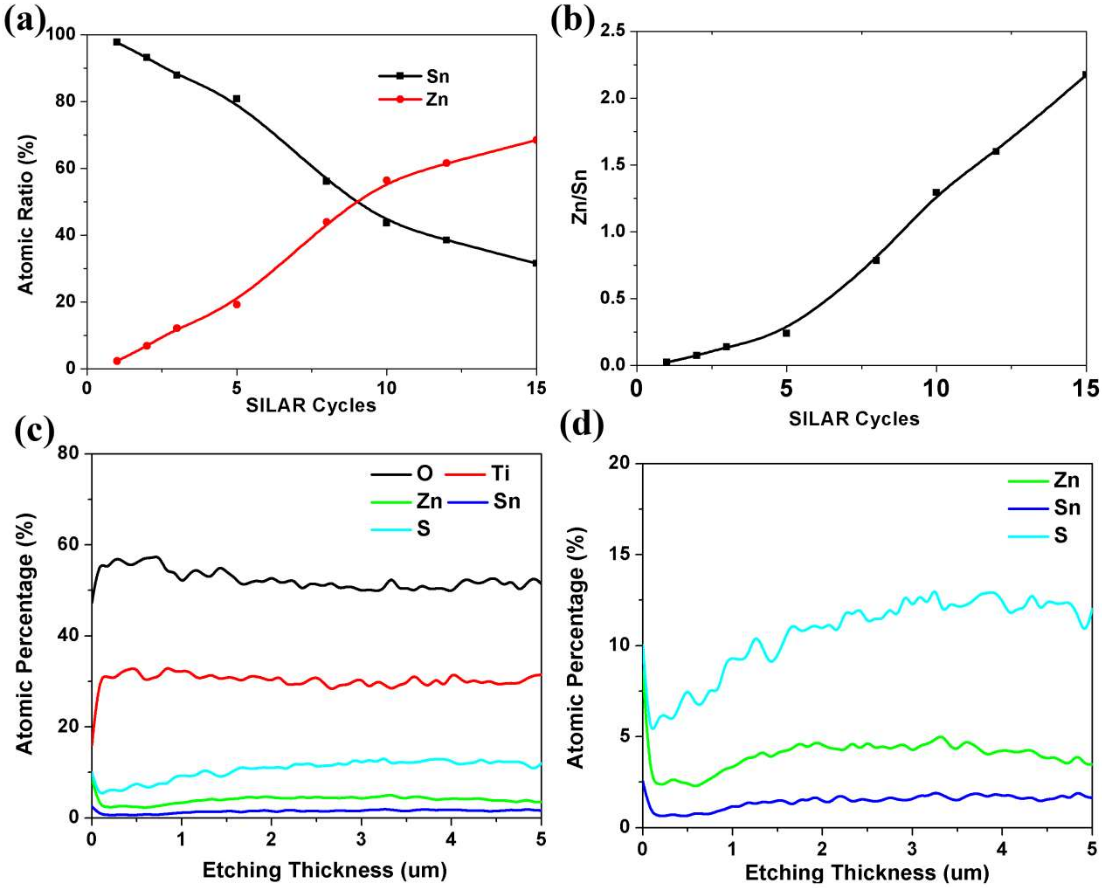

Figure 3.3 a) Atomic fractions of Zn and Sn in $ZnS/SnS_x/TiO_2$ system and b) the atomic ratio of Zn to Sn as a function of number of ZnS deposition cycles; c) XPS depth profile of $ZnS/SnS_x/TiO_2$ system after 10 $SnS_x$ and 15 ZnS SILAR cycles and d) the distribution of chalcogenide elements.

Figure 3.3b provides the atomic ratio of Zn/Sn with increasing ZnS deposition cycles. As can be seen, the quantity of zinc increases almost linearly with the increase of SILAR cycles, and after 15 cycles, the atomic ratio of Zn to Sn is approximately equal to 2. For the vertical distribution of Zn within the film to be quantified, XPS depth profiling was performed, and the results are shown in Figure 3.3c and d. After 15 cycles of SILAR 2, the distribution of both Zn and Sn inside the $TiO_2$ film is shown to be quite uniform, and the ratio of Zn/Sn is shown to be approximately two, matching well the ICP-OES results.

### 3.4.1.2 Cu incorporation

Subsequently, the ZnS (15 cycles)/SnSx (10 cycles)-coated $TiO_2$ mesoscopic film was immersed into 0.02 M $CuCl_2$ aqueous solution for different amounts of time. Direct color change from red-brown to black was observed, signaling the successful incorporation of copper into the film. This can be verified with Figure A.5, where the transmittance of the film as a function of Cu ion exchange time is given along with images of the film. For the optimum ion exchange time to be determined for obtaining a precursor deposit with CZTS, composition films were prepared at different immersion times and subsequently analyzed by ICP-OES. The atomic percent composition of the final precursors as a function of Cu ion-exchange time is shown in Figure 3.4a. As can be seen, the concentration of tin remains almost constant compared to those of the Zn and Cu elements. The fractions of copper and zinc significantly increase and decrease, respectively, in the first 10 min, thereafter slowing down and eventually leveling off. This behavior is attributed to the following metal exchange/ metathetic reaction 2 that is thermodynamically favorable:

$$ZnS_{(@TiO2)} + Cu^{2+}_{(aq)} \rightarrow CuS_{(@TiO2)} + Zn^{2+}_{(aq)} \qquad (2)$$

At around 9 min of metal exchange time (Figure 3.4a), an intersection point of Sn and Zn curves indicates the same atomic ratio of the two elements (~25%), whereas the concentration of Cu is nearly 50%, namely, twice that of Sn or Zn. This is a very satisfactory result as it corresponds to the stoichiometric ratio for $Cu_2ZnSnS_4$. This can be more clearly seen from Figure 3.4b, where the calculated atomic ratios of Cu/(Sn + Zn) and Sn/Zn are plotted as a function of metal exchange time. As can be seen, the intersection point represents the Cu:Zn:Sn stoichiometric ratio of 2:1:1. By selecting shorter ion exchange time, CZTS with copper-poor/zinc-rich composition is produced, whereas at longer ion-exchange time, CZTS with copper-rich/zinc-poor composition is obtained. Because the optical properties of CZTS depend on its stoichiometry[15] it becomes evident that the developed ion exchange/SILAR method becomes a powerful tool in tuning the performance of CZTS absorber films.

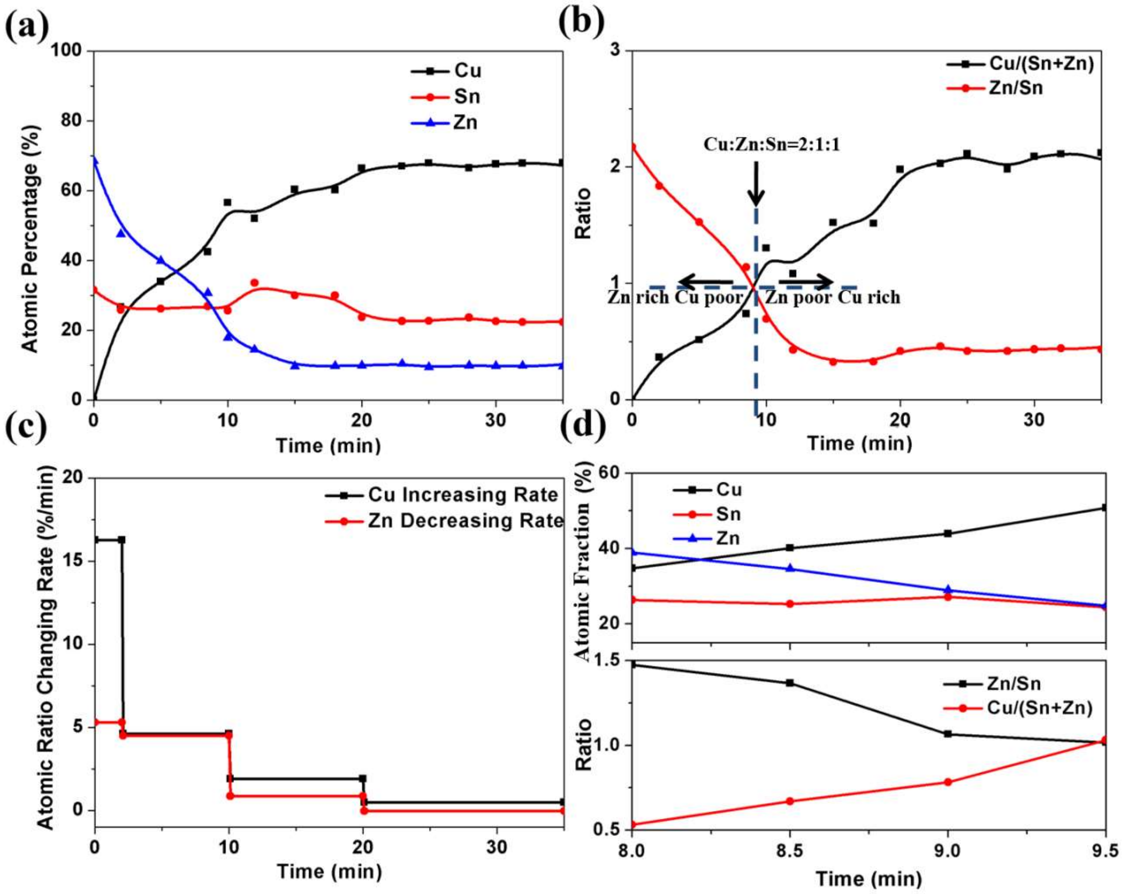

Figure 3.4 a) Atomic fraction of Cu, Sn and Zn in final precursor film as function of ion-exchange time; b) plots of Cu/(Sn+Zn) and Zn/Sn ratios vs. ion-exchange time; c) average element changing rate in different reaction stages; d) variation of atomic fraction of Cu, Sn and Zn over the range 8 min to 9.5 min

Upon further detailed analysis of the data plotted in Figure 3.4a and b, it is noticed that there is a greater increase of Cu (30%) in the first 2 min than the corresponding decrease of Zn (20%). Thus, it seems not to be a straightforward ion-exchange reaction as described by equation 2. To obtain further insight into the reaction, an additional experiment was performed by immersing the precursor $ZnS/SnS_x/TiO_2$ film in water with adjusted pH = 4 (same as 0.02 M $CuCl_2$ solution) and monitoring the release of Zn and Sn. The results (shown in Figure A.6) indicate no loss of Sn, implying that the ion-exchange process would not lead to Sn loss. Hence, by taking Sn to remain constant during the whole Cu incorporation step, the absolute element ratio changing rates of Cu and Zn (RCu or Zn) were calculated across four time periods: 0-2, 2-10, 10-20, and 20-35 min (Figure 3.4c) by using the equation

$$R_{\text{Cu or Zn}} = \left[\frac{C_{\text{Cu or Zn}}(t_0)}{C_{\text{Sn}}(t_0)} - \frac{C_{\text{Cu or Zn}}(t_1)}{C_{\text{Sn}}(t_1)}\right] / (t_1 - t_0)$$

Where $C_{Cu}$ or Zn(t) represents the atomic percentage of Cu or Zn at the starting ($t_0$) or ending ($t_1$) time of each period. At the beginning, the increasing rate of copper is approximately three times higher than the decreasing rate of zinc, indicating a more rapid copper incorporation reaction taking place than the release of Zn. The accelerated Cu incorporation rate is very likely due to redox reaction 3, which produces univalent $Cu^{1+}$ resulting in increased Cu incorporation in the form of $Cu_2S$ (see reaction 4). According to the stoichiometry of reaction 4 for each Zn released, 2 Cu are incorporated.

$$2Cu^{2+}_{(aq)} + Sn^{2+}_{(solid)} \rightarrow 2Cu^{1+}_{(surf)} + Sn^{4+}_{(solid)} \qquad (3)$$

$$ZnS_{(solid)} + 2Cu^{1+}_{(surf)} \rightarrow Cu_2S_{(solid)} + Zn^{2+}_{(aq)} \qquad (4)$$

The invoked redox reaction was supported by extra experiments as discussed/presented in Figure A.7. Returning to Figure 3.4c and looking at the data corresponding to the second reaction stage (2-10 min), the changing rates of copper and zinc are observed to be almost equal, which means the dominant reaction at that stage is simple metathetic ion-exchange represented by reaction 2. After that, the reaction remarkably slows down. It appears from this reaction analysis that reactions 2-4 are all involved in the final stage of Cu incorporation.

On the basis of the results obtained and presented in Figure 3.4a and b, it can be deduced that the present method involving the incorporation of Cu via a redox/ion exchange reaction provides the ability to fine-tune the CZTS composition, an important parameter for maximizing its optoelectronic response. The regulation of composition is further demonstrated by focusing on a narrow ion-exchange time range as shown in Figure 3.4d. As can be seen, when the ion-exchange time is 9.5 min, the Cu:Zn:Sn ratio is 2:1:1, which proves the possibility for composition control.

### 3.4.1.3 Precursor film composition

Having established that the new sequential deposition, ion-exchange method can produce CZTS precursors with tunable bulk composition, it is important to determine if the deposited CZTS/$TiO_2$ film is characterized by spatial composition uniformity. To this end, the film depth profile was measured using XPS as shown in Figure 3.5. This analysis was done for the precursor film after 9 min of Cu ionexchange reaction (slightly zinc-rich, copper-poor) (see Figure 3.4b and c). Figure 3.5a shows that the CZTS/$TiO_2$ film exhibits a uniform distribution of Ti and O with the CZTS constituent elements Cu, Zn, Sn, and S to be dispersed throughout the whole film together with $TiO_2$, indicating a thoroughly in situ-coated mesoscopic film. However, when zooming in to the low concentration range (Figure 3.5b), it is noticed that the distribution of our target elements Cu, Zn, Sn, and S are far from satisfactory. Sn is the most well-dispersed element, reflecting the fact that it did not participate in the final ion-exchange reaction as expected. Copper is highly concentrated in the shallow region of the film, whereas zinc is the opposite. This uneven distribution picture is likely due to the unmatched ion-exchange rate to the solution mass transport rate into the porous body of the film. In other words, it is suspected that the exchange of $Cu^{2+}$ with $Zn^{2+}_{(solid)}$ is faster than the rate of diffusion of $Cu^{2+}$ into the film's pores. As a result of this, the surface of the film starts reacting immediately as soon as it is exposed to the $Cu^{2+}$-containing solution, which leads to extensive local replacement of Zn by Cu in the shallow film region, whereas in the deeper film region, the slow inroad of $Cu^{2+}$ ions leads to a high zinc level. This uneven intrafilm Cu/Zn distribution is corrected by postannealing treatment as described in the final part of this paper. As far as sulfur is concerned, it is seen (Figure 3.5) to be relatively uniform and stay at a level of 12%, which with reference to that of 2.5% for Sn, seems to be sufficient for the formation of $Cu_2ZnSnS_4$. In fact, the average atomic ratio of each element has been calculated using the XPS depth profile data as Cu, 19.4%; Zn, 15.9%; Sn, 11.1%; and S, 53.6%; these results fit well with ICP-OES bulk analysis. It is noted that sulfur is in excess of the stoichiometric amount, which is expected to be beneficial during annealing of the film that is known to be associated with certain sulfur loss. This is confirmed with the annealing results presented in the next section.

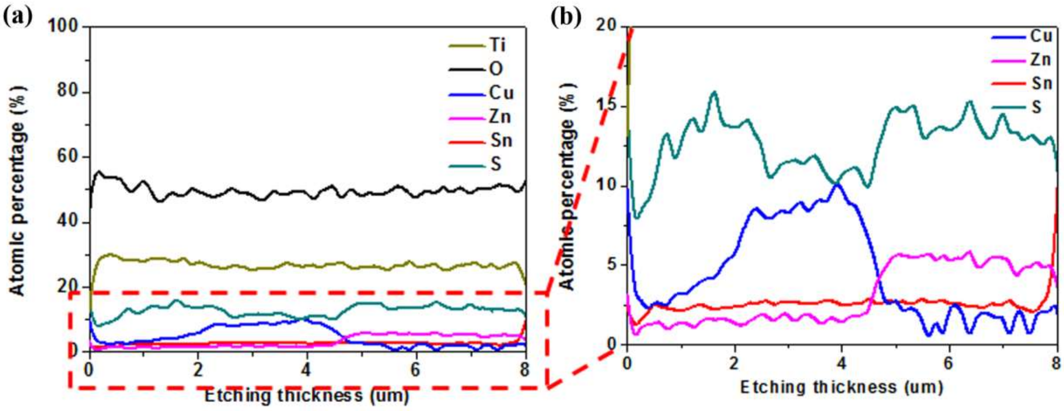

Figure 3.5 a) XPS depth profile of CZTS precursor/$TiO_2$ film after 9 min Cu ion-exchange reaction and b) the distribution of the film's chalcogenide elements

### 3.4.1.4 Precursor film morphology and crystallinity

The SEM image in Figure A.9 shows the cross-section of CZTS precursor coated on $TiO_2$/FTO substrates. By comparing it to the cross section morphology of the bare $TiO_2$/FTO film shown in Figure A.8, no significant difference can be distinguished after in situ deposition of the CZTS precursor. According to the maps of the major elements shown in the inset, only Ti, O, Sn (the concentrated Sn at the bottom is due to the conductive layer of FTO substrate), and S are uniformly distributed. By contrast, Cu is seen to be concentrated on the surface whereas Zn is in the deeper region, corresponding perfectly to the XPS depth profile data presented above and reconfirming the nonuniform distribution of copper and zinc. Therefore, despite the very low concentration of CZTS precursor elements, by combining different characterization techniques, a reasonable composition analysis of the composite film is obtained.

X-ray diffraction (XRD) analysis was performed for phase and crystallinity characterization. However, from Figure A.10 which shows the XRD patterns of the different prepared precursor films, no distinguishable peaks are evident except for the $TiO_2$/FTO background. This suggests that the deposited binary sulfides $CuS_y$/ZnS/$SnS_x$ are amorphous, which can be understood given the ambient temperature at which deposition was carried out. Therefore, annealing becomes inevitable to induce kesterite phase formation as well as crystallinity enhancement.

### 3.4.2 Annealing-Induced Kesterite Phase Formation

To promote the conversion of the poorly crystalline CZTS precursor coating into the crystalline kesterite phase, the CZTS/$TiO_2$ mesoscopic film was subjected to annealing. Upon selectively reviewing previous CZTS annealing investigations, as summarized in Table A.1, it is clearly shown that the annealing temperature is mostly set at around 500 °C. Time varies from a few minutes to even hours. Choices are also needed to be made for sulfur source supplementation during annealing as a means of suppressing S loss. In this work, the 500 °C1h condition has been tried without adding sulfur, just keeping continuous nitrogen flow the whole time to provide an inert atmosphere.

#### 3.4.2.1 Raman characterization

For characterization of the annealed films, Raman spectroscopy was employed as it provides a more reliable means for the case of the CZTS crystalline phase in comparison to the traditional X-ray diffraction method because of significant pattern overlapping of CZTS with Cu-Sn-S and ZnS phases in the latter case.[1b] However, for Raman measurements, the excitation wavelength sensitivity of different phases is quite variable due to varied optical interaction volume and near resonant excitation conditions. Therefore, it is important to select a suitable excitation wavelength that can provide high-resolution spectra for better phase identification. Here, four lasers with wavelengths of 488, 514, 633, and 785 nm were applied to capture Raman spectra of the precursor (obtained after 9 min ion-exchange time) before and after annealing at 500 °C for 1 h. The spectra taken before annealing and shown in Figure A.11 indicate the presence of a phase with a characteristic peak located at around 475 $cm^{-1}$ , which belongs to copper sulfide(s); the characteristic peaks for the other possible precursor phases like $SnS_x$ (314 $cm^{-1}$ ) and ZnS (351 $cm^{-1}$ ) could not be detected. In contrast, after annealing there is a rich Raman spectral signature (Figure 3.6). In all spectra, the formation of kesterite is revealed by the major peak located at around 338 $cm^{-1}$.[2b] It is further noticed that, as the excitation wavelength is increased from blue light (488 nm) to the near-infrared region (785 nm), the mean kesterite characteristic peak becomes sharper and new peaks around 366 and 375 $cm^{-1}$ show up along the shoulder of the main mode, which can be attributed to different Raman modes of kesterite.[1a, 2b] Herein, it proves that the new method is very effective for obtaining crystalline CZTS. Full Raman spectra from wavenumber 200 to 800 $cm^{-1}$ are depicted in Figure A.12a. Except for the characteristic Raman peak of kesterite (labeled with red dash lines), another three small peaks marked with blue dash lines are seen, which correspond well to the anatase Raman spectra shown in Figure A.12b.

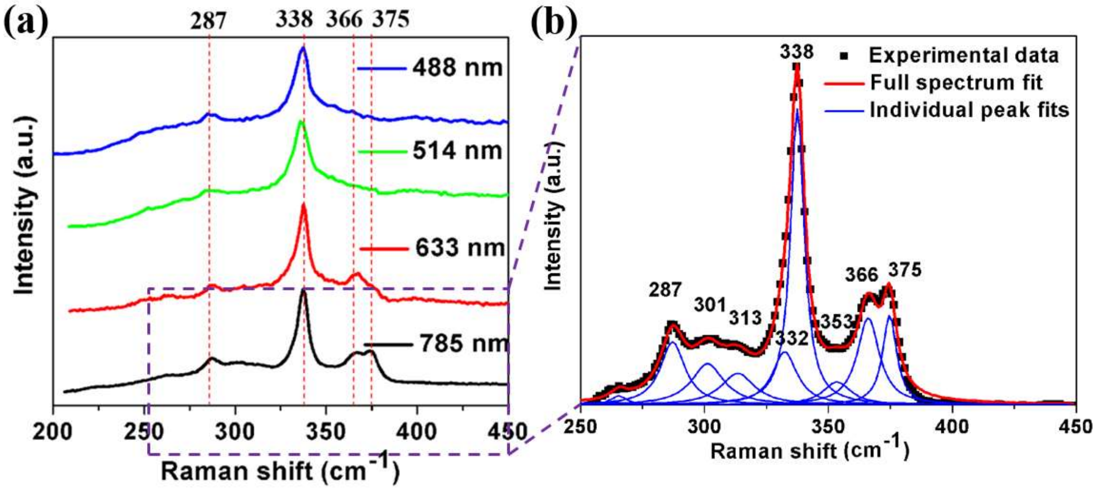

Figure 3.6 a) Multi-wavelength excitation Raman spectra of the CZTS/$TiO_2$ film (9min-precursor film) annealed at 500℃ for 1h and b) peak fitting results of the spectrum taken with 785 nm laser excitation.

Another question is why the anatase Raman peaks become much less visible after CZTS coating, especially when increasing the excitation wavelength to the near-infrared region. This most likely is due to strong visible light absorption by CZTS, a property that makes this material highly interesting for light-harvesting applications. As can be seen (Figure A.12b), there is no significant difference among the Raman spectra of $TiO_2$/FTO using different wavelength lasers. However, after applying CZTS coating, the anatase peaks are not only weaker but also differ in intensity with decreasing excitation wavelength. It is postulated that CZTS will largely absorb the incident light signal as well as the scattered Raman signal from $TiO_2$, which causes a huge decrease in the effective Raman detection depth for $TiO_2$. Moreover, the energy of signals with longer wavelength approaches the band gap of CZTS-kesterite (~1.5 eV), leading to a near resonant condition,[16] which as a result enhances the Raman scattering by CZTS, making the $TiO_2$ signal less visible. A similar phenomenon has been observed when incorporating CZTS with large bandgap semiconductors.[17]

According to the multiwavelength excitation Raman spectra in Figure 3.6a, the near resonant condition of 785 nm laser excitation has activated more kesterite Raman modes than the other wavelength lasers.[2b] Thus, further analysis of the spectrum captured with 785 nm light excitation is done by fitting the peaks with Lorentzian curves as shown in the high resolution plot of Figure 3.6b. The dominating peak centered at 338 $cm^{-1}$ is attributed to the main A mode of kesterite; there appears to also exist a slightly left-shifted one at 332 $cm^{-1}$ that makes the main peak broader, which may represent the degree of Cu/Zn disorder according to Scragg et al.[1a] The peak centered at 287 $cm^{-1}$ corresponds to the second A mode of kesterite, and the 366 and 375 $cm^{-1}$ peaks belong to its E and B modes, respectively. The peaks at 301 and 313 $cm^{-1}$ identified from the fitted curves also match well with the previously reported A and E modes, respectively. All of the fitted peaks belong to kesterite Raman modes, and no secondary phases have been identified.

#### 3.4.2.2 XPS and EDS spatial characterization

After annealing, the CZTS/$TiO_2$ film was investigated in terms of spatial element distribution using XPS and EDS mapping as done earlier with the precursor films. The XPS results are shown in Figure 3.7a and b. Ti and O remain constant as in the precursor film, implying that annealing has not affected $TiO_2$. By focusing on the CZTS constituent elements (Figure 3.7b), a number of comments can be made. First, there is no major change in the distribution of Sn and Zn before (Figure 3.5b) and after annealing except for Cu. Comparing Figure 3.7b to Figure 3.5b, it becomes evident that Cu is not only concentrated in the shallow region (as in the precursor film) but is also partly dispersed into the deeper region of the $TiO_2$ mesoscopic scaffold, which means annealing has induced its inward diffusion to form kesterite. This can be further confirmed by examining the EDS maps in Figure A.13. Second, it is still noticed that a significant amount of Cu has remained near the surface. That means that the composition of CZTS varies with film depth exhibiting a kind of grading, the significance of which in kesterite light-absorbing performance remains to be assessed. Nevertheless, the presence near the surface (<2 μm depth), where the excess of Cu/Zn>>2, of secondary CuS or $Cu_2S$ phases cannot be ruled as in case of ZnS at depth > 5 μm, where significant excess of Zn remains. With reference to S, there is no great change other than a slight decrease in the atomic fraction from 12 to 10% (on average), probably due to the commonly known sulfur-loss phenomenon when no sulfur supplement is provided during annealing. However, this limited loss of sulfur is acceptable because of the already excess S in the precursor (12% S to 2.5% Sn on average, more than 4:1 for CZTS).

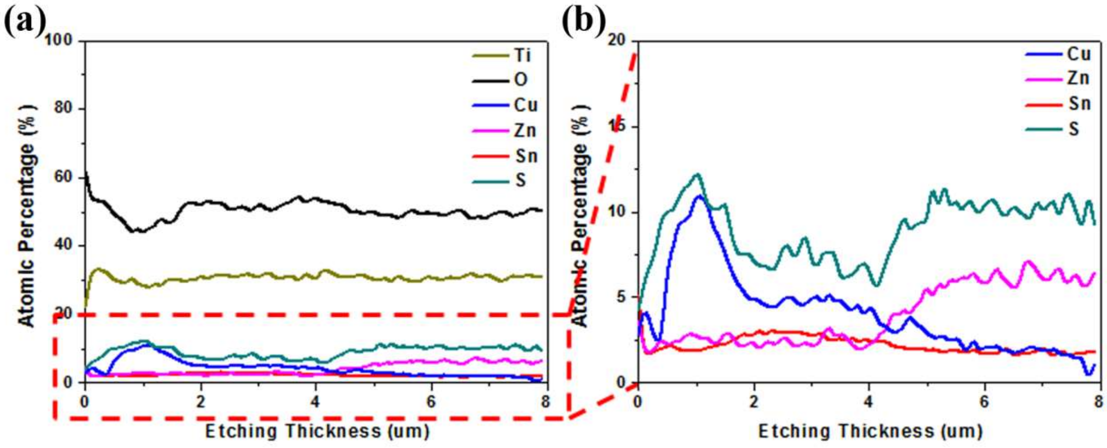

Figure 3.7 a) XPS depth profile of CZTS/TiO2 film after annealing and b) the distribution of the chalcogenide elements.

### 3.4.3 Hydrochloric Acid Etching to Remove Secondary Phases

As determined in the previous section, the annealed CZTS/$TiO_2$ mesoscopic film exhibited significant excess of Cu near the surface and Zn in the deeper region of the film. Between CuS and ZnS, the presence of ZnS as an impurity in CZTS is the least preferable from a solar cell application standpoint due to the large bandgap difference that causes internal barriers, preventing efficient charge transport. Therefore, it is necessary to find an effective approach to solve this problem. Chemical etching using hot (75 °C) concentrated hydrochloric acid has been used to remove secondary ZnS phase from CZTS,[18] but from an application point of view, the high volatility of HCl at 75 °C could lead to severe environmental and health occupational issues. This led us to develop a room-temperature HCl-based etching procedure as described next.

As a first step toward developing a selective ZnS etching method, the pseudosolubility of three possible bulk binary sulfides was tested by dissolving 20 mg of CuS, ZnS, and SnS in 20 mL of 4 M HCl for 1 h and then measuring the dissolved species with ICP-OES. The bar chart in Figure 3.8a shows that ZnS is highly soluble and SnS is partly soluble whereas bulk CuS is almost insoluble, which means this approach can easily remove ZnS in the deep region of our CZTS/$TiO_2$ film. These results are a rough estimation as the actual secondary phases may not have exactly the same composition as the theoretical stoichiometry not to mention that their nanosize and poor crystallinity can lead to larger levels of solubility. Therefore, another etching/dissolution experiment was performed by this time immersing the annealed CZTS/$TiO_2$ film into the 4 M HCl solution. For the maximum amount of soluble elements that can be removed from the film to be determined, the test involved multiple immersion steps with each one lasting 2 h before the film was taken out of solution, washed, dried, and then immediately immersed in another fresh HCl solution. The experiment was repeated 10 times in a total of 20 h of etching. As can be seen from Figure 3.8b, after the first 2 h of immersion, all three elements were solubilized to some degree with Zn and Sn exceeding the amount of Cu removed, reflecting the variable reactivity of the three binaries. After 20 h, it can be seen that there is hardly any dissolved cation concentration (~0.1 ppm level), signaling the removal of all impurity binary phases. The background solubility of ~0.1 ppm suggests that it represents the dissolution of the kesterite-phase CZTS itself. The amounts of Zn, Sn, and Cu removed from the film via this 20 h sequential immersion procedure were calculated to be approximately 53.4, 18.6, and 22.5%, respectively, by adding the removed elemental fraction after each etching step (Figure A.14) Therefore, the developed etching protocol is effective for removing the excess secondary phases.

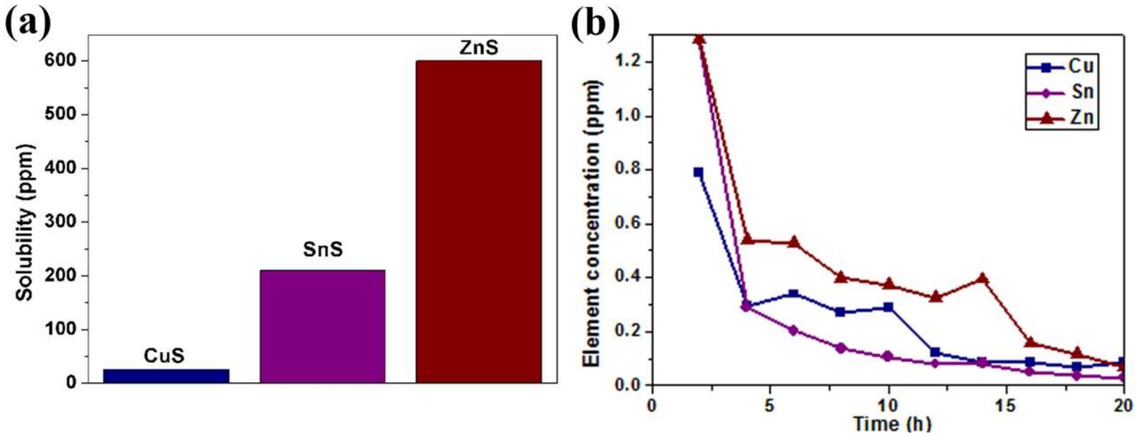

Figure 3.8 a) Pseudosolubility of the different bulk binaries in 4 M HCl solution and b) the residual ion concentration in 4M HCl solution after multiple etching steps of 2h each.

To verify the effectiveness of the etching procedure, the XPS depth profile analysis was carried out again. According to Figure 3.9a, the etching procedure seems to be a success, especially for the original Zn-rich region inside the film. After etching, Zn remains at the same level as Sn, whereas Sn has experienced a slight decrease in the deeper region. This is more clearly evident from the EDS mapping in the inset of Figure A.15, where Zn is seen to be uniformly dispersed throughout the whole film. The four CZTS elements copper, zinc, tin, and sulfur are seen to be present at a near stoichiometric ratio of $Cu_2ZnSnS_4$ in most parts of the film except for the near surface region, where copper is still significantly rich. However, when the film's composition is compared to the one before etching (Figure 3.7b), there is a reduction in the excess amount of copper sulfides. The latter because of the apparent nanocrystalline nature is believed to be more soluble that the bulk crystalline CuS used in the test of Figure 3.8a as predicted by the Gibbs-Thomson law,[19] hence explaining its partial removal. The remaining small amount of excess $Cu_xS$ near the surface (1-3 μm depth) may be removed using KCN treatment, which is widely used for either CIGS[20] or CZTS[21]. However, because of the extremely toxic nature of cyanide salts, it was avoided in the present study but remains an option for future optimization work.

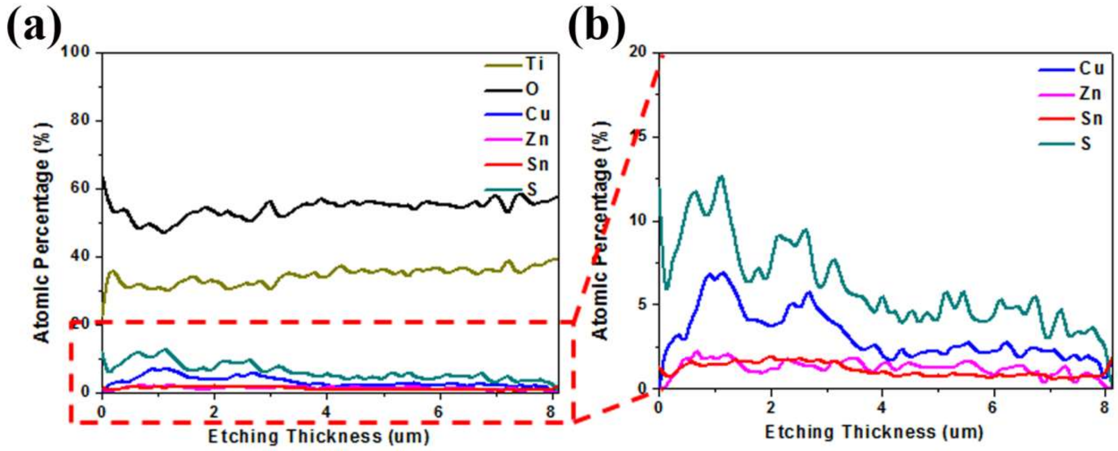

Figure 3.9 a) XPS depth profile of annealed CZTS/$TiO_2$ film after 4M HCl etching for 20h and b) the distribution of the chalcogenide elements.

Figure 3.10 provides the CZTS elemental distribution profiles and maps for the CZTS/$TiO_2$ mesoscopic film during the different fabrications, namely, before annealing, after annealing, and after etching. It is clear that after etching, notwithstanding the minor excess copper sulfide present near the surface, uniform element distribution is obtained throughout the film.

Additional XPS high-resolution spectra are shown in Figure A.16 as a support to the depth profile, where the existence of all four elements in our mesoporous film can be clearly seen. As the atomic fraction of the target material CZTS vis-a-vis the $TiO_2$ background is quite low, different analytical techniques have been combined to obtain reliable semiquantitative confirmation of the formation of kesterite phase and its composition. In this regard, it is important to examine whether the acid etching procedure could cause any damage to kesterite itself. To this end, the CZTS/$TiO_2$ film before and after etching were examined by Raman and XRD measurements (data shown in Figure A.17). The Raman measurements collected with 785 nm excitation (Figure A.17a) show no change in the profile and peak positions after etching, indicating that the hydrochloric acid treatment is effective for removing the secondary phases without visibly affecting the kesterite phase itself. Figure A.14b shows the XRD patterns of CZTS/$TiO_2$ before and after etching, where a strong peak at around 28.5°

corresponding to the 112 plane of kesterite can be clearly identified in both conditions, reconfirming the resistance of kesterite to HCl acidic solution attack.

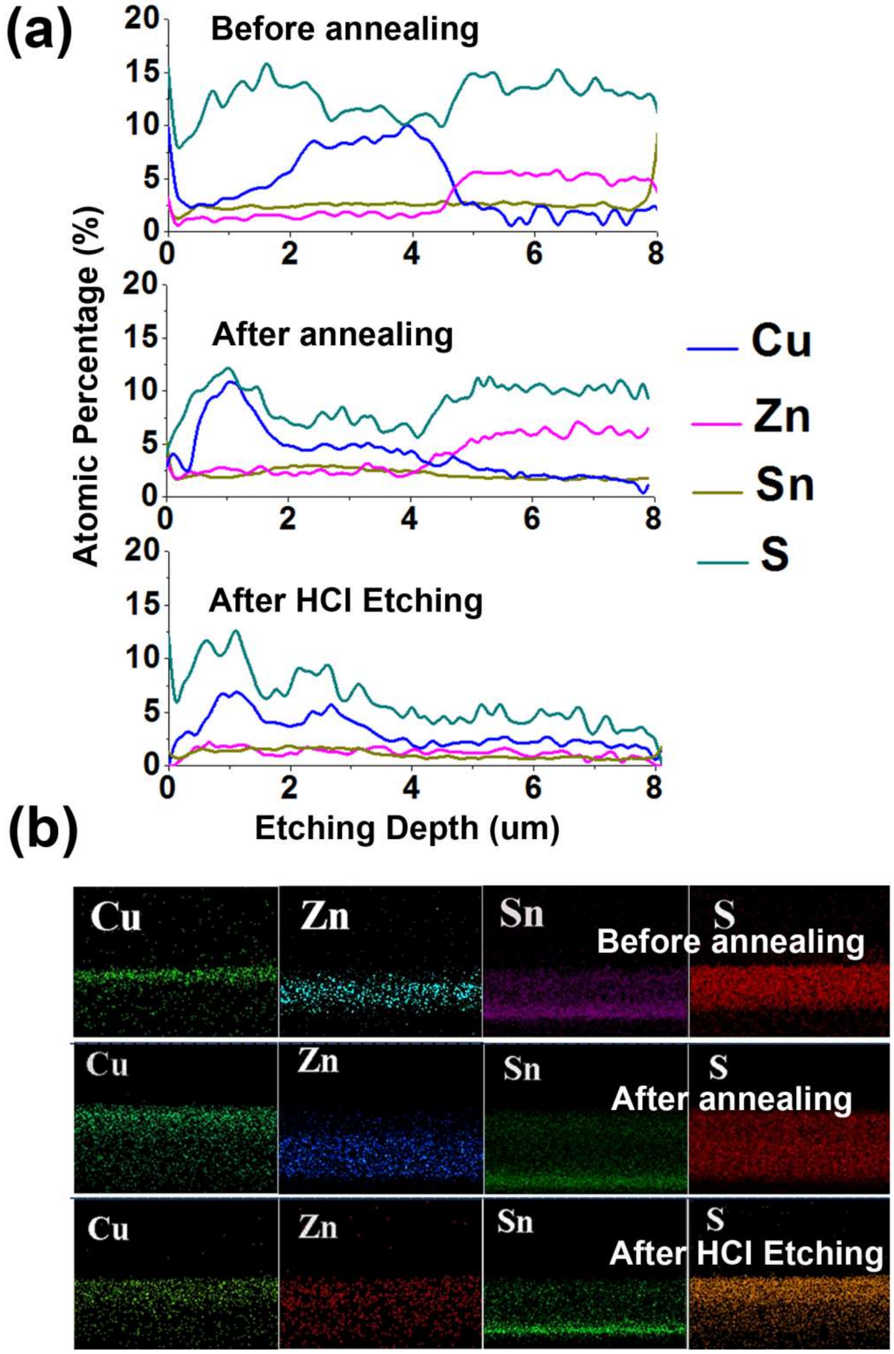

Figure 3.10 Comparison of CZTS element distribution from a) XPS depth profile and b) EDS cross-section mapping results among various CZTS/$TiO_2$ film samples before annealing, after annealing and after 4M HCl etching for 20 h

### 3.4.3.1 TEM and EDS characterization

The uniformity in elemental distribution is further verified with Figures A.18a and A.18b that show low and high magnification (microscale) EDS top-view maps, respectively. All elements are well dispersed throughout the whole film plane parallel to the substrate; meanwhile, the film surface remains flat without cracks or other superficial defects, indicating that the whole annealing-etching procedure is morphologically damage-free. To probe the nanoscale CZTS coating on the $TiO_2$ mesoporous film (made with ~20 nm particles), the final etched CZTS/$TiO_2$ film was scraped off and grounded into powder for TEM charaterization. Figure 3.11a shows the dark field TEM image and the corresponding nanoscale element maps of Ti, O, Cu, Zn, Sn, and S. As can be seen in even an area as small around as $50 \times 50$ $nm^2$ , the uniformity of all elements is still perfectly preserved. The EDS line-scan in Figure 3.11b also confirms the uniform distribution of all CZTS elements together with $TiO_2$ nanoparticles. These results thus provide direct evidence that our CZTS coating is indeed distributed uniformly at nanoscale among the $TiO_2$ nanoparticles that make the mesoporous film instead of forming isolated (segregated) clusters, proving the effectiveness of the solution deposition method and associated annealing and etching protocols developed.

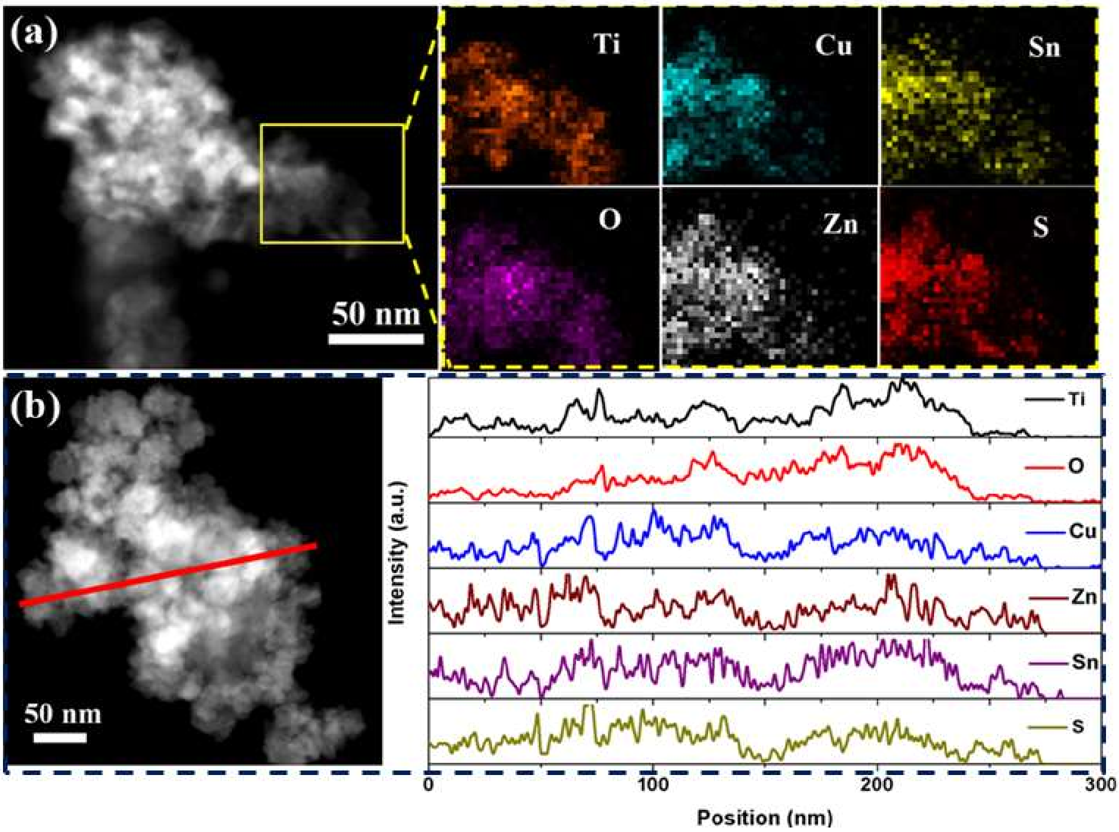

Figure 3.11 a) Nanoscale STEM-HAADF image and the corresponding EDS elemental maps and b) line scan of ground CZTS/$TiO_2$ composite powder

To explore deeper their morphological and intephasial features, high resolution bright field TEM images were taken and are shown in Figure 3.12. As evident from Figure 3.12a, the various nanoparticles are limited to around 10−20 nm in all dimensions. When further zooming in, as depicted in Figure 3.12b, it is clear to see the parallel fringes of two crystals with interplanar spacing of 3.09 and 3.42 Å, corresponding to the kesterite (112) and anatase (101) planes, respectively. The sizes of these two nanoparticles can also be estimated according to these two sets of clear fringes to be almost equal to 10 nm in diameter as also supported by Figure 3.12c and Figure A.19c and d. This suggests that the kesterite coating is in the form of kesterite nanocrystallites intermixed with the anatase nanoparticles instead of forming a core−shell structure. Toward the bottom of the film (close to the FTO substrate), there exists a region containing only anatase nanoparticles (Figure 3.12d) apparently due to the poor infiltration of copper ions. This $TiO_2$ predominantly bottom zone can act as barrier against undesirable CZTS/FTO contact that is known to lead to severe charge recombination losses. Overall, therefore, the built film with kesterite nanocrystallites coated throughout the mesoporous anatase film (except the zone near the FTO substrate) has the characteristics of a promising optoelectronic structure combining the light-harvesting property of kesterite with the transfer of the generated excitons to adjacent $TiO_2$ as conductor.

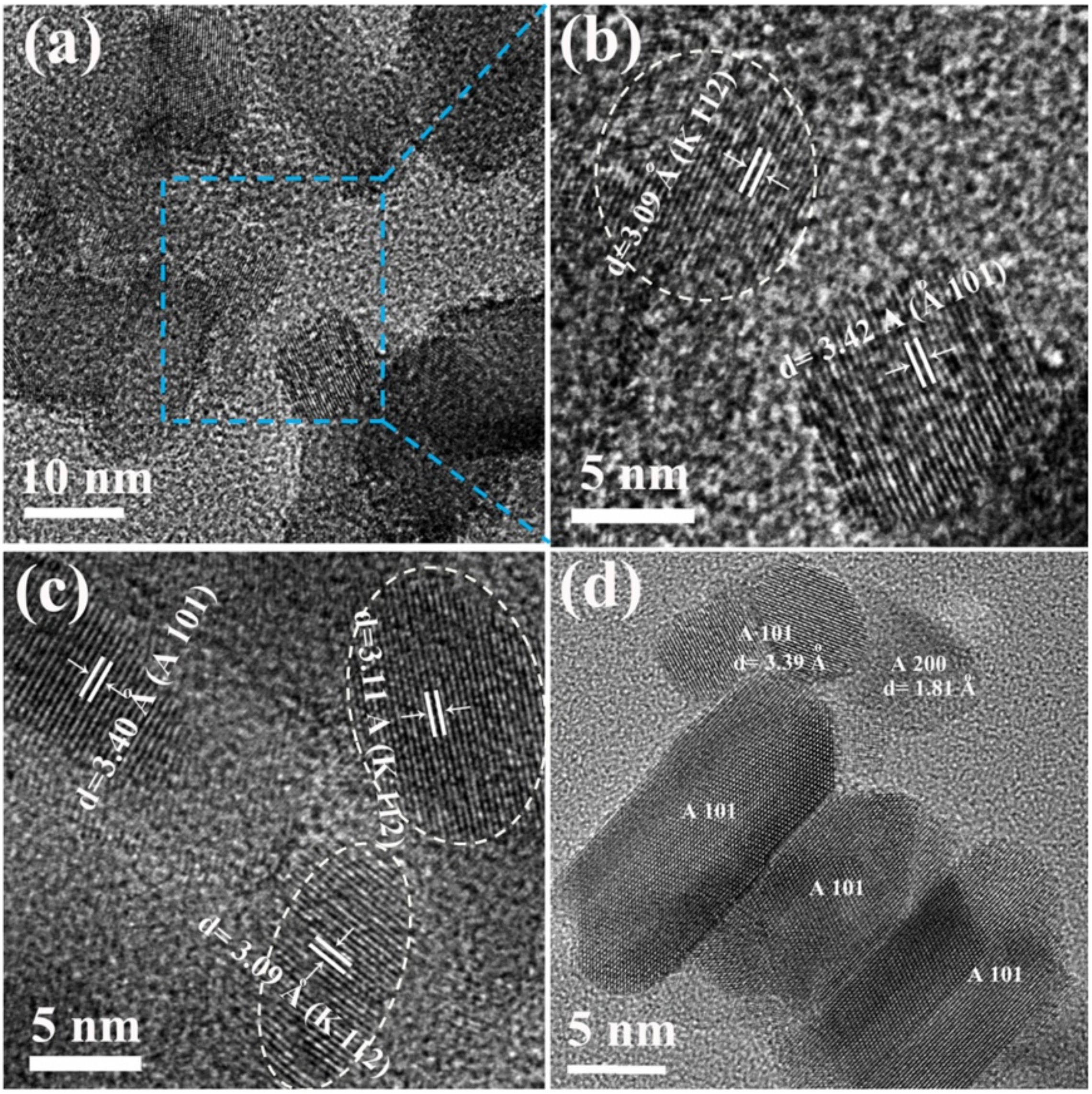

Figure 3.12 a) TEM high-resolution image of final $CZTS/TiO_2$ material and b) enlarged area revealing the existence of both kesterite and anatase phases; c) different area shown the existence of both kesterite and anatase; d) a selected area shown only anatase crystallites (K represents kesterite and A represents anatase)

### 3.4.3.2 Optical characterization

To evaluate/confirm the light-absorbing properties of the new CZTS/$TiO_2$ mesoporous film structure, transmittance measurements were taken as shown in Figure 3.13. As can be seen, there is a great difference in the transmittance at long wavelengths for the CZTS/$TiO_2$ film before and after hydrochloric acid treatment (etching) (Figure 3.13a). The theoretical bandgap of CZTS is 1.5 eV, which corresponds to a light absorption edge of approximately 826 nm. The low transmittance of the film before etching must be due to surface reflection or more likely absorption by secondary Cu-rich phases,[22] as it was noted significant decline of the transmittance at the long wavelength range before and after Cu incorporation in the precursor film (Figure A.5). After etching, there is significant enhancement of long-range wavelength transmittance, whereas in UV−vis region, the film is completely nontransparent, and a typical semiconductor absorption edge is perfectly displayed. This improvement in transmittance following HCl etching is attributed to the removal of interfering copper-rich secondary phases as already mentioned, hence confirming the effectiveness of the etching treatment. Using the equation $\alpha \approx -\ln(T)/d$,[23] where d is the thickness of the film, the absorption coefficient α was calculated as shown in Figure 3.13b. The derived band gap was estimated to be in the range of 1.4−1.5 eV by linearly fitting the absorption edge, which is near the theoretical value of pure crystalline kesterite.[24]

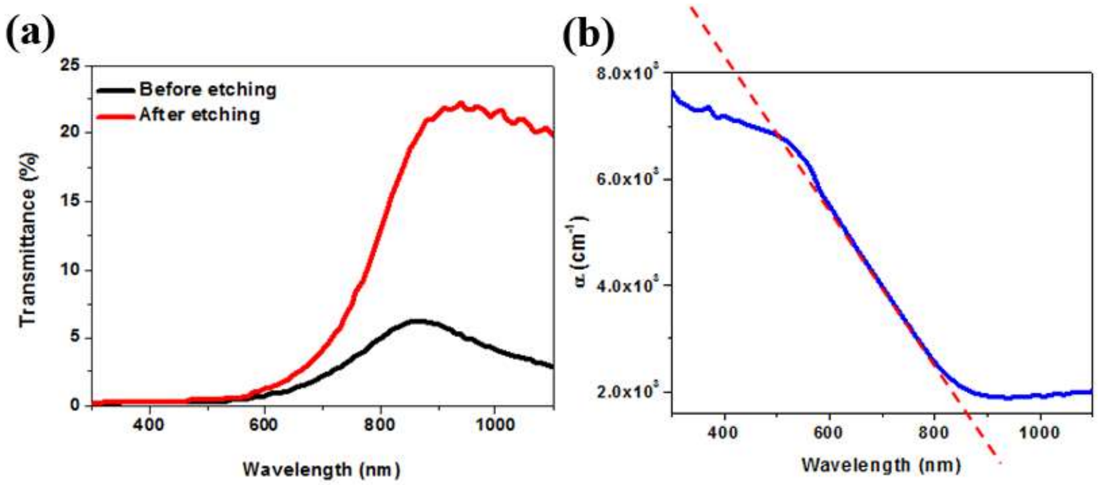

Figure 3.13 a) Transmittance measurement of CZTS/$TiO_2$ film before and after etching; and b) converted absorption curve of film after etching.

To further evaluate the potential of this new absorber film structure, the time-resolved photoluminescence (TRPL) measurement was applied on the CZTS/$TiO_2$ film before and after HCl treatment. The results are shown in Figure 3.14a, where the inset shows the steady-state PL spectra measured at room temperature, which is high compared to the liquid nitrogen temperature usually employed. As illustrated in Figure 3.14b, the luminescence spectrum of CZTS is usually dominated by two recombination channels:[25] The first is a band-to-band (BB) recombination, where a free electron recombines with a free hole, and a photon with band gap energy is emitted. This recombination is usually seen only at higher temperatures and higher dose excitation as it applies to the measurements made in this work.[26] The second is a band-to-tail (BT) recombination, where a free electron recombines with a hole that is localized in the valence band tail. The BB and BT recombination modes result in two characteristic PL peaks centered at 1.69 and 1.42 eV energy positions, respectively, as discussed by Grossberg et al.[27] Another noteworthy characteristic of the two steady-state PL spectra (inset in Figure 3.14a) is the disappearance of the shoulder around 600 nm (black curve) following HCl etching treatment (red curve). This is attributed to the removal of Cu/Zn-containing sulfide impurities. As reported by Peng et al. and Hou et al., ZnS shows a characteristic PL peak centered at ~400 nm, which gradually shifts toward a longer wavelength in the visible range at ~600 nm, as observed in this work.[28] The disappearance of the shoulder provides further evidence of the effectiveness of this acidic treatment in minimizing the presence of unwanted secondary phases. As for the TR-PL measurement, because of the pulsed nature of the excitation source, the initial excess carrier concentration created by each pulse of laser is significantly higher than the steady-state carrier concentration during continuous illumination at the same power density. Therefore, the number of carriers generated by a single pulse of laser in the measurement is at a high injection condition, which explains the initially fast decay of the spectra. The average carrier lifetime was determined by fitting a portion of each spectrum (3-30 ns from the starting of the decay), avoiding the initial decay by a single exponent.[29] The lifetimes of 7.9 and 8.7 ns are extracted for our CZTS/$TiO_2$ sample before and after HCl etching, respectively, indicating the effectiveness of the acid treatment in improving the optoelectronic property of this absorber film.

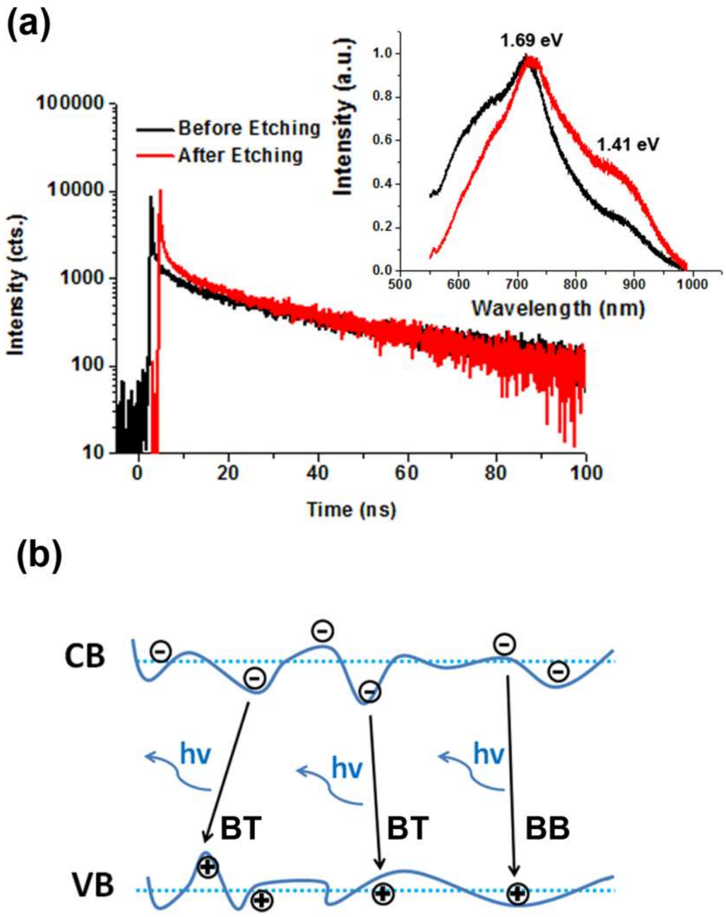

Figure 3.14 a) Time-resolved photoluminescence measurements of the CZTS/$TiO_2$ film before and after HCl etching. Inset shows the steady state PL spectra. b) Schematic of the band diagram for CZTS with possible band-tail (BT) and band-to-band (BB) recombination between delocalized donor and acceptor states.

The energy band alignment of CZTS-kesterite and $TiO_2$ is favorable for such applications as it can be evaluated from the energy diagram of Figure A.20. To complete the device, other than the electron conductor ($TiO_2$) and absorber (CZTS), a hole conductor with HOMO level matched to the valence band of kesterite is also needed. Besides liquid electrolyte (as in dye- or quantum dotsensitized solar cells), organic hole transfer materials (HTM) like

Spiro-OMeTAD, P3HT, as well as inorganic HTM, such as CuSCN and CuI, could potentially serve for this purpose.[30]

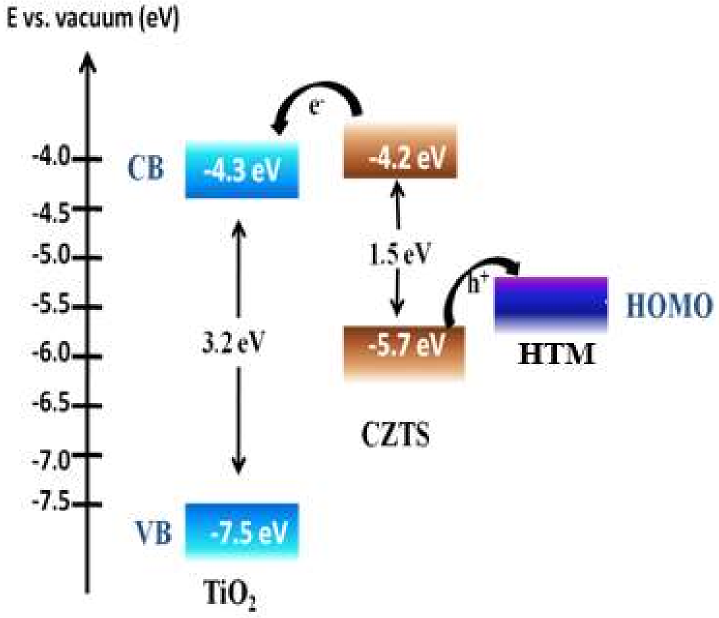

Figure 3.15 Theoretical energy band alignment of a CZTS/TiO$_2$ based solar cell

## 3.5 Conclusions

In this chapter, a novel fabrication route is presented to prepare nanoscale composition-controlled CZTS-coated TiO$_2$ mesoscopic films with potential for application as light absorption-conductor structure in ETA-type solar cells. The new process makes use of sequential aqueous solution deposition and exchange of binary sulfides ($SnS_x$-ZnS-CuS) as a first step to produce a CZTS precursor coating onto TiO$_2$. Via annealing at 500 °C, the precursor was successfully converted into crystalline kesterite phase. To improve the composition uniformity of the quaternary semiconductor, a hydrochloric acid etching treatment was properly adjusted, proving effective not only in removing excess ZnS trapped deep inside the mesoporous film but also Cu-rich surface deposits. The chemical reactions involved in precursor deposition and the formation of kesterite nanocrystallites were fully probed via a multitude of analytical and characterization tools. Upon etching, the CZTS/TiO$_2$ structure was shown via transmittance measurements to exhibit excellent light absorption response with a bandgap approaching its theoretical 1.5 eV value and longer carrier lifetime.

This newly developed method of in situ CZTS solution deposition into the $TiO_2$ mesoporous scaffold has overcome the previous problem of poor CZTS penetration as it was relying on nanocrystal ex situ coating, hence opening the road for absorber-conductor type solar cell applications. In addition, this study provides new ideas and nanoscale analysis for affecting controlled deposition of complex (quaternary) inorganic semiconductor structures with uniform composition.

## 3.6 References

1. (a) Scragg, J. J. S.; Choubrac, L.; Lafond, A.; Ericson, T.; Platzer-Björkman, C., A Low-Temperature Order-Disorder Transition in $Cu_2ZnSnS_4$ Thin Films. *Applied Physics Letters* **2014,** *104* (4), 041911; (b) Fontané, X.; Calvo-Barrio, L.; Izquierdo-Roca, V.; Saucedo, E.; Pérez-Rodriguez, A.; Morante, J. R.; Berg, D. M.; Dale, P. J.; Siebentritt, S., In-Depth Resolved Raman Scattering Analysis for the Identification of Secondary Phases: Characterization of $Cu_2ZnSnS_4$ Layers for Solar Cell Applications. *Applied Physics Letters* **2011,** *98* (18), 181905.

2. (a) Cattley, C. A.; Cheng, C.; Fairclough, S. M.; Droessler, L. M.; Young, N. P.; Warner, J. H.; Smith, J. M.; Assender, H. E.; Watt, A. A. R., Low Temperature Phase Selective Synthesis of $Cu_2ZnSnS_4$ Quantum Dots. *Chemical Communications* **2013,** *49* (36), 3745-3747; (b) Dimitrievska, M.; Fairbrother, A.; Fontané, X.; Jawhari, T.; Izquierdo-Roca, V.; Saucedo, E.; Pérez-Rodríguez, A., Multiwavelength Excitation Raman Scattering Study of Polycrystalline Kesterite $Cu_2ZnSnS_4$ Thin Films. *Applied Physics Letters* **2014,** *104* (2), 021901.

3. Just, J.; Lützenkirchen-Hecht, D.; Frahm, R.; Schorr, S.; Unold, T., Determination of Secondary Phases in Kesterite $Cu_2ZnSnS_4$ Thin Films by X-Ray Absorption Near Edge Structure Analysis. *Applied Physics Letters* **2011,** *99* (26), 021901.

4. Wang, W.; Winkler, M. T.; Gunawan, O.; Gokmen, T.; Todorov, T. K.; Zhu, Y.; Mitzi, D. B., Device Characteristics of CZTSSe Thin-Film Solar Cells with 12.6% Efficiency. *Advanced Energy Materials* **2013**, 1301465.

5. (a) Hodes, G.; Cahen, D., All-Solid-State, Semiconductor-Sensitized Nanoporous Solar Cells. *Accounts of Chemical Research* **2012,** *45* (5), 705-713; (b) Roelofs, K. E.; Brennan, T. P.; Bent, S. F., Interface Engineering in Inorganic-Absorber Nanostructured Solar Cells. *The Journal of Physical Chemistry Letters* **2014,** *5* (2), 348-360.

6. Wang, Y.; Li, C. X.; Yin, X. J.; Wang, H.; Gong, H., $Cu_2ZnSnS_4$ (CZTS) Application in $TiO_2$ Solar Cell as Dye. *ECS Journal of Solid State Science and Technology* **2013,** *2* (7), Q95-Q98.

7. Pathan, H. M.; Lokhande, C. D., Deposition of Metal Chalcogenide Thin Films by Successive Ionic Layer Adsorption and Reaction (SILAR) Method. *Bulletin of Materials Science* **2004,** *27* (2), 85-111.

8. Lee, H. J.; Bang, J.; Park, J.; Kim, S.; Park, S.-M., Multilayered Semiconductor (CdS/CdSe/ZnS)-Sensitized $TiO_2$ Mesoporous Solar Cells: All Prepared by Successive Ionic Layer Adsorption and Reaction Processes. *Chemistry of Materials* **2010,** *22* (19), 5636-5643.

9. (a) Sun, K.; Su, Z.; Yan, C.; Liu, F.; Cui, H.; Jiang, L.; Shen, Y.; Hao, X.; Liu, Y., Flexible $Cu_2ZnSnS_4$ Solar Cells Based on Successive Ionic Layer Adsorption and Reaction Method. *RSC Advances* **2014,** *4* (34), 17703-17708; (b) Kahraman, S.; Çetinkaya, S.; Çetinkara, H. A.; Güder, H. S., A Comparative Study of $Cu_2ZnSnS_4$ Thin Films Growth by Successive Ionic Layer Adsorption–Reaction and Sol-Gel Methods. *Thin Solid Films* **2014,** *550* (0), 36-39.

10. Fella, C. M.; Uhl, A. R.; Romanyuk, Y. E.; Tiwari, A. N., $Cu_2ZnSnSe_4$ Absorbers Processed from Solution Deposited Metal Salt Precursors under Different Selenization Conditions. *physica status solidi (a)* **2012,** *209* (6), 1043-1048.

11. Wang, Z.; Wang, H.; Liu, B.; Qiu, W.; Zhang, J.; Ran, S.; Huang, H.; Xu, J.; Han, H.; Chen, D.; Shen, G., Transferable and Flexible Nanorod-Assembled $TiO_2$ Cloths for Dye-Sensitized Solar Cells, Photodetectors, and Photocatalysts. *ACS Nano* **2011,** *5* (10), 8412-8419.

12. Charbonneau, C.; Lee, K. E.; Shan, G. B.; Gomez, M. A.; Gauvin, R.; Demopoulos, G. P., Preparation and DSSC Performance of Mesoporous Film Photoanodes Based on

Aqueous-Synthesized Anatase Nanocrystallites. *Electrochemical and Solid-State Letters* **2010,** *13* (8), H257-H260.

13. Becker, M. A.; Radich, J. G.; Bunker, B. A.; Kamat, P. V., How Does a SILAR CdSe Film Grow? Tuning the Deposition Steps to Suppress Interfacial Charge Recombination in Solar Cells. *The Journal of Physical Chemistry Letters* **2014,** *5* (9), 1575-1582.

14. Graetzel, M.; Janssen, R. A. J.; Mitzi, D. B.; Sargent, E. H., Materials Interface Engineering for Solution-Processed Photovoltaics. *Nature* **2012,** *488* (7411), 304-312.

15. (a) Dai, P.; Shen, X.; Lin, Z.; Feng, Z.; Xu, H.; Zhan, J., Band-Gap Tunable $(Cu_2Sn)_{x/3}Zn_{1-x}S$ Nanoparticles for Solar Cells. *Chemical Communications* **2010,** *46* (31), 5749-5751; (b) Redinger, A.; Berg, D. M.; Dale, P. J.; Siebentritt, S., The Consequences of Kesterite Equilibria for Efficient Solar Cells. *Journal of the American Chemical Society* **2011,** *133* (10), 3320-3323.

16. Frank, O.; Zukalova, M.; Laskova, B.; Kurti, J.; Koltai, J.; Kavan, L., Raman Spectra of Titanium Dioxide (Anatase, Rutile) with Identified Oxygen Isotopes (16, 17, 18). *Physical Chemistry Chemical Physics* **2012,** *14* (42), 14567-14572.

17. Liu, X.; Wang, C.; Xu, J.; Liu, X.; Zou, R.; Ouyang, L.; Xu, X.; Chen, X.; Xing, H., Fabrication of $ZnO/CdS/Cu_2ZnSnS_4$ P-N Heterostructure Nanorod Arrays via a Solution-Based Route. *CrystEngComm* **2013,** *15* (6), 1139-1145.

18. Fairbrother, A.; García-Hemme, E.; Izquierdo-Roca, V.; Fontané, X.; Pulgarín-Agudelo, F. A.; Vigil-Galán, O.; Pérez-Rodríguez, A.; Saucedo, E., Development of a Selective Chemical Etch to Improve the Conversion Efficiency of Zn-Rich $Cu_2ZnSnS_4$ Solar Cells. *Journal of the American Chemical Society* **2012,** *134* (19), 8018-8021.

19. Demopoulos, G. P., Aqueous Precipitation and Crystallization for the Production of Particulate Solids with Desired Properties. *Hydrometallurgy* **2009,** *96* (3), 199-214.

20. Liao, Y.-K.; Wang, Y.-C.; Yen, Y.-T.; Chen, C.-H.; Hsieh, D.-H.; Chen, S.-C.; Lee, C.-Y.; Lai, C.-C.; Kuo, W.-C.; Juang, J.-Y.; Wu, K.-H.; Cheng, S.-J.; Lai, C.-H.; Lai, F.-I.; Kuo, S.-Y.; Kuo, H.-C.; Chueh, Y.-L., Non-Antireflective Scheme for Efficiency Enhancement of $Cu(In,Ga)Se_2$ Nanotip Array Solar Cells. *ACS Nano* **2013,** *7* (8), 7318-7329.

21. Schubert, B.-A.; Marsen, B.; Cinque, S.; Unold, T.; Klenk, R.; Schorr, S.; Schock, H.-W., $Cu_2ZnSnS_4$ Thin Film Solar Cells by Fast Coevaporation. *Progress in Photovoltaics: Research and Applications* **2011,** *19* (1), 93-96.

22. (a) Kim, Y.-Y.; Walsh, D., Metal Sulfide Nanoparticles Synthesized via Enzyme Treatment of Biopolymer Stabilized Nanosuspensions. *Nanoscale* **2010,** *2* (2), 240-247; (b) Zhang, L.; Li, Y.; Jin, Z.; Yu, J. C.; Chan, K. M., An NIR-Triggered and Thermally Responsive Drug Delivery Platform through DNA/Copper Sulfide Gates. *Nanoscale* **2015,** *7* (29), 12614-12624; (c) Tanveer, M.; Cao, C.; Aslam, I.; Ali, Z.; Idrees, F.; Tahir, M.; Khan, W. S.; Butt, F. K.; Mahmood, A., Effect of the Morphology of CuS upon the Photocatalytic Degradation of Organic Dyes. *RSC Advances* **2014,** *4* (108), 63447-63456.

23. Tang, D.; Wang, Q.; Liu, F.; Zhao, L.; Han, Z.; Sun, K.; Lai, Y.; Li, J.; Liu, Y., An Alternative Route Towards Low-Cost $Cu_2ZnSnS_4$ Thin Film Solar Cells. *Surface and Coatings Technology* **2013,** *232* (0), 53-59.

24. Mitzi, D. B.; Gunawan, O.; Todorov, T. K.; Wang, K.; Guha, S., The Path towards a High-Performance Solution-Processed Kesterite Solar Cell. *Solar Energy Materials and Solar Cells* **2011,** *95* (6), 1421-1436.

25. Azimi, H.; Hou, Y.; Brabec, C. J., Towards Low-Cost, Environmentally Friendly Printed Chalcopyrite and Kesterite Solar Cells. *Energy & Environmental Science* **2014,** *7* (6), 1829-1849.

26. Romero, M. J.; Du, H.; Teeter, G.; Yan, Y.; Al-Jassim, M. M., Comparative Study of the Luminescence and Intrinsic Point Defects in the Kesterite $Cu_2ZnSnS_4$ and Chalcopyrite $Cu(In,Ga)Se_2$ Thin Films Used in Photovoltaic Applications. *Physical Review B* **2011,** *84* (16), 165324.

27. Grossberg, M. Microphotoluminescence Study of $Cu_2ZnSnS_4$ Polycrystals. *Journal of Photonics for Energy* **2013,** *3* (1), 030599.

28. (a) Peng, W. Q.; Cong, G. W.; Qu, S. C.; Wang, Z. G., Synthesis and Photoluminescence of ZnS:Cu Nanoparticles. *Optical Materials* **2006,** *29* (2–3), 313-317; (b) Hou, S.; Zhang, X.; Mao, H.; Wang, J.; Zhu, Z.; Jing, W., Photoluminescence and XPS Investigations of

$Cu^{2+}$-Doped ZnS Quantum Dots Capped with Polyvinylpyrrolidone. *physica status solidi (b)* **2009,** *246* (10), 2333-2336.

29. Shin, B.; Gunawan, O.; Zhu, Y.; Bojarczuk, N. A.; Chey, S. J.; Guha, S., Thin Film Solar Cell with 8.4 % Power Conversion Efficiency Using an Earth-Abundant $Cu_2ZnSnS_4$ Absorber. *Progress in Photovoltaics* **2013,** *21* (1), 72-76.

30. (a) Snaith, H. J., Perovskites: The Emergence of a New Era for Low-Cost, High-Efficiency Solar Cells. *Journal of Physical Chemistry Letters* **2013,** *4* (21), 3623-3630; (b) Park, N.-G., Organometal Perovskite Light Absorbers Toward a 20% Efficiency Low-Cost Solid-State Mesoscopic Solar Cell. *The Journal of Physical Chemistry Letters* **2013,** *4* (15), 2423-2429.

# CHAPTER 4

–

## UNDERSTANDING THE PHASE FORMATION KINETICS OF NANO-CRYSTALLINE KESTERITE DEPOSITED ON MESOSCOPIC SCAFFOLDS VIA IN SITU MULTI-WAVELENGTH RAMAN-MONITORED ANNEALING

Chapter 3 has presented the detailed synthesis of CZTS kesterite on $TiO_2$ mesoscopic scaffold via sequential aqueous solution deposition of a precursor comprising binary chalcogenides that is subsequently converted to crystalline CZTS by annealing. The focus of the work described in Chapter 3 was the solution deposition method giving emphasis on achieving compositional control. In this Chapter the focus shifts to annealing and in particular in understanding the kesterite phase formation/crystallization kinetics. This is done by applying in situ Raman spectroscopy. This chapter has been published as: Z. Wang, S. Elouatik, and G. P. Demopoulos, *Physical Chemistry Chemical Physics,* 2016, *18*, pp. 29435-29446. Appendix B describes the Supporting Information.

## 4.1 Abstract

Kesterite, a promising photo-absorbing crystalline form of $Cu_2ZnSnS_4$ (CZTS), has been prepared via various routes. However, the lack of in-depth understanding of the dynamic phase formation process of kesterite leads to difficulties in optimizing its annealing conditions, hence its light harvesting performance. In this chapter, in situ Raman monitored-annealing is applied to study the phase formation kinetics of nanocrystalline kesterite from a precursor deposited on a $TiO_2$ mesoscopic scaffold. By performing in situ Raman annealing under different experimental conditions and wavelengths, several facts

have been discovered: kesterite crystallization starts at as low as 170 °C, but after short time annealing at 300 °C followed by cooling, the initially formed kesterite is found to decompose. Annealing at 400 °C or higher is proven to be sufficient for stabilizing the kesterite phase. Annealing at the higher temperature of 500 °C is necessary though to promote a complete reaction and thus eliminate the parasitic copper tin sulfide (CTS) impurity intermediates identified at lower annealing temperatures. More importantly, the real-time temperature dependence of Raman peak intensity enhancement, shift and broadening for CZTS is established experimentally at 500 °C for 1 h, providing a valuable reference in future CZTS research. This work demonstrates the effectiveness of using in situ Raman spectroscopy in elucidating the kesterite phase formation kinetics, a critical step towards full crystal phase control a prerequisite for developing fully functional CZTS-based optoelectronic devices.

## 4.2 Introduction

Typically, the progress of a functional material synthesis process is monitored via ex situ characterizations. However, in this case only partial info is obtained leaving a significant gap in our understanding of the true material growth mechanism. In contrast, in situ real time characterizations have been employed, aiming at realizing controllable materials synthesis as well as revealing the intrinsic compound growth kinetics. So far in situ characterizations have been developed based on scattering techniques including X-ray,[1] neutron,[2] and photoelectron[3]; imaging techniques like transmission electron microscopy (TEM),[4] and scanning probe[5]; and also optical spectroscopy. Among them, optical techniques, owing to their favorable characteristics such as non-intrusive, contact-less, non-destructive and fast response, are much more suitable for in situ characterizations.[6] Raman spectroscopy in this respect is particularly advantageous for in situ real time characterization of compound formation.[7]

Copper zinc tin sulfide ($Cu_2ZnSnS_4$ or CZTS) is an attractive semiconductor due to its great potential in low-toxic solar energy conversion applications.[8] Kesterite is the most common and thermodynamically stable phase for crystalline $Cu_2ZnSnS_4$.[9] After the quaternary metal sulfide precursor is prepared via solution deposition, annealing is the critical step for inducing the formation and growth of the crystalline kesterite phase. So far, different annealing conditions have been applied ranging from 180 to 750 °C and a few minutes to hours with various metal sulfide sources to obtain crystalline CZTS. But the rationale for such largely varied annealing conditions applied for the preparation of kesterite remains unclear as it is the actual mechanism of the phase formation crystallization process, imposing difficulties in optimizing the annealing process. Therefore, an in-depth understanding of the kesterite phase formation and crystal evolution mechanisms is required. In situ characterization would be the best solution for this purpose.

Raman is by-far the most common method to characterize kesterite due to the reasonably well-resolved main characteristic vibration modes of bulk CZTS (338 $cm^{-1}$), $Cu_3SnS_4$ (318 $cm^{-1}$), $Cu_2SnS_3$ (298 $cm^{-1}$), and $Cu_{2-x}S$ (475 $cm^{-1}$).[10] According to ex situ Raman investigations, kesterite is reported to form in the temperature range 300–500 °C,[11] in a sulfur excess environment provided by elemental S, $H_2S$ or SnS in order to prevent decomposition,[12] while the cooling rate is reported to profoundly affect the degree of Cu–Zn anti-site disorder in CZTS.[13] Very recently, Awadallah, et al. attempted in situ Raman characterization of the thermal stability of CZTS,[14] but this was done in open air not corresponding to kesterite formation conditions. As such to the best of our knowledge, the real-time dependent phase formation kinetics of kesterite in an inert gas-protected environment to avoid decomposition has not yet been determined/probed. To fill this gap, in the present work in situ Raman monitored annealing is applied to specifically investigate the real time phase formation kinetics of nanoscale kesterite, which is built on the mesoscopic $TiO_2$ scaffold with the potential for photovoltaic application.[15] Several previously unrevealed facts have been discovered via this new approach that involved multi-wavelength in situ Raman monitoring: the phase formation temperature of CZTS is much lower ($<$300 °C) than previously thought but sufficiently higher temperature ($>$400 °C) is necessary to form stable and crystalline kesterite; the annealing time is an important factor in attaining full crystallinity. This study is of significance not only for further optimizing the annealing treatment of CZTS in our pursuit of higher performing light harvesting kesterite nanostructured phases, but also more generally in understanding crystalline phase formation kinetics in annealing-based synthesis research.

## 4.3 Experimental Section

The $TiO_2$ mesoscopic scaffold was prepared by doctor-blading of anatase paste followed by sintering at 450 °C. Kesterite was grown on the mesoscopic film via modified SILAR (Successive Ionic Layer Adsorption and Reaction) deposition of the CZTS precursor followed by annealing which was described in Chapter 3. In situ annealing was performed with a cold/hot stage (Linkam) mounted on the LEICA microscope. The glass window of the stage allows the transmission of optical signals. The heating and cooling rate was controlled at 30 °C $min^{-1}$ and constant $N_2$ flow is kept to provide an inert atmosphere inside the sample chamber for the whole time. Raman spectroscopy was performed using a Renishaw inVia Raman spectrometer equipped with four lasers with wavelengths of 488 nm, 514 nm, 633 nm and 785 nm. Normalized intensities were used to describe Raman profile changes during annealing. They were calculated by defining the highest peak intensity of kesterite (or copper sulfide) as 1 and plotting the ratio of the rest. FWHM and peak center positions were extracted by fitting the spectra with symmetrical Lorentz peaks using the residual method. For more details refer to the Appendix B.

## 4.4 Results and Discussion

### 4.4.1 In situ Raman-monitored annealing at 300 $^{o}C$ and 400 $^{o}C$ (514 nm laser)

Based on previous reports,[11] the kesterite formation temperature is at least 300 °C, thus fast in situ Raman-monitored annealing tests were performed at 300 °C and 400 °C for 1 min holding time, respectively, using 514 nm laser as the light source. The raw spectra are shown in Figure 4.1, where the characteristic peaks of different phases have been labeled. To assist the understanding of the phase formation process, the normalized characteristic peak intensity of CZTS and the CuS phase are plotted in Figure 4.2. According to Figure 4.1, only the copper sulfide Raman peak appears at room temperature before annealing. Other precursor phases like $SnS_x$ (314 $cm^{-1}$) and ZnS (351 $cm^{-1}$) cannot be seen apparently due to their poor crystallinity arising from the room temperature synthesis route. As the temperature is increased to above approximately 170 °C (5 min), the copper sulfide peak starts to shrink down while a new peak at around 330 $cm^{-1}$ emerges (red dash line in Figure 4.1a), which signals the initial nucleation of crystalline CZTS. As the temperature keeps increasing, the intensity of this peak rapidly increases while the corresponding peak of the copper sulfide phase keeps decreasing up to 300 °C, where the intensity of the CZTS peak reaches its maximum while the copper sulfide phase is seen to remain nil. Herein, our target material has been synthesized, and we could consider 170 °C as the nucleation temperature for initiation of kesterite phase formation with 300 °C being sufficient for crystallization.

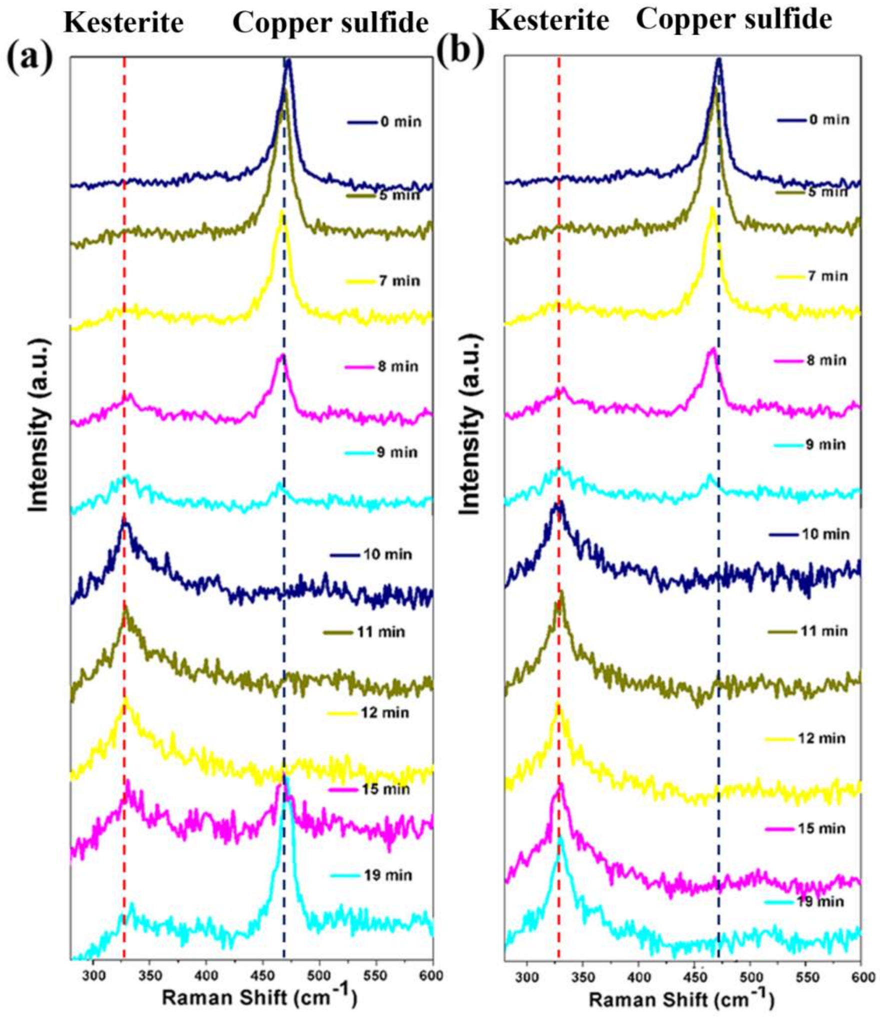

Figure 4.1. In-situ Raman-monitored annealing up to a) 300℃, 1min holding and up to b) 400℃, 1min holding with 514 nm laser. Spectra were taken every minute for a total of 19 minutes.

When we cool down the system (Figure 4.2a), however, the copper sulfide phase appears again (down to 250 °C) with increasing peak intensity, while unexpectedly the peak of CZTS keeps disappearing and eventually stays at a relatively low level. Therefore, annealing at 300 °C for 1 min is not sufficient for obtaining crystallized CZTS. This unusual phenomenon could be due to the incomplete transformation (CZTS precursor → kesterite) reaction that did not lead to a significant growth of the nanocrystal nuclei to form thermodynamically stable kesterite crystals.

Even though the best condition has not been achieved yet, the superiority of the in situ method is obvious. By using in situ Raman monitoring of the annealing process, the decomposition process after annealing at 300 °C has been detected, which has gone unnoticed by previous ex situ studies. In fact, the reaction (nucleation) started at as low as 170 °C. This also helps to explain why solution-processed methods at such low temperature (180–230 °C) can form well-crystallized CZTS instead of the commonly reported high temperature.[16] This indicates that the phase formation temperature of kesterite is actually quite low, and therefore, how to stabilize the formed kesterite becomes a critical issue. We also performed annealing at 300 °C for 60 min to verify if a longer reaction time can promote a more complete crystallization, but this did not prove to be effective; as can be seen in Figure B.1, the peak of copper sulfide is still dominant after the system is cooled down. One could think that the cooling rate may not be high enough to avoid decomposition, however, according to a previous report by Scragg et al.,[17] once kesterite is formed, the slow cooling rate is beneficial for ordering the crystal structure of kesterite. Therefore, we conclude that the kesterite formed at 300 °C is metastable prone to decomposition upon cooling. By increasing the annealing temperature to 400 °C though, kesterite was found to stabilize even after only 1 min holding time.

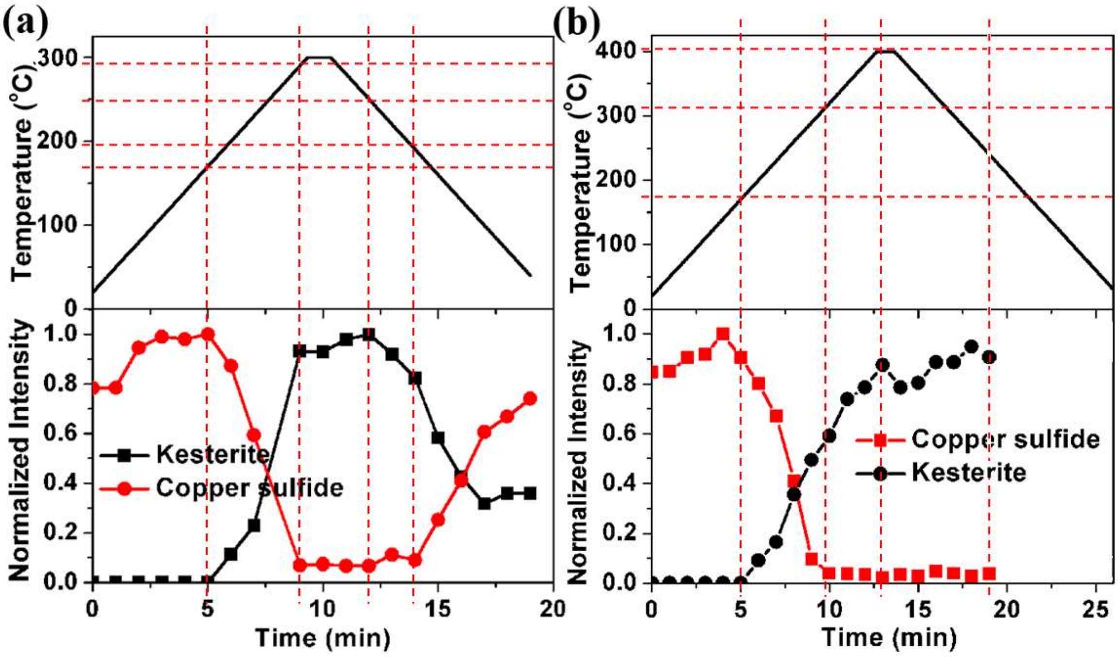

Figure 4.2. Normalized intensity change of characteristic Raman peaks for kesterite (328~337 cm$^{-1}$) and copper sulfide (465~475 cm$^{-1}$) during in-situ annealing up to a) 300℃, 1min and up to b) 400℃, 1min (514 nm laser for excitation).

As shown in Figure 4.2b, the phase evolution process is different from that of 300 °C annealing condition for higher temperature annealing (400 °C). The first 10 min (heating up from RT to 300 °C) are exactly the same as shown in Figure 4.2a, confirming the reproducibility of this experiment. Then as the temperature keeps increasing, the peak intensity of the kesterite phase continues to increase while that of copper sulfide levels off after reaching 300 °C (10 min). Further, the kesterite peak arrives at its climax when being heated up to 400 °C and remains at the same level until cooled down, and this time the copper sulfide phase (475 cm$^{-1}$) does not appear again. After the sample was entirely cooled down, we performed Raman measurement at room temperature (Figure 4.3 at 514 nm excitation), and this time no significant copper sulfide phase could be seen while the kesterite characteristic peak was clearly visible. In other words, when annealing is done under this condition (400 °C vs. 300 °C), it can be seen that the target kesterite phase to be stabilized during the real time monitored phase formation process. The fact that the intensity of the kesterite phase keeps increasing after around 10 min also indicates that the annealing reaction at 300 °C is incomplete, proving that full crystallization at the proper temperature is necessary for rendering the formation of stable crystalline CZTS irreversible.

### 4.4.2 Multi-wavelength excitation Raman

Up to this point, we have successfully obtained some important information about kesterite phase formation with in situ Raman monitored annealing using a wavelength of 514 nm for excitation. However, for Raman measurement, the sensitivity of different phases to different wavelengths is quite variable, due to the varied optical interaction volume and resonant excitation conditions for different materials. Therefore, it is important to select a suitable excitation wavelength that can provide high resolution spectra for better phase identification. Here except for 514 nm laser, we used three other lasers with wavelengths of 488 nm, 633 nm and 785 nm and captured Raman spectra after annealing at 400 °C for1 min, as shown in Figure 4.3. It is clear that when increasing the wavelength from the blue (488 nm) to near infrared region (785 nm), the mean characteristic peak of kesterite (~338 cm$^{-1}$) gets sharper and new peaks appear on both sides of the main mode (labeled with red dash line), which are attributed to different Raman modes of kesterite.[18] Meanwhile, copper sulfide ($Cu_xS$), with a characteristic Raman peak at 475 cm$^{-1}$, is identified as a co-existing secondary phase. In contrast, $TiO_2$ peaks (398 cm$^{-1}$, 518 cm$^{-1}$, 639 cm$^{-1}$) are not clearly shown, especially when increasing the wavelength to the near infrared region. It is very likely that the strong visible light absorption of CZTS and its enhanced Raman scattering make the $TiO_2$ signal hardly visible. Hence the resolution of the CZTS peaks becomes higher and interference from $TiO_2$ phases becomes negligible with a long wavelength laser source. In addition, the light absorbance spectrum of the CZTS/$TiO_2$ film is shown in Figure B.2 to understand the effect of different excitation wavelengths.[15] From the spectrum we can see that CZTS has a higher light absorbing ability at a wavelength lower than 600 nm, and a near-linear decrease after that. Less light absorption indicates that the signal can be collected from a deeper film region, which explains the superiority of using a longer wavelength for CZTS Raman characterization.

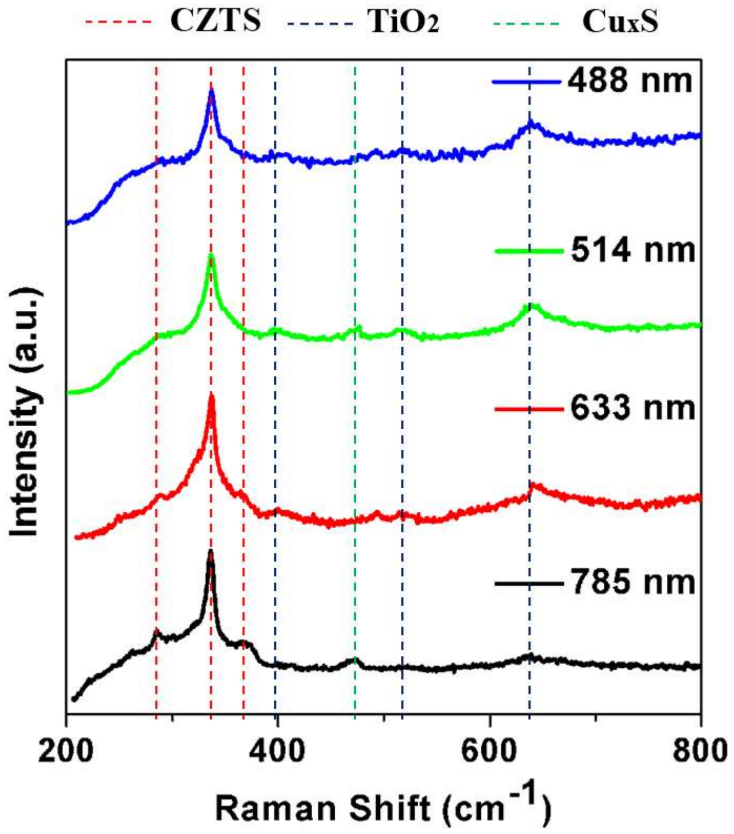

Figure 4.3. Multi-wavelength excitation Raman spectra of the CZTS sample annealed at 400℃ for 1min.

### 4.4.3 In situ Raman monitored-annealing at 400 °C and 500 °C (633 nm laser)

Since the Raman sensitivity of kesterite is different for different wavelengths, 633 nm laser was also applied for in situ Raman monitored annealing at 400 °C and 500 °C at the same ramping heating rate. Detailed spectral evolution is depicted in Figure B.3, which reveals a similar trend of kesterite formation with the concomitant decomposition of copper sulfide as seen at 514 nm excitation. Unlike the previous measurements, this time we have monitored the complete annealing process including the cooling stage so as to understand the changes occurring during cooling with a more Raman sensitive excitation wavelength. Figure 4.4a shows the temperature dependence of the Raman peak profile. During cooling, we observe a significant increase of the kesterite peak intensity associated with narrowing of the peak width.[19] It has been reported that the cooling procedure has a significant effect on order–disorder transition for kesterite.[17] Due to the similarity of Cu and Zn atoms, Cu/Zn antisites lead to a disordered kesterite crystalline structure. Accordingly, the method of cooling, as reported by Scragg et al.[17] is important for the formation of ordered (anti site-free) kesterite. Drawing from Bragg and Williams' classic description of order–disorder transitions in crystalline materials,[20] the critical temperature for order–disorder transition estimated by Scragg et al. is 260 °C, which means controlled cooling below this key temperature is vital for promoting ordering among Cu and Zn. In our experiment, it is observed the slope of the main mode of kesterite (attributed to the ordered kesterite phase) to rise steeply (Figure B.3b) upon cooling down to 300 °C and below, which is thought to relate to the order–disorder transition.

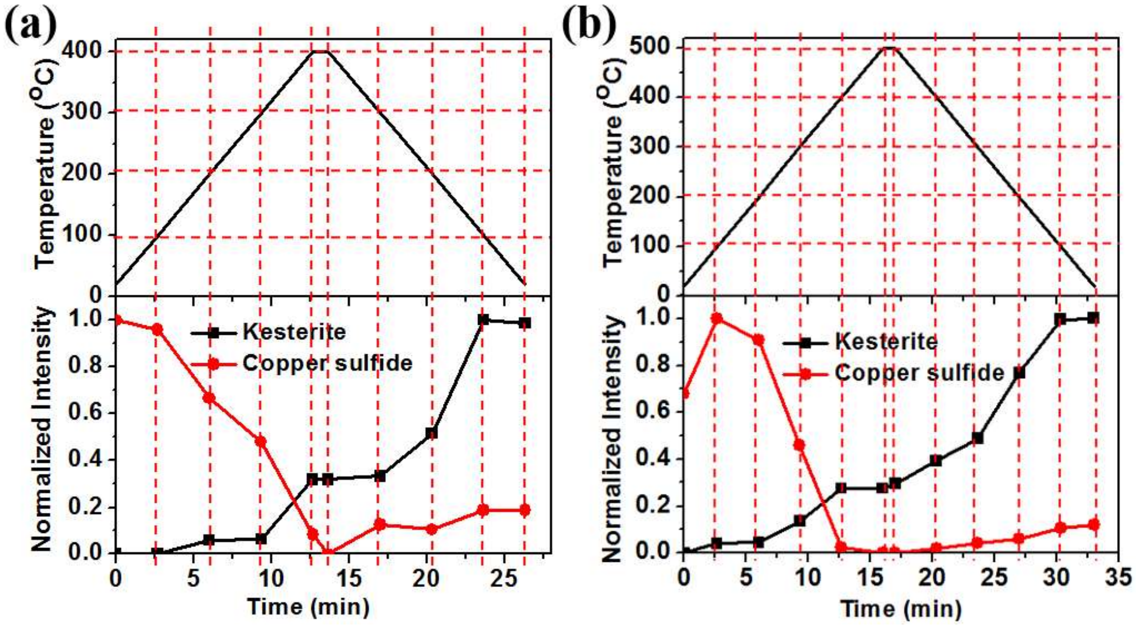

Figure 4.4. Normalized intensity change of characteristic Raman peaks for kesterite (328~337 $cm^{-1}$) and copper sulfide (465~475 $cm^{-1}$) during in-situ Raman monitored-annealing up to a) 400 °C, 1min and up to b) 500 °C, 1min (633 nm laser for excitation).

For annealing at 500 °C, the converted normalized intensity of kesterite and copper sulfide with different times is plotted in Figure 4.4b. The intensity of kesterite kept increasing before reaching 400 °C as is also shown in Figure 4.4a. However, when it reached 400 °C, the kesterite phase peak stopped increasing signaling that the transformative reaction involving the precursors is very likely to have reached completion at 400 °C.

### 4.4.4 Time effect of in situ Raman monitored-annealing (633 nm laser)

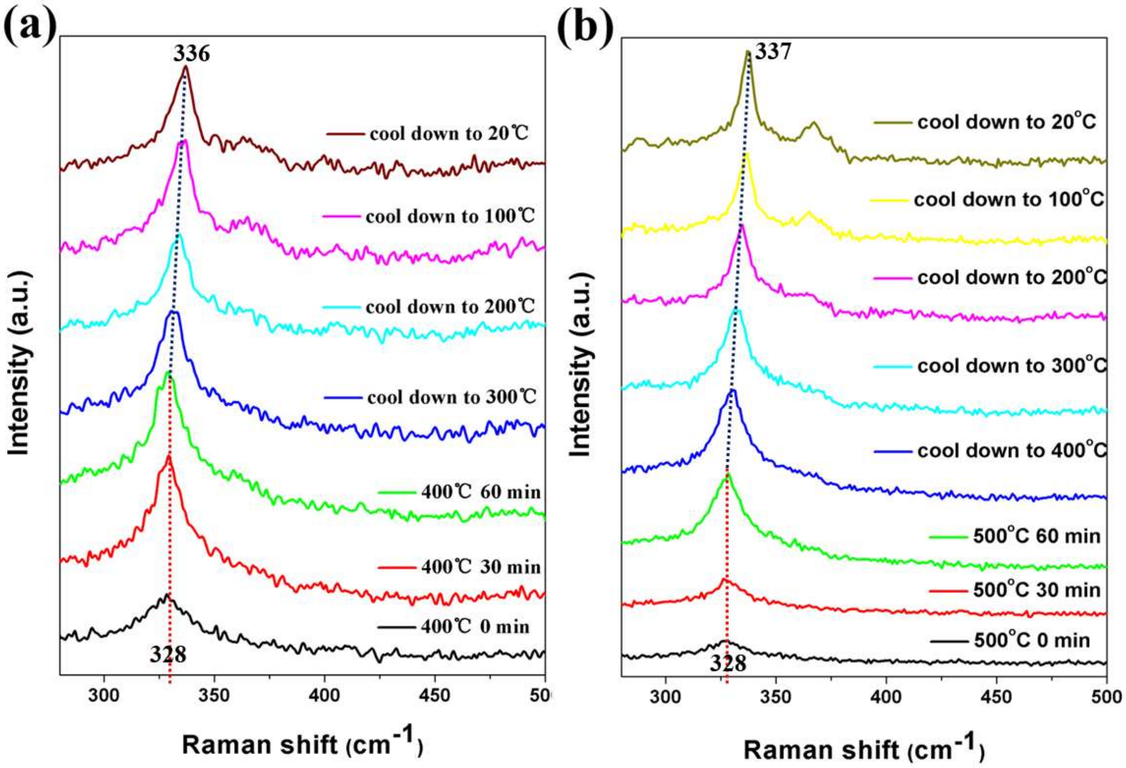

Figure 4.5. In-situ Raman spectra of 1h annealing process at a) 400 °C and b) 500 °C and the followed cooling down process.

Having established the effect of annealing temperature in crystallizing the kesterite phase, next, the effect of annealing time was investigated at 400 °C and 500 °C. In reporting the data, the heating period is left out to avoid unnecessary duplication, as it is the same with the short time annealing tests. Figure 4.5 clearly shows an enhancement of peak intensity in both cases during the temperature holding period while the cooling-induced peak intensity enhancement is less significant. Meanwhile, a temperature-dependent peak shift has been observed in both cases (marked with dash line). To clearly understand the effect of annealing time on kesterite crystallization we focused on the 500 °C experiment by calculating the normalized intensity of both kesterite and copper sulfide phases. The data are shown in Figure 4.6. In the same figure for a more thorough evaluation, we also recorded the kesterite peak center position, as well as the corresponding full width at half maximum (FWHM) evolution with time by fitting the main kesterite mode with Lorentz peaks (Figure B.4).

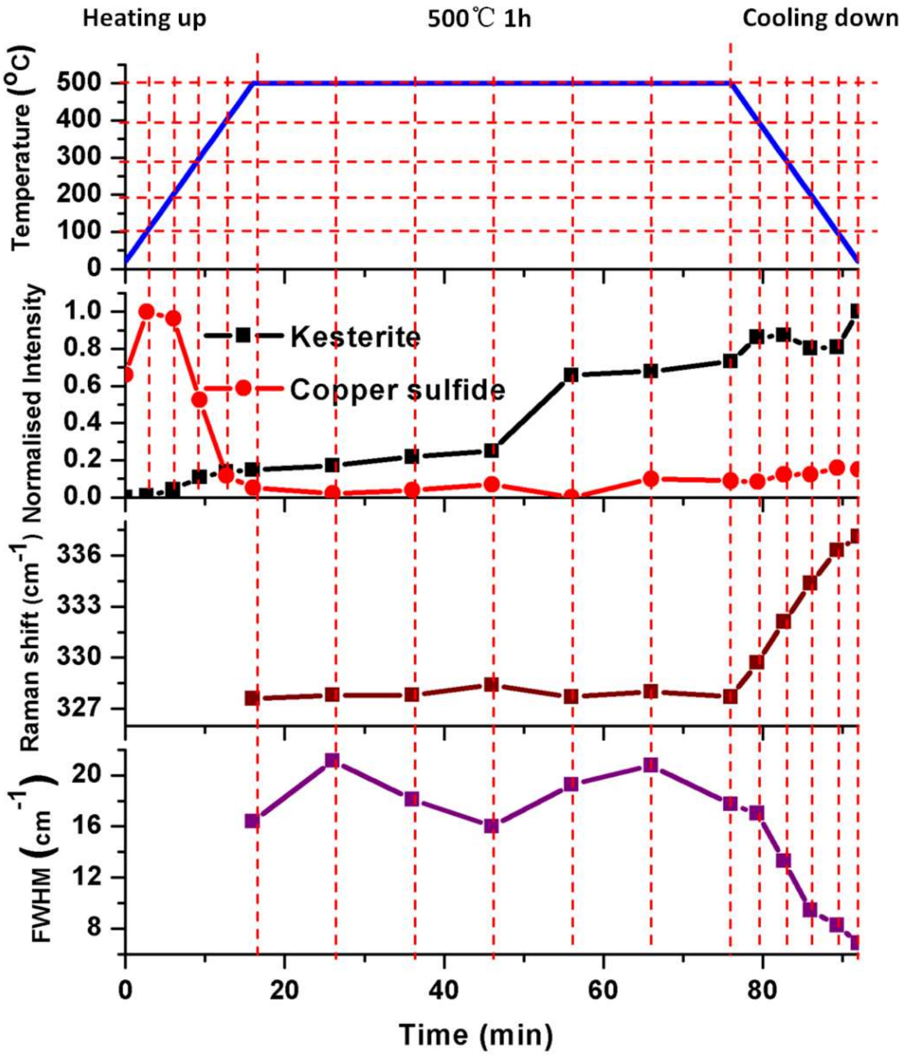

Figure 4.6. In-situ Raman-monitored formation of kesterite phase at 500 °C using 633 nm laser.

As can be seen in Figure 4.6, the heating-up response was exactly the same as the case of fast annealing at 500 °C (1 min), so were the trends of kesterite and copper sulfide evolution before 16 min. From this point onwards, the temperature was kept at 500 °C for one hour. During this entire period, there is no significant change in the kesterite phase peak center position and FWHM, but an unexpected sharp rise of the Raman peak intensity is observed after annealing for approximately 30 min (or 46 min total time), which then nearly levels off by the time cooling period starts. The enhanced peak intensity indicates an enhancement of crystallinity, apparently caused by thermal induced crystal refinement (defect elimination). Meanwhile the FWHM does not decrease correspondingly, indicating that the nano-size-induced phonon confinement effect is not significant.[21] However, during the cooling period, the FWHM of the kesterite characteristic peaks did decrease along with a linear red-shift of the peak position. Such behavior is due to the temperature-induced expansion/shrinking of the lattice.[22]

The peak position shift of kesterite with temperature is in good agreement with the equation that describes the temperature dependence of the Raman photon frequency:[23]

$$\delta(\mathrm{T}) = \delta_0 - \frac{\mathrm{A}}{e^{\frac{\mathrm{B}\hbar\delta_0}{k_\mathrm{B}\mathrm{T}}} - 1} \quad (1)$$

where T is the absolute temperature, $\delta_0$ is the Raman phonon frequency at 0 K, $k_B$ is the Boltzmann constant, ħ is the reduced Planck's constant and A and B are fitting parameters. The equation can be simplified to

$$\Delta\delta \approx -\left(\frac{\mathrm{A}k_\mathrm{B}}{\mathrm{B}\hbar\delta_0}\right)\Delta\mathrm{T} \quad (2)$$

which perfectly explains the linearly red-shifted kesterite peak position with decreasing temperature in Figure 4.6. In the meantime, the temperature-induced peak broadening can be described by the formula[22]

$$\Gamma(\mathrm{T}) = \Gamma_0\left[1 + \frac{2}{e^{\frac{\hbar\delta_0}{2k_\mathrm{B}\mathrm{T}}} - 1}\right] \quad (3)$$

where $\Gamma_0$ is the FWHM at 0 K, T is the absolute temperature, $\delta_0$ is the Raman phonon frequency at 0 K, $k_B$ is the Boltzmann constant, ħ is the reduced Planck's constant. Similarly, it can be simplified as

$$\Delta\Gamma \approx \left(\frac{4\Gamma_0 k_\mathrm{B}}{\hbar\delta_0}\right)\Delta\mathrm{T} \quad (4)$$

This equation well explains the near-linear descending trend of the temperature-dependent FWHM during the cooling process shown in Figure 4.6.

### 4.4.5 Comparison of Raman spectra of different annealed kesterite samples at RT (633 nm laser)

For further in-depth investigation the effect of different annealing conditions on kesterite crystal formation, we compared the room temperature Raman spectra of the different annealed samples under the same conditions (summarized in Figure 4.7). As can be seen, the sharpest characteristic peaks of kesterite are exhibited from the sample annealed at 500 °C for 1 h, implying that these annealing conditions lead to a high quality of crystalline CZTS.

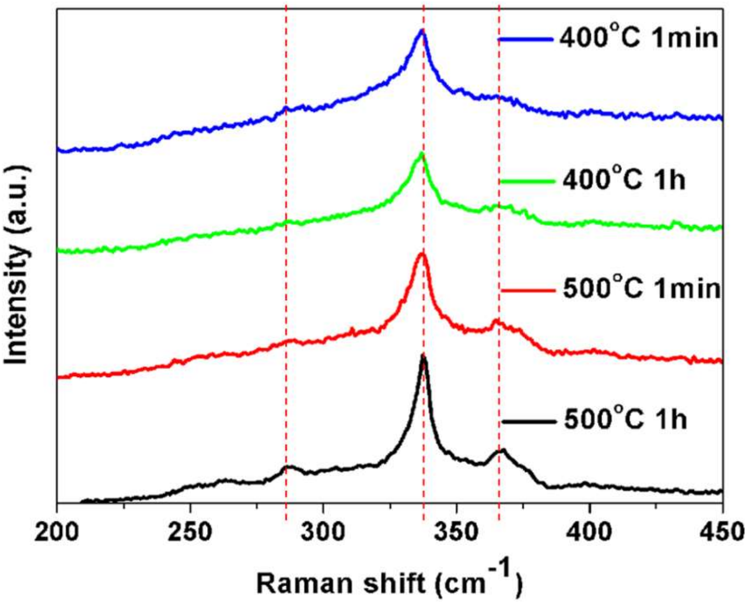

Figure 4.7. Room temperature Raman spectra of products obtained at different annealing conditions with the aid of 633 nm laser excitation. The red dash lines correspond to the main kesterite Raman modes.

In order to obtain a clearer view, all the four spectra were fitted with Lorentzian peaks as shown in Figure 4.8, where the filled areas represent the main mode of kesterite (~338 $cm^{-1}$) and the second strongest peak contributes to the broadening of the spectrum (~332 $cm^{-1}$). For all four cases, the main A Raman mode (~338 $cm^{-1}$) is clearly identified, confirming the general effectiveness of these annealing conditions in yielding crystalline CZTS. However, great differences can be observed when comparing these two fitted peaks among the four samples. As can be seen annealing performed at 500 °C tends to give a much larger $I_{338}/I_{332}$ ratio ($I_{338}$ represents the intensity of the peak centered at 336–338 $cm^{-1}$ and $I_{332}$ is that at 330–333 $cm^{-1}$). According to previous reports, this parameter should reflect the degree of disorder of kesterite,[21b, 24] that is, the higher ratio of $I_{338}/I_{332}$ indicates the less disordered kesterite. However, the unusually broadened peak at 332 $cm^{-1}$ in the case of 400 °C may also be due to peak overlapping thus potentially interfering with the fitting analysis. Consequently, higher resolution Raman spectra are necessary for a more accurate analysis. To this end, the 785 nm laser was applied to obtain near-resonant Raman measurements.

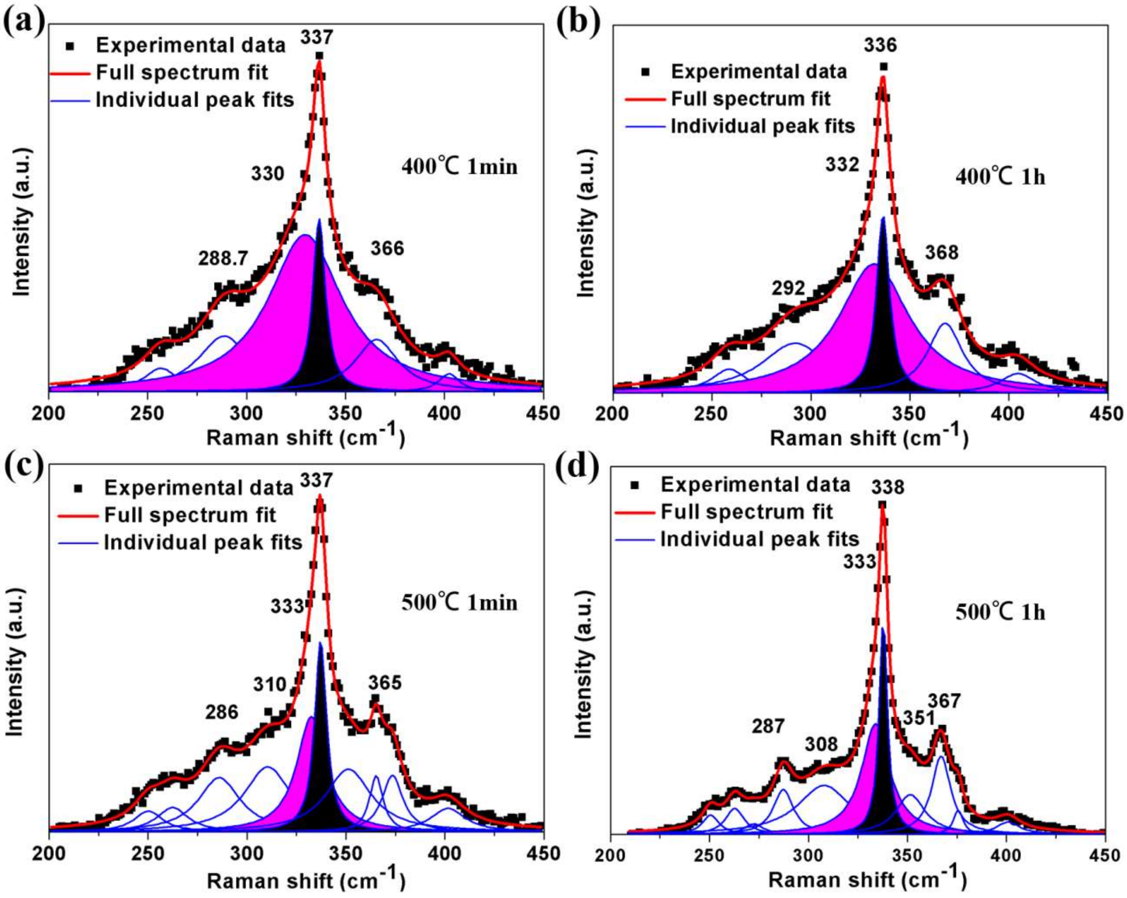

Figure 4.8. Room temperature high resolution Raman spectra excited by 633 nm laser and peak fitting results of the products annealed at different conditions: a) 400 °C, 1min; b) 400 °C, 1h; c) 500 °C, 1min and d) 500 °C, 1h.

### 4.4.6 Near-resonant Raman spectra of different annealed samples at RT

The 785 nm Raman spectra are given in Figure 4.9. Considering firstly the spectral region from 200 cm$^{-1}$ to 800 cm$^{-1}$, we see a clear bump at around 475 cm$^{-1}$ for the 400 °C 1 min annealed sample, which can be attributed to the residual copper sulfide secondary phases. However, when the annealing temperature and time increase, this bump becomes less significant, and finally almost disappears after annealing at 500 °C for 1 h. Furthermore, when looking at the spectrum of the 400 °C 1 min annealed sample, another detail that can be noticed is the “shoulder” to the left of the main kesterite peak, which is not really visible for the other samples.

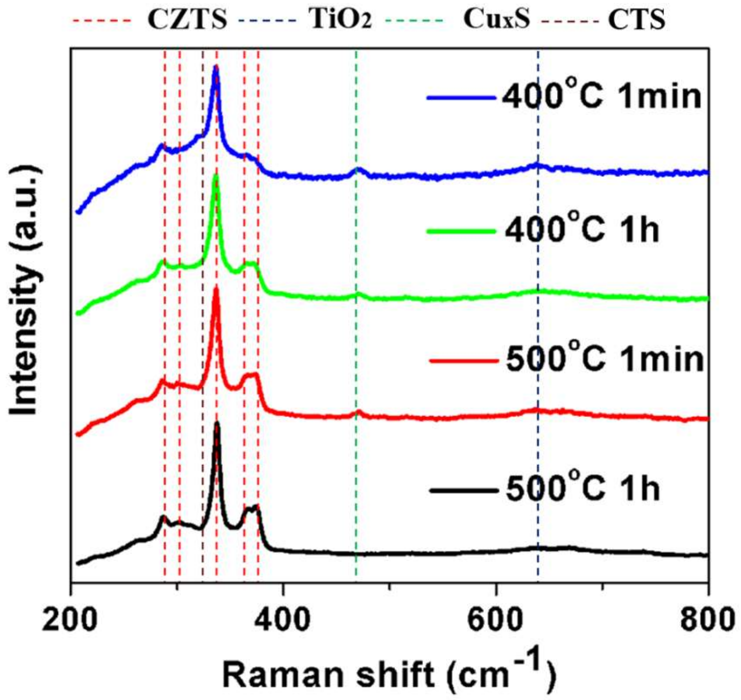

Figure 4.9. Room temperature Raman spectra of CZTS products obtained at different annealing conditions with the aid of 785 nm laser excitation.

Subsequently, a detailed analysis was performed by fitting the spectrum range from 200 cm$^{-1}$ to 450 cm$^{-1}$ as shown in Figure 4.10. Figure 4.10a shows the room temperature high resolution Raman spectrum of the sample produced after annealing at 400 °C for 1 minute, from which the ‘‘shoulder’’ as a fitted peak centered at 320 cm$^{-1}$ can be clearly seen, attributed to the secondary phase of copper-tin-sulfide (CTS) commonly considered as a by-product of incomplete reaction.[10c, 25] Meanwhile, there is a fitted peak at 351 cm$^{-1}$ contributing to the spectrum broadening, however, the source of this peak is uncertain. CTS has a characteristic peak at 348 cm$^{-1}$, which could be a possible explanation, but another common by-product as ZnS has a characteristic peak at 355 cm$^{-1}$ and even CZTS has a B Raman mode peak located at around 353 cm$^{-1}$.[18] When prolonging the annealing time to 1 h, the CTS impurity shoulder is less significant, but still a peak could be identified at 318 cm$^{-1}$ signaling at all likelihood of the presence of the residual CTS (Figure 4.10b). As we move to the 500 °C annealed samples (Figure 4.10c and d), even after a very short annealing period (1 min), the CTS impurity phase completely disappears. All peaks that are clearly resolvable can be attributed to different Raman modes of kesterite: the dominating peak centered at 336–338 cm$^{-1}$ is attributed to the main A mode; a slightly left-shifted one at 332 cm$^{-1}$ that causes broadening of the main peak represents most likely the partially disordered kesterite phase;[17] the peak centered at 287 cm$^{-1}$ corresponds to the second A mode of kesterite and the peaks at 366 cm$^{-1}$ and 375 cm$^{-1}$ belong to E and B modes, respectively; peaks at 301 cm$^{-1}$, 313 cm$^{-1}$ and 353 cm$^{-1}$ identified from the fitted curves can also be matched well with the previously reported A, E, and B modes, respectively.[18] Hence the annealing temperature is the key factor for promoting complete crystallization reaction and ensuring high crystal order and purity.

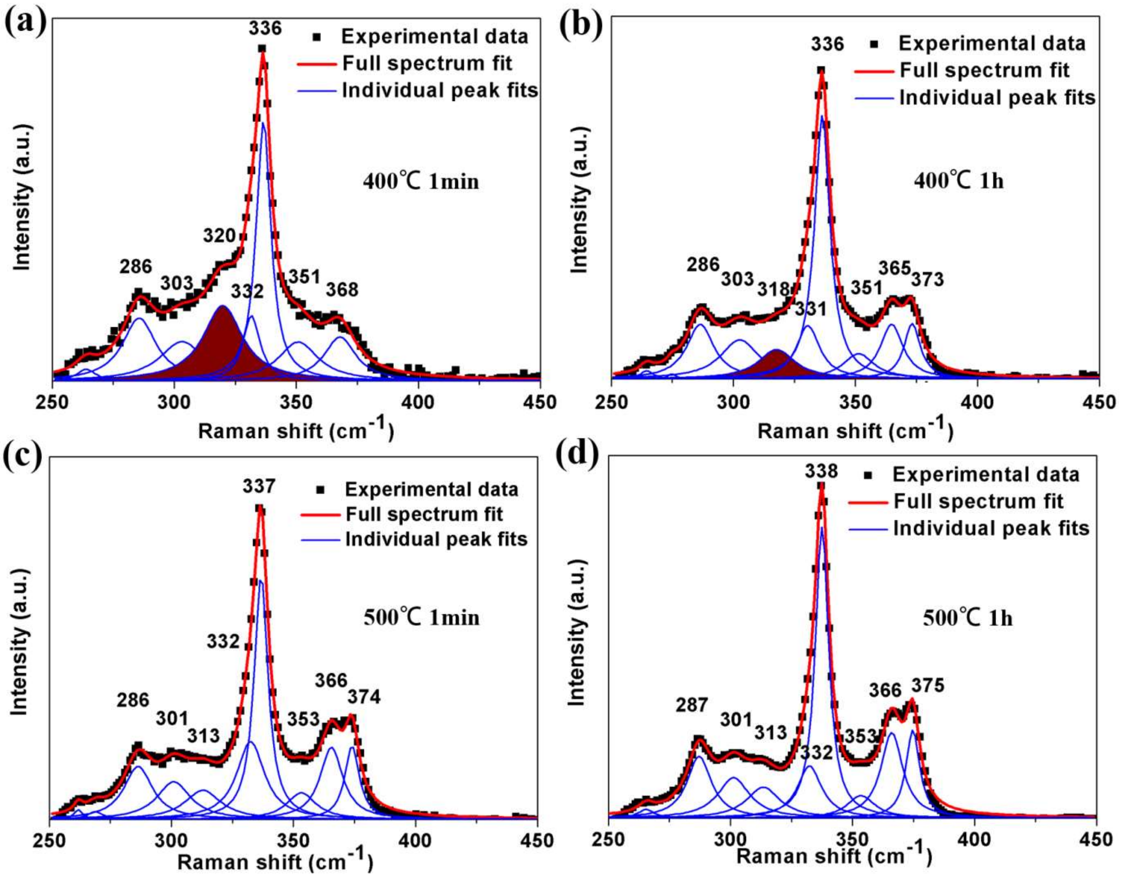

Figure 4.10. Room temperature high resolution Raman spectra captured with 785 nm laser excitation and peak fitting results of the products annealed at different conditions: a) 400 °C, 1 min; b) 400 °C, 1 h; c) 500 °C, 1 min and d) 500 °C, 1 h.

By introducing the near-resonant Raman for CZTS phase identification, we were able to get highly resolvable spectra and hence more easily distinguish the different vibration modes. Therefore, merely depending on the fitting results from the former spectra taken at 633 nm excitation (Figure 4.8) to decide the quality of the film as done in most of the studies is inaccurate, especially when we ex situ compare the ratio of $I_{338}/I_{332}$ to determine the order/disorder degree. However, even in this case, a comparison between 400 °C and 500 °C is still not applicable due to the interference of the CTS impurity peak which is too close to that at 332 $cm^{-1}$, creating as a result peak fitting errors in this specific case. Besides, under different annealing conditions the crystal grain sizes are expected to be different as kesterite crystals grow bigger for long time annealing at higher temperatures,[26] which makes order/disorder transition not the only reason for the varied ratio of $I_{338}/I_{332}$ (Table 4.1). In Scragg et al.'s work, the Q factor was introduced for quantitatively determining the degree of disorder defined by the ratio of $I_{287}/I_{301}$ ($I_{287}$ represents the intensity of peak centered at 286–287 $cm^{-1}$ and $I_{301}$ is that at 301–303 $cm^{-1}$);[17] a larger Q factor represents a more ordered sample. Here we compared the four cases and calculated their Q factors. Additionally, we also calculated the FWHM of the main A mode, which could provide supporting evidence of the disorder extent. The obtained results are shown in Table 1. However, we cannot see a great difference in either the Q factors or the FWHM main modes, which indicates a similar degree of disorder in the formed kesterite for all four cases using this method. The slightly reduced $FWHM_{337}$ and enhanced Q factor for higher temperatures might be due to the better developed crystallinity and a longer cooling procedure it experienced, since cooling has a significant effect on the formation of the ordered keterite phase.[17] But the differences are minor, which may be explained by Scragg's conclusion that ordering among Cu and Zn begins only when cooling down below the critical temperature of 533 K. We may therefore conclude that all four annealed samples have a similar degree of disorder due to their similar cooling rate, leading to a similar order–disorder transition process at the critical temperature and below. The highest ratio of $I_{338}/I_{332}$ identified for the 500 °C 1 h annealed sample is probably caused by the enhanced crystallinity corresponding to the sudden increase of the main A mode intensity after keeping for 30 min at that temperature (Figure 4.6).

Table 4.1. Calculated $I_{287}/I_{301}$ and $FWHM_{337}$ for samples annealed at different conditions with 785 nm laser excitation.

| Annealing Conditions | 400℃ 1min | 400℃ 1h | 500℃ 1min | 500℃ 1h |
|---|---|---|---|---|
| $I_{338}/I_{332}$ | 3.45 | 4.91 | 3.13 | 5.56 |
| $I_{287}/I_{301}$ | 1.59 | 1.39 | 1.40 | 1.52 |
| $FWHM_{337}$ ($cm^{-1}$) | 7.31 | 7.73 | 6.92 | 6.62 |

## 4.4.7 XRD characterization

After we completed the in situ investigation of the kesterite phase formation kinetics under different annealing conditions, X-ray diffraction (XRD) was performed in order to verify the crystallinity and phase identity of our CZTS-coated $TiO_2$ mesoscopic film. Diffraction patterns obtained from the four different annealed samples are shown in Figure 4.11 and compared to standards either from database or prepared from commercial bulk materials. From this figure the formation of the kesterite phase in all four samples can be clearly seen as evidenced by the strongest kesterite characteristic peak centered at 28.51°. Similarly to the Raman spectra, the XRD patterns clearly indicate that with increasing annealing temperature and time, the crystallinity increases (a characteristic peak of kesterite at 28.51° becomes sharper). It matches well with our near-resonant Raman data in Figure 4.9 and 4.10, which shows the sharpest kesterite main A mode to be after annealing at 500 °C and 1 h. Therefore, 500 °C /1 h is considered to be the optimal annealing condition in terms of obtaining the best crystallinity among the different conditions applied.

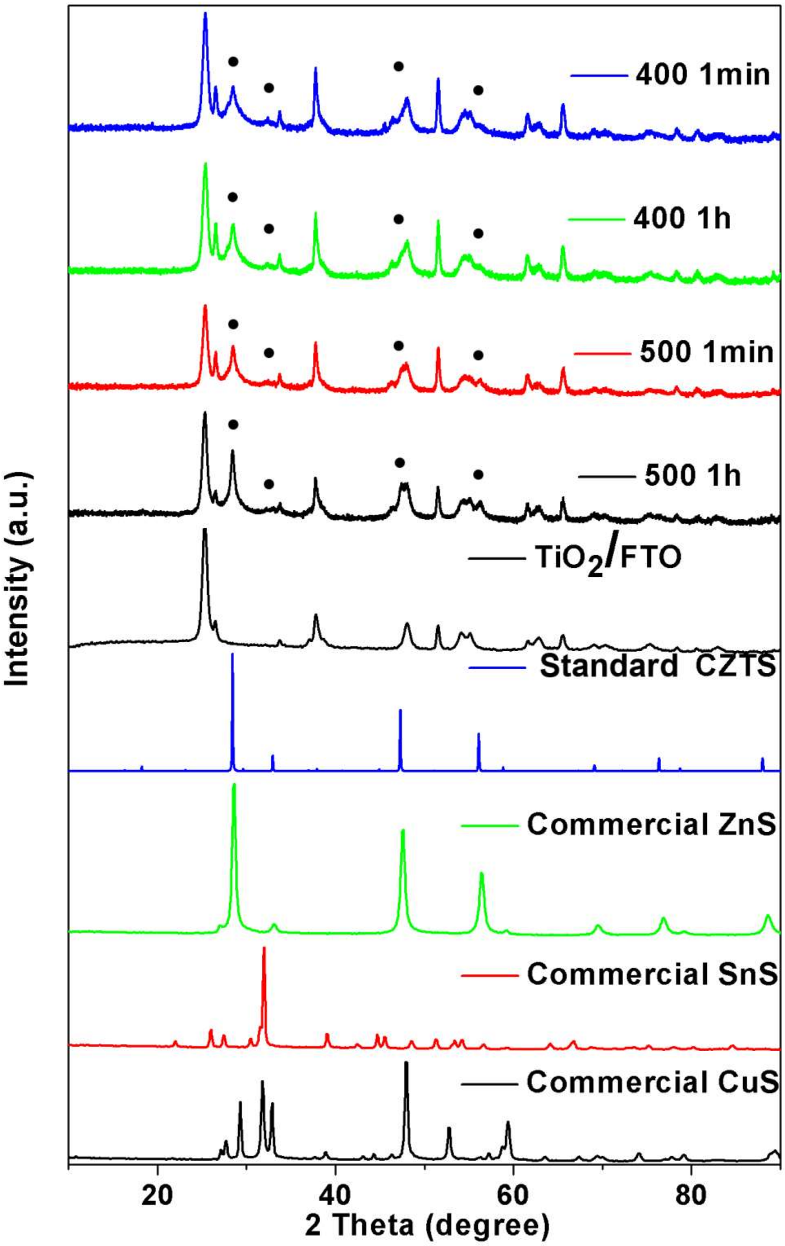

Figure 4.11. XRD patterns of the CZTS products obtained at different annealing conditions and the experimental standards of $TiO_2$/FTO, ZnS, SnS and CuS, as well as the bulk powder diffraction pattern simulated from the theoretical kesterite crystal structure. Black round dots represent the identified kesterite phase.

## 4.5 Conclusion

In this chapter, in situ Raman was applied to monitor real time phase formation and crystallinity evolution of kesterite on a $TiO_2$ mesoscopic scaffold by annealing in an inert atmosphere. This study has revealed that nucleation of primary kesterite crystallites starts at a temperature (~170 °C) significantly lower than what previous ex situ studies have reported. The failure of previous studies to observe the onset of kesterite crystallization at low temperatures is proposed to be arising from the discovery that kesterite forming at ≤300 °C suffers decomposition upon cooling. A thermodynamically stable kesterite phase has been obtained above 400 °C. The application of in situ Raman monitored-annealing under different conditions (400 °C, 1 min, 400 °C, 1 h, 500 °C, 1 min, and 500 °C, 1 h) using multiple wavelength lasers allowed for deeper probing of the development of high degree crystallinity, order and purity kesterite. In particular, a breakthrough insight was obtained using the near-resonant Raman at 785 nm excitation, which through higher resolution spectra made possible the detection of the inactive CTS impurity revealing that complete crystallization of high order CZTS can be obtained above 400 °C and more specifically at 500 °C, for 1 h. Another major finding in this chapter that can provide valuable reference information for further CZTS research is the observed temperature dependence of the Raman peak profile change for CZTS.

## 4.6 References

1. Norby, P.; Johnsen, S.; Iversen, B. B., In Situ X-ray Diffraction Study of the Formation, Growth, and Phase Transition of Colloidal $Cu_{2-x}S$ Nanocrystals. *ACS Nano* **2014,** *8* (5), 4295-4303.

2. Woo, W.; Feng, Z.; Wang, X.-L.; An, K.; Hubbard, C. R.; David, S. A.; Choo, H., In Situ Neutron Diffraction Measurement of Transient Temperature and Stress Fields in a Thin Plate. *Applied Physics Letters* **2006,** *88* (26), 261903.

3. Lu, Y.-C.; Crumlin, E. J.; Veith, G. M.; Harding, J. R.; Mutoro, E.; Baggetto, L.; Dudney, N. J.; Liu, Z.; Shao-Horn, Y., In Situ Ambient Pressure X-ray Photoelectron Spectroscopy Studies of Lithium-Oxygen Redox Reactions. *Scientific Reports* **2012,** *2*,715.

4. Wang, C.-M.; Genc, A.; Cheng, H.; Pullan, L.; Baer, D. R.; Bruemmer, S. M., In-Situ TEM Visualization of Vacancy Injection and Chemical Partition during Oxidation of Ni-Cr Nanoparticles. *Scientific Reports* **2014,** *4*,3683.

5. Wen, R.; Hong, M.; Byon, H. R., In Situ AFM Imaging of Li–$O_2$ Electrochemical Reaction on Highly Oriented Pyrolytic Graphite with Ether-Based Electrolyte. *Journal of the Americian Chemical Society* **2013,** *135* (29), 10870-10876.

6. Bundesmann, C.; Schubert, M.; Ashkenov, N.; Grundmann, M.; Lippold, G.; Piltz, J., Combined Raman Scattering, X‐ray Fluorescence and Ellipsometry in‐Situ Growth Monitoring of $CuInSe_2$‐Based Photoabsorber Layers on Polyimide Substrates. *AIP Conference Proceedings* **2005,** *772* (1), 165-166.

7. (a) Rao, R.; Pierce, N.; Liptak, D.; Hooper, D.; Sargent, G.; Semiatin, S. L.; Curtarolo, S.; Harutyunyan, A. R.; Maruyama, B., Revealing the Impact of Catalyst Phase Transition on Carbon Nanotube Growth by in Situ Raman Spectroscopy. *ACS Nano* **2013,** *7* (2), 1100-1107; (b) Li-Pook-Than, A.; Lefebvre, J.; Finnie, P., Type- and Species-Selective Air Etching of Single-Walled Carbon Nanotubes Tracked with in Situ Raman Spectroscopy. *ACS Nano* **2013,** *7* (8), 6507-6521; (c) Guimbretière, G.; Desgranges, L.; Canizarès, A.; Caraballo, R.; Duval, F.; Raimboux, N.; Omnée, R.; Ammar, M. R.; Jégou, C.; Simon, P., In Situ Raman Monitoring of $He^{2+}$ Irradiation Induced Damage in a $UO_2$ Ceramic. *Applied Physics Letters* **2013,** *103* (4), 041904.

8. (a) Suehiro, S.; Horita, K.; Kumamoto, K.; Yuasa, M.; Tanaka, T.; Fujita, K.; Shimanoe, K.; Kida, T., Solution-Processed $Cu_2ZnSnS_4$ Nanocrystal Solar Cells: Efficient Stripping of Surface Insulating Layers Using Alkylating Agents. *The Journal of Physical Chemistry C* **2014,** *118* (2), 804-810; (b) Xu, J.; Yang, X.; Yang, Q.-D.; Wong, T.-L.; Lee, C.-S., $Cu_2ZnSnS_4$ Hierarchical Microspheres as an Effective Counter Electrode Material for Quantum Dot Sensitized Solar Cells. *The Journal of Physical Chemistry C* **2012,** *116* (37), 19718-19723.

9. Suryawanshi, M. P.; Agawane, G. L.; Bhosale, S. M.; Shin, S. W.; Patil, P. S.; Kim, J. H.; Moholkar, A. V., CZTS Based Thin Film Solar Cells: a Status Review. *Materials Technology* **2013,** *28* (1-2), 98-109.

10. (a) Lin, X.; Kavalakkatt, J.; Kornhuber, K.; Levcenko, S.; Lux-Steiner, M. C.; Ennaoui, A., Structural and Optical Properties of $Cu_2ZnSnS_4$ Thin Film Absorbers from ZnS and

$Cu_3SnS_4$ Nanoparticle Precursors. *Thin Solid Films* **2013,** *535* (0), 10-13; (b) Berg, D. M.; Djemour, R.; Gütay, L.; Siebentritt, S.; Dale, P. J.; Fontane, X.; Izquierdo-Roca, V.; Pérez-Rodriguez, A., Raman Analysis of Monoclinic $Cu_2SnS_3$ Thin Films. *Applied Physics Letters* **2012,** *100* (19), 192103; (c) Fontané, X.; Calvo-Barrio, L.; Izquierdo-Roca, V.; Saucedo, E.; Pérez-Rodriguez, A.; Morante, J. R.; Berg, D. M.; Dale, P. J.; Siebentritt, S., In-Depth Resolved Raman Scattering Analysis for the Identification of Secondary Phases: Characterization of $Cu_2ZnSnS_4$ Layers for Solar Cell Applications. *Applied Physics Letters* **2011,** *98* (18), 181905.

11. (a) Fairbrother, A.; Fontané, X.; Izquierdo-Roca, V.; Espíndola-Rodríguez, M.; López-Marino, S.; Placidi, M.; Calvo-Barrio, L.; Pérez-Rodríguez, A.; Saucedo, E., On the Formation Mechanisms of Zn-Rich $Cu_2ZnSnS_4$ Films Prepared by Sulfurization of Metallic Stacks. *Solar Energy Materials and Solar Cells* **2013,** *112* (0), 97-105; (b) Wang, Y.; Gong, H., Low Temperature Synthesized Quaternary Chalcogenide $Cu_2ZnSnS_4$ from Nano-Crystallite Binary Sulfides. *Journal of The Electrochemical Society* **2011,** *158* (8), H800-H803.

12. (a) Redinger, A.; Berg, D. M.; Dale, P. J.; Siebentritt, S., The Consequences of Kesterite Equilibria for Efficient Solar Cells. *Journal of the American Chemical Society* **2011,** *133* (10), 3320-3323; (b) Scragg, J. J.; Kubart, T.; Watjen, J. T.; Ericson, T.; Linnarsson, M. K.; Platzer-Bjorkman, C., Effects of Back Contact Instability on $Cu_2ZnSnS_4$ Devices and Processes. *Chem Mater* **2013,** *25* (15), 3162-3171.

13. Choubrac, L.; Paris, M.; Lafond, A.; Guillot-Deudon, C.; Rocquefelte, X.; Jobic, S., Multinuclear (67Zn, 119Sn and 65Cu) NMR Spectroscopy - an Ideal Technique to Probe the Cationic Ordering in $Cu_2ZnSnS_4$ Photovoltaic Materials. *Physical Chemistry Chemical Physics* **2013,** *15* (26), 10722-10725.

14. (a) Awadallah, O.; Zhe, C. In situ Raman Characterization of $Cu_2ZnSnS_4$ Solar Absorber Material, *Photovoltaic Specialist Conference (PVSC), 2015 IEEE 42nd,* 2015; 1-6; (b) Awadallah, O.; Cheng, Z., In Situ Raman Monitoring of $Cu_2ZnSnS_4$ Oxidation and Related

Decomposition at Elevated Temperatures. *Ieee Journal of Photovoltaics* **2016,** *6* (3), 764-769.

15. Wang, Z.; Demopoulos, G. P., Nanoscale Photo-Absorbing Kesterite Grown on Anatase Mesoscopic Films by Sequential Binary Chalcogenide Solution Deposition-Exchange, Annealing, and Etching. *Crystal Growth & Design* **2016**.

16. (a) Sekou Mariama, C.; Lingling, W.; Xintong, Z., Easy Hydrothermal Preparation of $Cu_2ZnSnS_4$ (CZTS) Nanoparticles for Solar Cell Application. *Nanotechnology* **2013,** *24* (49), 495401; (b) Zhou, H.; Duan, H.-S.; Yang, W.; Chen, Q.; Hsu, C.-J.; Hsu, W.-C.; Chen, C.-C.; Yang, Y., Facile Single-Component Precursor for $Cu_2ZnSnS_4$ With Enhanced Phase and Composition Controllability. *Energy & Environmental Science* **2014,** *7* (3), 998-1005; (c) Singh, A.; Geaney, H.; Laffir, F.; Ryan, K. M., Colloidal Synthesis of Wurtzite Cu2ZnSnS4 Nanorods and Their Perpendicular Assembly. *Journal of the American Chemical Society* **2012,** *134* (6), 2910-2913.

17. Scragg, J. J. S.; Choubrac, L.; Lafond, A.; Ericson, T.; Platzer-Björkman, C., A Low-Temperature Order-Disorder Transition in $Cu_2ZnSnS_4$ Thin Films. *Applied Physics Letters* **2014,** *104* (4), 041911.

18. Dimitrievska, M.; Fairbrother, A.; Fontané, X.; Jawhari, T.; Izquierdo-Roca, V.; Saucedo, E.; Pérez-Rodríguez, A., Multiwavelength Excitation Raman Scattering Study of Polycrystalline Kesterite $Cu_2ZnSnS_4$ Thin Films. *Applied Physics Letters* **2014,** *104* (2), 021901.

19. Hadjiev, V. G.; Rafailov, P. M.; Jantoljak, H.; Thomsen, C.; Kelly, M. K., Influence of the Crystal Field on the Raman Intensity of C 60 Fullerites. *Physical Review B* **1997,** *56* (5), 2495-2500.

20. Bragg, W. L.; Williams, E. J., The Effect of Thermal Agitation on Atomic Arrangement in Alloys. *Proceedings of the Royal Society of London. Series A* **1934,** *145* (855), 699-730.

21. (a) Liu, W. C.; Guo, B. L.; Wu, X. S.; Zhang, F. M.; Mak, C. L.; Wong, K. H., Facile Hydrothermal Synthesis of Hydrotropic $Cu_2ZnSnS_4$ Nanocrystal Quantum Dots: Band-Gap Engineering and Phonon Confinement Effect. *Journal of Materials Chemistry A* **2013,** *1* (9),

3182-3186; (b) Kumar Samji, S.; Tiwari, B.; Krishna Surendra, M.; Ramachandra Rao, M. S., Light Induced Phase Change in $Cu_{2-x}Zn_{1.3}SnS_4$ Thin Films. *Applied Physics Letters* **2014,** *104* (15), 152106.

22. Liu, M. S.; Bursill, L. A.; Prawer, S.; Nugent, K. W.; Tong, Y. Z.; Zhang, G. Y., Temperature Dependence of Raman Scattering in Single Crystal GaN Films. *Applied Physics Letters* **1999,** *74* (21), 3125-3127.

23. Guhel, Y.; Bernard, J.; Boudart, B., In Situ Raman Characterization of $CeO_2$ Thin Films Sputtered on (111) Si in Order to Optimize the Post Growth Annealing Parameters. *Microelectronic Engeering* **2014,** *118*, 29-34.

24. Caballero, R.; Garcia-Llamas, E.; Merino, J. M.; León, M.; Babichuk, I.; Dzhagan, V.; Strelchuk, V.; Valakh, M., Non-Stoichiometry Effect and Disorder in $Cu_2ZnSnS_4$ Thin Films Obtained by Flash Evaporation: Raman Scattering Investigation. *Acta Materialia* **2014,** *65* (0), 412-417.

25. Tan, J. M. R.; Lee, Y. H.; Pedireddy, S.; Baikie, T.; Ling, X. Y.; Wong, L. H., Understanding the Synthetic Pathway of a Single-Phase Quarternary Semiconductor Using Surface-Enhanced Raman Scattering: A Case of Wurtzite Cu2ZnSnS4 Nanoparticles. *Journal of the American Chemical Society* **2014,** *136* (18), 6684-6692.

26. Jiang, C.; Liu, W.; Talapin, D. V., Role of Precursor Reactivity in Crystallization of Solution-Processed Semiconductors: The Case of $Cu_2ZnSnS_4$. *Chemistry of Materials* **2014,** *26* (13), 4038-4043.

# CHAPTER 5

–

# GROWTH OF $Cu_2ZnSnS_4$ NANOCRYSTALLITES ON $TiO_2$ NANOROD ARRAYS AS NOVEL EXTREMELY THIN ABSORBER SOLAR CELL STRUCTURE VIA THE SUCCESSIVE-ION-LAYER-ADSORPTION-REACTION METHOD

Chapter 3 and Chapter 4 have studied the aqueous solution synthesis and annealing of nano-CZTS kesterite on $TiO_2$ (anatase) mesoscopic scaffold, from which the composition controlled kesterite phase was successfully obtained. The optical properties characterized in Chapter 3 has proven the potential of this type of kesterite nanocrystallites in optoelectronic applications. However, when this CZTS-$TiO_2$ mesoporous film was applied as photoanode in sensitized solar cell structure (Figure 2.11, Page 30), there was hardly any photocurrent output leading to an ineffective device (~0.01 % efficiency). This was concluded to be due to the enlarged active surfaces and grain boundaries of the anatase built mesoscopic film. Especially when defect-prone kesterite nanocrystallites are used as light absorber, significant interfacial charge recombination takes place preventing the collection of photoelectrons. To overcome these inherent shortcomings of the mesoporous $TiO_2$ sub-structure, the decision was taken to investigate one-dimensional $TiO_2$ sub-structure that potentially can provide improved electron transport/collection results. Thus, in this chapter the successive-ionic-layer-adsorption-reaction method (chapter 3) is used to deposit CZTS on $TiO_2$ nanorod arrays instead of the mesoporous film, featuring short electron pathways and less grain boundary nanostructured photoanode. Characterization of this novel nanostructure and evaluation of its early stage photovoltaic performance were performed. This chapter has been published as: Z. Wang and G. P. Demopoulos, *ACS Applied Materials and Interfaces*, 2015, 7, pp. 22888-22897. Appendix C describes the Supporting Information.

## 5.1 Abstract

In this chapter, a novel absorber-conductor structure featuring in situ successive-ion-layer-adsorption-reaction (SILAR)-deposited CZTS nanocrystallites as a light absorber on one-dimensional $TiO_2$ (rutile) nanorods as an electron conductor was fabricated and tested. The effectiveness of the nanoscale heterostructure in visible light harvesting and photoelectron generation is demonstrated with an initial short circuit current density of 3.22 mA/cm$^2$ and an internal quantum efficiency of ~60% at the blue light region, revealing great potential in developing CZTS extremely thin absorber (ETA) solar cells.

## 5.2 Introduction

In developing inorganic semiconductor sensitized extremely thin absorber (ETA) solar cell, the choice of $TiO_2$ nanostructure is equally critical as the conventional nanoparticle-based mesoporous film suffers from severe recombination losses,[1] especially for the high density defects containing kesterite nanoparticles.[2] By far vertically aligned single crystalline nanowires or nanorods because of their short electron pathway[3] can offer an advantageous conducting network in this regard. Ho et al. attempted recently to deposit CZTS via a chemical bath method on rutile nanorods but their deposits were not uniform and they had to resort to predeposition of a CdS adhesion layer.[4] However, evaluation of its photovoltaic application potential is missing; moreover, a nanoscale study of the rutile/CZTS interface without the interference from the presence of CdS is a critical prerequisite in understanding and ultimately enabling the development of extremely thin absorbing CZTS based solar cells.

With the view of overcoming the limitations of previous efforts in preparing CZTS on $TiO_2$ nanostructures in an extremely thin absorbing solar cell configuration, we have developed and presented a SILAR-based approach that allows for better light absorber penetration. To this end we employ a three-step successive ionic layer adsorption and reaction (SILAR) method followed by high temperature annealing to control the in situ deposition and growth of CZTS nanocrystallites on rutile $TiO_2$ nanorod arrays (TNR@CZTS) that are subjected to nanoscale characterization and early stage optoelectronic performance evaluation and optimization. The newly configured TNR@CZTS heterostructure is successfully demonstrated to be effective in visible light-driven photoelectron generation, revealing a great potential for devising all inorganic stable and green PV devices.

## 5.3 Experimental Section

### 5.3.1 Material synthesis

As shown in Figure S1, in the first step, in order to grow vertically aligned $TiO_2$ nanorods, a piece of precleaned fluorine doped tin oxide (FTO) glass (Sigma-Aldrich, 7 Ω/sq) was placed with the conductive side facing downward in a 125 mL Teflon container. An acidic solution was added by mixing 10 mL of DI water, 10 mL of concentrated hydrochloric acid solution (36.5% by weight, Fisher Scientific), and 1 mL of titanium butoxide (97%, Sigma- Aldrich). The whole container was then placed into a stainless steel autoclave and kept at 150 °C for 2 h. After the hydrothermal reaction, well aligned $TiO_2$ nanorod arrays had been deposited on the FTO glass that were subsequently subjected to thermal treatment-annealing at 450 °C in air.

To deposit the CZTS precursor material containing Cu, Zn, Sn, and S on the $TiO_2$ nanorod array, three successive-ion-layer-adsorption reaction (SILAR) steps were applied. For the first SILAR step (SILAR 1), 100 mL of 0.02 M $CuCl_2$ (99%, Alfa Aesar) and 0.16 M $Na_2S$ (98%, Sigma-Aldrich) aqueous solution was prepared separately in two containers. Then the as-prepared $TiO_2$ film on FTO glass was immersed into $CuCl_2$ aqueous solution and $Na_2S$ aqueous solution successively with a 1 min interval time. This process was repeated for 10 times and the color of the sample was observed to change from white to light green. The second SILAR step (SILAR 2) was similar to the difference that instead of $Cu^{2+}$, 0.02 M $SnCl_2$ (98%, Sigma- Aldrich) and 0.16 M $Na_2S$ aqueous solutions were prepared in which the film from SILAR step 1 was alternatively dipped in and out 10 times. The obtained film was slightly reddish after SILAR 2. To complete the precursor preparation, the last SILAR step was performed using 0.1 M $ZnCl_2$ (99.99%, Sigma-Aldrich) aqueous solution as the cationic ion provider with the same $Na_2S$ solution and the sequential dipping was repeated 5 times. Via this three SILAR step sequence, all four CZTS elements were successfully deposited on the $TiO_2$ nanorod array film. After that, the film was subjected to annealing at 500 °C for 1 h in the tube furnace in the presence of 0.1 g of elemental sulfur at inert atmosphere to prevent decomposition of CZTS during annealing. The color of the annealed film changed from light green to light brown. To effect the removal of any excess ZnS as well any incompletely reacted $Cu_yS/SnS_x$ impurity phases, the films were also subjected to further treatment by immersion in strong HCl acid (4 M).

### 5.3.2 Characterization methods

Thermo Scientific K-Alpha X-ray photoelectron spectroscopy (XPS) was used for chemical state and element depth profile analysis. For the depth profile, etching was performed using Ar ion gun sputtering at 3 keV and high current to achieve a maximum etching rate. A Hitachi SU3500 scanning electron microscope (SEM) was used for morphology investigation. Raman spectroscopy was performed using a Renishaw inVia Raman spectrometer equipped with a LEICA optical microscope. A near-infrared laser (785 nm) was used as the excitation source. Transmission electron microscopes (FEI Tecnai G2 F20 200 kV Cryo-STEM equipped with EDAX Octane T Ultra W/Apollo XLT2 SDD and TEAM EDS Analysis System) were used for nanostructure investigation. Inductively coupled plasma-optical emission spectrometry (ICP-OES) was applied to determine the metallic elemental ratio of CZTS. An IPCE/EQE system from PVM Inc. was used for optical and external quantum efficiency measurements. The Newport AM1.5 solar simulator was used for J−V characteristic measurement.

## 5.4 Results and Discussion

### 5.4.1 Fabrication and morphology of TNR@CZTS nanostructure

The preparation of the TNR@CZTS nanostructure includes three main steps as described by the schematic in Figure C.1: (1) growth of $TiO_2$ nanorod arrays (TNR) on FTO glass; (2) deposition of CZTS precursor containing copper, zinc, tin, and sulfur elements onto the TNR film, in this step, the successive ionic layer adsorption and reaction (SILAR) method was used to ensure a uniform CZTS precursor deposit composition on each nanorod; (3) annealing to induce formation of crystalline CZTS on TNR.

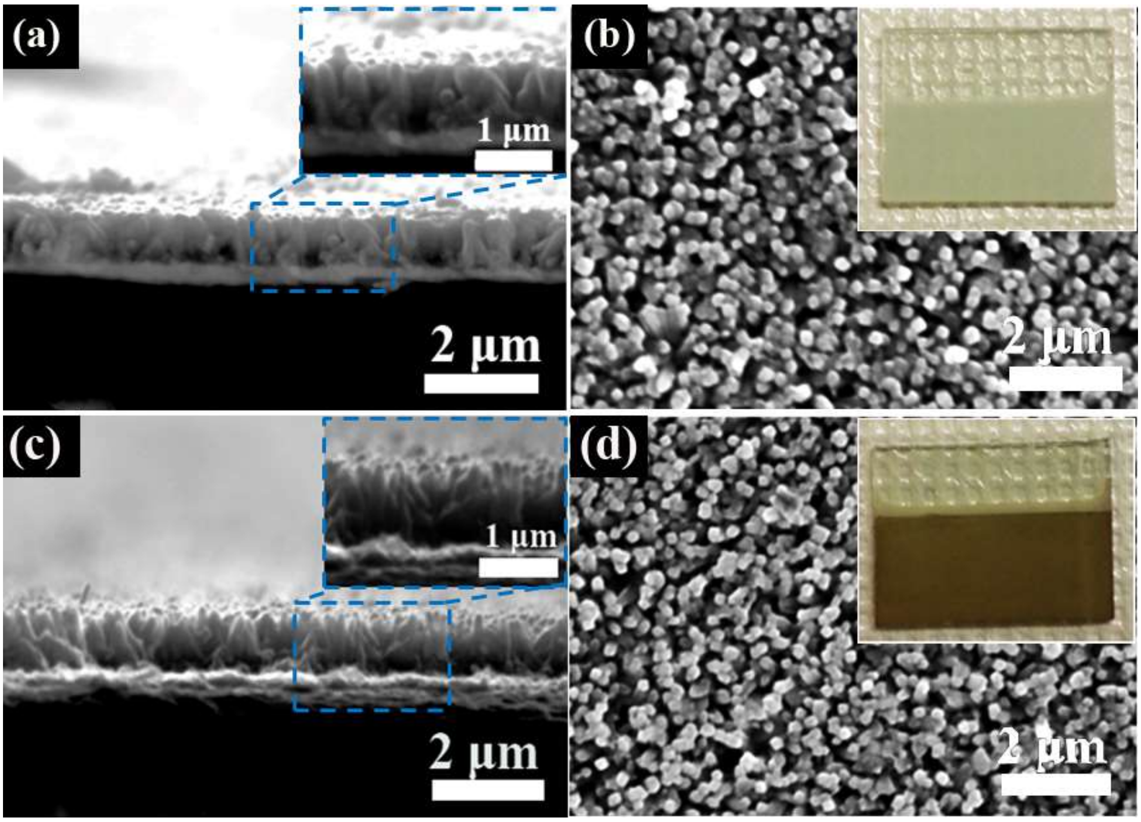

Figure 5.1. (a) Cross-section and b) top view SEM images of the TiO2 nanorod arrays on FTO glass; (c) cross-section and (d) top view SEM images after CZTS deposition. The insets of parts b and d show digital photographs of the TNR on FTO glass before and after CZTS deposition, respectively.

After the completion of TNR@CZTS nanostructure construction, scanning electron microscopy (SEM) was applied to study the morphology of the final product. Figure 1a,c shows the cross-sectional SEM images of the $TiO_2$ nanorod arrays before (upper) and after (lower) CZTS deposition, where the insets depict the higher magnification image of the marked area. The near-vertically aligned hydrothermally grown $TiO_2$ nanorods are clearly seen,[3a, 5] In addition, the top view image in Figure 5.1b,d helps to verify the vertically grown nanostructure and confirm its uniformity to a certain extent. From the inset digital photographs, the clear color darkening signifies the formation of visible light absorbing material on the final product; however, no significant microstructure differences could be seen under this resolution; this means that the $TiO_2$ morphology has been well preserved following its exposure to the harsh chemical and thermal steps involved with CZTS deposition; the deposition of the latter CZTS crystallites was positively identified with further characterization.

### 5.4.2 Spatial composition and phase characterization of TNR@CZTS film

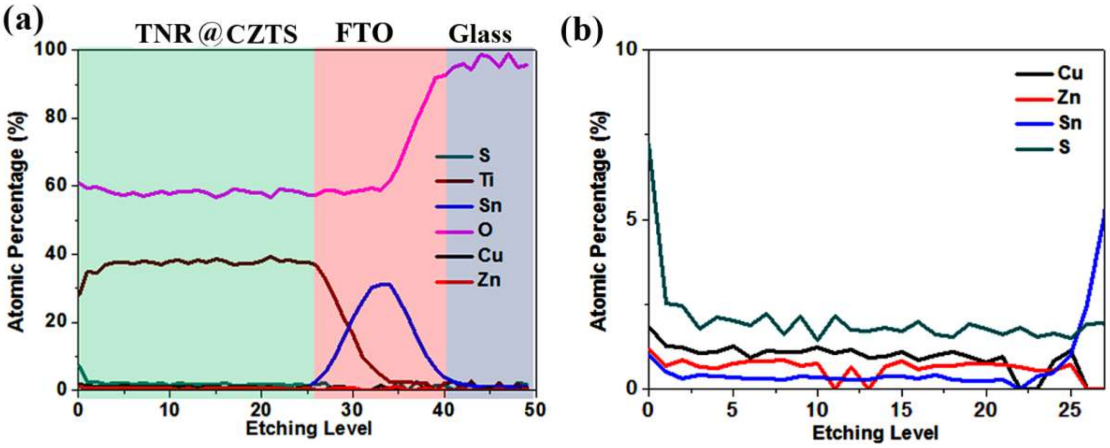

Figure 5.2. (a) XPS depth profile of all elements and (b) the “zoom in” view of the CZTS elements of the TNR@CZTS region (Ti and O excluded)

In order to prove the presence of all elements in TNR@CZTS, X-ray photoelectron spectroscopy (XPS) was applied. Figure C.2 shows the high-resolution XPS spectra. The clearly distinguishable peaks of Cu, Zn, Sn, and S as well as Ti and O confirm the validity of our initial nanostructure design. After employing the 3 keV Ar ion gun to etch the surface for 1 min and in situ capturing of new spectra (Figure C.3), the signals of Cu, Zn, and Sn are seen to become weaker but still to show up as distinct peaks. However, the spatial distribution of elements still remains unclear. Hence we kept using Ar ion gun to etch through the entire film and the overall depth profile obtained is shown in Figure 5.2a, where the boundaries between the target layer, presumably TNR@CZTS film (green region), FTO layer (pink region), and glass substrate (purple region) are clearly marked. When zooming in to study the vertical distribution of Cu, Sn, Zn, and S (Figure 5.2b), impressively, all four elements are quite uniform through the whole depth of the vertically aligned TNR array. The calculated elemental ratio from XPS high-resolution spectra seems to be near stoichiometric in this case; however, it would be a very challenging task to trace the exact ratio of Cu/Zn/Sn/S given their low signal level.

So far the presence of all constituent elements has been confirmed and it has been verified that all Cu, Zn, Sn, and S have distributed inside the film made of TNR. Further, as for crystalline CZTS phase identification, figure 3 shows the Raman spectra of the TNR@CZTS film obtained with 785 nm laser to provide a high-resolution image. Comparing the spectra, before and after CZTS deposition in Figure 5.3b, the only significant difference is seen at the small wavenumber range (250-400 $cm^{-1}$), where the crystalline CZTS characteristic peak clearly shows up. Further, to better evaluate the quality of crystalline CZTS, the marked region was replotted in Figure 5.3a together with the Lorentzian curve fitted peaks to identify different Raman modes. The dominating peak centered at 338 $cm^{-1}$ is attributed to the main A mode of CZTS; further there is a slightly left-shifted one at 332 $cm^{-1}$ broadening the main peak, which usually represents the degree of Cu/Zn disorder.[6] The peak centered at 287 $cm^{-1}$ corresponds to the second A mode of CZTS and 367 and 376 $cm^{-1}$ belong to E and B modes, respectively. Other less significant peaks identified from the fitted curves also agree with previous findings.[7] Besides, in previous research, the intensity ratio of the peaks centered at 287−303 $cm^{-1}$ ($I_{287}/I_{303}$) and 332−338 cm−1 ($I_{332}/I_{338}$) were investigated as indicators for the degree of Cu/Zn disorder,[6, 8] that is, the quality of crystalline CZTS. According to the fitting results, $I_{287}/I_{303}$ is 2.45 while $I_{332}/I_{338}$ is 0.15 for our in situ formed CZTS crystallites on TNR; these values are comparable to those of highly ordered kesterite reported by Scragg et al. and Caballero et al., again serving to confirm the very good quality of the crystalline CZTS.

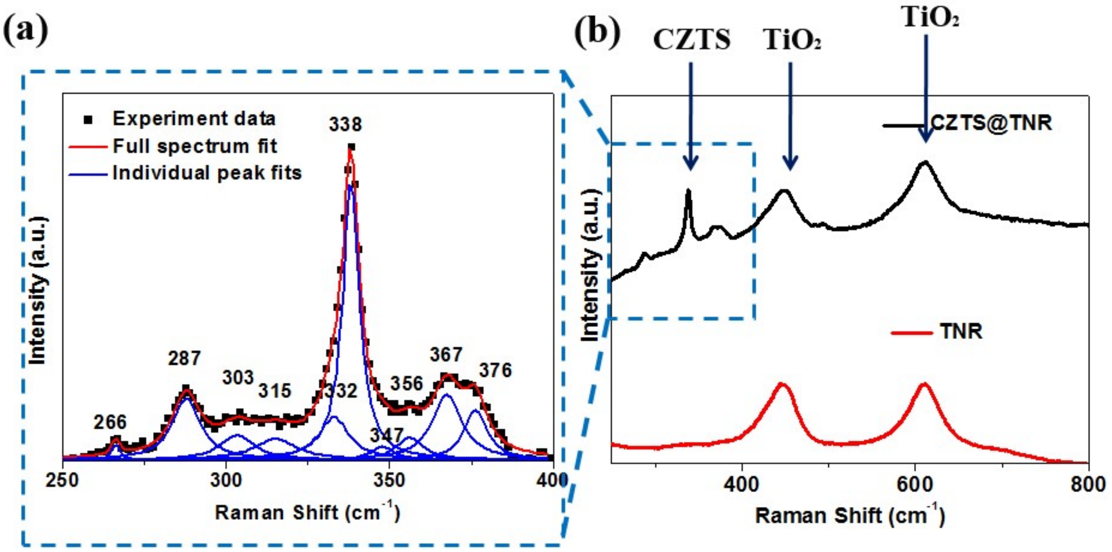

Figure 5.3. (a) Raman spectrum in the small wavenumber range with fitted peaks and (b) the overall spectrum of TNR@CZTS (black line) comparedto that of pure TNR.

### 5.4.3 TEM nanoscale characterization

So far, the deposition of CZTS crystallites has been proven and its spatial distribution within the TNR scaffold has been studied. However, we have not yet got any evidence of CZTS with SEM but only the rutile substrate, which makes us think that CZTS is in the form of very tiny crystallites bonded onto the TNRs. In order to substantiate this supposition, the TNR@CZTS heterostructure was examined by transmission electron microscopy (TEM). The obtained TEM images show (refer to Figure 5.4) the composite material to consist of $TiO_2$ nanorods of different sizes that are decorated with very fine nanocrystallites. Figure 5.4a-c shows the bright field TEM images of three typical types of CZTS decorated nanorods scraped from the TNR@CZTS film, and Figure 5.4d−f depicts their corresponding high-angle annular dark-field images (HAADF) under scanning transmission electron microscope (STEM) working mode. The length of these three rods varied from ~100 nm to ~500 nm to ~1 µm while their widths increased from ~20 nm to ~50 nm to ~150 nm, respectively. In Figure 5.4c, the CZTS nanocrystallites are not quite visible due to their significantly smaller size (10-20 nm) in comparison to the other nanorod specimens. More interestingly, in Figure 5.4c, there is a smaller rod attached to the larger one, which is of the same length as that in Figure

5.4b. This is a fortunate evidence that the ultrafine decorated bar is indeed the subunit from which the film is constructed. As HAADF-STEM forms the annular dark field image only by very high angle, incoherently scattered electrons are highly sensitive to variations in the atomic number of atoms (Z-contrast images) allowing to distinguish between $TiO_2$ and $Cu_2ZnSnS_4$ phases. This allows us to obtain a good knowledge of how these two phases are distributed, as $Cu_2ZnSnS_4$ has much higher overall atomic number than $TiO_2$. In the lower half of Figure 5.4, especially in parts d and e, the deposited nanoparticles can be seen to have contrasting brightness vis-à-vis the nanorods that clearly suggest that they are CZTS while the bar is rutile.

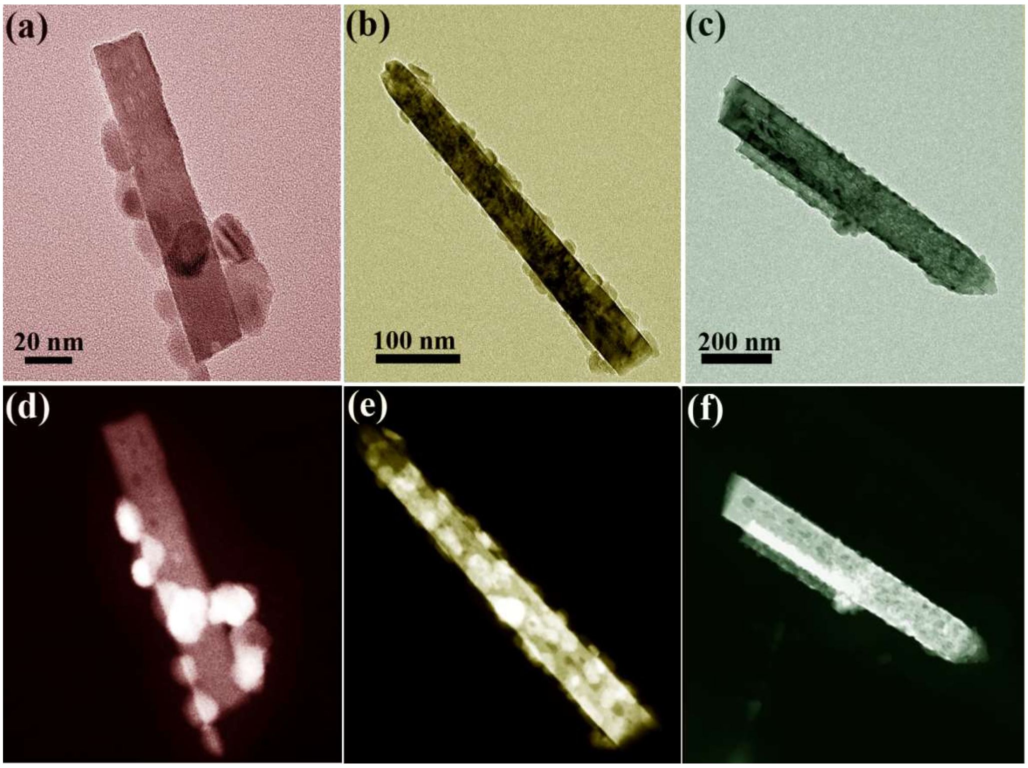

Figure 5.4. (a-c) Bright field TEM images of three different TNR@CZTS decorated nanorods with varied sizes and (d-f) their corresponding STEM-HAADF images.

To confirm the formation of CZTS on the $TiO_2$ nanorods, herein EDS maps were collected from the bar shown in Figure 5.4f. A small area was selected (red dashed line marked area in Figure 5.5a) where a few bright particles could be seen attached on the big nanorod. From the mapping results in Figure 5.5d, the phase distribution can be inferred. $TiO_2$ constitutes the bulk area while Cu, Zn, Sn, and S are clearly concentrated on the edge, as evident by the higher brightness of HAADF-STEM. In order to ensure that the same configuration exists throughout the TNR@CZTS film, the whole nanocomposite bar was mapped and similar results have been found as shown in Figure C.4, thus supporting our conclusion.

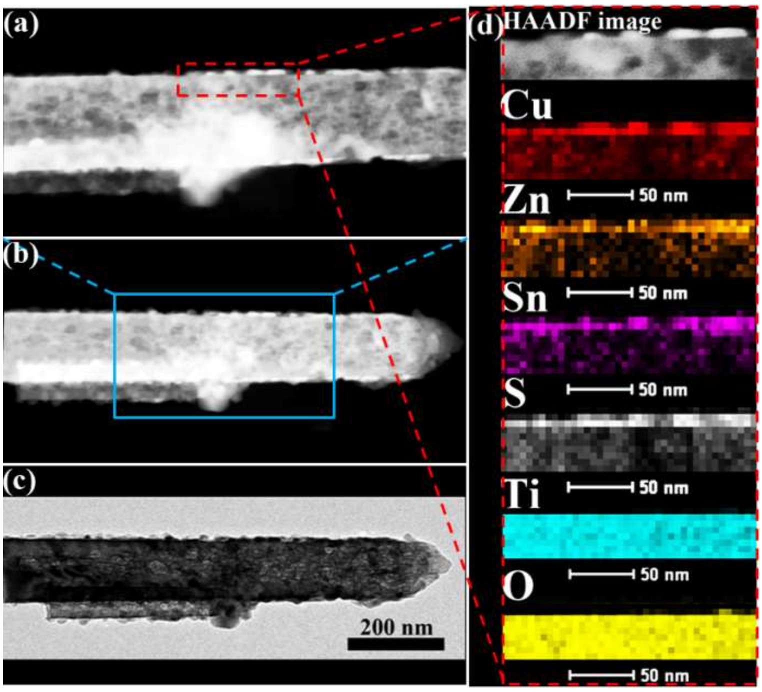

Figure 5.5. (a,b) STEM-HAADF and (c) bright field TEM image of the TNR@CZTS nanostructure and (d) magnified STEM-HAADF image of the rectangular dashed line area with the corresponding EDS element maps.

So far we have verified the CZTS nanoparticle-decorated $TiO_2$ nanorod structure. Next the detailed features of the CZTS@$TiO_2$ structure was further investigated by performing high-resolution TEM imaging (HRTEM) on the smallest decorated nanorod (Figure 5.6a). In the inset, the magnified HRTEM image of the marked area, with lattice fringes at $d_{R110}$≈3.2 Å and $d_{R001}$≈2.9 Å interplanar spacings, is consistent with the rutile-$TiO_2$ phase.[3a, 5] HRTEM images of the boundary areas, where CZTS nanocrystallites and $TiO_2$ nanorod coexisted, were taken and shown in Figure 5.6b,c. The dominant kesterite CZTS (112) interplanar distance in both cases was determined to be ~3.1 Å, which is slightly smaller than that of rutile (110) as reported by previous researchers.[9] The CZTS nanocrystallites attached to the nanorod are of different shape as seen in Figure 5.6b,c and their average size was estimated to be approximately 5-20 nm.

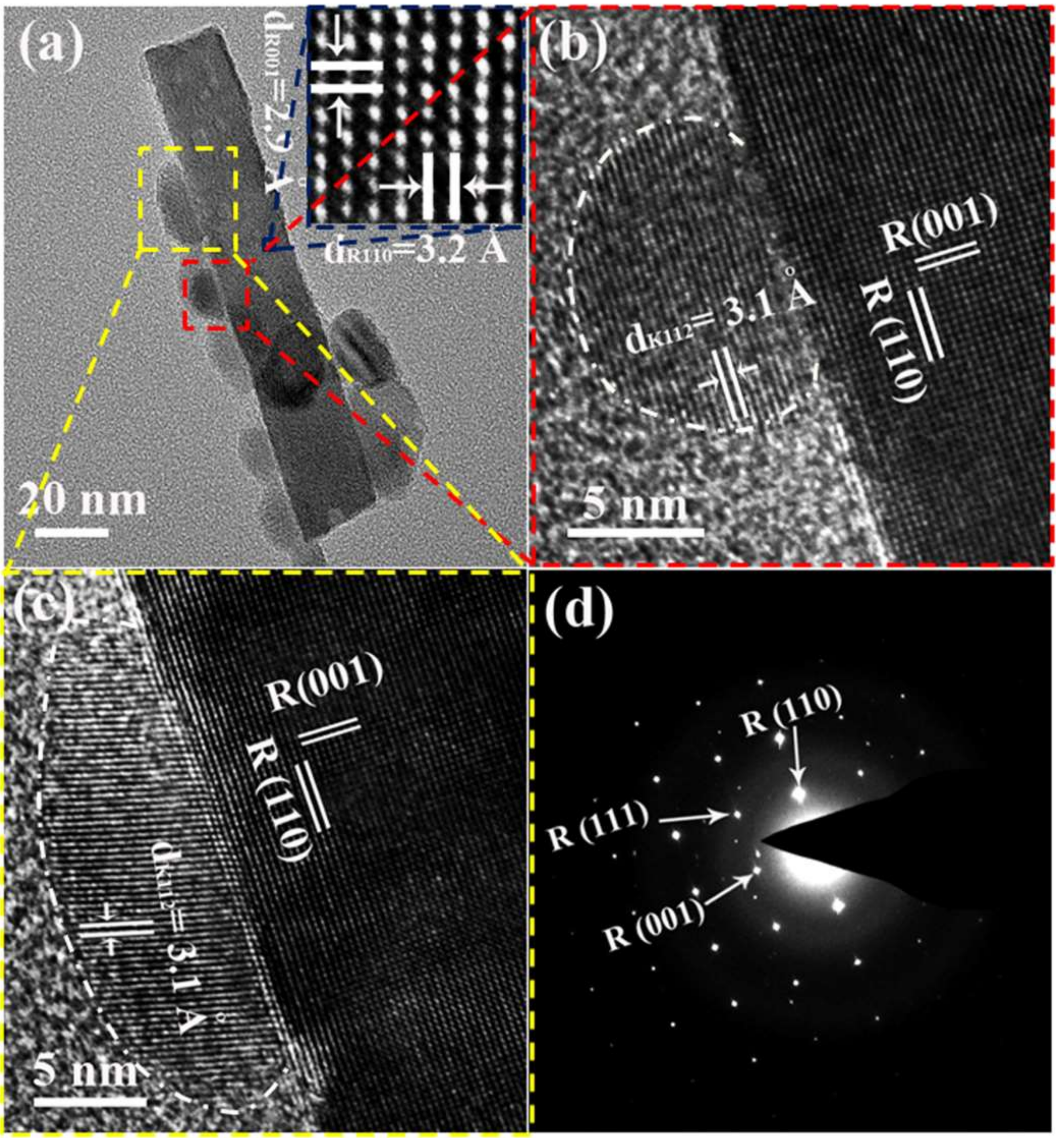

Figure 5.6. (a) Bright field TEM image of CZTS nanoparticles on a single rutile $TiO_2$ nanorod; the inset shows a magnified highresolution image of the mark area on TNR; (b,c) HRTEM images of the TNR@CZTS structure with marked interplanar distance; (d) corresponding SAED pattern (K represents kesterite CZTS phase and R rutile $TiO_2$).

One noteworthy point here is the good bonding/interfacing between CZTS and $TiO_2$. Such in situ epitaxial-like growth is advantageous in allowing the photoelectrons generated from CZTS to be efficiently injected to $TiO_2$ with less recombination occurrence. A selected area electron diffraction (SAED) image was also taken for this small region in Figure 5.6d. The sharp diffraction pattern clearly indicates the nanorod to be single crystal rutile; at the same time there are several isolated dots that are attributed to the small CZTS crystallites. Two additional low-magnification TEM images of the larger TNR@CZTS heterostructures are provided in Figure C.5a,c together with their corresponding SAED patterns in Figure C.5b,d. In this instance, since there are more CZTS crystallites decorating the bigger rutile rod, instead of having randomly located isolated dots, we can observe a ringlike diffraction pattern formed close to the strong diffractive R(110) plane, which is much likely due to differently oriented kesterite (112) plane.

### 5.4.4 Photovoltaic performance evaluation of TNR@CZTS photoanode

After having successfully built this TNR@CZTS heterostructure, it is important to prove its functionality; in other words, to answer the question whether the photoelectrons generated from the CZTS nanocrystalline light absorber can “hop” to the nanorod carrier conductor before being recombined. Incident photon-to-current efficiency (IPCE) that quantifies the percentage of photons being converted into finally collected electrons at different photon energies could reveal indeed the visible-light-driven photon-electron conversion performance. To measure the optoelectronic performance, we simply employed the “sandwich” photoelectrochemical cell configuration with Pt as the counter electrode and $I^-/I_3^-$ as the hole conductor-electrolyte.[3c] Results are shown in Figure 5.7a.

To eliminate the interference of TNR itself, which is ultraviolet photosensitive, the pure TNR electrode was also studied and a significant difference in the visible region (colored in blue) was noticed. This difference perfectly confirms the effectiveness of the deposited CZTS nanocrystallites as a visible light absorber. The quantum efficiency cutoff of this TNR@CZTS photoanode is at around 800 nm, which is consistent with the reported 1.5 eV bandgap of kesterite-CZTS. Unfortunately, the external quantum efficiency (EQE) is relatively low compared to the well-studied CZTS thin film solar cells,[10] only ~12% at the blue light region. The external quantum efficiency is governed by three factors: the light harvesting efficiency ($\eta_{lh}$), the charge injection efficiency ($\eta_{inj}$), and the charge collection efficiency ($\eta_{cc}$). The relation among them is expressed by

$$\eta_{IPCE} = \eta_{lh}\eta_{inj}\eta_{cc}$$

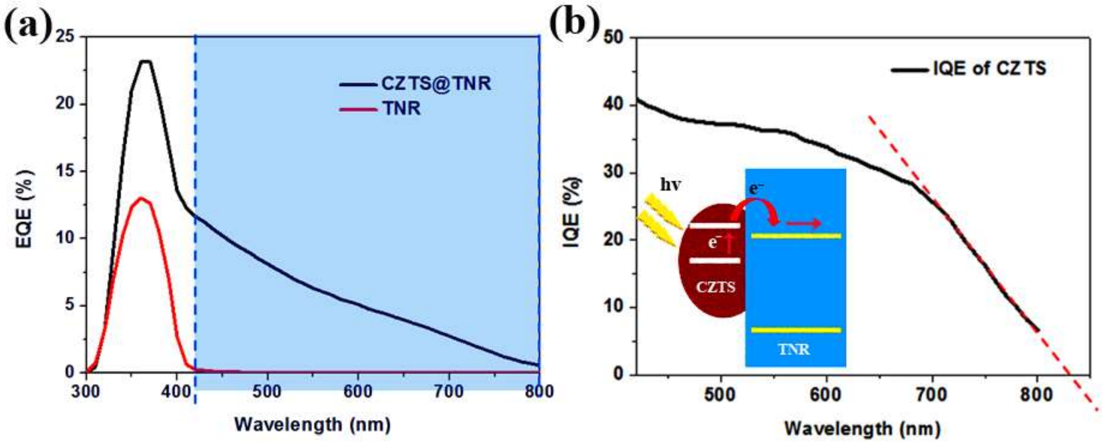

Figure 5.7. (a) External quantum efficiency (EQE) of devices with TNR@CZTS photoanode compared to that with only TNR and (b) calculated internal quantum efficiency of CZTS in the visible range.

One possible reason for the low EQE value could be due to optical loss. To evaluate the effect of this factor, we measured the optical transmittance (Figure C.6a) and reflectance (Figure C.6b) for both TNR films before and after CZTS deposition and then calculated the true light absorption (A) of the isolated CZTS nanomaterial alone by adding up the reduced portion of reflection (R) and transmittance (T) after CZTS deposition:

$$A_{CZTS} = (T_{TNR} - T_{TNR@CZTS}) + (R_{TNR} - R_{TNR@CZTS})$$

In Figure C.6c, the blue region under the plot demonstrates that less than 20% of illumination in the visible region contributes to photon-electron conversion. This prompted us to further probe the optoelectronic property of CZTS nanocrystallites by calculating its internal quantum efficiency in the visible region. The result shown in Figure 5.7b indicates a value of nearly 40% in the blue light region. This means that if we could manage to reduce the optical loss of the photoanode, it would be possible to significantly increase the device photocurrent. We did a linear fit of the efficiency curve edge and found the cutoff wavelength to be around 830 nm, which corresponds to a bandgap of approximately 1.49 eV, perfectly matching the theoretical semiconductor characteristic of kesterite-CZTS.[11] However, this IQE value is still low compared to thin-film kesterite PV devices. This could be attributed to inefficient charge injection ($\eta_{inj}$) and/or collection ($\eta_{cc}$). For successful injection good band alignment is a prerequisite, namely, the conduction band bottom of the absorber should be above that of the electron conductor to supply sufficient injection overpotential.[1a] Since the photogenerated electrons were successfully collected, it is implied the interfacial energy band alignment to be as shown in the inset of Figure 5.7b, proving thus the photovoltaic activity of the TNR@CZTS nanostructure. Hence the competition between injection/collection and recombination play a vital role in device performance that needs to be controlled for optimum results. The J−V characteristic curves shown in Figure C.7 reveal a higher short circuit current density of 1.65 mA/cm$^2$ than previously reported values with CZTS sensitized solar cell structures by Wang et al.[12] (0.71 mA/cm$^2$) and by Dai et al.[13] (0.36-0.71 mA/cm$^2$). The better contact due to the in situ epitaxial-like growth of CZTS on TNR and the one-dimensional electron conductor with shorter electron pathway are responsible for the increased current.

To improve the device optoelectronic performance further work focusing on controlling the CZTS deposit properties was pursued. This was done by varying the cycles of copper sulfide deposition from 2 to 12 times (Cu2 ~ Cu12 for short) during SILAR 1, while other conditions remained unchanged. This round of investigation revealed a strong dependency of photoelectrochemical response on CuS deposition cycles as can be seen in Figure 5.8. In Figure 5.8a, 5 SILAR cycles of Cu predeposition leads to the highest $J_{sc}$ of around 3 mA/cm$^2$, almost doubling the previous value. EQE and IQE curves in Figure 5.8b,c reveal ~20% and ~50% external and internal quantum efficiency at the blue light region for the champion device, respectively. As a complex material, optimization of CZTS as an inorganic sensitizer is not straightforward meaning that there is a lot of work to be done toward achieving competitive solar cell efficiency level. However, the observed improvement via alternation of SILAR cycle numbers serves to show that device optimization can prove very fruitful.

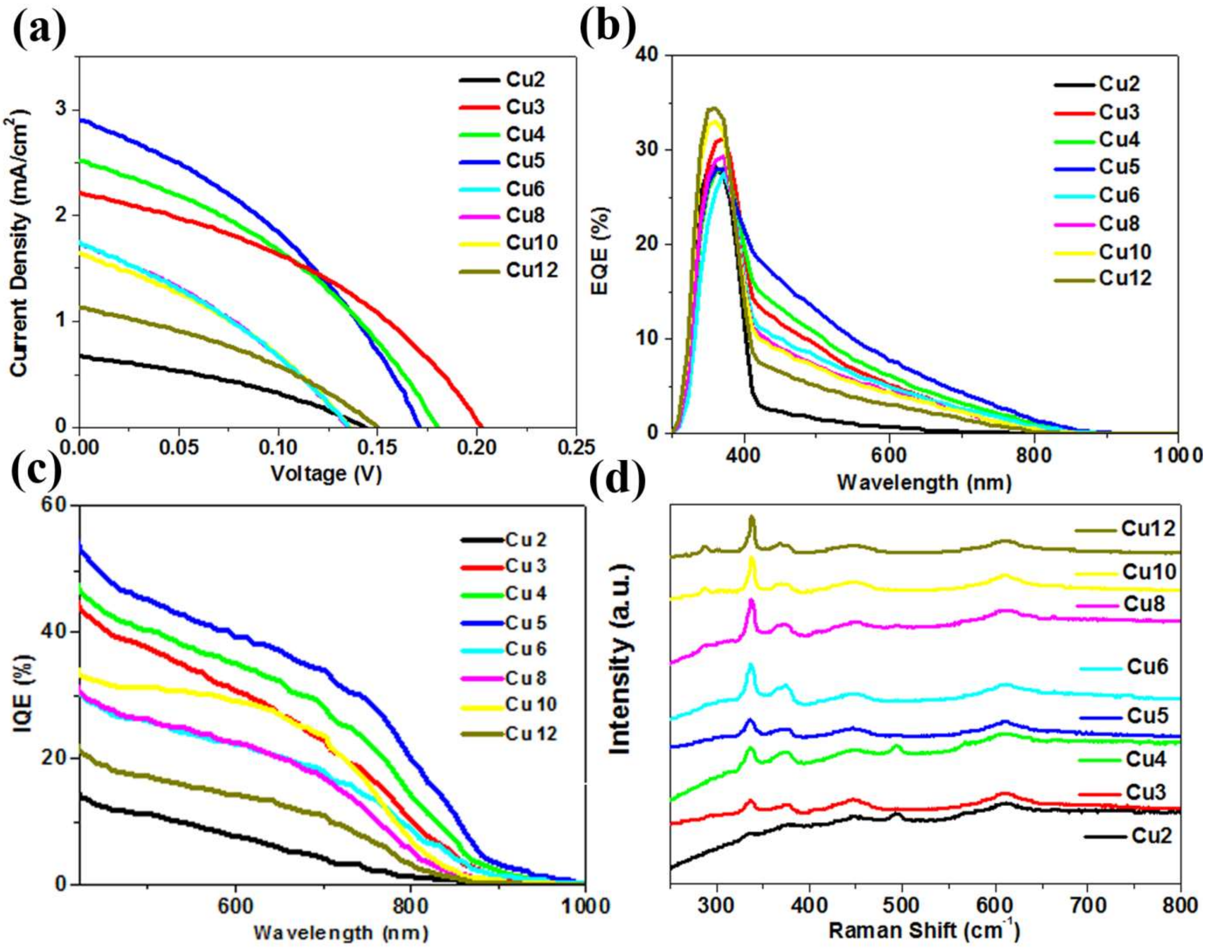

Figure 5.8. (a) J−V curves, (b) external quantum efficiency, and (c) calculated internal quantum efficiency of ETA devices based on TNR@CZTS photoanodes prepared with different CuS SILAR deposition cycles, and (d) Raman spectra of the respective photoanodes.

To understand the effect of CuS SILAR deposition cycle on CZTS quality, Raman spectroscopy was performed with 785 nm laser. The intensity of CZTS characteristic peak at ~337 cm$^{-1}$ was found to keep increasing with the number of Cu SILAR deposition cycles (Figure 5.8d) apparently due to CZTS crystallite size growth,[14] and the probably varied composition of CZTS with different initial copper ratios may also cause the profile changes of the Raman spectra. According to the photoelectrochemical device performance among the different SILAR deposited photoanodes, the Cu5 yields the best relatively results. To understand the reason for the enhancement of performance, we applied ICP-OES to obtain more accurate compositional information by dissolving those CZTS crystallites (after HCl treatment) in aqua regia. The results presented in Figure C.9 show great variations of the Cu/Sn/Zn ratio with a Cu5 sample suggesting a copper-poor zinc-rich near-stoichiometric composition, which is generally accepted to have a better electronic property[15] over other compositions.

While the varied precursor deposition procedure led to photocurrent output increase, the $V_{oc}$ remained still low at ~0.2 V. Surface passivation with metal oxides (i.e., $Al_2O_3$, $ZrO_2$) or metal chalcogenides (i.e., CdSe, ZnS) have proven in the past to effectively reduce interfacial recombination and hence increase photovoltage in the case of quantum-dot sensitized solar cells and other extremely thin absorber solar cells.[16] This approach was also tested in this work after first treating the TNR@CZTS photoanodes with a strong HCl acid solution (4 M) to remove acid-soluble impurities.[17] To this end, two additional SILAR cycles were applied to deposit extra ZnS similar to the SILAR 3 step. The J−V curves for the best performed Cu5 device before and after ZnS treatment are shown in Figure 5.9a. It is clear that the surface passivation had a measurable effect in rising both the $J_{sc}$ and $V_{oc}$ to 3.22 mA/cm$^2$ and 0.21 V, respectively; hence, the overall efficiency is improved from 0.2 % to 0.25 %. The highest external and internal quantum efficiencies at the blue light region are ~22 % and ~60 %, respectively. Although the improvement is modest, this result indicates a feasible direction for further performance improvement. According to recent progress in quantum-dot sensitized solar cells reported by Zhao et al.,[18] their efficiency increased more than 3 times after an optimized ZnS/$SiO_2$ passivation treatment applied to control severe interfacial recombination arising from surface defect states. For semiconductor nanocrystals with quaternary composition like CZTS the problem of surface defects, inhomogeneity, and impurities is deemed to be even more prevalent in comparison to binary metal chalcogenides; hence, the pursuing in future work of optimized surface passivation approaches is of great importance in further boosting its IQE. Meanwhile, when evaluating the light absorption by CZTS (compare Figure 5.9c to Figure C.6c), neither the number of copper sulfide SILAR cycles during precursor preparation nor the application of ZnS passivating film are seen to have a measurable effect on the light harvesting capacity of TNR@CZTS photoanodes. Still less than a quarter of visible light energy contributes to the photon-electron conversion. This implies that the amount of CZTS nanocrystal loading should be increased and on the other hand interfacial recombination suppressed, a strategy that we pursue via the growth of denser CZTS nanocrystallites on longer rutile nanorods capped with a continuous CZTS film properly passivated

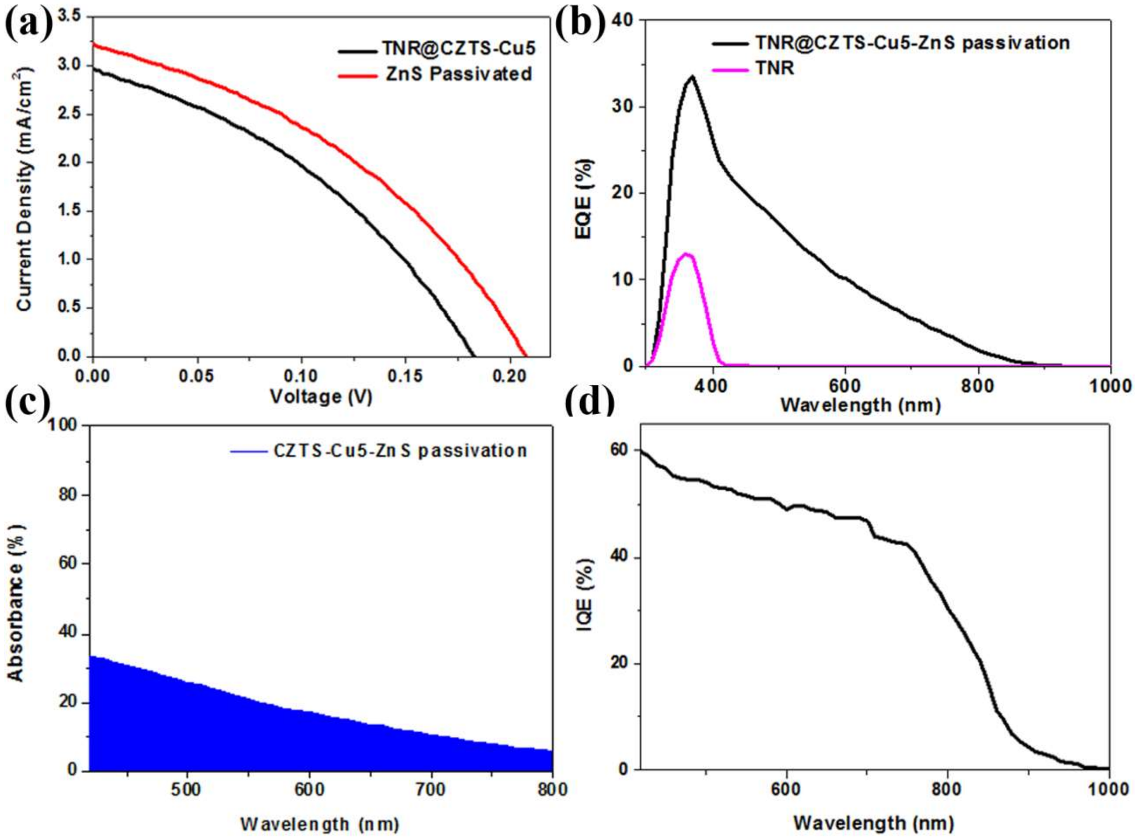

Figure 5.9. (a) J−V curves, (b) external quantum efficiency, (c) measured light absorption, and (d) calculated internal quantum efficiency of ETA cells based on TNR@CZTS photoanodes prepared with 5 CuS SILAR deposition cycles and passivated with ZnS.

A certain amount of sodium has been reported to improve the performance of CZTS solar cells;[19] however, too much sodium could become an issue. Since our experiment involved deposition from sodium sulfide solution, we checked the sodium content in our TNR@CZTS photoelectrode and the data is shown in Figure C.10. The XPS depth profile of the Cu5 TNR@CZTS (without additional ZnS layer) did reveal a significant amount of sodium to be present in the film (more than 5%). The excess sodium could have contributed to some extent to the low $V_{oc}$ exhibited by the photoanode, an issue that deserves further investigation. Furthermore, because the stability of CZTS in contact with the $I^-/I_3^-$ electrolyte is an open question, the present device as tested is considered as a "half-cell" useful only in demonstrating the activity of TNR@CZTS in visible-light driven photoelectron generation. In order to fully realize its potential, a suitable electrolyte is needed on one hand to stabilize the inorganic photoanode and on the other hand to more efficiently extract positive charges from CZTS. The widely used polysulfide electrolyte in quantum-dot sensitized solar cell research would be a good choice, which could allow us having more choices of passivation layers, CdS, for example, is unstable in the $I^-/I_3^-$ electrolyte but can be used as a buffer layer in the polysulfide system.[20] Eventually, solid state hole transport materials (HTM) with higher stability (like CuSCN or Spiro-MeOTAD) could replace the liquid electrolyte,[1a] so as to fully unlock the optoelectronic device potential of the CZTS extremely thin absorber solar cell.

## 5.5 Conclusion

We have developed a SILAR-controlled method to in situ deposit, following annealing in S vapor atmosphere, quaternary semiconductor $Cu_2ZnSnS_4$ nanocrystallites of uniform composition on rutile-$TiO_2$ nanorod array films of ~1.5 μm thickness. The nanoengineered TNR@CZTS photoanode structure consists of 5-20 nm kesterite-CZTS nanocrystallites well bonded on rutile nanorods with variable sizes. Then we have demonstrated the feasibility of generating and injecting photoelectrons from CZTS to the closely attached $TiO_2$ nanorods. Further we demonstrated that by adjusting the number of CuS SILAR cycles, the growth of CZTS nanocrystallites can be controlled for improved photocurrent response. Finally surface passivation with ZnS is shown to be partly effective in suppressing interfacial recombination yielding a short circuit current density of 3.22 $mA/cm^2$ corresponding to an internal quantum efficiency of ~60% in the blue light region. However, the open circuit voltage is only 0.21 V, which is concluded to be due to the down shift of Fermi level of $TiO_2$ after CZTS deposition as well as incomplete suppression of interfacial recombination and instability introduced by the $I^-/I_3^-$ electrolyte. We believe that this new extremely thin absorber CZTS-conductor TNR configuration via further optimization of the TNR@CZTS/HTM interface has the potential for enabling the development of environmentally friendly and low-cost photovoltaic devices made of abundant materials.

## 5.6 References

1. (a) Roelofs, K. E.; Brennan, T. P.; Bent, S. F., Interface Engineering in Inorganic-Absorber Nanostructured Solar Cells. *The Journal of Physical Chemistry Letters* **2014,** *5* (2), 348-360; (b) Hodes, G.; Cahen, D., All-Solid-State, Semiconductor-Sensitized Nanoporous Solar Cells. *Accounts of Chemical Research* **2012,** *45* (5), 705-713.

2. Kumar, M.; Dubey, A.; Adhikari, N.; Venkatesan, S.; Qiao, Q., Strategic Review of Secondary Phases, Defects and Defect-Complexes in Kesterite CZTS-Se Solar Cells. *Energy & Environmental Science* **2015,** *8* (11), 3134-3159.

3. (a) Liu, B.; Aydil, E. S., Growth of Oriented Single-Crystalline Rutile $TiO_2$ Nanorods on Transparent Conducting Substrates for Dye-Sensitized Solar Cells. *Journal of the American Chemical Society* **2009,** *131* (11), 3985-3990; (b) Yan, P.; Wang, X.; Zheng, X.; Li, R.; Han, J.; Shi, J.; Li, A.; Gan, Y.; Li, C., Photovoltaic Device Based on $TiO_2$ Rutile/Anatase Phase Junctions Fabricated in Coaxial Nanorod Arrays. *Nano Energy* **2015,** *15* (0), 406-412; (c) Wang, Z.; Ran, S.; Liu, B.; Chen, D.; Shen, G., Multilayer $TiO_2$ Nanorod Cloth/Nanorod Array Electrode for Dye-Sensitized Solar Cells and Self-Powered UV Detectors. *Nanoscale* **2012,** *4* (11), 3350-3358.

4. Ho, T.-Y.; Chen, L.-Y., The Study of $Cu_2ZnSnS_4$ Nanocrystal/$TiO_2$ Nanorod Heterojuction Photoelectrochemical Cell for Hydrogen Generation. *Energy Procedia* **2014,** *61*, 2050-2053.

5. Wang, Z.; Wang, H.; Liu, B.; Qiu, W.; Zhang, J.; Ran, S.; Huang, H.; Xu, J.; Han, H.; Chen, D.; Shen, G., Transferable and Flexible Nanorod-Assembled $TiO_2$ Cloths for Dye-Sensitized Solar Cells, Photodetectors, and Photocatalysts. *ACS Nano* **2011,** *5* (10), 8412-8419.

6. Scragg, J. J. S.; Choubrac, L.; Lafond, A.; Ericson, T.; Platzer-Björkman, C., A Low-Temperature Order-Disorder Transition in $Cu_2ZnSnS_4$ Thin Films. *Applied Physics Letters* **2014,** *104* (4), 041911.

7. Dimitrievska, M.; Fairbrother, A.; Fontané, X.; Jawhari, T.; Izquierdo-Roca, V.; Saucedo, E.; Pérez-Rodríguez, A., Multiwavelength Excitation Raman Scattering Study of Polycrystalline Kesterite $Cu_2ZnSnS_4$ Thin films. *Applied Physics Letters* **2014,** *104* (2), 021901.

8. Caballero, R.; Garcia-Llamas, E.; Merino, J. M.; León, M.; Babichuk, I.; Dzhagan, V.; Strelchuk, V.; Valakh, M., Non-Stoichiometry Effect and Disorder in $Cu_2ZnSnS_4$ Thin Films Obtained by Flash Evaporation: Raman Scattering Investigation. *Acta Materialia* **2014,** *65* (0), 412-417.

9. (a) Liu, W. C.; Guo, B. L.; Wu, X. S.; Zhang, F. M.; Mak, C. L.; Wong, K. H., Facile Hydrothermal Synthesis of Hydrotropic $Cu_2ZnSnS_4$ Nanocrystal Quantum Dots: Band-Gap Engineering and Phonon Confinement Effect. *Journal of Materials Chemistry A* **2013,** *1* (9), 3182-3186; (b) Guo, Q.; Hillhouse, H. W.; Agrawal, R., Synthesis of $Cu_2ZnSnS_4$ Nanocrystal Ink and its Use for Solar Cells. *Journal of the American Chemical Society* **2009,** *131* (33), 11672-11673.

10. Shin, B.; Gunawan, O.; Zhu, Y.; Bojarczuk, N. A.; Chey, S. J.; Guha, S., Thin Film Solar Cell with 8.4% Power Conversion Efficiency Using an Earth-Abundant $Cu_2ZnSnS_4$ Absorber. *Progress in Photovoltaics* **2013,** *21* (1), 72-76.

11. (a) Katagiri, H.; Saitoh, K.; Washio, T.; Shinohara, H.; Kurumadani, T.; Miyajima, S., Development of Thin Film Solar Cell Based on $Cu_2ZnSnS_4$ Thin Films. *Solar Energy Materials and Solar Cells* **2001,** *65* (1–4), 141-148; (b) Ichimura, M.; Nakashima, Y., Analysis of Atomic and Electronic Structures of $Cu_2ZnSnS_4$ Based on First-Principle Calculation. *Japanese Journal of Applied Physics* **2009,** *48* (9R), 090202.

12. Wang, Y.; Li, C. X.; Yin, X. J.; Wang, H.; Gong, H., $Cu_2ZnSnS_4$ (CZTS) Application in $TiO_2$ Solar Cell as Dye. *ECS Journal of Solid State Science and Technology* **2013,** *2* (7), Q95-Q98.

13. Dai, P.; Shen, X.; Lin, Z.; Feng, Z.; Xu, H.; Zhan, J., Band-Gap Tunable $(Cu_2Sn)_{x/3}Zn_{1-x}S$ Nanoparticles for Solar Cells. *Chemical Communications* **2010,** *46* (31), 5749-5751.

14. (a) Becker, M. A.; Radich, J. G.; Bunker, B. A.; Kamat, P. V., How Does a SILAR CdSe Film Grow? Tuning the Deposition Steps to Suppress Interfacial Charge Recombination in Solar Cells. *The Journal of Physical Chemistry Letters* **2014,** *5* (9), 1575-1582; (b) Li, B.-J.; Yin, P.-F.; Zhou, Y.-Z.; Gao, Z.-M.; Ling, T.; Du, X.-W., Single Crystalline $Cu_2ZnSnS_4$ Nanosheet Arrays for Efficient Photochemical Hydrogen Generation. *RSC Advances* **2015,** *5* (4), 2543-2549.

15. Wang, W.; Winkler, M. T.; Gunawan, O.; Gokmen, T.; Todorov, T. K.; Zhu, Y.; Mitzi, D. B., Device Characteristics of CZTSSe Thin-Film Solar Cells with 12.6% Efficiency. *Advanced Energy Materials* **2013**, *4* (7), 1301465.

16. Roelofs, K. E.; Brennan, T. P.; Dominguez, J. C.; Bailie, C. D.; Margulis, G. Y.; Hoke, E. T.; McGehee, M. D.; Bent, S. F., Effect of $Al_2O_3$ Recombination Barrier Layers Deposited by Atomic Layer Deposition in Solid-State CdS Quantum Dot-Sensitized Solar Cells. *The Journal of Physical Chemistry C* **2013,** *117* (11), 5584-5592.

17. Fairbrother, A.; García-Hemme, E.; Izquierdo-Roca, V.; Fontané, X.; Pulgarín-Agudelo, F. A.; Vigil-Galán, O.; Pérez-Rodríguez, A.; Saucedo, E., Development of a Selective Chemical Etch To Improve the Conversion Efficiency of Zn-Rich Cu2ZnSnS4 Solar Cells. *Journal of the American Chemical Society* **2012,** *134* (19), 8018-8021.

18. Zhao, K.; Pan, Z.; Mora-Seró, I.; Cánovas, E.; Wang, H.; Song, Y.; Gong, X.; Wang, J.; Bonn, M.; Bisquert, J.; Zhong, X., Boosting Power Conversion Efficiencies of Quantum-Dot-Sensitized Solar Cells Beyond 8% by Recombination Control. *Journal of the American Chemical Society* **2015,** *137* (16), 5602-5609.

19. Zhou, H.; Song, T.-B.; Hsu, W.-C.; Luo, S.; Ye, S.; Duan, H.-S.; Hsu, C.-J.; Yang, W.; Yang, Y., Rational Defect Passivation of $Cu_2ZnSn(S,Se)_4$ Photovoltaics with Solution-Processed $Cu_2ZnSnS_4$:Na Nanocrystals. *Journal of the American Chemical Society* **2013,** *135* (43), 15998-16001.

20. Lee, Y.-L.; Chang, C.-H., Efficient Polysulfide Electrolyte for CdS Quantum Dot-Sensitized Solar Cells. *Journal of Power Sources* **2008,** *185* (1), 584-588.

# CHAPTER 6

–

# NANOSCTRUCTURAL AND PHOTOELECTROCHEMICAL PROPERTIES OF CLEAR SOLUTION SPIN-COATED $CU_2ZNSNS_4$ -$TIO_2$ NANOROD FORREST FILM WITH IMPROVED PHOTOVOLTAIC PERFORMANCE

Chapter 5 has presented a novel solution approach to enable the growth of $Cu_2ZnSnS_4$ nanocrystallites in situ on $TiO_2$ nanorod (NR) arrays and obtained clear photovoltaic response of an initial short circuit current density ($J_{sc}$) of 3.22 mA/cm$^2$, an open circuit voltage ($V_{oc}$) of 0.21 V, and an overall conversion efficiency ($\eta$) of 0.25 %. It was concluded that the amount of CZTS nanocrystal loading on the Rutile NRs should be increased and interfacial CZTS/$TiO_2$ recombination suppressed by modifying the solution deposition approach. Although the successive ionic layer adsoption-reaction (SILAR) coating method was a complete aqueous solution based approach, in order to form sufficient thickness of absorber coating, tedious repetitions are needed as the deposition rate is very low. To overcome this technical complexity, in this chapter, a water-ethanol based clear solution coating method is developed to facilitate the absorber deposition and this resulted in an 8-fold increase in energy conversion efficiency after synthesis optimization and interface passivation. The results of this investigation have been published as: Z. Wang, R. Gauvin and G. P. Demopoulos, *Nanoscale,* 2017, 9 (22), 7650-7665. Supporting Information is provided in Appendix D.

## 6.1 Abstract

The previous chapters have demonstrated that $Cu_2ZnSnS_4$ (CZTS), other than in standard p-n junction device architecture, can be employed as broad light absorber upon coating onto a

wide bandgap electron conducting $TiO_2$ film. Further in this chapter, a water-ethanol solution spin coating approach has been applied to directly deposit CZTS nanocrystallites on rutile $TiO_2$ nanorods grown on FTO substrate (TNR) for evaluation in a sensitized solar cell configuration. The FTO@TNR@CZTS photoanode following controlled annealing is shown to exhibit improved photovoltaic properties. Focused-ion beam cross-sections of CZTS nanocoating onto $TiO_2$ nanorod forest film have revealed nanoscale morphological details and electrochemical impedance spectroscopy helped identify $TiO_2$ nanorod film growth characteristics for reduced charge recombination. The band alignment of CZTS and $TiO_2$ has been determined by XPS helping to explain the origin of $V_{oc}$ deficit. An all-solid state device featuring spiro OMeTAD as HTM and CdS as buffer layer has been designed with 2 % efficiency.

## 6.2 Introduction

As mentioned in Chapter 2, the early study to explore CZTS as sensitizer[1] was performed by depositing solid state reaction pre-processed CZTS particles. The low efficiency of 0.29 % was concluded due to poor sensitizer infiltration into the electron conductor $TiO_2$ framework. Recently, the infiltration problem was considerably overcome by applying the hot injection method to prepare CZTS nanocrystal colloidal “inks”. Thus Jiang et. al.[2] reported an efficiency of 2.8 % for a CZTS sensitized ZnO nanorod based solid state device; while Bai et al.[3] achieved even higher conversion efficiency (4.7 % ) with a liquid electrolyte junction device based on deposition of the CZTS “ink” into a $TiO_2$ mesoporous film. However, the hot injection method is a relatively low-yield, vacuum and toxic organic solvent based synthesis route that necessitates intricate multi-step extraction, purification, and re-dispersion of the pre-synthesized nanocrystals rendering it unattractive from a scalable manufacturing perspective.

Direct solution coating, as alternative to the nanocrystal “ink” route, has been proven effective in fabricating CZTS thin film solar cells.[4] This approach offers all advantages of non-vacuum deposition such as the possibility to use low-cost and high-throughput equipment, low wastage of raw materials, high uniformity of layer properties over large area and finally, potential deployment of large-scale production with low capital investment. Numerous organic solvents (mostly toxic) have been studied, among which the most successful example is hydrazine with record efficiency of 12.6 %[5]. Later dimethyl sulfoxide (DMSO) as a safer solvent has been used to achieve over 11 % efficiency.[6] Besides, mixtures of alcohols[7], ethylene glycol[8], 2-methoxyethanol[9], pyridine[10], N,N-dimethylformamide (DMF)[11] have been employed to thin film CZTS solar cell fabrication. But none of these organic solvent-based routes is as attractive as the water-ethanol route regarding their suitability for large-scale application, out of which an over 5 % CZTS thin film device has been described recently.[12]

As for the CZTS sensitized solar cell configuration, pyridine was used for direct solution coating of CZTS onto a ZnO nanorod film yielding 1.2 % efficiency.[13] However, in this case it was found the ZnO nanorod structure not being well persevered after coating with CZTS showing signs of instability upon exposure to the sulfide-rich environment of the coating solution. In contrast, $TiO_2$ has higher chemical stability and comparable electron conducting property, which makes for a more suitable candidate in this application. Based on the early stage results and experience in Chapter 5 where a aqueous solution processed FTO@TNR@CZTS photoanode has been constructed, in this chapter a water-ethanol direct solution coating method was developed to eventually realized increased absorber loading and interface engineering, which gives an energy conversion efficiency of 2 % for CZTS sensitized solid state solar cell. As such this works serves as valuable reference for further development of CZTS sensitized optoelectronic devices.

## 6.3 Experimental Section

### 6.3.1 Material synthesis

The preparation of $TiO_2$ nanorods was similar to Chapter 5, except that different reaction time and titanium butoxide concentration were investigated this time. The deposition of CZTS precursor material containing Cu, Zn, Sn and S on the $TiO_2$ nanorod array was done via clear solution spin coating. Specifically, 0.09 M $CuCl_2$ (99 %, Alfa Aesar), 0.06 M $ZnCl_2$

(99.99 %, Sigma-Aldrich), 0.07 M $SnCl_2$ (98 %, Sigma-Aldrich) and 0.4 M thioacetamide were dissolved in 20 mL ethanol/water ($V_{ethanol}$: $V_{water}$ = 3: 1) to form a clear yellowish solution. The prepared solution was spin-coated on the $TiO_2$ nanorods/FTO substrate at 2,500 rpm for 20 s. Annealing was performed afterwards in a tube furnace (MTI mini CVD tube furnace) at different temperatures and times in the presence of tin and sulfur powder to promote crystallization of CZTS on the surface of the $TiO_2$ nanorods. For all annealing experiments, the heat ramping rate was set at 10 °C/min. The colour of annealed film changed from white to brownish, indicating the crystallization of CZTS. A further treatment with HCl (4 M) was employed to ensure dissolution/removal of any impurity by-products like ZnS[14].

For solid state device, the hole-transporting material (HTM) was formed on the TNR-CZTS film by spin-coating the 2,2′,7,7′-tetrakis(N,N-pdimethoxyphenylamino)-9,9′-spirobifluorene (spiro-OMeTAD) solution at 2,500 rpm for 20 s, where 72.3 mg of spiro-OMeTAD was mixed with 28.8 µL of 4-tert-butylpyridine and 17.5 µL of lithium bis(trifluoromethylsulfonyl) imide (LiTFSI) solution (520 mg of LiTFSI in 1 mL of acetonitrile) in 1 mL of chlorobenzene. Finally, 80 nm of Au was deposited using a thermal evaporator at a deposition rate of 1.0 Å/s. CdS was prepared via chemical bath deposition (CBD)[15] at 65 °C for 20 min on $TiO_2$ nanorod film before coating CZTS precursor.

### 6.3.2 Characterization methods

Thermo Scientific K-Alpha X-Ray Photoelectron Spectroscopy (XPS) was used for chemical state and element depth profile analysis. For depth profile, etching was performed using Ar ion gun sputtering at 3 keV and high current to achieve a maximum etching rate. For high resolution XPS spectra comparison, C 1s peak at binding energy of 285 eV was used for charge correction. A Hitachi SU3500 Scanning Electron Microscope (SEM) was used for $TiO_2$ nanorod preliminary morphology study. The Hitachi SU-8230 Field Emission-STEM (FE-STEM) equipped with Oxford EBSD and INCA EDS was used for high resolution SEM secondary electron and backscatter electron image capturing and EDS mapping. The FEI Helios Nanolab 660 DualBeam system was used to perform focused ion beam (FIB) cutting to prepare TNR@CZTS cross-section samples. Raman spectroscopy was performed using a Renishaw inVia Raman spectrometer equipped with a LEICA optical microscope with different laser excitation sources. Transmission Electron Microscopy (FEI Tecnai G2 F20 200 kV Cryo-STEM equipped with EDAX Octane T Ultra W /Apollo XLT2 SDD and TEAM EDS Analysis System) was employed for high resolution nanostructure investigation. An IPCE/EQE system from PVM Inc. was used for optical and external quantum efficiency measurements. A Newport AM 1.5 (ABA) solar simulator was used for J-V photovoltaic measurements. Electrochemical impedance spectra (EIS) analysis was performed by using a VSP-potentiostat system (BioLogic) under dark condition, applying a 5 mV AC signal and scanning in a frequency range between 100 kHz and 100 mHz at reversed bias from 0.1 V to 0.5 V.

## 6.4 Results and Discussion

### 6.4.1 Clear solution direct coating processed CZTS/$TiO_2$ structure

As shown in the schematic of Figure 6.1, the preparation of CZTS/$TiO_2$ nanocomposite film involves three main steps: 1. Hydrothermal growth of $TiO_2$ nanorods (TNR) on FTO glass (Figure 6.1a); 2. Spin-coating of precursor solution containing Cu, Zn, Sn and S on TNR substrate (Figure 6.1b); 3. Annealing of as-prepared film to induce CZTS in-situ crystallization on TNR (Figure 6.1c). In Step 1, 0.15 M titanium butoxide was added in HCl solution for 2 h hydrothermal reaction, the same as described in the previous work.[16] The $TiO_2$ nanorods are made of rutile[16-17]. The morphological features of obtained TNR film were characterized by SEM and are shown in Figure D.1a and D.1b. The $TiO_2$ film is clearly seen consisting of compact nanorods with a thickness of roughly 1.5 μm. Figure D.1d shows the photograph of an as-prepared TNR film on FTO glass. In step 2, the ethanol/water solution containing $CuCl_2$, $ZnCl_2$, $SnCl_2$, and thioacetamide was spin coated on the TNR film. Figure 6.1d shows the clear yellowish alcoholic solution. The clear solution coating approach as opposed to the nanoparticle suspension-based coating method[1-3, 18] was adopted seeking to obtain compositional homogeneity of deposited CZTS throughout the three-dimensional nanorod film. Figure 6.1e shows a photograph of obtained CZTS-coated TNR film following annealing. The uniform colour change from white to brown of the film is attributed indeed to good intra-film CZTS.

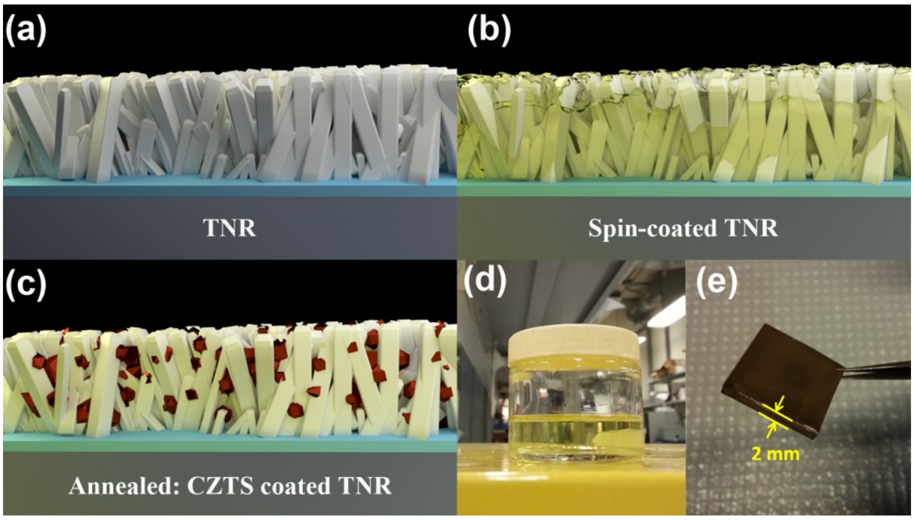

Figure 6.1. Three-dimensional schematic depiction of a) the vertically aligned $TiO_2$ nanorods (TNR) grown on FTO glass substrate, b) the film after coating TNR with CZTS precursor solution and c) after annealing to form CZTS crystallites on TNR; d) photograph of the CZTS precursor solution and CZTS coated TNR film after annealing.

### 6.4.2 Preliminary annealing temperature effect on photovoltaic response

Annealing plays a key role in the quality of CZTS film. Annealing temperatures ranging from 350 °C to 750 °C have been reported[19] that made necessary careful selection of this parameter. To this end TNR@CZTS films were annealed at different temperatures (350 to 550 °C) and their annealing-dependent optoelectronic response was assessed. For this work, the sandwich structure used in dye[20] or quantum-dot[21] sensitized solar cells featuring Pt as counter electrode and $I^-/I_3^-$ as hole conductor-electrolyte was adopted. As shown in Figure 6.2a, the photoelectrons generated from CZTS are injected into the conduction band of TNR while the holes are recovered by the redox species in electrolyte, thus enabling the functioning of this photoelectrochemical cell.[16] The J-V characteristics of different CZTS/TNR devices tested under AM 1.5 one sun illumination are shown in Figure 6.2b and Table 6.1. It is clear that the annealing temperature plays a vital role in the light absorbing property of CZTS, more specifically, the short-circuit current density is seen to increase as the annealing temperature increased from 350 to 550 °C. This trend is further confirmed with the Incident

Photon-Electron Conversion Efficiency (IPCE) test results in Figure 6.2c, where the external quantum efficiency in the visible light range (over >400 nm) is seen to increase with higher temperature annealing. Raman spectroscopy was employed to characterize the CZTS/TNR films obtained at different annealing temperature. Raman characterization was done at 785 nm laser excitation as at this wavelength the near-resonant spectra are highly resolvable facilitating distinction between the kesterite CZTS phase and the undesirable commonly co-existing impurity phase of $Cu_3SnS_4$[22]. At around 300~400 $cm^{-1}$ which is in the range of CZTS characteristic peaks (338 and 375 $cm^{-1}$) the peaks are broad with poor resolution in the case of the lower temperature annealed films (350 °C /400 °C). This is indicative of formation of early stage kesterite crystallized phase hence the poor PV response (Table 1). At this lower annealed temperatures the films exhibit a relatively sharp peak at ~495 $cm^{-1}$ and a smaller one at 570 $cm^{-1}$, which most likely are due to the complex carbon residue arising from the partial decomposition of thioacetamide.[23] As the annealing temperature is raised to 450 °C and above, the CZTS characteristic peaks located around 337 $cm^{-1}$ and 375 $cm^{-1}$ are getting stronger and sharper while the carbon impurity residual peaks at 495 $cm^{-1}$ and 570 $cm^{-1}$ keep disappearing. After annealing at 550 °C, the most distinguishable CZTS characteristic Raman peaks can be seen co-existed with the rutile phase (440 $cm^{-1}$ and 610 $cm^{-1}$) from the TNR[16]. Therefore, higher temperature is beneficial in eliminating the impurity residuals as well as developing better crystallinity of CZTS, which is concluded contribute to the observed increased photocurrent generation. But the efficiency does not seem to follow the trend of the photocurrent; instead, it stays at a low constant value of 0.1% over the 450-550 °C annealing temperature range. This behavior is attributed to the reduced open circuit voltage as the temperature increases. Having considered the CZTS side of the CZTS/TNR absorber-conductor interface we decided to examine next how the rutile nanorods influence the device performance.

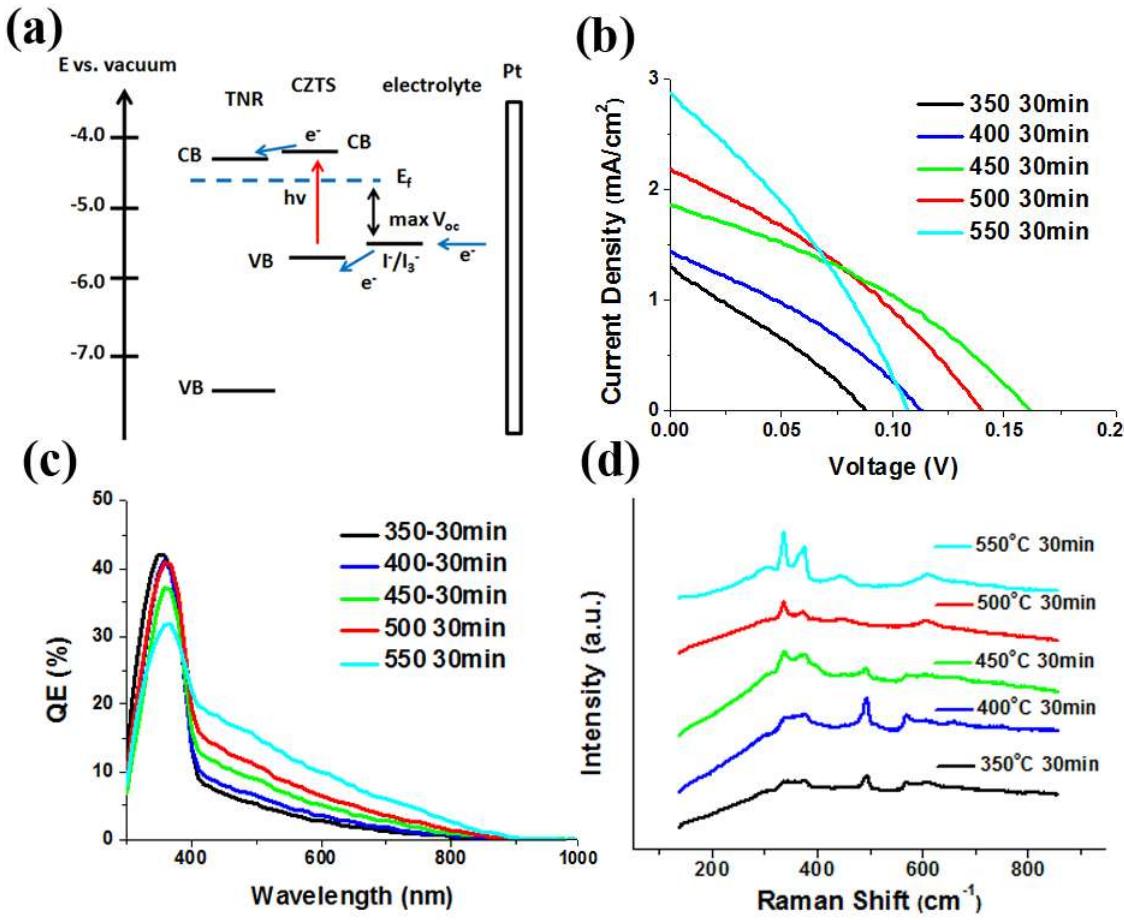

Figure 6.2. a) Working principle of a TNR@CZTS sensitized solar cell device. b) J-V, c) EQE, and d) Raman results (785 nm laser) of CZTS/TNR photoanodes annealed at different temperatures.

Table 6.1. Preliminary Study of the Annealing Temperature Effect on Solar Cell Performance

| | Efficiency (%) | FF (%) | $J_{sc}$ (mA/cm$^2$) | $V_{oc}$ (mV) |
|---|---|---|---|---|
| 350℃ 30min | 0.03 | 28.4 | 1.31 | 88 |
| 400℃ 30min | 0.05 | 32.3 | 1.44 | 113 |
| 450℃ 30min | 0.1 | 34.8 | 1.87 | 161 |
| 500℃ 30min | 0.1 | 32.9 | 2.18 | 140 |
| 550℃ 30min | 0.1 | 32.1 | 2.87 | 107 |

### 6.4.3 Effect of $TiO_2$ nanorod growth conditions on photovoltaic response

The crystal properties of the nanostructured $TiO_2$ can influence the device performance in terms of effective charge transfer and recombination control.[20, 24] In this context, adjustments to the TNR hydrothermal growth process were made in terms of Ti(IV) concentration and reaction time to evaluate its property as electron conductor in CZTS-sensitized TNR solar cell configuration. In this series of tests the annealing temperature of TNR@CZTS photoanode was kept constant at 550 °C. After various attempts it was found the titanium source concentration to be a vital parameter in TNR growth. Generally, with higher concentration of titanium butoxide, the nanorod film tends to grow thicker and denser. Here four TNR films grown at different conditions are summarized in Table 2: TNR 1, TNR 2, TNR 3 (initial/default experimental condition) and TNR 4. Figure 6.3 shows the SEM images of the four TNR films. After 8 h, 6 h and 2 h reaction, the TNR 1, TNR 2 and TNR 3 films all reach the thickness of ~1.5 um; it is further clear that the higher concentration of titanium source produces the denser nanorod film. However, we found the films grown at high concentration, independent of the reaction time (TNR 3 and TNR 4), start to detach from the FTO substrate that adversely impacts device efficiency (Table 6.2).

Table 6.2. Characteristics of $TiO_2$ nanorods (TNR) prepared at different conditions and the corresponding efficiency of the CZTS/TNR devices.

| Film ID | Titanium Butoxide | HCl Aqueous Solution | Reaction Time | Nanorod Length | Device Efficiency |
|---|---|---|---|---|---|
| TNR 1 | 0.04 M | 18% | 8 h | ~ 1.5 μm | 0.18% |
| TNR 2 | 0.075 M | 18% | 6 h | ~ 1.5 μm | 0.25 % |
| TNR 3 | 0.15 M | 18% | 2 h | ~ 1.5 μm | 0.1 % |
| TNR 4 | 0.15 M | 18% | 6 h | ~ 2.5 μm | 0.03 % |

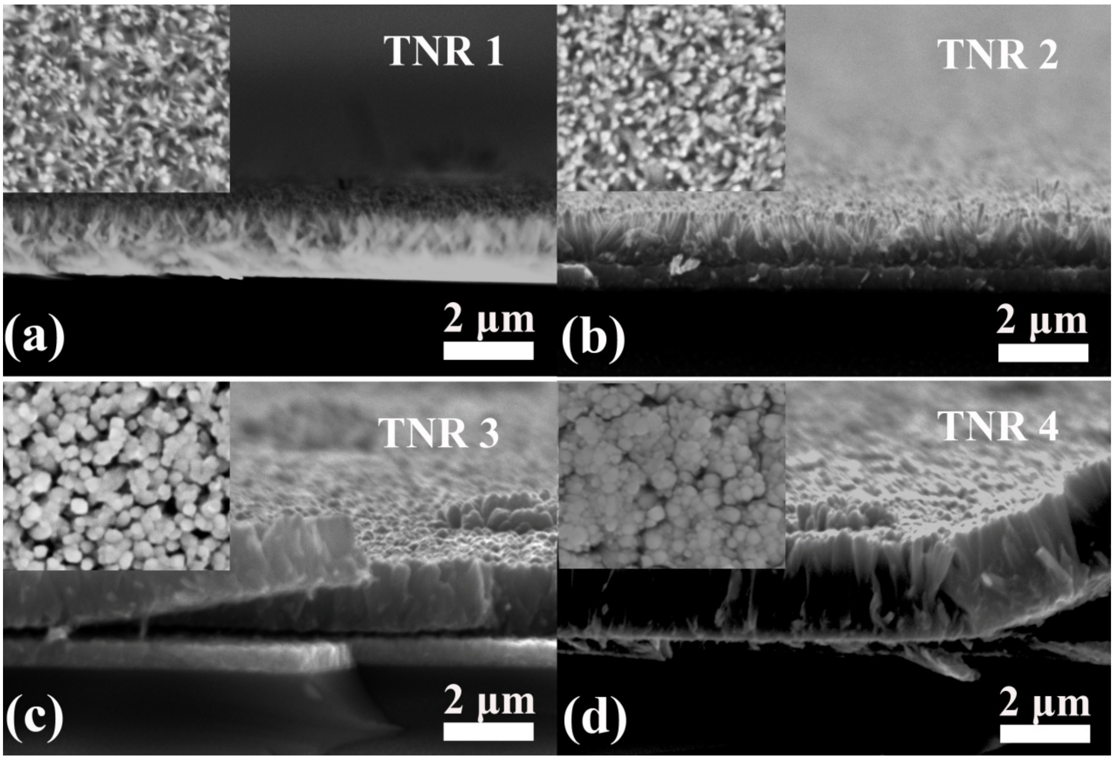

Figure 6.3. SEM cross section and top view (inset) images of TNR films grown at different hydrothermal conditions noted as: a) TNR 1, b) TNR 2, c) TNR 3, d) TNR 4 (refer to Table 2 for preparation conditions).

The J-V curves of the different CZTS sensitized-TNR film based photoelectrochemical cells are shown in Figure 6.4a, from which it can be seen that TNR 2 has the highest efficiency of 0.25 % comparing to the other candidates. Figure 6.4b compares the shunt resistance of the four TNR films with TNR 2 showing much higher $R_{sh}$, meaning a better anti-recombination property manifested by the higher photocurrent ($J_{sc}$) and photovoltage ($V_{oc}$) recorded-see Figure 6.4a. To further verify this effect, electrochemical impedance spectroscopy (EIS) was performed on these four assembled devices under dark condition at different bias ranging from 0 V to 0.4 V and the collected results are shown in Figure D.2. The semicircle in the middle frequency range represents the interfacial charge recombination process between photoanode and electrolyte. As it ca be seen, it becomes smaller for each film as higher bias voltage is applied; this is caused by the increased electron concentration when the Fermi level in the photoanode gets closer to the lower edge of the conduction band of TNR and thus leads to a decrease in recombination resistance ($R_{rec}$).[20] The simplified equivalent circuit is shown in Figure D.2 by introducing a constant phase elements (CPE) instead of capacitance element to better fit the non-ideal semicircle.[25] The fitting results of $R_{rec}$ shown in Figure D.2e are very consistent with the registered J-V characteristics and the extracted shunt resistance, where TNR 2 represents the best anti-recombination property over all four conditions. In Figure 6.4c their EIS Nyquist spectra at 0.2V bias are selectively re-ploted, from which a clear difference of the semicircle profiles becomes evident. The largest diameter indicates the highest value of charge recombination resistance for the TNR 2-based device. Moreover, open-circuit-voltage decay (OCVD) measurements were performed (Figure D.2f) to evaluate the dynamic charge transport properties of different TNRs. The $V_{oc}$ during the decay process can be expressed as:[26]

$$V_{oc} = \frac{E_{Fn} - E_{F0}}{e} = \frac{K_B T}{e} \ln \frac{n}{n_0}$$

Where $E_{Fn}$ and $E_{F0}$ stand for the quasi-equilibrium state under AM 1.5 condition and the dark equilibrium state, respectively, n is the free electron concentration, $n_0$ is the electron concentration in dark condition, $K_B$ is the Boltzmann constant ($1.38\times10^{-23}$ J/K), T is the absolute temperature, and e is the elementary charge. The logarithmic change of the free charge concentration can be easiliy mesured, which is defined as the modified recombination rate ($R_k$) according to the formula: [20]

$$R_k = -\frac{d\ln(n)}{dt} = -\frac{e}{K_B T}\frac{dV_{oc}}{dt}$$

And the carrier lifetime is represented by the inverse of recombination rate:[27]

$$\tau = -\frac{K_B T}{e}\left(\frac{dV_{oc}}{dt}\right)^{-1}$$

Since the starting $V_{oc}$ of those devices was not at the same level, the electron lifetime versus $V_{oc}$ though this dynamic process is calculated for a better comparison. The same trend is shown in Figure 6.4d, reconfirming the slowest recombination rate of the TNR 2 electrode. The higher recombination resistance of this film is attributed to optimized coverage of FTO glass by TNR preventing direct contact between CZTS and FTO glass (also electrolyte and FTO glass). As a result the TNR 2 film was retained for the next step of optimization.

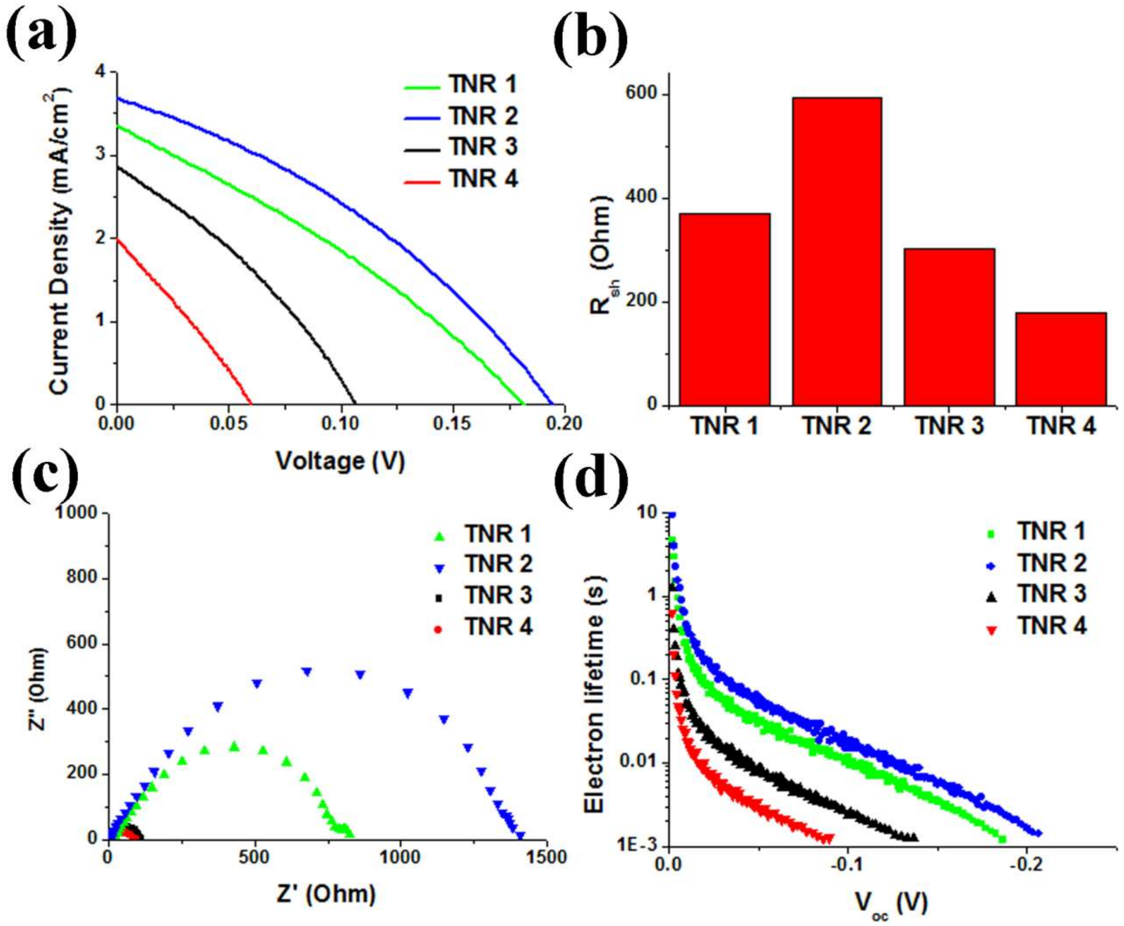

Figure 6.4. a) J-V curves, b) shunt resistance, c) Nyquist plots of electrochemical impedance sprectra measured under 0.2V bias, and d) electron lifetimes extracted from open-circuit-voltage decay (OCVD) curves for different CZTS/TNR sensitized solar cells with TNR synthesized at different hydrothermal growth conditions.

### 6.4.4 Annealing optimization

After selecting TNR 2 film, annealing was revisited this time pushing the annealing temperature to 600 °C and considering the effect of annealing time. As depicted in Figure 6.5a, the 600 °C -annealed CZTS/TNR photoanode shows much better device performance in comparison to the one annealed at 550 °C. What is more, unlike in Figure 6.2b, the $V_{oc}$ of the TNR 2 based device increases together with its photocurrent, indicating the importance of the quality of TNR electron conducting film. As shown in Table 6.3, the efficiency of the single-step clear solution spin-coated CZTS/TNR after 600 °C annealing has increased to 0.42 % from 0.25 %. Figure 6.5b shows the corresponding external quantum efficiency spectra of the two devices. It is noticed that the EQE profile of the 600 °C annealed photoanode based device is slightly different than that of the 550 °C annealed one. The EQE value has been enhanced in the visible light region (over 400 nm), corresponding to the increased $J_{sc}$ (Figure 6.5a) apparently reflecting the better quality of CZTS nanocoating on TNR (removal of defects at elevated temperature).

Table 6.3 Solar cell performance of 550 °C and 600 °C annealed CZTS/TNR photoanodes

| | Efficiency (%) | FF (%) | $J_{sc}$ (mA/cm$^2$) | $V_{oc}$ (mV) |
|---|---|---|---|---|
| 550 °C 30 min | 0.25 | 34.5 | 3.69 | 195 |
| 600 °C 30 min | 0.42 | 37.2 | 4.47 | 250 |

Near resonant Raman spectroscopy using 785 nm laser source excitation was performed on the CZTS/TNR films annealed at 550 °C and 600 °C and the results are shown in Figure 6.5c. These spectra confirm the earlier suggestion made of better quality CZTS nanocoating at elevated annealing temperature. Thus the CZTS characteristic peaks centered at around 337 cm$^{-1}$ and 375 cm$^{-1}$ are found to be strengthened for the 600 °C annealed film reflecting its better developed crystalline structure. The structure of the 600 °C annealed CZTS has been further probed with the aid of the high resolution Raman spectrum shown in Figure 6.5d together with the Lorentzian peak fits of the CZTS characteristic wavenumber range. The dominating peak centered at 337 cm$^{-1}$ is attributed to the main A mode of CZTS;[28] The peak centered at 365 cm$^{-1}$ and 375 cm$^{-1}$ belong to E and B modes, respectively. Other less significant peaks identified also agree with previous findings[29]. Further, the green laser excitation (514 nm) was applied in order to characterize a larger Raman wavenumber range. Except for the enhanced peak intensity as the annealing temperature increases (Figure 6.5e), the initial significant peak located at ~1,440 cm$^{-1}$ of the 500 °C annealed sample is found to decrease dramatically after being annealed at a higher temperature, and completely disappearing for the samples going through 600 °C 30 min annealing. It is generally accepted that this peak belongs to carbon characteristic Raman mode[30]. Hence annealing at 550→600 °C does not only improve the crystallinity of CZTS but equally important helps eliminate the carbon residual by promoting a more complete reaction, thus removing a source of recombination loss

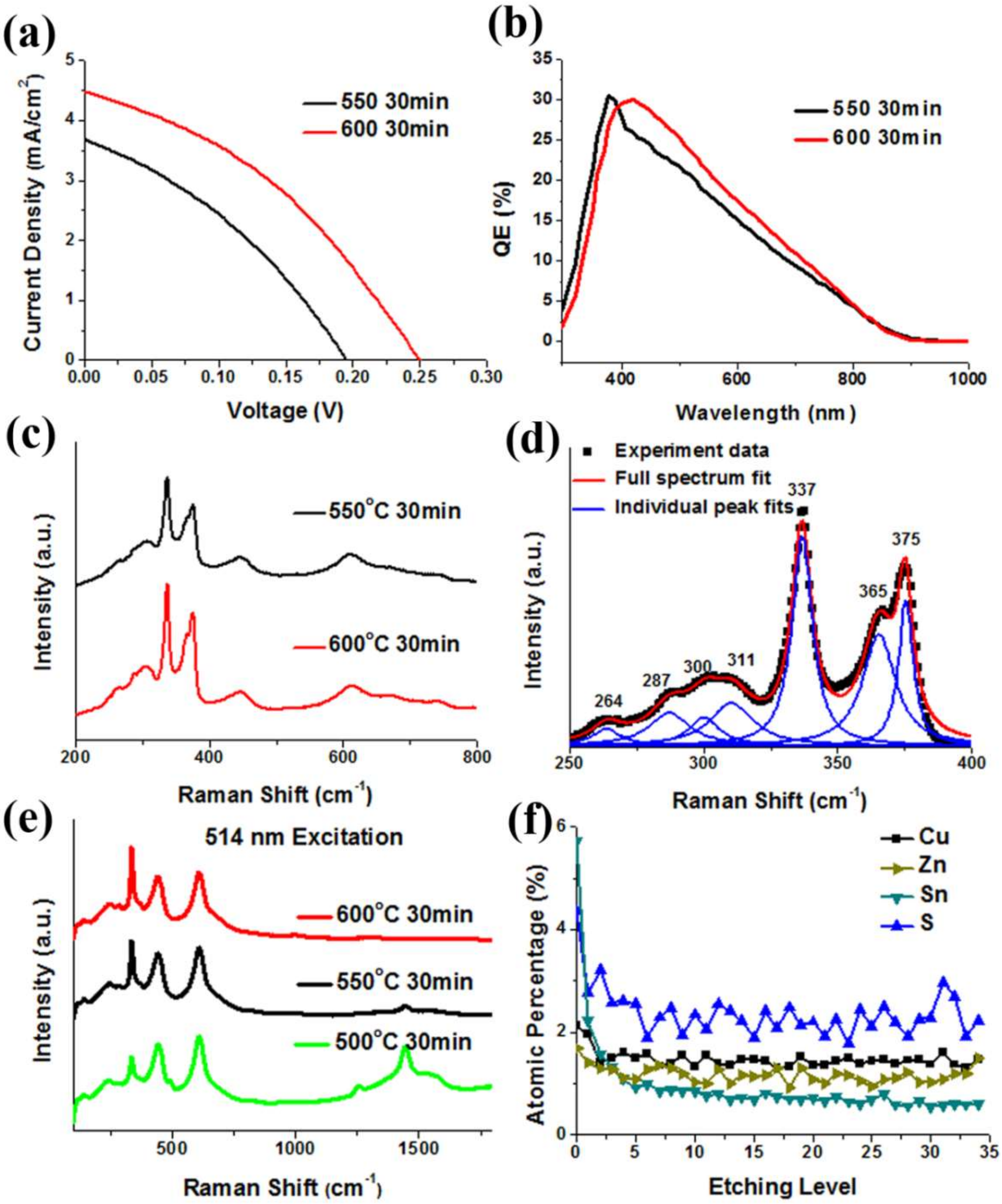

Figure 6.5. a) J-V curves of TNR 2 based CZTS sensitized film annealed at 550 °C and 600 °C for 30 min and b) their IPCE and c) Raman spectra at 785 nm laser excitation. d) High resolution spectrum fitting of the Raman spectrum of the 600 °C annealed film; e) Raman spectra at 514 nm laser excitation; f) XPS depth profile of the CZTS/TNR film annealed at 600 °C for 30 min showing only Cu, Zn, Sn and S.

To have a better understanding of the CZTS spatial distribution on the TNR three-dimensional scaffold, XPS depth profile was performed by using 3 keV Ar ion gun to etch through the CZTS/TNR film annealed at 600 °C. Figure D.3 shows the spatial element distribution of all six elements of CZTS and $TiO_2$, from which it can be seen the fraction of CZTS to $TiO_2$ is significantly low. To have a better view the range where it has only Cu, Zn, Sn and S is selected and magnified as shown in Figure 6.5f. As it can be seen, homogeneous CZTS distribution and the desired copper-poor zinc-rich composition have been achieved, which can be attributed to the clear solution spin-coating technique adopted in this work.

XPS high resolution spectra were also collected to study the effect of annealing temperature on the surface of CZTS/TNR, as the nanoscale region near the semiconductor surface is considered to have the most impact on its optoelectronic response. In Figure D.4 the Cu 2p and Zn 2p core line spectra show the tendency of peak shifting to a lower binding energy, which could be due to the change of element chemical states after higher temperature annealing. The broadening of O 1s peak to the left in comparison to the pure TNR (refer to Figure D.5c) is also observed, indicating that possibly additional oxides other than $TiO_2$ having been formed upon annealing. To verify this possibility, quantitative information of the surface element composition is extracted and plotted into Figure 6.6, where the pure TNR was added as reference. All elements are displayed in their ratio to titanium in Figure 6.6a, from which it can be noticed that the oxygen level is much higher than that of pure $TiO_2$ nanorods. When only plotting the fraction of Cu, Zn, Sn and S elements in Figure 6.6b, it is seen that sulfur has experienced significant loss with elevated annealing temperature especially at 600 °C this expected given the volatility of S. But surprisingly, the tin fraction was found to have been dramatically increased with annealing temperature. Therefore, it is reasonable to attribute the additional oxygen and tin content to the formation of $SnO_2$ impurity on the surface of $TiO_2$. In other words, it becomes evident that although the higher annealing temperature contributes to complete reaction and better crystallinity on one hand on the other it has a negative effect in terms of surface oxidation. To further investigate and ultimately control the parasitic surface oxidation, annealing tests at different times at 600 °C from 5 min to 120 min were performed and details are provided in Appendix D, where 30 min is deemed the right annealing time in lowering the carbon residual content and avoiding significant loss of sulfur, or tin oxide impurity formation.

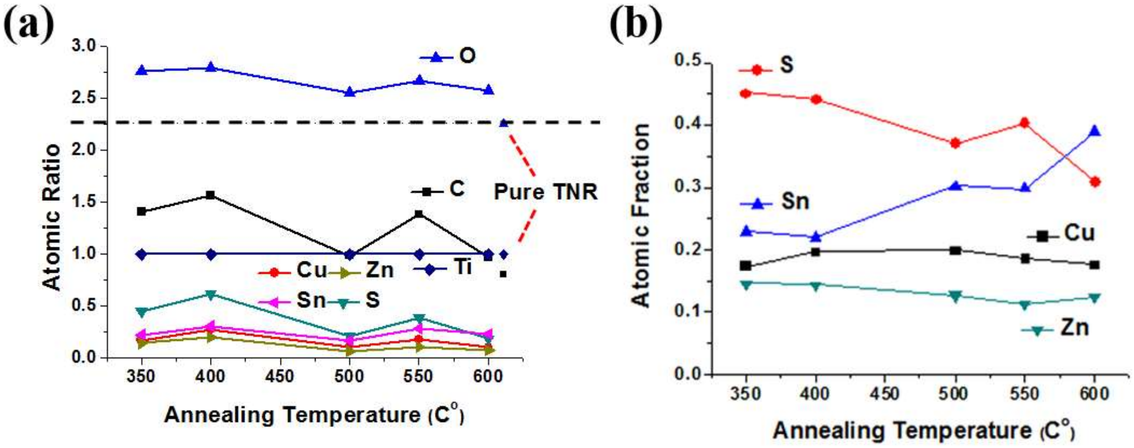

Figure 6.6. XPS quantitative analysis of the CZTS/TNR film (annealed at 600 °C) surface by a) calculating the annealing temperature dependent ratio of all the other elements to titanium and b) annealing temperature dependent composition change of CZTS.

### 6.4.5 The composition effect on solar cell performance

It is generally accepted by the thin film CZTS photovoltaic community that a copper-rich, zinc poor composition is favorable towards better optoelectronic performance.[31] As a different device configuration applied here, the composition effect on the CZTS/TNR photoelectrode should be understood as well. Therefore, the films have been prepared by varying the composition of the spin-coated precursor solution. To ensure reliable reproducibility each coating condition involved fabrication of four cells. The results are shown in Figure 6.7 and Figure D.11. The best performing device with an efficiency of ~0.4% was obtained with a solution containing 0.09 M $CuCl_2$, 0.06 M $ZnCl_2$, and 0.07 M $SnCl_2$ with fixed thioacetamide concentration of 0.4 M. However, when the ratio of Cu/Zn is increasing and getting close to the stoichiometric composition of $Cu_2ZnSnS_4$, the efficiency drops dramatically.

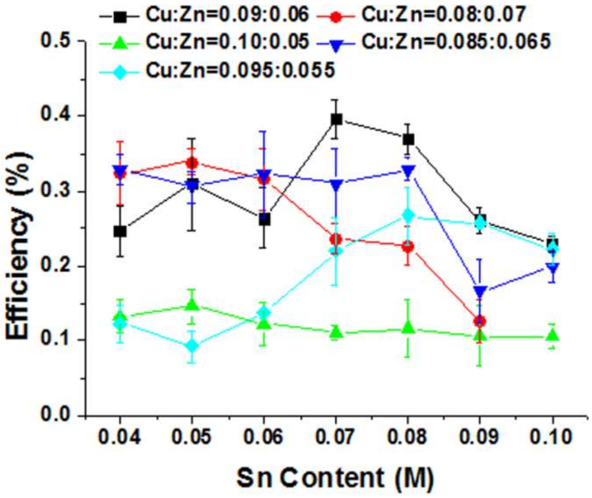

Figure 6.7. Composition dependent solar cell device efficiency chart.

To have a better understanding of the composition effect, ICP-OES was performed on the *aqua regia* digested CZTS/TNR film samples, and plotted the composition dependent efficiency contour in Figure D.12a. The contour has been divided into five regions according to the ratio range of Cu/Zn. When the tin content was kept at an optimal content, Cu poor Zinc rich (Cu/Zn~1.4~1.9) sensitized films fall into the efficiency "hot" zone, while too much copper will lead to dramatic efficiency decrease. This is explained by the 785 nm laser excited Raman spectra of the five different groups shown in Figure D.12b to D.12f. For the copper-rich, zinc-poor composition, their Raman spectra always show an almost pure CZTS crystalline phase, while when it gets closer to the stoichiometric, another peak centered at ~318 cm$^{-1}$ shows up and gets strengthened when the composition becomes copper-rich. This peak is identified to belong to the undesirable copper tin sulfide (CTS) [32] secondary phase. Therefore, a copper-poor zinc-rich composition is still preferred in our CZTS/TNR structure as it can prevent the formation of CTS impurity.

### 6.4.6 Electron microscope analysis of the CZTS/TiO$_2$ heterostructure

Scanning Electron Microscopy (SEM) was used to study the morphology features of the CZTS/TNR electrode. Figure D.13 shows the low-magnification SEM images of pure TNR (Figure D.13a,b) and CZTS/TNR composite film (Figure D.13c,d). As an atomic number contrast sensitive technique, BSE images can distinguish the phase separation with high resolution. In Figure D.13b the contrast is homogeneous, indicating a pure $TiO_2$ phase for the TNR film, while in Figure D.13d it is much brighter on the gap/edge of the nanorods, indicating a different phase with higher average atomic number being coated. This higher contrast phase could be CZTS due to its much higher overall atomic number than $TiO_2$. High resolution SEM images of the 4-face elongated nanorods are shown in Figure 6.8, where detailed morphology features of this brighter phase are revealed. From Figure 6.8a and 6.8b it can be seen clearly the CZTS nanocrystallites to have preferentially grown along the meeting edge of neighboring nanorods as dictated by the classical "terrace-step-kink" surface crystallization model[33]. Via the higher zoom-in views provided in Figure 6.8c and 6.8d it can be seen the CZTS nanocrystallites to have grown to a few to tens of nanometers in size. It seems the clear-solution coating method has favored multiple nucleation events along the meeting edge of neighboring nanorod planes hence the appearance of CZTS coating as an assembly of inter-connected nanoparticles bonded to TNR film ridges.

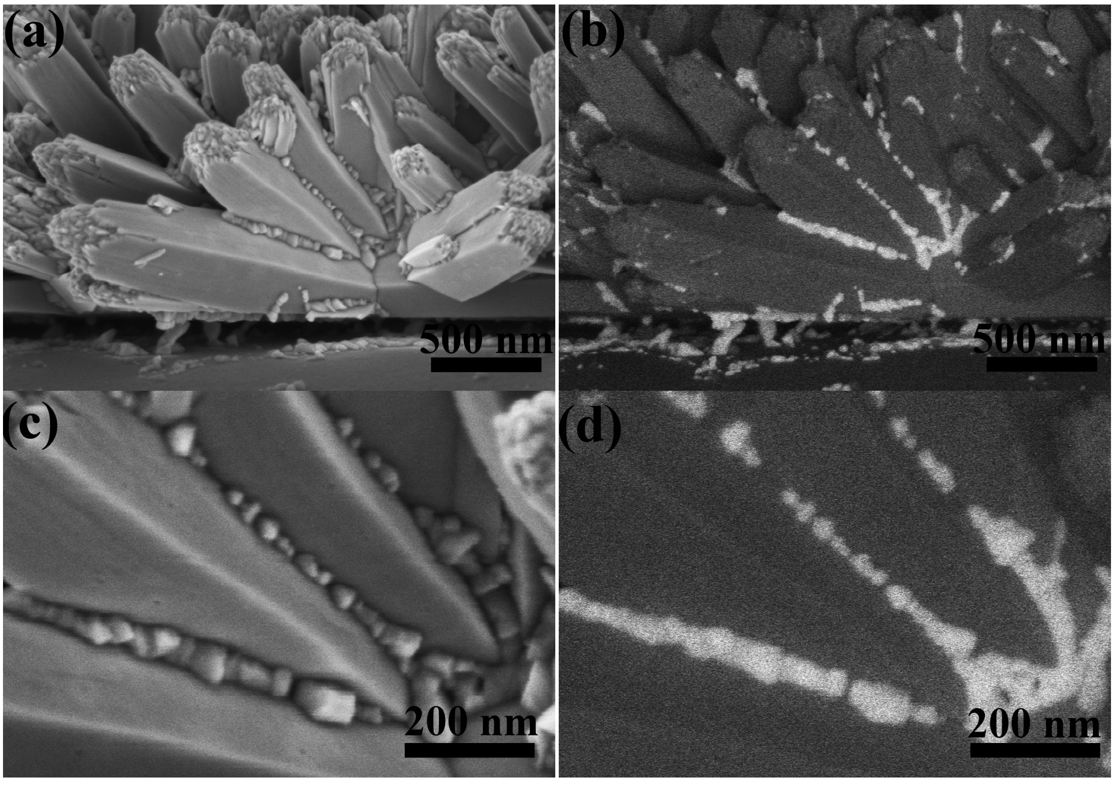

Figure 6.8. a,c) SEM Secondary Electron (SE) and b,d) Backscatter Electron (BSE) images of angled view CZTS nanocrystallites coated on TNR film.

In order to confirm the brighter BSE phase to be CZTS, EDS was performed. As shown in Figure 6.9, Cu, S, Zn and Sn are found to have the same spatial distribution with those high contrast nanocyrstallites. Therefore, the film is proven to be constituted of CZTS nanocrysallites (a few to tens of nanometers) deposited on $TiO_2$ nanorods (hundreds of nanometers) as proposed. Further, the focused ion beam (FIB) method was applied to prepare a cross-section that was characterized by SEM as shown in Figure D.14. An overlayer of conductive carbon was deposited on top of the film to facilitate FIB cutting as evident in Figure 6.10b. In general the nanorods are slightly tilted and well aligned on FTO substrate, and the small nanoparticles with higher BSE contrast are visibly located on the edge of each rod. A mixed EDS mapping was also performed and depicted in Figure 6.11a, where the orange colour represents S, blue represents Ti and bright yellow represents Sn. Hence the uniform distribution of S on the TNR scaffold can be clearly seen. Sn is mainly concentrated on the substrate as it is the composition of FTO layer. From the individual element maps in Figure D.15, Cu, Zn, Sn and S are concentrated at same location, meaning S can be used to represent CZTS in Figure 6.10a.

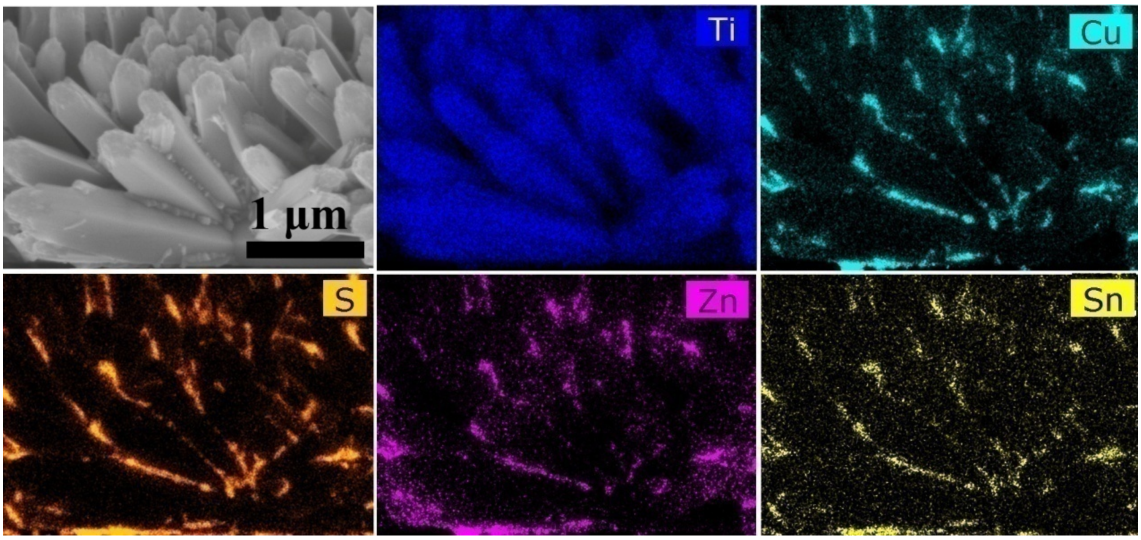

Figure 6.9. EDS maps of CZTS nanocrystallites coated on TNR film.

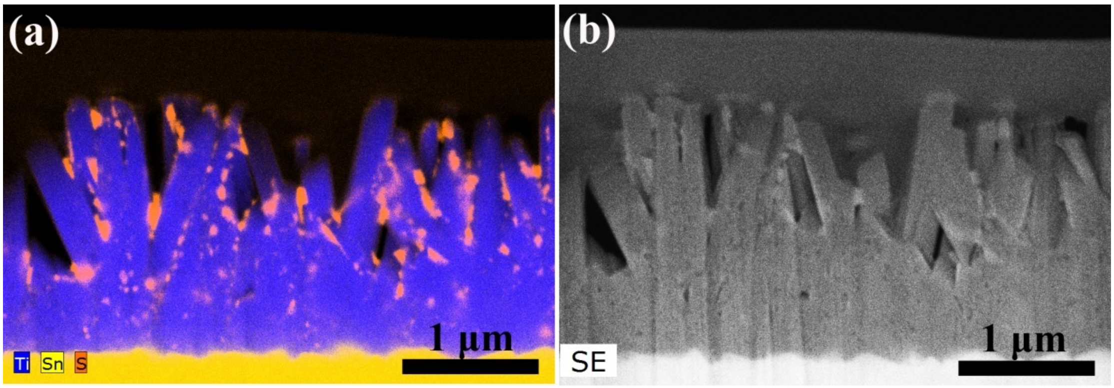

Figure 6.10. a) EDS mixed map and b) SEM image of FIB prepared CZTS/TNR cross section.

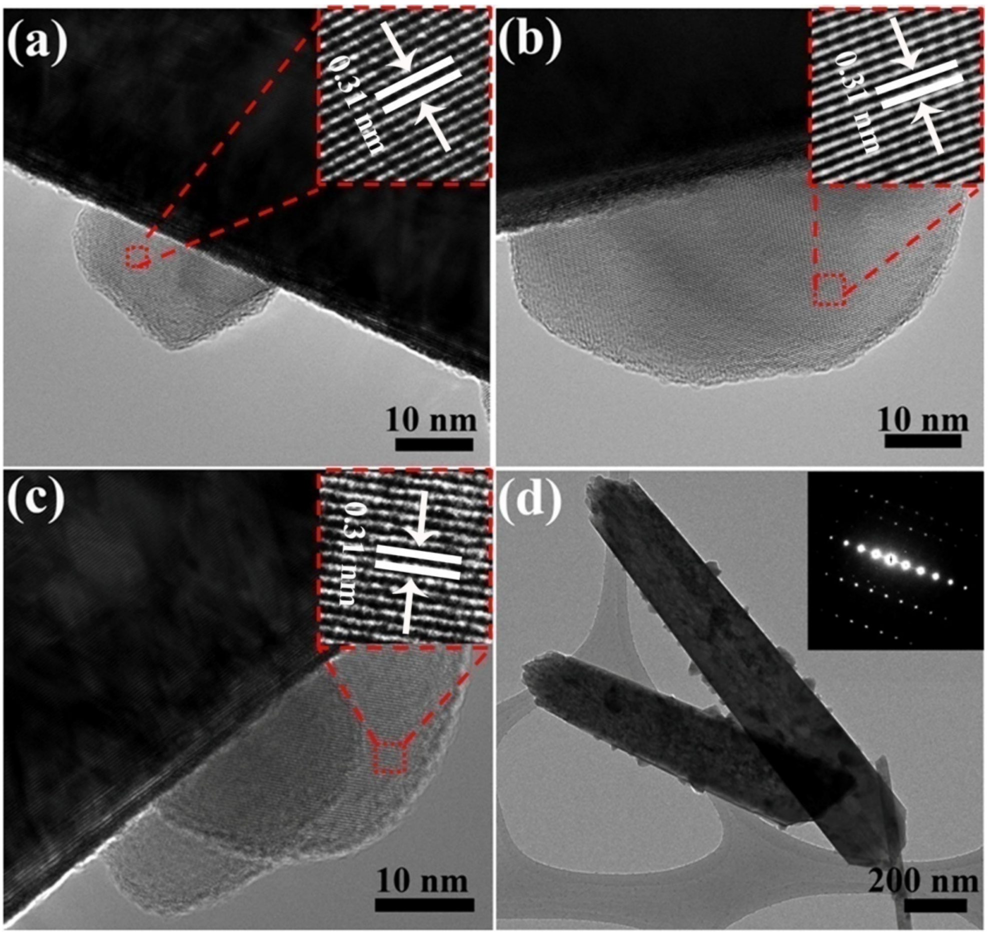

Figure 6.11. a, b, c) High resolution bright field TEM images of CZTS nanocrystallites on TNR; insets show the highly magnified area of CZTS crystallites with marked interplanar lattice distance; and d) low magnification image of CZTS/TNR structure with the SAED pattern shown as inset.

Detailed nanoscale features of the CZTS deposit on TNR are further revealed with high resolution TEM imaging in Figure 6.11. Three different locations where the nanorod coexists with CZTS crystals were selected. The good physical contact can be seen in all cases between CZTS and TNR, which could indicate a clear pathway for the generated photoelectrons. The interplanar lattice distance of all three crystallites in these images is of a similar value of ~0.31 nm, which represents the dominant kesterite CZTS (112) plane. Figure 6.11d shows a low magnification TEM image of a two stand-alone nanorods coated with CZTS crystallites. The inset shows the selected area electron diffraction (SAED) image from this region where the bright dots correspond to the diffraction pattern of the rutile phase of which the nanorods are made.

### 6.4.7 Two layer coating and surface etching

So far the effectiveness of the solution coating method has been demonstrated in preparing well-distributed CZTS nanocrystallites throughout the TNR network with reasonable photovoltaic response. To improve light absorption by the photoelectrode hence its PV performance, a "double layer" coating procedure was performed aiming at higher CZTS loading onto the TNR network. To this end after spin coating, the film was subjected to a short duration (5 min) pre-annealing step at 600 °C (10 °C/min ramping rate with presence of S and Sn powder) under the Sn/S inert atmosphere, and then applied another solution coating layer following by regular annealing at 600 °C for 30 min. This strategy proved effective as seen in Figure 6.12 and Table 6.4 data, where 1L stands for the one layer coated photoanode and 2L NE means "double layer" coated photoanode without additional treatment. Double layer coating with intermittent annealing led to significant enhancement in photocurrent density (from 4.2 mA/cm$^2$ to 6.3 mA/cm$^2$) that matches the enhanced light absorption and EQE spectral response in correspondence to increased CZTS loading. Meanwhile there was no improvement in $V_{oc}$ or FF. Hence the improved efficiency from 0.41 % to 0.56 % (Table 6.4) can be solely attributed to the double-layer's enhanced light absorbing ability.

Table 6.4. Solar cell performance of CZTS/TNR photoanodes prepared following different protocols

| Photoanode | Efficiency (%) | FF (%) | $J_{sc}$ (mA/cm$^2$) | $V_{oc}$ (mV) |
|---|---|---|---|---|
| 1L | 0.41 | 39.3 | 4.2 | 247 |
| 2L NE | 0.56 | 35.1 | 6.3 | 253 |
| 2L E-1h | 0.63 | 35.0 | 7.0 | 261 |
| 2L E-5h | 0.67 | 37.0 | 7.1 | 256 |
| 2L E-18h | 0.67 | 35.7 | 7.3 | 259 |

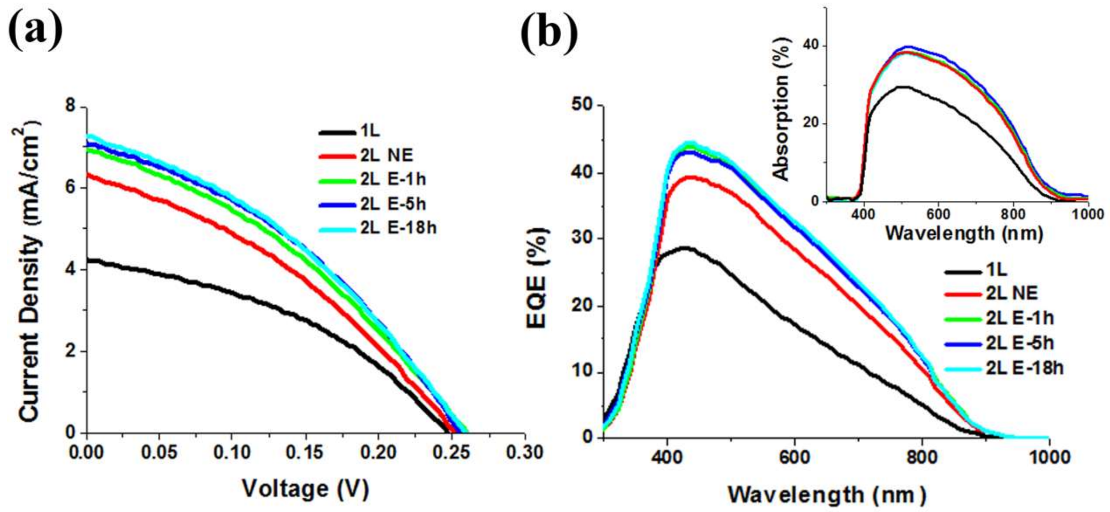

Figure 6.12. a) J-V characteristics and b) IPCE spectra of one-layer and two-layer spin-coated/annealed CZTS/TNR photoanodes with different acidic surface treatment. Inset of b) shows the light absorption spectra of CZTS after excluding the TNR.

As our solution deposition approach aimed at a copper-poor zinc-rich composition CZTS nanocoating, there is risk of some ZnS co-deposition as impurity, which could cause photocurrent loss as it forms “cold” spots.[34] To ensure removal of such ZnS spots, the film was subjected to HCl etching initially developed by Fairbrother et al.[35] and lately applied by our group into CZTS-$TiO_2$ mesoporous film[14]. Four groups of photoanode samples were post-treated with 4 M HCl solution for variable times (0h, 1h, 5h and 18h) and named as 2L NE, 2L E-1h, 2L E-5h and 2L E-18h. Results in Figure 6.12 show an enhancement of their photocurrent density. According to Table 6.4, the $J_{sc}$ increases to over 7 mA/cm$^2$ after only 1h HCl etching and the efficiency is improved to 0.63%. There was no noticeable improvement after etching for longer time neither deterioration proving HCl treatment for 1h to be sufficient. From XPS high resolution core line spectroscopy in Figure D.16, as expected, there is a sharp decrease of the Zn and S 2p signal after 1h etching while not much change was found for Cu. Surprisingly, a significant decrease of Sn peak after etching and a slight O signal reduction on the left shoulder of its main peak can be noticed. The reduced oxygen shoulder is attributed to Sn-O bond as discussed before. Therefore, it is concluded that HCl can also help to reduce the $SnO_2$ impurity once formed. Further applying another layer of coating followed by 5h HCl etching (3L E-5h) has also been tried in order to increase the light absorption of photoanode. Although the $J_{sc}$ of the device slightly increased (Figure D.17a) as well as the EQE and light absorption (Figure D.17b), the FF has been greatly reduced which leads to no net gain of efficiency. This is concluded to be due to the subsequently increased interface recombination as more CZTS being introduced. Therefore, a careful study of CZTS-$TiO_2$ interface becomes important to enable the design of fully functioning devices.

### 6.4.8 Band alignment of CZTS nanocoating and rutile $TiO_2$ nanorods

The CZTS/TNR photoanode design aims at injecting the photogenerated electrons from light absorbing CZTS nanocrystallites to $TiO_2$ nanorods; this one-direction path is only feasible when the conduction band bottom energetic level of CZTS is higher than that of rutile.[36] Previous studies have reported a positive injection overpotential when the energetic levels of the conduction band of the pure CZTS and $TiO_2$ are at equilibrium state.[1, 3, 16] However, an important fact that has not been assessed is the energy band re-alignment taking place after new interface is formed. Also, different synthesis/deposition/annealing methods could lead to different energy band structure, hence the experimental investigation of CZTS/TNR interfacial energy band alignment was undertaken. Here we report the use of high-resolution XPS to determine the band offsets of CZTS/TNR interface based on core level shifts, adopting the method by Scanlon et al.[37] The binding energy difference between the Ti $2p_{3/2}$

core line and the valence band was first determined in samples of pure rutile nanorods on FTO glass, and the same was done for Cu $2p_{3/2}$ in as-prepared CZTS. Further the core-line offset was determined by the peak position difference of Ti $2p_{3/2}$ and Cu $2p_{3/2}$ for the CZTS/TNR composite. Details are provided in Appendix D.

The XPS-determined band offset of CZTS/TNR interface in shown in Figure 6.13. The positive overpotential of CZTS to TNR is beneficial in supplying enough driving force to facilitate electron injection from CZTS to TNR. However, the conduction band of $TiO_2$ is too close to the valence band of CZTS. This unfavorable alignment could induce significant open-circuit voltage deficit, [36] which explains the low $V_{oc}$ being obtained in this study. Also, the injected photoelectron in the conduction band of rutile could be easily re-captured by the holes left in CZTS with this band structure. Therefore, proper interface engineering/passivation is required for the full potential of CZTS/TNR heterostructure in optoelectronic applications to be realized, which will be addressed in the next section.

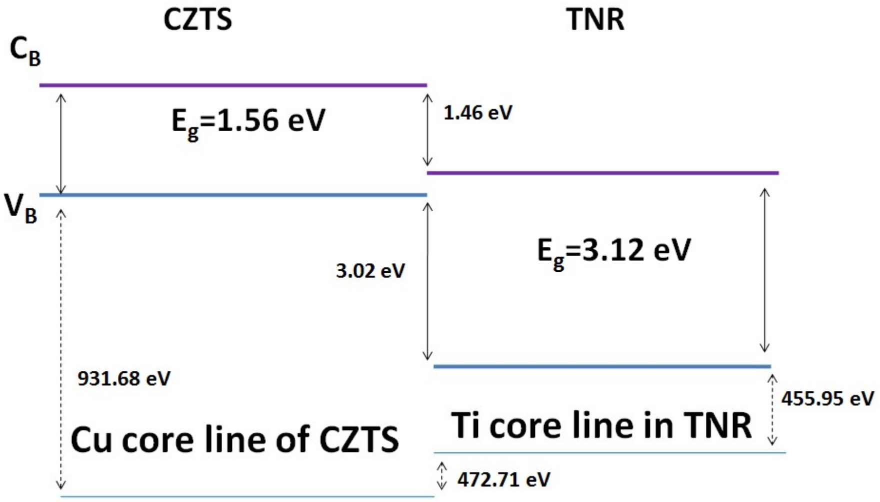

Figure 6.13. Band alignment of CZTS and TNR interface using XPS.

### 6.4.9 Solid state device and interface

As being stated in the previous chapter, the stability/compatibility of CZTS in contact with the $I^-/I_3^-$ electrolyte is an open question, in fact, this polar solvent electrolyte designed for dye-sensitized solar cells has been found to be corrosive to many light absorber materials like inorganic quantum dots[38] and perovskite[39], causing a rapid deterioration to the device performance. Therefore, a solid state electrolyte or hole transfer material (HTM) is preferable. 2,2′,7,7′-tetrakis(N,N-p-dimethoxy-phenylamino)-9,9′-spirobifluorene (spiro-OMeTAD) has been used in solid state dye-sensitized solar cells and the recent impressive perovskite solar cells, hence selected to be tested in the present system too (with gold as back contact).

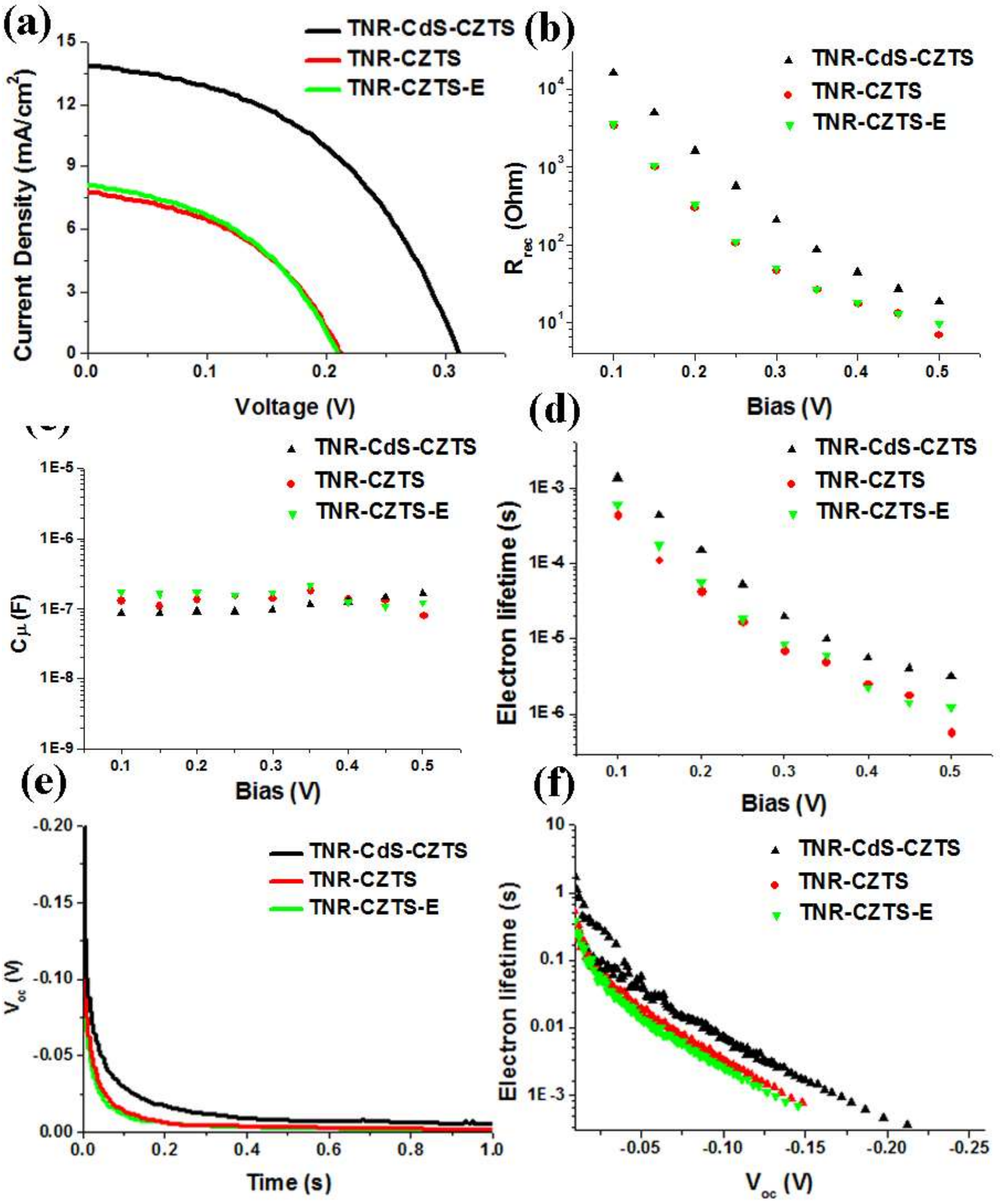

Figure 6.14. Characteristics of three all-solid-state TNR-CZTS devices: a) J-V curves, b) recombination resistances ($R_{rec}$), c) chemical capacitances ($C_{\mu}$), and d) electron lifetimes extracted from EIS Nyquist plots under reverse bias 0.1V-0.5V; e) open-circuit voltage decay (OCVD) plots and f) extracted electron lifetimes during the dynamic process.

Firstly, the HCl etching effect was re-investigated by fabricating the electrode after 5 h acid treatment named “TNR-CZTS-E”. The photovoltaic response can been seen in Figure 6.14a, where nearly identical J-V curves were measured for TNR-CZTS and TNR-CZTS-E. Though a slight increase of photocurrent after HCl treatment concords with the result from liquid state device (Table 6.5), it is too small to have impact on the overall conversion efficiency (~ 0.75 %), indicating that impurities like ZnS and $SnO_2$ are not interfering when the spiro-OMeTAD solid state electrolyte in lieu of the liquid one.

Table 6.5. Solar cell performance of solid state devices

| Photoanode | Efficiency (%) | FF (%) | $J_{sc}$ (mA/cm$^2$) | $V_{oc}$ (mV) |
|---|---|---|---|---|
| TNR-CdS-CZTS | 2.00 | 46.2 | 13.9 | 312 |
| TNR-CZTS | 0.74 | 44.5 | 7.8 | 213 |
| TNR-CZTS-E | 0.75 | 43.9 | 8.1 | 210 |

The above TNR-CZTS and TNR-CZTS-E device results featuring the spiro-OMeTAD solid electrolyte are encouraging by comparison to the corresponding liquid junction device (0.75% vs. 0.67 % efficiency). However, the performance of this proof-of-concept device is still far from being satisfactory. The XPS characterization (Figure 6.13) demonstrated an unfavorable energy band position at the $TiO_2$/CZTS interface. Thus a buffer layer was introduced at the interface to overcome losses due to high impedance. In analogy to CZTS thin film solar cells, where CdS is used for this purpose this buffer layer was chosen to be tested in order to facilitate charge transfer and reduce interface recombination[40]. CdS was applied by chemical bath deposition on TNR before the coating of the latter with CZTS precursor layer. The complete device architecture is depicted in Figure D.21. The solar cell made with the TNR-CdS-CZTS photoelectrode showed a significant improvement in both $J_{sc}$ and $V_{oc}$, leading to an overall energy conversion efficiency of 2.0 % (Table 6.5). To further verify that the performance differences among the three devices arise at the TNR/CZTS interface , EIS analysis was carried out on them under dark condition. The Nyiquist plots under bias of 0.1 V ~ 0.5 V are shown in Figure D.22, while the equivalent circuit as shown in Figure D.2 is used to extract the recombination resistances ($R_{rec}$) presented in Figure 6.14b. The significantly enhanced $R_{rec}$ due to the introduced CdS buffer layer, as can be directly deduced from Figure D.22e, is believed to contribute to the reduced recombination rate and hence the improved photovoltaic performance. The reduced dark current in Figure D.22a also confirms the improved device quality after the introduction of the buffer layer. Consequently, the electron lifetime ($\tau = R_{rec}C_{\mu}$) has been extended - as there is no apparent change of the chemical capacitance ($C_{\mu}$), leading to a better functioning device. Similar trend was obtained with the open-circuit voltage decay (OCVD) measurements (Figure 6.14e and 6.14f), reconfirming the validity of the EIS results. The devices of TNR-CZTS and TNR-CZTS-E showed almost the same value of τ from EIS and identical trend of OCVD, which means HCl etching (or removal of the ZnS and $SnO_2$ impurities ) has almost no impact on the recombination process of these solid-state devices.

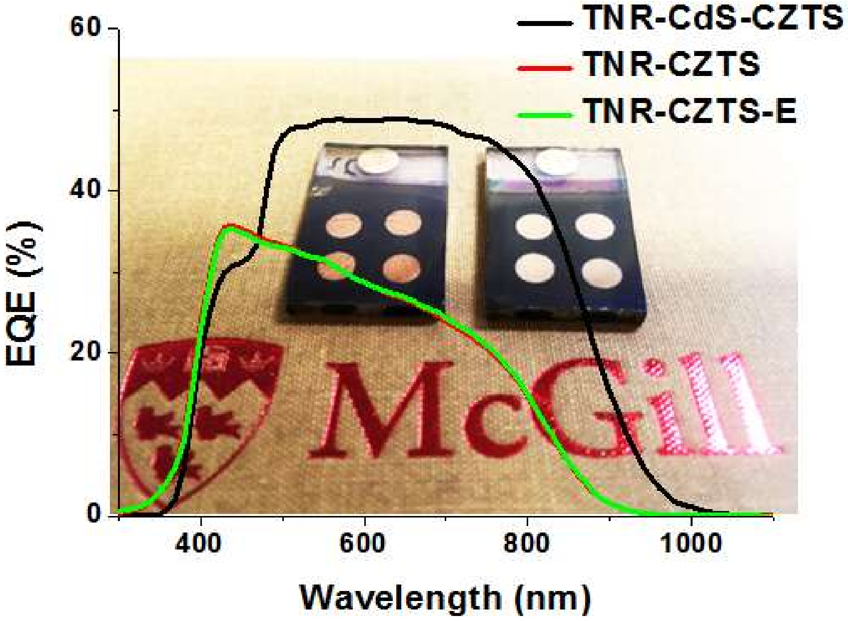

Figure 6.15. External quantum efficiency (EQE) measurement of the three solid state devices and photographic images of the complete TNR-CZTS devices with (right) and without (left) CdS buffer layer.

IPCE measurements were also made to understand the origin of the observed $J_{sc}$ improvement. As it can be seen in Figure 6.15, different IPCE profile was found after adding the CdS buffer layer. The reduced interfacial recombination rate/increased electron lifetime leads to more efficient charge transfer/collection process, which contributes to the greatly improved EQE value in the visible range. However, for the CdS containing device, a noticeable difference can be seen at 420 ~ 460 nm wavelength where a lower EQE is found and a sharp increase occurs afterwards. This efficiency loss at short wavelength range is attributed to the CdS window layer which blocks part of light that should have been absorbed by CZTS.[41] To further verify this effect, the light absorption spectra of both CZTS and CdS-CZTS were captured and are shown in Figure D.22f, where extra light absorption is seen at short wavelength range (420 ~460 nm) after CdS deposition in comparison to the film of CZTS alone (in both cases the contribution of $TiO_2$ was subtracted), agreeing well with the range of inefficient photon-electron conversion from EQE measurement. Therefore, though CdS layer helps to largely reduce interface recombination, its visible light absorbing property partially affects the amount of photons captured by CZTS. From 500 nm to 700 nm where the most energy of the solar spectrum is contained, Figure D.22f shows almost the same light absorption for the photoanodes with and without CdS layer; this suggests that the enhanced EQE of TNR-CdS-CZTS sample in this range can be attributed to more efficient electron injection/collection instead of any optical benefits from CdS itself. Another noteworthy phenomenon is the spectrum broadening of both IPCE and optical absorption after incorporating CdS, leading to a narrowing of absorber bandgap from 1.51 eV to 1.37 eV. According to a previous study, it is reasonable to attribute this result partial Cd substitution of Zn during the thermal treatment.[41-42] This cation substitution is found to lower the bandgap of CZTS having as consequence improved photocurrent generation by extending the light absorption range to nearly infrared region.

In summary, the CdS layer is proven to effectively reduce the interface recombination and broaden the light absorption range, enabling the solid state functioning device to yield an efficiency of 2 %.

## 6.5 Conclusion

In this chapter, a clear solution spin-coating method combined with controlled annealing has been developed to directly grow CZTS nanocrystallites on $TiO_2$ nanorod (TNR)-structured film investigated as photoanodes. The homogeneous composition of CZTS nanocoating and its uniform spatial distribution within the TNR forest film demonstrates the superiority of this clear solution deposition method. The PV performance of the CZTS/TNR photoanodes has been improved in a liquid junction sensitized cell configuration by studying in depth the effects of rutile nanorod growth, annealing temperature and time, compostion, double layer coating, HCl etching, and eventually realized the solid state device via applying spiro OMeTAD as hole transfer material. Furthermore, the first experimental study of the band alignment of CZTS and rutile interface has been performed *via* XPS, which provides valuable insight as to the possible reason for the significant $V_{oc}$ deficit. In light of this insight, CdS was tested as buffer layer achieving to significantly suppress interfacial recombination. In conclusion, this work via the systematic examination of processing and nanoscale heterostructure effects on the semiconductor-sensitized photoanode, has achieved to raise the device conversion efficiency from an initial ~0.1 % to ~2.0 %, providing a valuable reference for further development of CZTS-$TiO_2$ optoelectronic devices.

## 6.6 References

1. Wang, Y.; Li, C. X.; Yin, X. J.; Wang, H.; Gong, H., $Cu_2ZnSnS_4$ (CZTS) Application in $TiO_2$ Solar Cell as Dye. *ECS Journal of Solid State Science and Technology* **2013,** *2* (7), Q95-Q98.

2. Jiang, M.; Wu, J.; Di, G.; Li, G., Nanostructured Solar Cell Based on Solution Processed $Cu_2ZnSnS_4$ Nanoparticles and Vertically Aligned ZnO Nanorod Array. *physica status solidi (RRL) – Rapid Research Letters* **2014,** *8* (12), 971-975.

3. Bai, B.; Kou, D.; Zhou, W.; Zhou, Z.; Tian, Q.; Meng, Y.; Wu, S., Quaternary $Cu_2ZnSnS_4$ Quantum Dot-Sensitized Solar Cells: Synthesis, Passivation and Ligand Exchange. *Journal of Power Sources* **2016,** *318*, 35-40.

4. Romanyuk, Y. E.; Fella, C. M.; Uhl, A. R.; Werner, M.; Tiwari, A. N.; Schnabel, T.; Ahlswede, E., Recent Trends in Direct Solution Coating of Kesterite Absorber Layers in Solar Cells. *Solar Energy Materials and Solar Cells* **2013,** *119* (0), 181-189.

5. Wang, W.; Winkler, M. T.; Gunawan, O.; Gokmen, T.; Todorov, T. K.; Zhu, Y.; Mitzi, D. B., Device Characteristics of CZTSSe Thin-Film Solar Cells with 12.6 % Efficiency. *Advanced Energy Materials* **2013**, 1301465.

6. Haass, S. G.; Diethelm, M.; Werner, M.; Bissig, B.; Romanyuk, Y. E.; Tiwari, A. N., 11.2% Efficient Solution Processed Kesterite Solar Cell with a Low Voltage Deficit. *Advanced Energy Materials* **2015,** *5* (18), 1500712.

7. Fella, C. M.; Uhl, A. R.; Romanyuk, Y. E.; Tiwari, A. N., $Cu_2ZnSnSe_4$ Absorbers Processed from Solution Deposited Metal Salt Precursors under Different Selenization Conditions. *physica status solidi (a)* **2012,** *209* (6), 1043-1048.

8. Sun, Y.; Zong, K.; Zheng, H.; Wang, H.; Liu, J.; Yan, H.; Zhu, M., Ethylene Glycol-Based Dip Coating Route for the Synthesis of $Cu_2ZnSnS_4$ Thin Film. *Materials Letters* **2013,** *92*, 195-197.

9. Tanaka, K.; Oonuki, M.; Moritake, N.; Uchiki, H., Thin Film Solar Cells Prepared by Non-Vacuum Processing. *Solar Energy Materials and Solar Cells* **2009,** *93* (5), 583-587.

10. Fischereder, A.; Rath, T.; Haas, W.; Amenitsch, H.; Albering, J.; Meischler, D.; Larissegger, S.; Edler, M.; Saf, R.; Hofer, F.; Trimmel, G., Investigation of $Cu_2ZnSnS_4$ Formation from Metal Salts and Thioacetamide. *Chemistry of Materials* **2010,** *22* (11), 3399-3406.

11. Masato, K.; Kunihiko, T.; Katsuhiko, M.; Hisao, U., Fabrication of Three-Dimensional-Structure Solar Cell with $Cu_2ZnSnS_4$. *Japanese Journal of Applied Physics* **2012,** *51* (10S), 10NC33.

12. Park, S.-N.; Sung, S.-J.; Sim, J.-H.; Yang, K.-J.; Hwang, D.-K.; Kim, J.; Kim, G. Y.; Jo, W.; Kim, D.-H.; Kang, J.-K., Nanostructured P-Type CZTS Thin Films Prepared by a Facile Solution Process for 3D P-N Junction Solar Cells. *Nanoscale* **2015,** *7* (25), 11182-11189.

13. Dongwook, L.; Kijung, Y., Solution-Processed $Cu_2ZnSnS_4$ Superstrate Solar Cell Using Vertically Aligned ZnO Nanorods. *Nanotechnology* **2014,** *25* (6), 065401.

14. Wang, Z.; Demopoulos, G. P., Nanoscale Photo-Absorbing Kesterite Grown on Anatase Mesoscopic Films by Sequential Binary Chalcogenide Solution Deposition-Exchange, Annealing, and Etching. *Crystal Growth & Design* **2016**, *16* (7), 3618–3630

15. Liu, F.; Yan, C.; Huang, J.; Sun, K.; Zhou, F.; Stride, J. A.; Green, M. A.; Hao, X., Nanoscale Microstructure and Chemistry of $Cu_2ZnSnS_4$/CdS Interface in Kesterite $Cu_2ZnSnS_4$ Solar Cells. *Advanced Energy Materials* **2016,** *6* (15), 1600706.

16. Wang, Z.; Demopoulos, G. P., Growth of $Cu_2ZnSnS_4$ Nanocrystallites on $TiO_2$ Nanorod Arrays as Novel Extremely Thin Absorber Solar Cell Structure via the Successive-Ion-Layer-Adsorption-Reaction Method. *ACS Applied Materials & Interfaces* **2015,** *7* (41), 22888-22897.

17. Wang, Z.; Wang, H.; Liu, B.; Qiu, W.; Zhang, J.; Ran, S.; Huang, H.; Xu, J.; Han, H.; Chen, D.; Shen, G., Transferable and Flexible Nanorod-Assembled $TiO_2$ Cloths for Dye-Sensitized Solar Cells, Photodetectors, and Photocatalysts. *ACS Nano* **2011,** *5* (10), 8412-8419.

18. Aftab Akram, M.; Javed, S.; Islam, M.; Mujahid, M.; Safdar, A., Arrays of CZTS Sensitized ZnO/ZnS and ZnO/ZnSe Core/Shell Nanorods for Liquid Junction Nanowire Solar Cells. *Solar Energy Materials and Solar Cells* **2016,** *146*, 121-128.

19. (a) Just, J.; Lützenkirchen-Hecht, D.; Frahm, R.; Schorr, S.; Unold, T., Determination of Secondary Phases in Kesterite $Cu_2ZnSnS_4$ Thin Films by X-Ray Absorption Near Edge Structure Analysis. *Applied Physics Letters* **2011,** *99* (26), 262105; (b) Hou, Y.; Azimi, H.; Gasparini, N.; Salvador, M.; Chen, W.; Khanzada, L. S.; Brandl, M.; Hock, R.; Brabec, C. J., Low-Temperature Solution-Processed Kesterite Solar Cell Based on in Situ Deposition of Ultrathin Absorber Layer. *ACS Applied Materials & Interfaces* **2015,** *7* (38), 21100-21106; (c) Fella, C. M.; Romanyuk, Y. E.; Tiwari, A. N., Technological Status of $Cu_2ZnSn(S,Se)_4$ Thin Film Solar Cells. *Solar Energy Materials and Solar Cells* **2013,** *119* (0), 276-277.

20. Wang, Z.; Ran, S.; Liu, B.; Chen, D.; Shen, G., Multilayer $TiO_2$ Nanorod Cloth/Nanorod Array Electrode for Dye-Sensitized Solar Cells and Self-Powered UV Detectors. *Nanoscale* **2012,** *4* (11), 3350-3358.

21. Zhao, K.; Pan, Z.; Mora-Seró, I.; Cánovas, E.; Wang, H.; Song, Y.; Gong, X.; Wang, J.; Bonn, M.; Bisquert, J.; Zhong, X., Boosting Power Conversion Efficiencies of Quantum-Dot-Sensitized Solar Cells Beyond 8% by Recombination Control. *Journal of the American Chemical Society* **2015,** *137* (16), 5602-5609.

22. Wang, Z.; Elouatik, S.; Demopoulos, G. P., Understanding the Phase Formation Kinetics of Nano-Crystalline Kesterite Deposited on Mesoscopic Scaffolds via in Situ Multi-Wavelength Raman-Monitored Annealing. *Physical Chemistry Chemical Physics* **2016**. 2016, *18* (42), 29435-29446

23. (a) Socrates, G., *Infrared and Raman characteristic group frequencies : tables and charts*. 3rd ed.; Wiley: Chichester ; New York, 2001; p xv, 347 p; (b) Anthoni, U.; Nielsen, P. H., A Study of the Raman Spectrum of Thioacetamide Single Crystals Using the Possible 13C and 15N Substituted Species. *Journal of Molecular Structure* **1984,** *116* (1), 175-187.

24. (a) O'Regan, B.; Gratzel, M., A Low-Cost, High-Efficiency Solar Cell Based on Dye-Sensitized Colloidal $TiO_2$ Films. *Nature* **1991,** *353* (6346), 737-740; (b) Liu, B.; Aydil, E. S., Growth of Oriented Single-Crystalline Rutile $TiO_2$ Nanorods on Transparent Conducting Substrates for Dye-Sensitized Solar Cells. *Journal of the American Chemical Society* **2009,** *131* (11), 3985-3990.

25. Todinova, A.; Idígoras, J.; Salado, M.; Kazim, S.; Anta, J. A., Universal Features of Electron Dynamics in Solar Cells with $TiO_2$ Contact: From Dye Solar Cells to Perovskite Solar Cells. *The Journal of Physical Chemistry Letters* **2015,** *6* (19), 3923-3930.

26. Zaban, A.; Greenshtein, M.; Bisquert, J., Determination of the Electron Lifetime in Nanocrystalline Dye Solar Cells by Open-Circuit Voltage Decay Measurements. *ChemPhysChem* **2003,** *4* (8), 859-864.

27. Shi, Y.; Dong, X., Coupled Analysis of Steady-State and Dynamic Characteristics of Dye-Sensitized Solar Cells for Determination of Conduction Band Movement and Recombination Parameters. *Physical Chemistry Chemical Physics* **2013,** *15* (1), 299-306.

28. Scragg, J. J. S.; Choubrac, L.; Lafond, A.; Ericson, T.; Platzer-Björkman, C., A Low-Temperature Order-Disorder Transition in $Cu_2ZnSnS_4$ Thin Films. *Applied Physics Letters* **2014,** *104* (4), 041911.

29. Dimitrievska, M.; Fairbrother, A.; Fontané, X.; Jawhari, T.; Izquierdo-Roca, V.; Saucedo, E.; Pérez-Rodríguez, A., Multiwavelength Excitation Raman Scattering Study of Polycrystalline Kesterite $Cu_2ZnSnS_4$ Thin Films. *Applied Physics Letters* **2014,** *104* (2), 021901.

30. Wang, Y.; Alsmeyer, D. C.; McCreery, R. L., Raman Spectroscopy of Carbon Materials: Structural Basis of Observed Spectra. *Chemistry of Materials* **1990,** *2* (5), 557-563.

31. Liu, X.; Feng, Y.; Cui, H.; Liu, F.; Hao, X.; Conibeer, G.; Mitzi, D. B.; Green, M., The Current Status and Future Prospects of Kesterite Solar Cells: a Brief Review. *Progress in Photovoltaics: Research and Applications* **2016,** *24* (6), 879-898.

32. Dzhagan, V. M.; Litvinchuk, A. P.; Kruszynska, M.; Kolny-Olesiak, J.; Valakh, M. Y.; Zahn, D. R. T., Raman Scattering Study of $Cu_3SnS_4$ Colloidal Nanocrystals. *The Journal of Physical Chemistry C* **2014,** *118* (47), 27554-27558.

33. (a) Bustingorry, S.; Centres, P. M., Relaxation of Surface Steps after Thermal Quenches: A Numerical Study Within the Terrace-Step-Kink Model. *Physical Review E* **2011,** *84* (1), 011613; (b) Larsen, K.; Bechgaard, K.; Stipp, S. L. S., The Effect of the $Ca^{2+}$ to Activity Ratio on Spiral Growth at the Calcite Surface. *Geochimica et Cosmochimica Acta* **2010,** *74* (7), 2099-2109; (c) Burton, W. K.; Cabrera, N.; Frank, F. C., The Growth of Crystals and the Equilibrium Structure of their Surfaces. *Philosophical Transactions of the Royal Society of London. Series A, Mathematical and Physical Sciences* **1951,** *243* (866), 299-358.

34. Kumar, M.; Dubey, A.; Adhikari, N.; Venkatesan, S.; Qiao, Q., Strategic Review of Secondary Phases, Defects and Defect-Complexes in Kesterite CZTS-Se Solar Cells. *Energy & Environmental Science* **2015,** *8* (11), 3134-3159.

35. Fairbrother, A.; García-Hemme, E.; Izquierdo-Roca, V.; Fontané, X.; Pulgarín-Agudelo, F. A.; Vigil-Galán, O.; Pérez-Rodríguez, A.; Saucedo, E., Development of a Selective Chemical Etch To Improve the Conversion Efficiency of Zn-Rich $Cu_2ZnSnS_4$ Solar Cells. *Journal of the American Chemical Society* **2012,** *134* (19), 8018-8021.

36. Roelofs, K. E.; Brennan, T. P.; Bent, S. F., Interface Engineering in Inorganic-Absorber Nanostructured Solar Cells. *The Journal of Physical Chemistry Letters* **2014,** *5* (2), 348-360.

37. (a) Scanlon, D. O.; Dunnill, C. W.; Buckeridge, J.; Shevlin, S. A.; Logsdail, A. J.; Woodley, S. M.; Catlow, C. R. A.; Powell, M. J.; Palgrave, R. G.; Parkin, I. P.; Watson, G. W.; Keal, T. W.; Sherwood, P.; Walsh, A.; Sokol, A. A., Band Alignment of Rutile and Anatase $TiO_2$. *Nature Materials* **2013,** *12* (9), 798-801; (b) Veal, T. D.; King, P. D. C.; Hatfield, S. A.; Bailey, L. R.; McConville, C. F.; Martel, B.; Moreno, J. C.; Frayssinet, E.; Semond, F.; Zúñiga-Pérez, J., Valence Band Offset of the ZnO/AlN Heterojunction Determined by X-Ray Photoemission Spectroscopy. *Applied Physics Letters* **2008,** *93* (20), 202108.

38. Li, L.; Yang, X.; Gao, J.; Tian, H.; Zhao, J.; Hagfeldt, A.; Sun, L., Highly Efficient CdS Quantum Dot-Sensitized Solar Cells Based on a Modified Polysulfide Electrolyte. *Journal of the American Chemical Society* **2011,** *133* (22), 8458-8460.

39. Park, N.-G., Perovskite Solar Cells: an Emerging Photovoltaic Technology. *Materials Today* **2015,** *18* (2), 65-72.

40. (a) Haight, R.; Barkhouse, A.; Gunawan, O.; Shin, B.; Copel, M.; Hopstaken, M.; Mitzi, D. B., Band Alignment at the $Cu_2ZnSn(S_xSe_{1-x})_4$/CdS Interface. *Applied Physics Letters* **2011,** *98* (25), 253502; (b) Suryawanshi, M. P.; Agawane, G. L.; Bhosale, S. M.; Shin, S. W.; Patil, P. S.; Kim, J. H.; Moholkar, A. V., CZTS Based Thin Film Solar Cells: a Status Review. *Materials Technology* **2013,** *28* (1-2), 98-109.

41. Tajima, S.; Umehara, M.; Hasegawa, M.; Mise, T.; Itoh, T., $Cu_2ZnSnS_4$ Photovoltaic Cell with Improved Efficiency Fabricated by High-Temperature Annealing after CdS Buffer-Layer Deposition. *Progress in Photovoltaics: Research and Applications* **2017,** *25* (1), 14-22.

42. Su, Z.; Tan, J. M. R.; Li, X.; Zeng, X.; Batabyal, S. K.; Wong, L. H., Cation Substitution of Solution-Processed $Cu_2ZnSnS_4$ Thin Film Solar Cell with over 9% Efficiency. *Advanced Energy Materials* **2015,** *5* (19), 1500682.

# CHAPTER 7

–

## SYNOPSIS

This chapter brings together the conclusions drawn individually in Chapters 3-6. The conclusions are followed by original contributions to knowledge made during the course of this research. Finally, several possible directions of future work are proposed.

## 7.1 Conclusions

- A new process that makes use of sequential aqueous solution deposition and exchange of binary sulfides ($SnS_x$-ZnS-CuS) was developed to produce a CZTS precursor coating onto $TiO_2$ mesoporous film upon annealing. Preliminary optical transmittance measurements provided evidence of good light absorption response with a CZTS bandgap approaching the theoretical 1.5 eV value.
- The chemical reactions involved in precursor deposition and the formation of kesterite nanocrystallites were fully probed. Optimal composition of a Cu-poor, Zn-rich CZTS film stoichiometry was obtained by applying 10 SILAR cycles of $SnS_x$ deposition, 15 SILAR cycles of ZnS deposition, and one cycle (9.5 min) of ion exchange involving immersion in a $CuCl_2$ solution.
- A hydrochloric acid etching treatment was devised to improve compositional uniformity by removing excess ZnS trapped deep inside the mesoporous film but also Cu-rich surface deposits.
- In situ Raman spectroscopy was applied to monitor real-time phase formation and crystallinity evolution of kesterite on the $TiO_2$ mesoscopic scaffold during annealing in an inert atmosphere. It was determined nucleation of primary kesterite crystallites to start at a temperature as low as 170 °C, but stable kesterite is obtained only upon annealing at

400 °C or higher temperature. Annealing at 500 °C was determined to be required for obtaining complete reaction that eliminates formation of the parasitic copper tin sulfide (CTS) impurity phase seen to be present at lower annealing temperatures.

- CZTS coated on mesoporous $TiO_2$ (anatase) sub-structure did not yield any photovoltaic effect (photo-conversion efficiency <0.01%) due to apparent large charge recombination losses arising at grain boundaries of the conductor ($TiO_2$) network. Replacement of the mesoporous $TiO_2$ sub-structure with $TiO_2$ (rutile) nanorod (TNR) arrays proved effective in at least partially overcoming this obstacle. In particular, by applying CZTS via a modified aqueous successive-ionic-layer-adsorption-reaction (SILAR) method was onto the $TiO_2$ rutile nanorods (TNR) a preliminary photovoltaic efficiency of 0.25 %, short-circuit current density of 3.22 mA/cm$^2$, and internal quantum efficiency of over 60% in the blue light region was achieved.
- The TNR@CZTS photoanode structure was characterized to consist of 5−20 nm kesterite-CZTS nanocrystallites well bonded on rutile nanorods whose length varied from 100 nm to 1 μm. The $TiO_2$ nanorods were grown on FTO glass substrate via hydrothermal acidic treatment of titanium butoxide solution.
- Having demonstrated that the TNR@CZTS photoanode structure exhibits photovoltaic response different measures were taken to improve its performance. This led in identifying direct solution (water-ethanol) spin coating as superior to SILAR deposition method, as did annealing at 600 °C/30 min. The latter condition led to better crystallization of CZTS and less carbon residual contamination. Additionally, the growth of $TiO_2$ nanorod arrays was optimized (treatment of 0.075 M of Ti(IV) butoxide-$Ti(OC_4H_9)_4$ for 6 h at 150 °C). The combination of these measures that included HCl etching helped increase the efficiency to ~0.7%.
- All above devices featuring the improved TNR@CZTS photoanode were based on the standard liquid $I^-/I_3^-$ electrolyte that is corrosive to chalcogenide semiconductors. This prompted the evaluation of the well known solid-state electrolyte (hole transfer material-HTM) piro-OMeTAD achieving an all solid-state device configuration (with

gold as back contact) efficiency of ~0.75 %.

- Upon application of a CdS buffer layer by chemical bath deposition (CBD), interfacial recombination losses were reduced and electron lifetimes prolonged as verified by impedance spectroscopy helping to improve the overall efficiency to 2%. The other PV parameters of this "champion" device were: 13.9 mA/cm$^2$ ($J_{sc}$), 312 mV ($V_{oc}$), and 46 % Fill Factor.
- Finally, in an effort to probe the origin of the rather low $V_{oc}$ (300 mV only), the band offset of CZTS/TNR interface was determined by XPS. This determined the conduction band of $TiO_2$ (rutile) to be too close to the valence band of CZTS causing the large open-circuit potential deficit and interface recombination. This finding can be useful in guiding future interfacial engineering work to overcome this limitation hence helping to materialize the full potential of CZTS/TNR optoelectronic devices.

## 7.2 Claims to Originality

The contributions to original knowledge made during the course of this study are summarized below:

- The controlled solution deposition of nanoscale coating of CZTS on anatase mesoscopic or rutile nanorod films with high composition uniformity- a challenge for complex absorbers like quaternary CZTS;
- In elucidation of phase formation kinetics of nanocrystalline kesterite from a CZTS precursor deposited on a $TiO_2$ mesoscopic scaffold via in-situ Raman monitored-annealing;
- The engineering, nanoscale characterization, and PV performance analysis of a novel extremely thin absorber solar cell structure in which the photoanode is made of solution deposited and annealed CZTS nanocrystallites as a light absorber and one-dimensional $TiO_2$ (rutile) nanorod arrays as an electron conductor (CZTS/TNR);
- The interfacing of the novel CZTS/TNR photoanode with solid-state electrolyte and CdS as buffer layer in an all solid-state sensitized solar cell configuration yielding 2 % efficiency and its analysis by impedance spectroscopy;

- The determination of band alignment of CZTS-$TiO_2$ interface by XPS and its implications with reference to open circuit voltage deficit.

## 7.3 Future Work

To unlock the full potential of the CZTS-$TiO_2$ heterostructure, future work is proposed as follows:

- As demonstrated in Chapter 6, the interface engineering plays an important role in this type of nanostructured solar cells. Therefore, it is recommended to focus on studying the effect of different buffer layers, including CdS, ZnS, $In_2S_3$, $Al_2O_3$, HfO, etc.
- Doping of Ag, Na, Cd, Ge, In, etc. has been reported to reduce the density of defects in the CZTS absorber and improve thin film solar cell device efficiency; this strategy would also be valuable to investigate in the novel CZTS/$TiO_2$ sensitized solar cell structure.
- Different kinds of solid-state hole transfer materials (HTM) other than spiro-OMeTAD should be studied, including Poly(3-hexylthiophene-2,5-diyl) (P3HT), CuSCN, CuI, $NiO_x$, etc.
- Other than $TiO_2$ semiconductor nanostructures as electron conductor should also be investigated.

# APPENDIX A

## SUPPORTING INFORMATION TO CHAPTER 3

Chapter 3 has been published as: Z. Wang and G. P. Demopoulos, *Crystal Growth & Design*, 2016, 16, pp. 3618–3630. Appendix A here is the Supporting Information that constitutes for Chapter 3.

CZTS precursor was prepared by a three-step SILAR method. Figure A.1-A.3 show the photographic images of the deposition procedure.

Figure A.4 represents the element distribution vis-a-vis film thickness as a function of number of cycles: 5 (a,d), 10 (b, e) and 20 (c, f).

Figure A.5 shows film transmittance reduction as a function of immersion time into Cu solution; inset shows digital photos of $TiO_2$/FTO film (left image), after ZnS(15)/SnS(10) SILAR deposition cycles (middle image) and after final precursor deposition involving Cu ion-exchange for 9.5 min.

The data plotted in Figure A.6 give the Sn and Zn concentration released into water with adjusted pH=4 (same as 0.02M $CuCl_2$ solution) upon immersion of the precursor $ZnS/SnS_x/TiO_2$ film. The film was immersed for 30 min initially. Since the concentration was extremely low, eight similar immersion experiments were carried out in order to obtain statistically reliable results. These experiments were performed to evaluate the stability of the precursor film prior to Cu incorporation. From Figure S3 we can see that there is almost no loss of Sn from the precursor while a certain loss of Zn is evident. However, compared to the total amount of Zn (around 5~10 ppm) in the precursor the released Zn is rather negligible (<2% in one immersion).

Figure A.7 presents the data from another series of experiments. In the first experiment we prepared $SnS_x/TiO_2$ via SILAR 1 procedure and then directly immersed into $CuCl_2$ solution without SILAR 2. As the results (% of each element in the film) plotted in Figure 4a show in this case that Cu is gradually incorporated into the film implying a reaction between $Cu^{2+}$ and $Sn^{2+}$. To further confirm that the observed reaction was redox and not simple ion-exchange reaction, another experiment was carried out by dipping the pre-prepared $CuS/TiO_2$ film into $SnCl_2$ solution. As the results in Figure 4b suggest the reaction can still happen in spite of the reverse sequence. As we know simple ion-exchange will proceed into one direction. Therefore, this experiment proves the existence of redox reaction between $Cu^{2+}$ and $Sn^{2+}$.

Figure A.8 shows SEM cross-section image of $TiO_2$ on FTO glass and EDS mapping.

Figure A.9 shows SEM cross-section image of CZTS precursor coated on $TiO_2$ and the EDS elemental maps.

Figure A.10 presents the XRD patterns of precursor films before and after in-situ deposition compared to various reference compounds.

Figure A.11 shows the Raman spectra of the CZTS precursor/$TiO_2$ film collected at different wavelength excitation.

Figure A.12 presents the Raman spectra of a) the CZTS/$TiO_2$ film after annealing collected at different wavelength excitation and b) pure $TiO_2$/FTO film for comparison.

Figure A.13 shows the SEM cross-section image of annealed CZTS/$TiO_2$ film and the EDS elemental maps.

Removal of cations from annealed CZTS/$TiO_2$ film after multiple HCl etching steps of 2h each measured by ICP-OES (Figure A.14)

Figure A.15 shows the SEM cross-section image of the annealed CZTS/$TiO_2$ film after HCl etching and the EDS elemental maps.

Figure A.16 shows the high resolution XPS analysis of CZTS/$TiO_2$ film after HCl etching. C1s peak position is measured to be at 284.9 eV.

Figure A.17 shows Raman and XRD patterns of the final product after 4M HCl etching for 20h (the black dots represent the identified kesterite phase).

Figure A.18 shows the top view SEM image of the final (after etching) CZTS/$TiO_2$ film and the corresponding EDS maps.

Figure A.19 shows TEM images of CZTS/$TiO_2$ ground powder and the corresponding SAED pattern.

Figure A.20 presents the theoretical energy band alignment of a CZTS/$TiO_2$ based ETA solar cell.

Table A.1 presents a summary of various CZTS annealing conditions reported in literature.

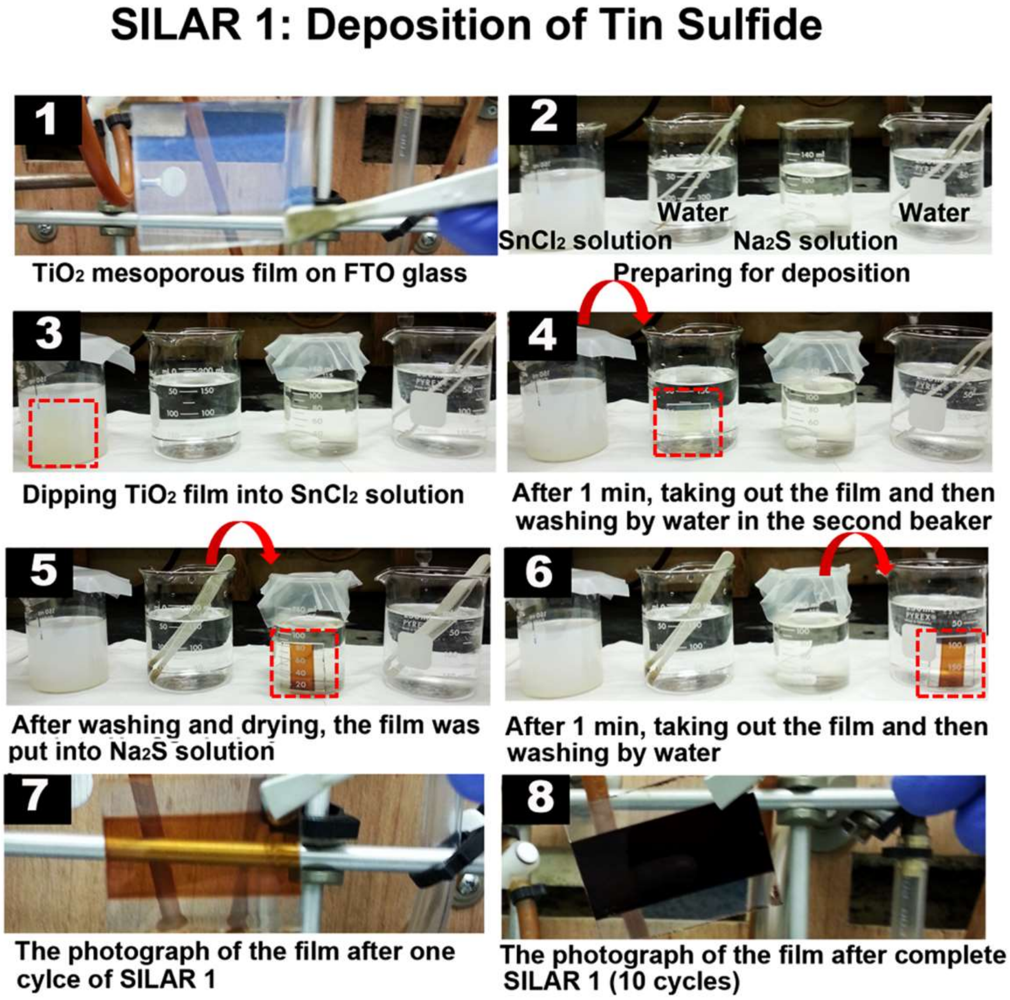

Figure A.1. SILAR 1 procedure for tin sulfide deposition.

## SILAR 2: Deposition of Zinc Sulfide

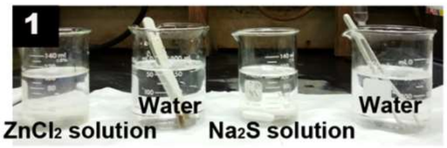

Preparing for deposition

Dipping the film from SILAR 1 into $ZnCl_2$ solution

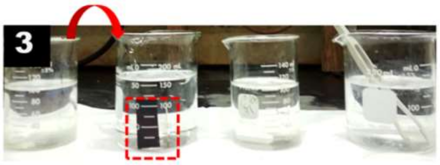

After 1 min, taking out the film and then washing by water

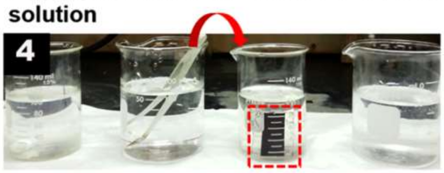

After washing and drying, the film was put into $Na_2S$ solution

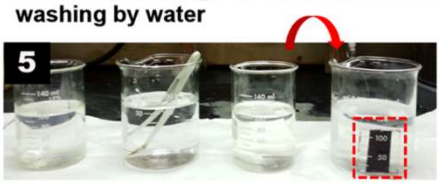

After 1 min, taking out the film and then washing by water

The photograph of the film after complete SILAR 2 (15 cycles)

Figure A.2. SILAR 2 procedure for zinc sulfide deposition.

## Step 3: Ion-Exchange for Copper Incorporation

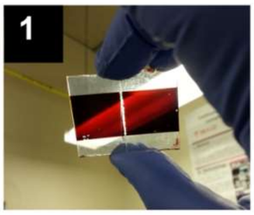

Photograph of the film after SILAR 1 and SILAR 2 (cut into two)

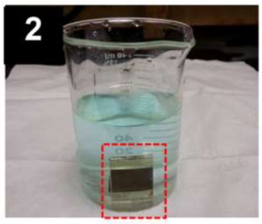

Dipping one piece of the prepared film into CuCl2 aqueous solution for ion-exchange

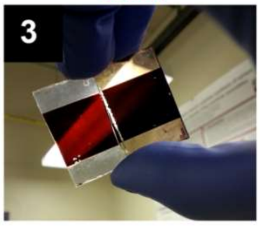

Photograph of the film after ion-exchange (right half) comparing to the one without ion - exchange( left half)

Figure A.3. Step 3 procedure of Cu incorporation via ion-exchange.

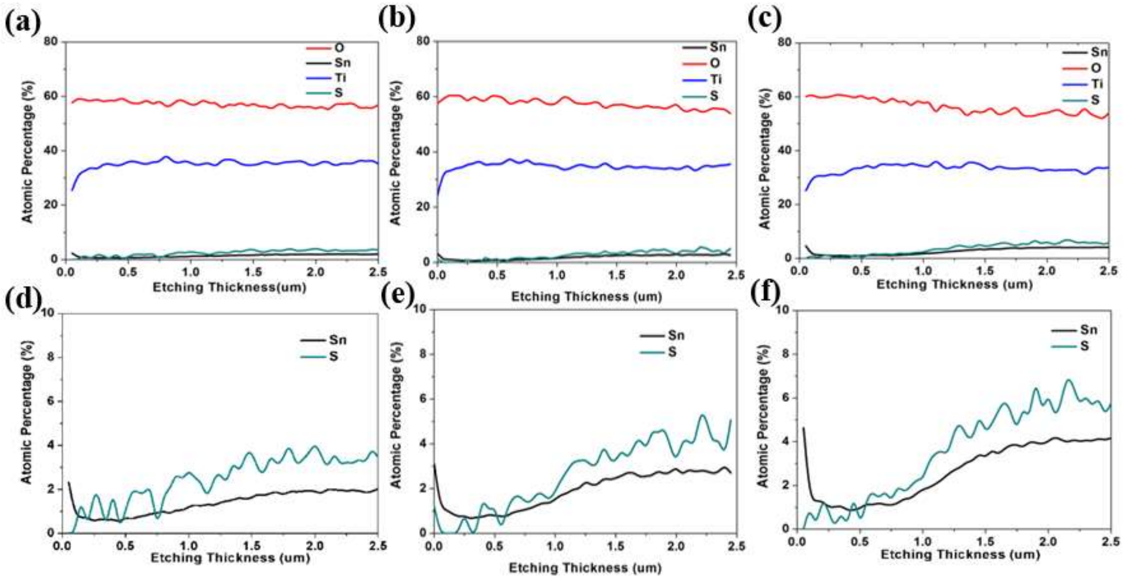

Figure A.4. SnS SILAR deposition: Element distribution vis-a-vis film thickness as a function of number of cycles: 5 (a,d), 10 (b, e) and 20 (c, f).

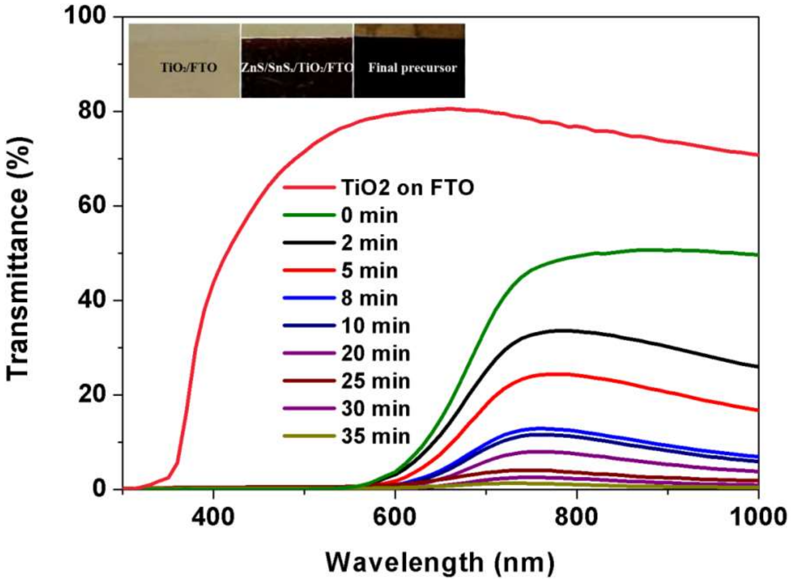

Figure A.5. Film transmittance reduction as a function of immersion time into Cu solution; inset shows digital photos of $TiO_2$/FTO film (left image), after ZnS(15)/SnS(10) SILAR deposition cycles (middle image) and after final precursor deposition involving Cu ion-exchange for 9.5 min.

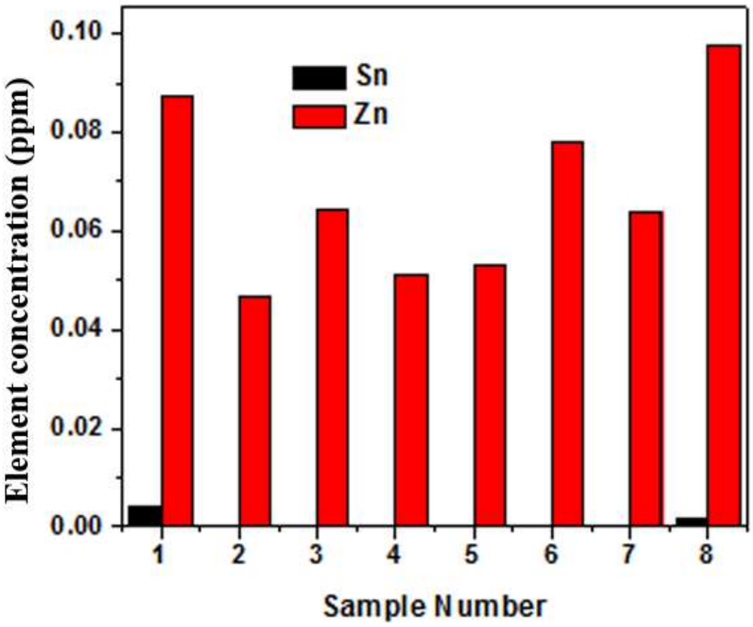

Figure A.6. Released Zn and Sn from ZnS/SnS$_x$/TiO$_2$ immersed in water (pH=4)

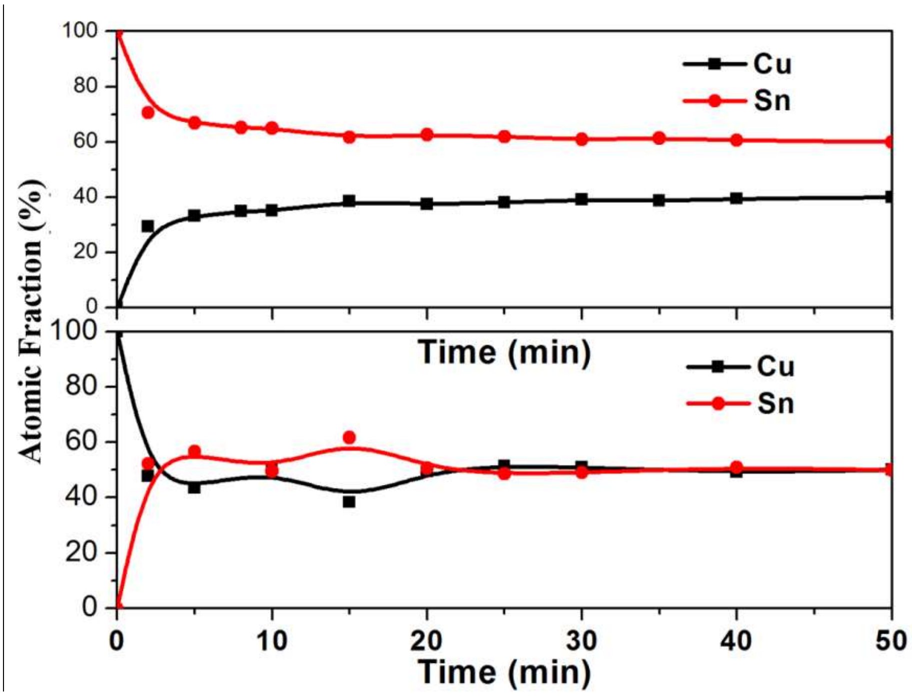

Figure A.7. Cu and Sn atomic fraction change in the film as a function of the immersion time of a) SnS$_x$/TiO$_2$ into CuCl$_2$ solution and b) CuS/TiO$_2$ into SnCl$_2$ solution.

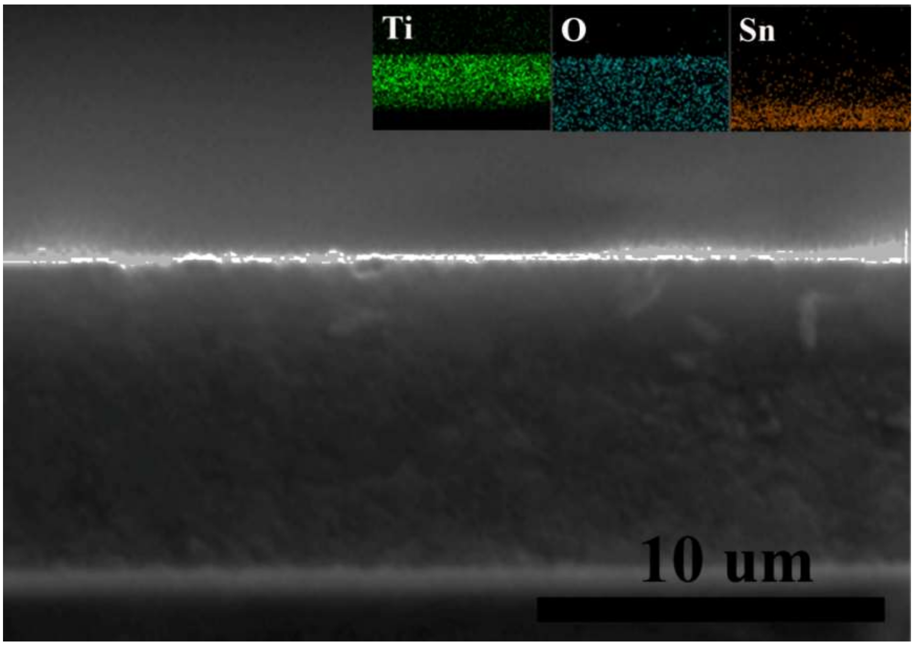

Figure A.8. SEM cross-section image of $TiO_2$ on FTO glass and EDS mapping.

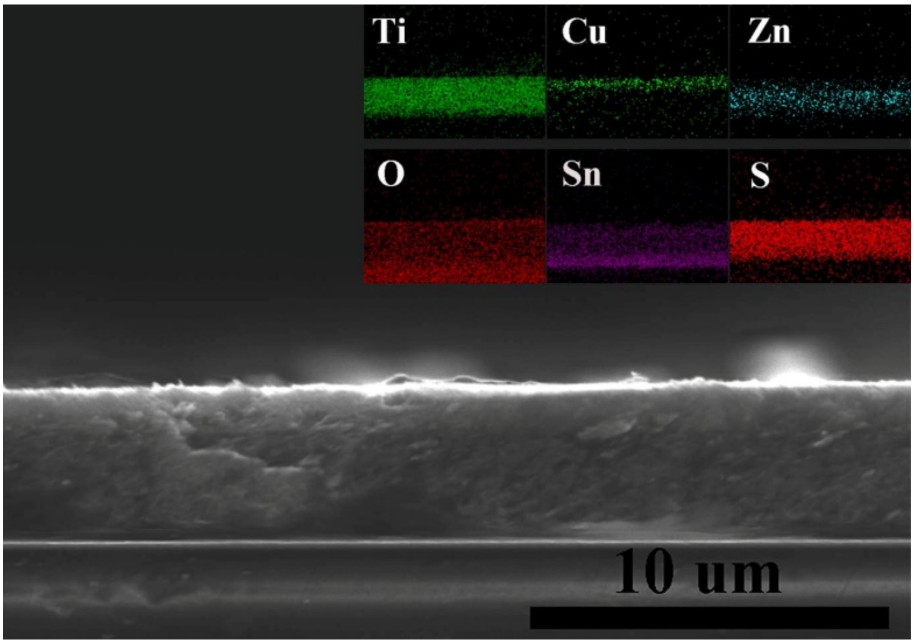

Figure A.9. SEM cross-section image of CZTS precursor coated on $TiO_2$ and the EDS elemental maps.

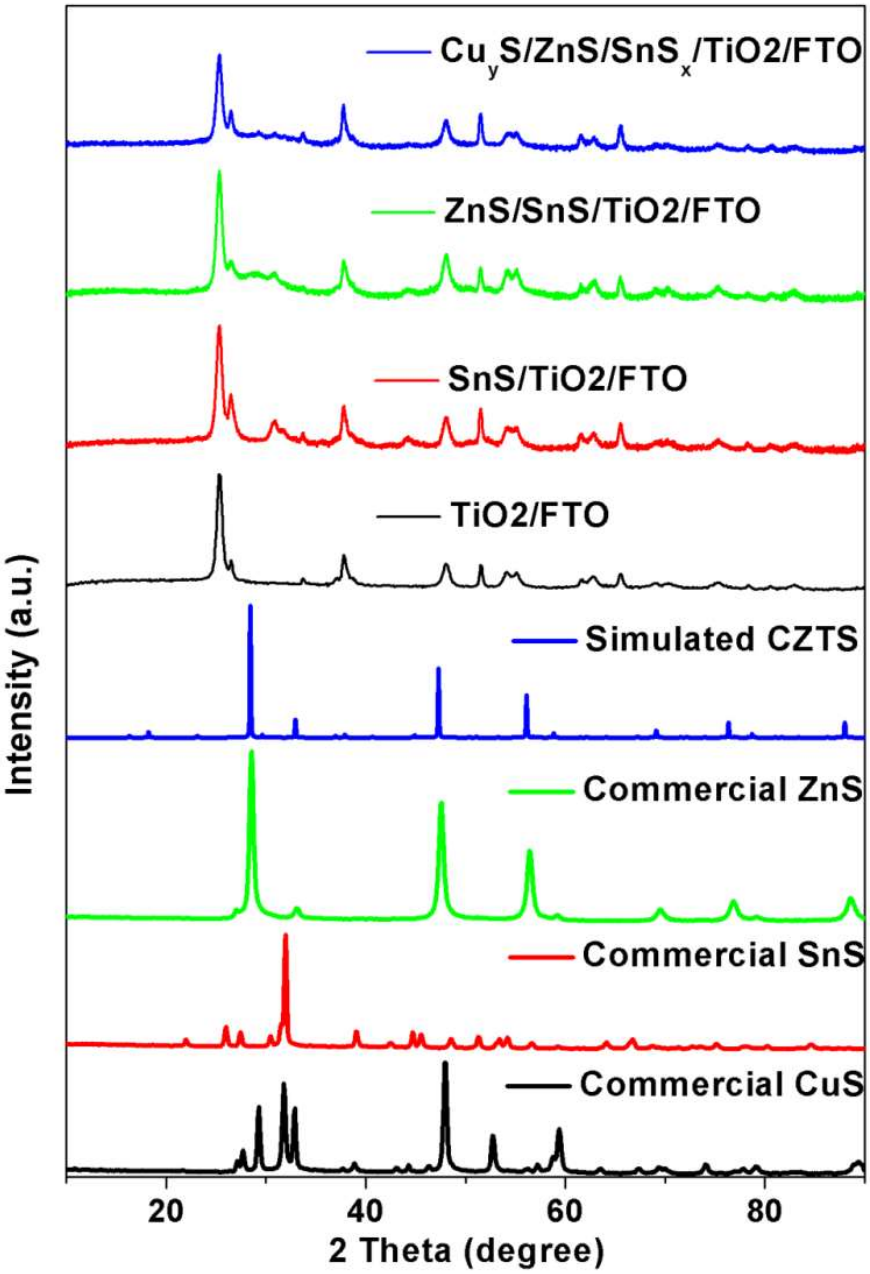

Figure A.10. XRD patterns of precursor films before and after in-situ deposition compared to various reference compounds.

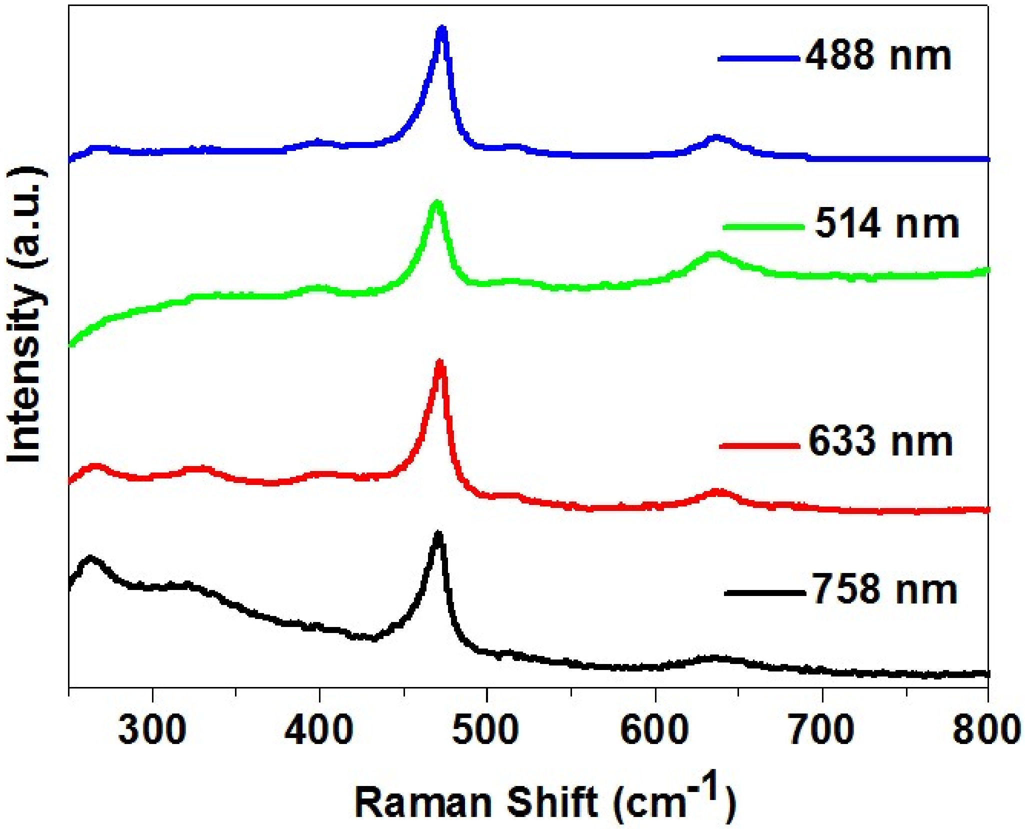

Figure A.11. Raman spectra of the CZTS precursor/$TiO_2$ film collected at different wavelength excitation.

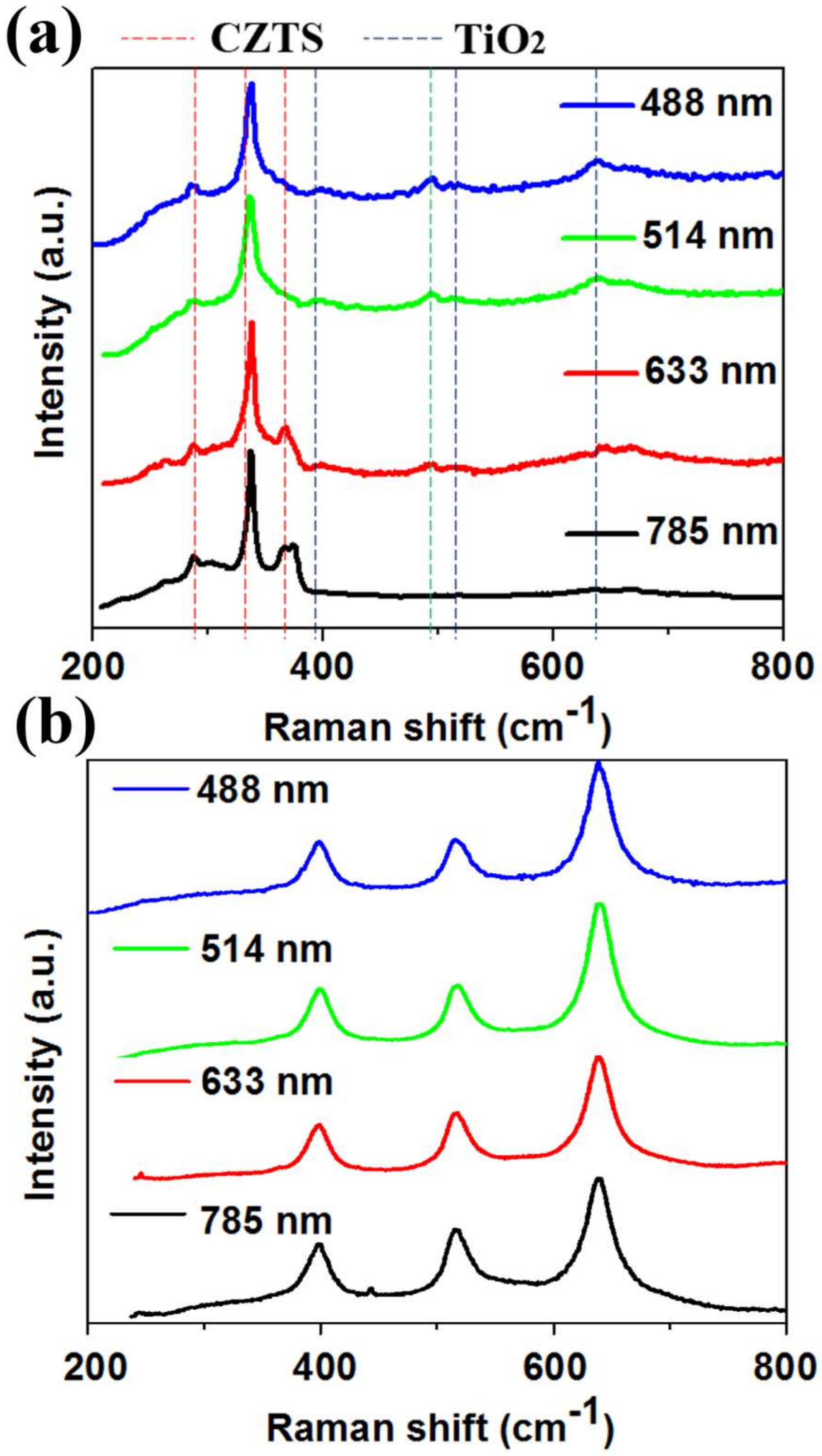

Figure A.12. Raman spectra of a) the CZTS/$TiO_2$ film after annealing collected at different wavelength excitation and b) pure $TiO_2$/FTO film for comparison.

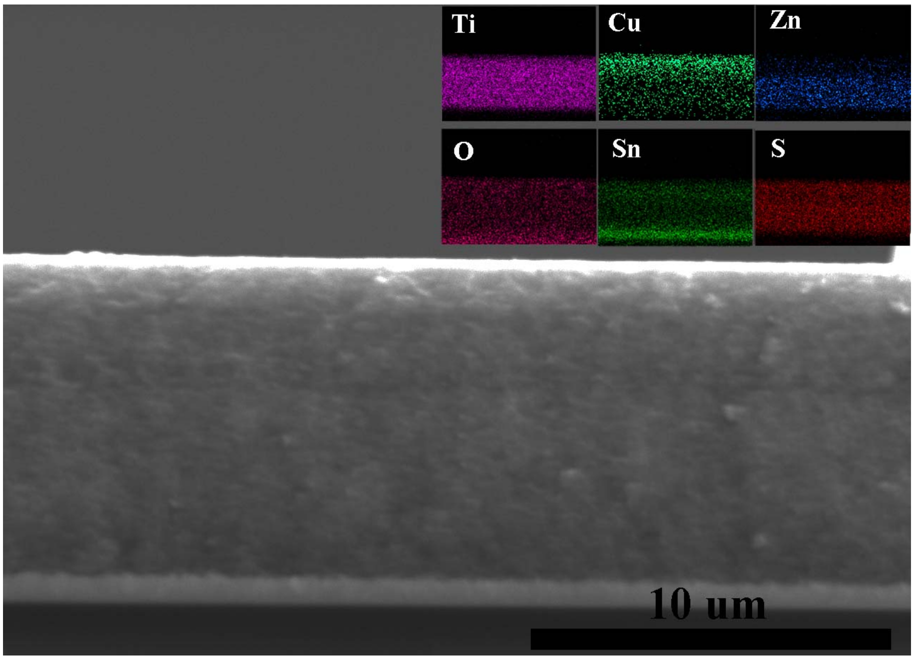

Figure A.13. SEM cross-section image of annealed CZTS/$TiO_2$ film and the EDS elemental maps.

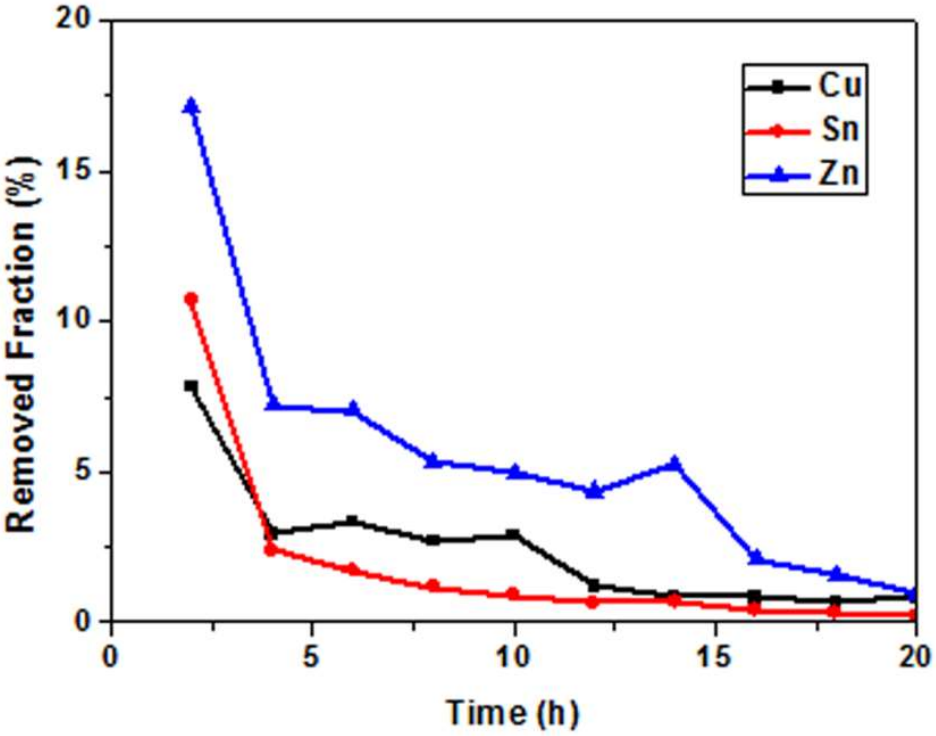

Figure A.14. Removal of cations from annealed CZTS/$TiO_2$ film after multiple HCl etching steps of 2h each.

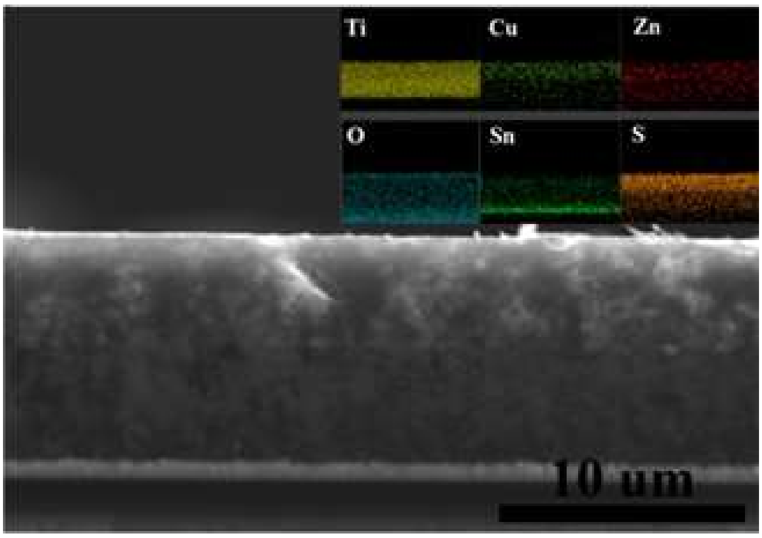

Figure A.15. SEM cross-section image of the annealed CZTS/$TiO_2$ film after HCl etching and the EDS elemental maps.

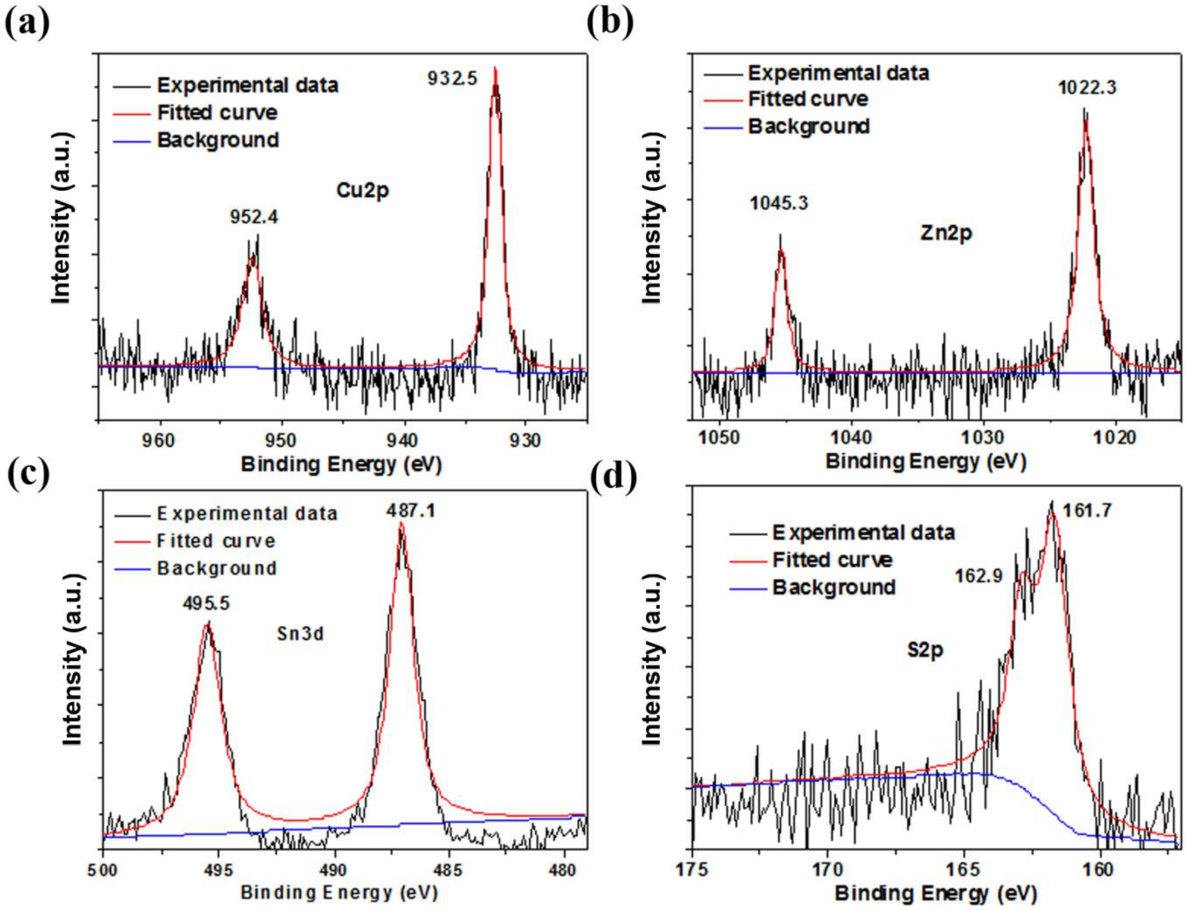

Figure A.16. High resolution XPS analysis of CZTS/$TiO_2$ film after HCl etching. C1s peak position is measured to be at 284.9 eV.

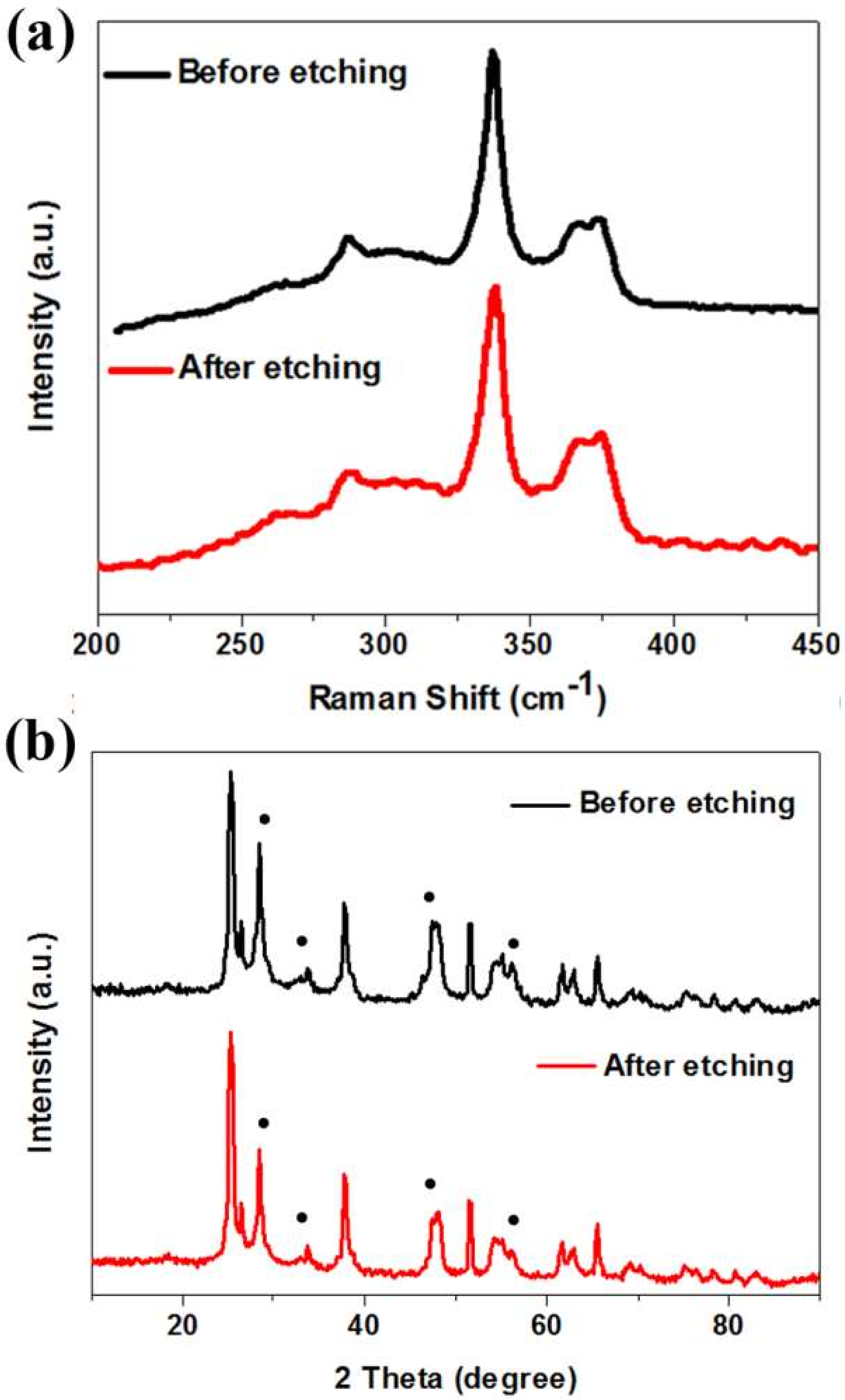

Figure A.17. a) Raman and b) XRD patterns of the final product after 4M HCl etching for 20h (the black dots represent the identified kesterite phase).

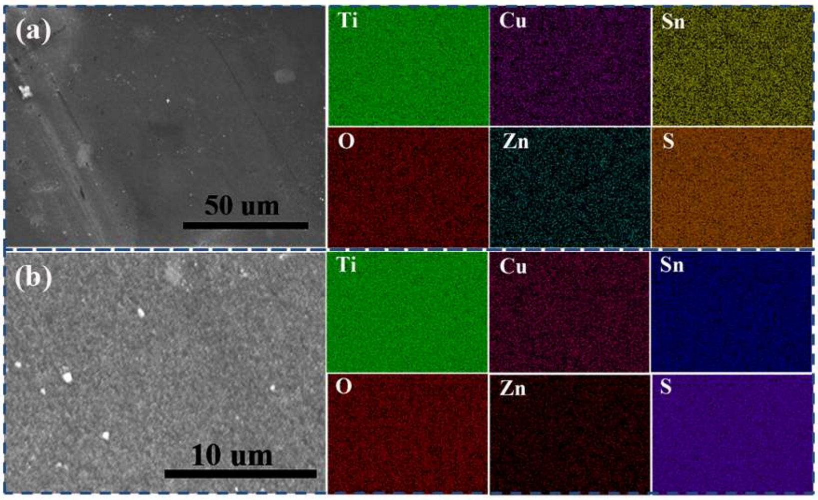

Figure A.18. a) Top view SEM image of the final (after etching) CZTS/$TiO_2$ film at low magnification and the corresponding EDS maps; b) Top view SEM image of the final (after etching) CZTS/$TiO_2$ film at high magnification and the corresponding EDS maps.

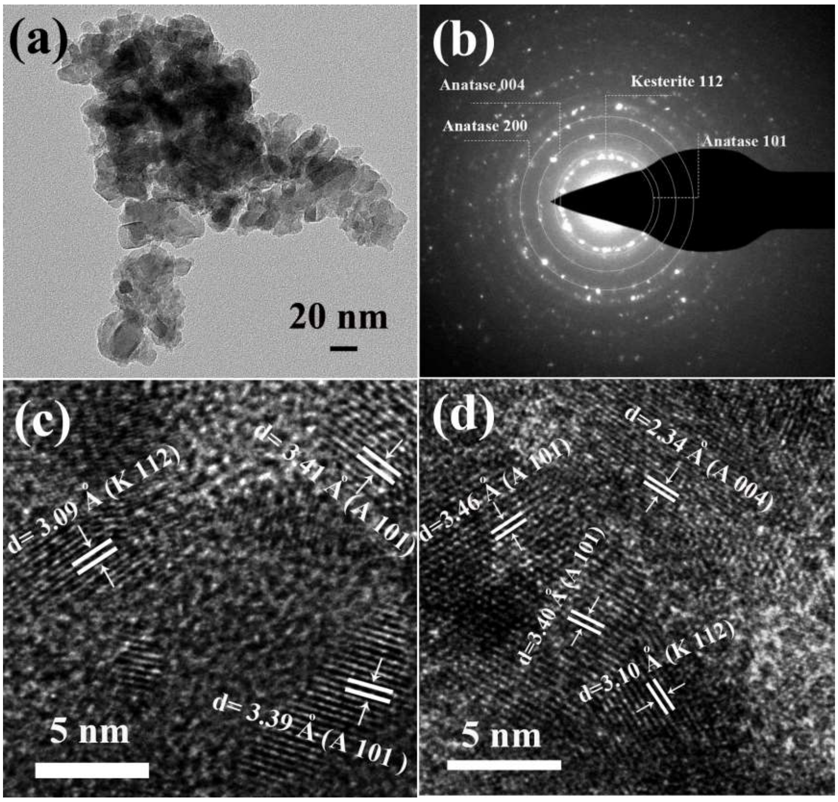

Figure A.19. a) TEM image of CZTS/$TiO_2$ ground powder at relatively low magnification and b) the corresponding SAED pattern; c, d) high resolution images of interphasial zones where both kesterite and anatase exist. (K represents kesterite while A represents anatase).

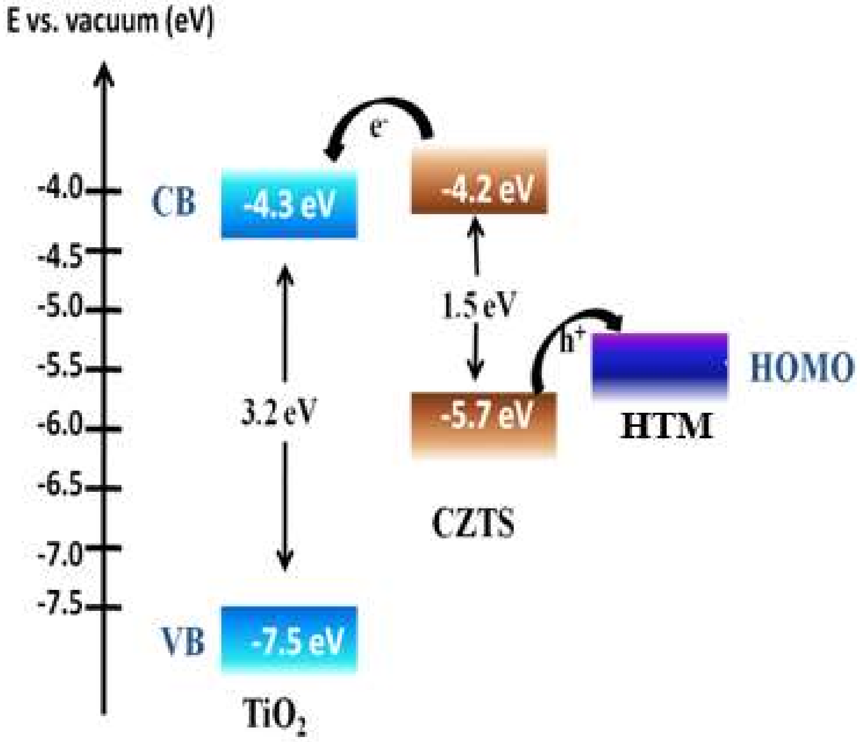

Figure A.20. Theoretical energy band alignment of a CZTS/$TiO_2$ based ETA solar cell.

Table A.1. Summary of various CZTS annealing conditions reported in literature.

| Type of Sample | Precursor preparation | Annealing Temperature | Sulfur Supply |
|---|---|---|---|
| Powder[1] | Cu-Zn-Sn oxide particles | 550 °C/ 30 min | Element S |
| Powder[2] | CuS, SnS and ZnS mixture | 450 °C/ 1h | Element S |
| Thin film[3] | Chemical bath deposition of CuS/ZnS/SnS | 500 °C/ 2h | $H_2S$ |
| Thin film[4] | ALD deposited $Cu_2S/SnS_2/ZnS$ | 450 °C/ 2h | None |
| Thin film[5] | Printed with CZTS precursor powder | 550 °C 10min | Element S |
| Thin film[6] | Spin coated sol-gel solution | 450-475 °C 2h | None |
| Thin film[7] | Hydrothermal prepared particle paste | 450 °C | None |
| Thin film[8] | Co-sputtering of Cu/Sn/Zn under $H_2S$ atmosphere | 560-570 °C 10min | Element S |
| Thin film[9] | Electrodeposition | 580 °C 2h | $H_2S$ |
| Thin film[10] | Spray pyrolysis | 550 °C 2h | None |
| Thin film[11] | Dip coated CZTS precursor | 420 °C 20min | None |
| Thin film[12] | Electrodeposition | 572 °C 2h | $H_2S$ |
| Thin film[13] | Co-evaporation | 560 °C 2h | Element Sn and S |

## A.1 References:

1. Tang, D.; Wang, Q.; Liu, F.; Zhao, L.; Han, Z.; Sun, K.; Lai, Y.; Li, J.; Liu, Y., An Alternative Route towards Low-Cost $Cu_2ZnSnS_4$ Thin Film Solar Cells. *Surface and Coatings Technology* **2013,** *232* (0), 53-59.

2. Wang, Y.; Gong, H., Low Temperature Synthesized Quaternary Chalcogenide $Cu_2ZnSnS_4$ from Nano-Crystallite Binary Sulfides. *Journal of The Electrochemical Society* **2011,** *158* (8), H800-H803.

3. Wangperawong, A.; King, J. S.; Herron, S. M.; Tran, B. P.; Pangan-Okimoto, K.; Bent, S. F., Aqueous Bath Process for Deposition of $Cu_2ZnSnS_4$ Photovoltaic Absorbers. *Thin Solid Films* **2011,** *519* (8), 2488-2492.

4. Thimsen, E.; Riha, S. C.; Baryshev, S. V.; Martinson, A. B. F.; Elam, J. W.; Pellin, M. J., Atomic Layer Deposition of the Quaternary Chalcogenide $Cu_2ZnSnS_4$. *Chemistry of Materials* **2012,** *24* (16), 3188-3196.

5. Todorov, T.; Kita, M.; Carda, J.; Escribano, P., $Cu_2ZnSnS_4$ Films Deposited by a Soft-Chemistry Method. *Thin Solid Films* **2009,** *517* (7), 2541-2544.

6. Sarswat, P. K.; Free, M. L., Demonstration of a Sol–Gel Synthesized Bifacial CZTS Photoelectrochemical Cell. *Physica Status Solidi (a)* **2011,** *208* (12), 2861-2864.

7. Sekou Mariama, C.; Lingling, W.; Xintong, Z., Easy Hydrothermal Preparation of $Cu_2ZnSnS_4$ (CZTS) Nanoparticles for Solar Cell Application. *Nanotechnology* **2013,** *24* (49), 495401.

8. Scragg, J. J.; Kubart, T.; Wätjen, J. T.; Ericson, T.; Linnarsson, M. K.; Platzer-Björkman, C., Effects of Back Contact Instability on $Cu_2ZnSnS_4$ Devices and Processes. *Chemistry of Materials* **2013,** *25* (15), 3162-3171.

9. Gurav, K. V.; Pawar, S. M.; Shin, S. W.; suryawanshi, M. P.; Agawane, G. L.; Patil, P. S.; Moon, J.-H.; Yun, J. H.; Kim, J. H., Electrosynthesis of CZTS Films by Sulfurization of CZT Precursor: Effect of Soft Annealing Treatment. *Applied Surface Science* **2013,** *283* (0), 74-80.

10. Kamoun, N.; Bouzouita, H.; Rezig, B., Fabrication and Characterization of $Cu_2ZnSnS_4$ Thin Films Deposited by Spray Pyrolysis Technique. *Thin Solid Films* **2007,** *515* (15), 5949-5952.

11. Liu, X.; Wang, C.; Xu, J.; Liu, X.; Zou, R.; Ouyang, L.; Xu, X.; Chen, X.; Xing, H., Fabrication of $ZnO/CdS/Cu_2ZnSnS_4$ P-N Heterostructure Nanorod Arrays via a Solution-Based Route. *CrystEngComm* **2013,** *15* (6), 1139-1145.

12. Scragg, J. J.; Berg, D. M.; Dale, P. J., A 3.2% Efficient Kesterite Device from Electrodeposited Stacked Elemental Layers. *Journal of Electroanalytical Chemistry* **2010,** *646* (1–2), 52-59.

13. Redinger, A.; Berg, D. M.; Dale, P. J.; Siebentritt, S., The Consequences of Kesterite Equilibria for Efficient Solar Cells. *Journal of the American Chemical Society* **2011,** *133* (10), 3320-3323.

# APPENDIX B

## SUPPORTING INFORMATION TO CHAPTER 4

Chapter 4 has been published as: Z. Wang, S. Elouatik, and G. P. Demopoulos, *Physical Chemistry Chemical Physics,* 2016, *18*, pp. 29435-29446. Appendix B here is the Supporting Information that constitutes for Chapter 4.

## B.1 Experimental Section:

### B.1.1 Precursor preparation

$TiO_2$ mesoscopic film was prepared by doctor-blading of commercially available anatase paste (Dyesol, 18NR-T) on cleaned FTO glass, then slowly heated up to 450℃ and kept for 30 min to form the porous mesoscopic film. After, there are three steps for the quaternary precursor to be in-situ deposited and coated onto the mesoscopic $TiO_2$ film: 1. 100 mL 0.02 M $SnCl_2$ and 0.16 M $Na_2S$ aqueous solution were prepared separately in two containers. Then the as-prepared $TiO_2$ film on FTO glass was immersed into aqueous cationic solution containing $Sn^{2+}$ and aqueous anionic solution containing excess $S^{2-}$ successively with one-minute interval time; the process was repeated for 10 times to form a $SnS_x$ coating on the walls of the $TiO_2$ mesopores. 2. Similarly, ZnS was in-situ deposited with another 15 SILAR rounds, instead of $SnCl_2$, 100 mL 0.1 M $ZnCl_2$ aqueous solution was used as the cationic source. 3. To complete the precursor preparation, copper was incorporated by an additional ion-exchange step. Briefly, 100 mL 0.02 M copper(II) chloride aqueous solution (pH~4) was prepared, then the ternary sulfide (Sn-Zn-S) coated $TiO_2$ film was immersed into the Cu solution and kept for 9 minutes. At the end of this immersion stage, the color of the film changed from red-brown to black indicating that ion-exchange had led to CZTS precursor coated onto $TiO_2$ mesoporous film. Finally, the films were washed with deionized water before subjected to characterization and annealing. More details are provided in a previous publication (ref. 23, Crystal Growth & Design, 2016, 16, 3618–3630).

### B.1.2 In-situ Raman annealing/characterizations

Raman spectroscopy was performed using a Renishaw inVia Raman spectrometer equipped with a LEICA optical microscope. Available excitation light sources are four lasers with wavelength of 488 nm, 514 nm, 633 nm and 785 nm with measured power of 0.5 mW, 0.5 mW, 0.2 mW and 0.1 mW, respectively (the power indicated were measured on the laser illumination out of the 5X object lens of the optical microscope by power meter); Transmission Electron Microscope (FEI Tecnai G2 F20 200 kV Cryo-STEM equipped with EDAX Genesis EDS) is used to investigate the size and shape of CZTS nanocrystals coated on $TiO_2$ as well as the uniformity of distribution at nanoscale.

In-situ annealing was performed with a cold/hot stage (Linkam) mounted under the LEICA microscope. The glass window of the stage allows the transmission of optical signals. Heating and cooling rate was controlled at 30 K/min and constant $N_2$ flow is kept to provide an inert atmosphere inside the sample chamber for the whole time. When starting the heating program, hot plate temperature under sample is precisely controlled and Raman spectrum is captured at the mean time. It is clarified here that when a holding time at a certain annealing temperature is given for a sample, say 1min, it should be understood that the sample has already gone through the heat-up period at the fixed rate of 30 °C /min. The laser power applied has been optimized on one hand to obtain better revolved kesterite Raman peaks, on the other hand to avoid the issue of illumination damage/peak broadening. Meanwhile, to reduce the light exposing time (accumulated heat from illumination), we set the program to close the light shutter once spectrum capturing is finished. By these means we ensure that the light induced damage is minimized during the in-situ Raman measurements. However, the other issues like the in-situ Raman spectrum acquisition delay during the annealing could induce errors for analysis of phase formation kinetics. Improvement to this regard is underway as future work.

### B.1.3 Data processing for Raman spectra

The normalized intensity was presented to better study the Raman profile change for a sample during in-situ Raman. It was calculated by defining the highest peak intensity of kesterite or copper sulfide as 1 and plotting the ratio of the rest. FWHM and peak center position were extracted by fitting the spectra with symmetrical Lorentz peaks using the residuals method; instead of using two peaks to fit the main kesterite mode, only one peak was used to best describe the main mode.

Figure B.1 presents the in-situ Raman spectra during annealing with 514 nm laser at 300 °C for 60min followed by cooling down.

Figure B.2 shows the light absorbance spectrum of a CZTS-coated $TiO_2$ mesoporous film.

Figure B.3 shows the in-situ Raman spectra during annealing at 400 °C and 500 °C for 1min with 633 nm laser.

Figure B.4 presents the Lorentzian peak fits of the 500 °C, 1h in-situ Raman spectra; the peaks filled with black represent the main kesterite mode.

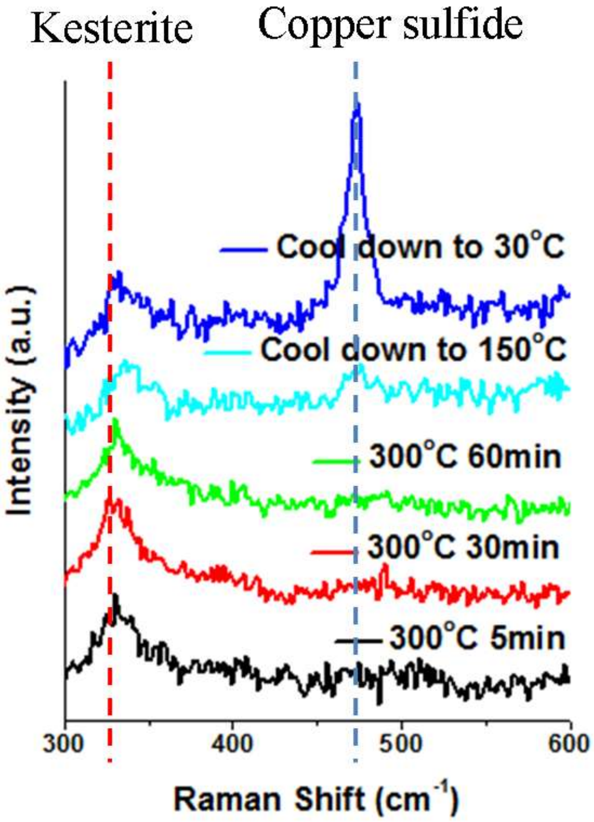

Figure B.1. In-situ Raman monitored annealing with 514 nm laser at 300 °C for 60min followed by cooling down.

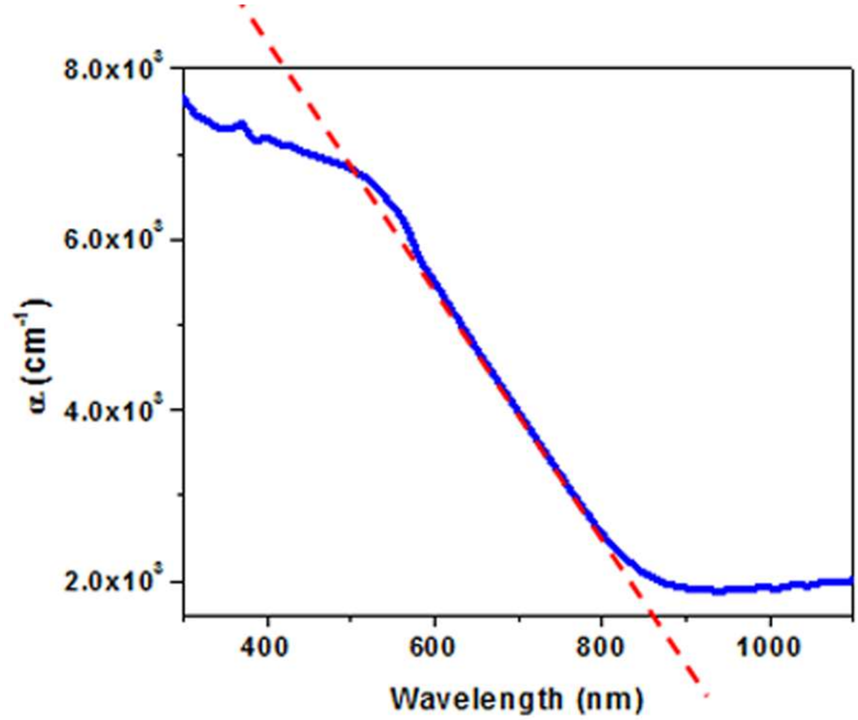

Figure B.2. Light absorbance spectrum of a CZTS-coated $TiO_2$ mesoporous film.

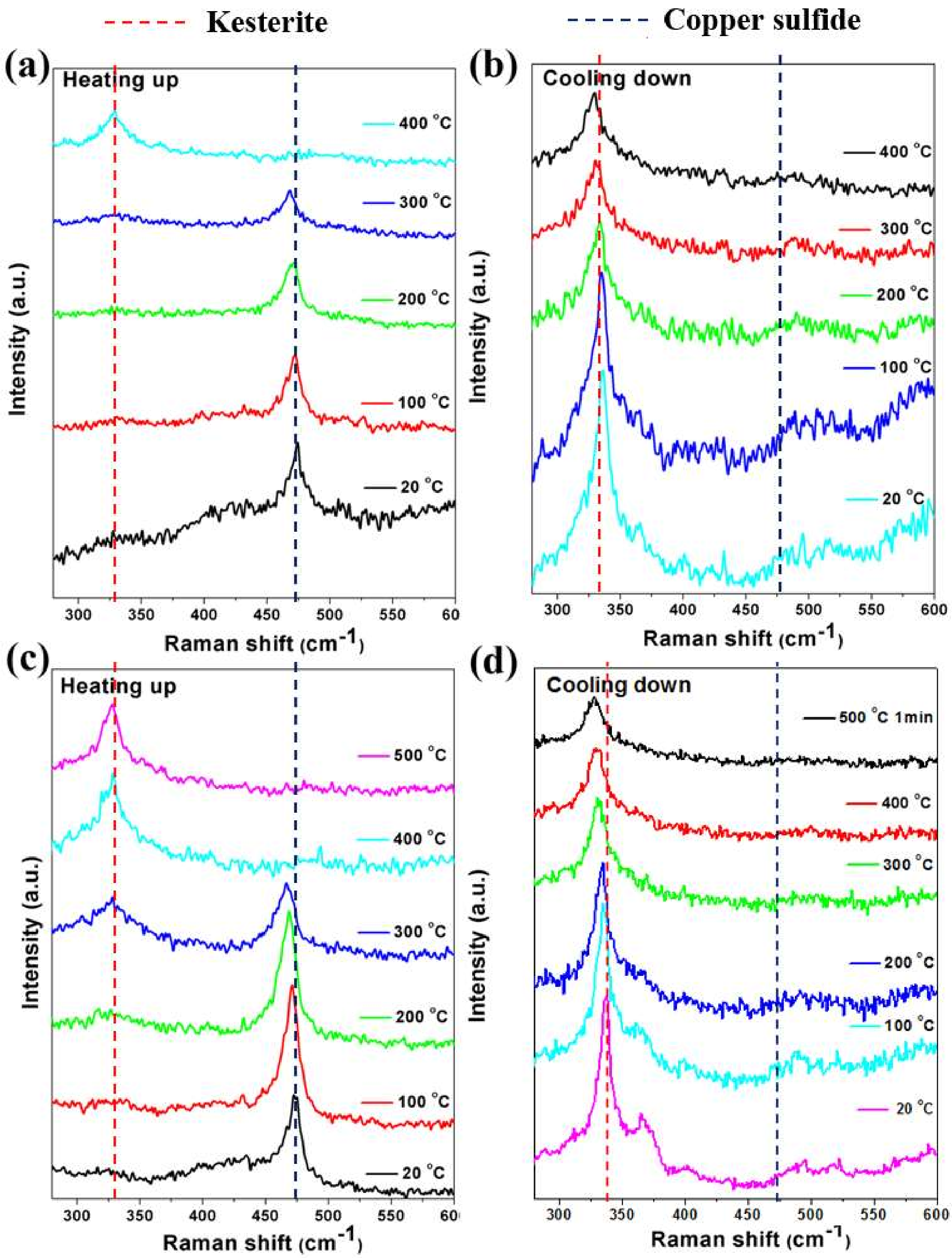

Figure B.3. In-situ Raman monitored annealing at a), b) 400 °C 1min; and c), d) 500 °C 1min with 633 nm laser. Spectra were taken every minute for a total of 19 minutes.

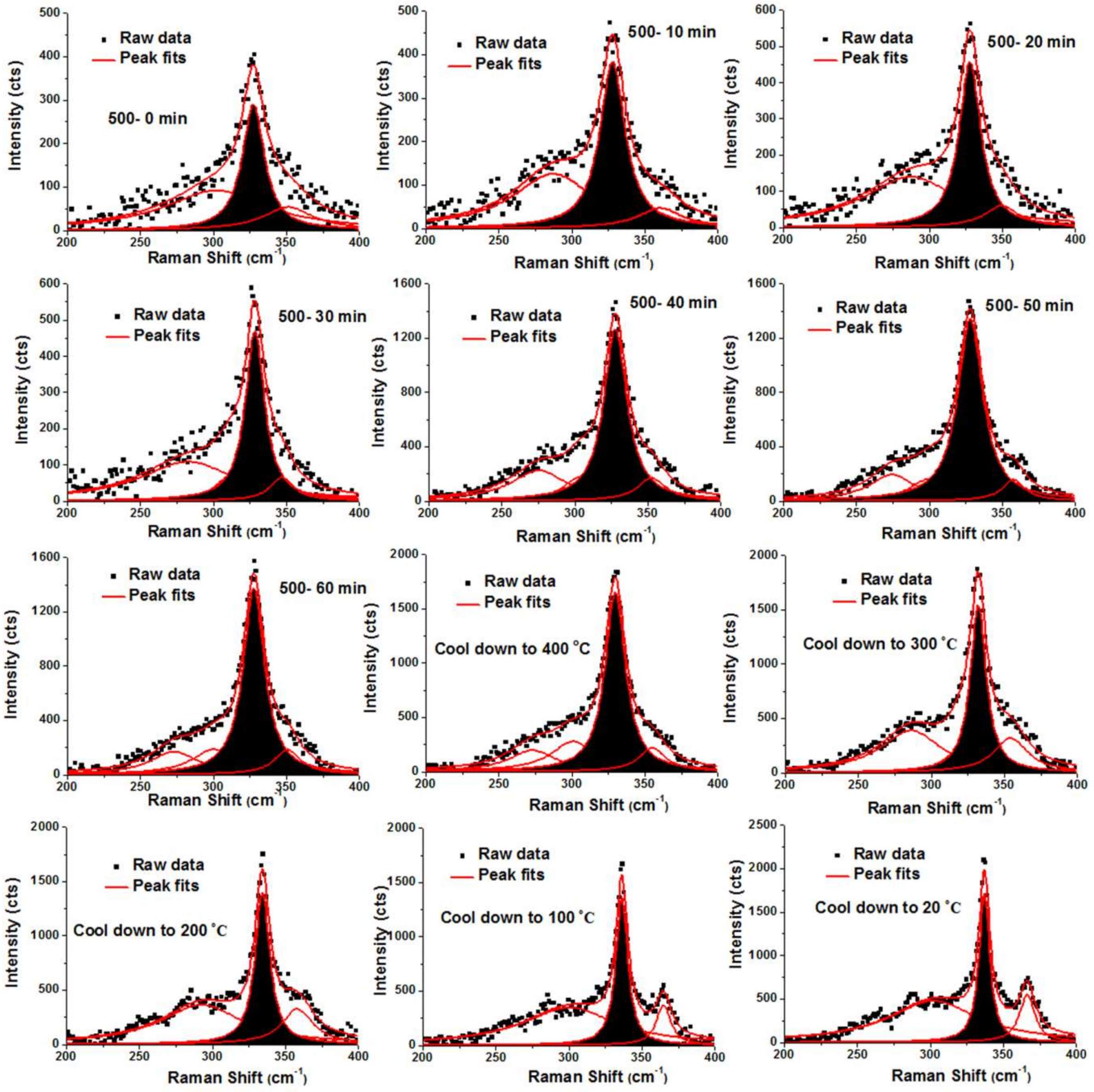

Figure B.4 Lorentzian peak fits of the 500 °C, 1h in-situ Raman spectra; the peaks filled with black represent the main kesterite mode.

# APPENDIX C

## SUPPORTING INFORMATION TO CHAPTER 5

Chapter 5 has been published as: Z. Wang and G. P. Demopoulos, *ACS Applied Materials and Interfaces*, 2015, 7, pp. 22888-22897. Appendix C here is the Supporting Information that constitutes for Chapter 5.

CZTS was deposited onto $TiO_2$ nanorod arrays via a three-step SILAR method, Figure C.1 presents schematic process sequence for the in-situ deposition and annealing of CZTS on $TiO_2$ nanorod arrays to form the TNR@CZTS absorber-conductor nanostructure.

Figure C.2 shows the X-ray photoelectron spectra (XPS) of individual elements on the TNR@CZTS surface, using C 1s peak set to 285.00 eV for charge correction.

Figure C.3 shows the comparison of XPS spectra on the surface and after the first level of Ar etching.

Figure C.4. shows the bright field TEM image of a small $TiO_2$ nanorod attached on a relatively large size one coated with CZTS nanocrystallites and the corresponding STEM-HAADF image and EDS element maps.

Figure C.5 shows TEM images of two different TNR@CZTS kesterite-decorated rutile nanorods and their corresponding SAED patterns.

Figure C.6 presents optical properties of FTO glass supported TNR@CZTS photoelectrode.

Figure C.7 shows the early stage photovoltaic performance of devices with TNR and TNR@CZTS photoanodes.

Figure C.8 shows the energy band diagram of $TiO_2$/CZTS/electrolyte/CE system.

Figure C.9 shows Metallic element ratio of CZTS with different initial Cu SILAR cycles determined by ICP-OES.

Figure C.10 shows the XPS depth profile of Cu5 sample with high resolution spectrum depth profile of sodium and chlorine.

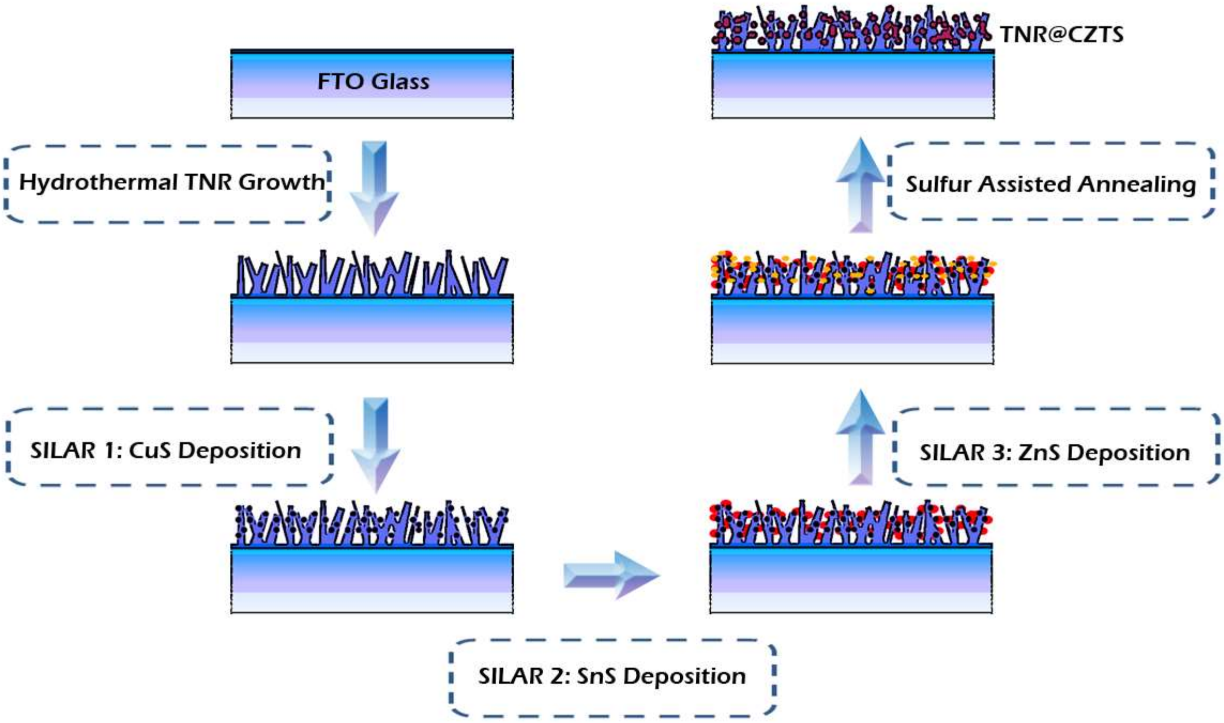

Figure C.1. Schematic process sequence for the in-situ deposition and annealing of CZTS on $TiO_2$ nanorod arrays to form the TNR@CZTS absorber-conductor nanostructure.

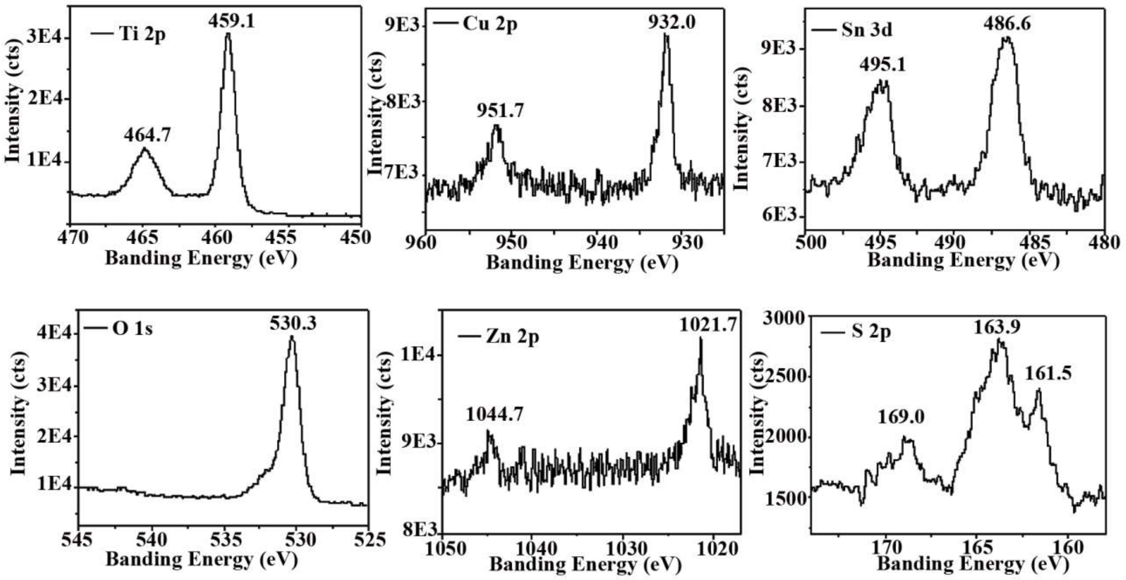

Figure C.2. X-ray photoelectron spectra of individual elements on the TNR@CZTS surface, using C 1s peak set to 285.00 eV for charge correction.

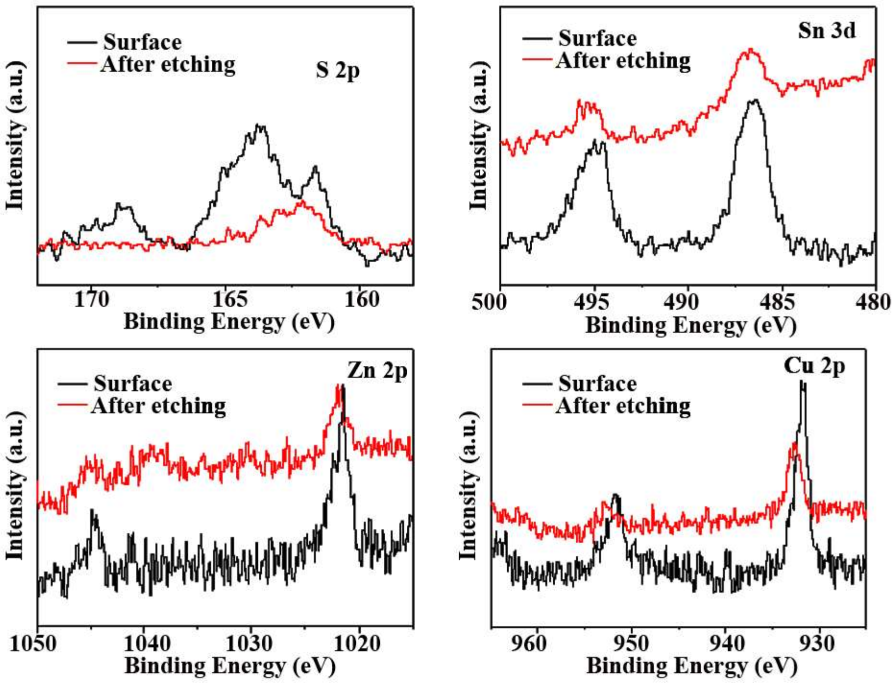

Figure C.3. Comparison of XPS spectra on the surface (black) and after the first level of Ar etching (red).

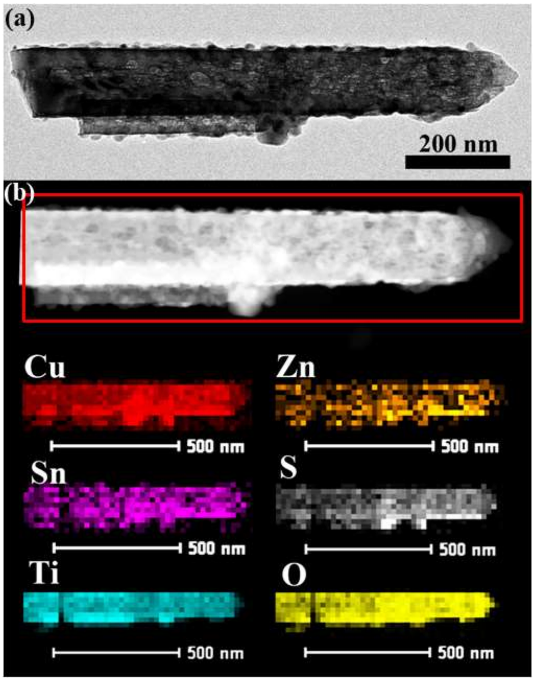

Figure C.4. a) Bright field TEM image of a small $TiO_2$ nanorod attached on a relatively large size one coated with CZTS nanocrystallites and b) the corresponding STEM-HAADF image and EDS element maps.

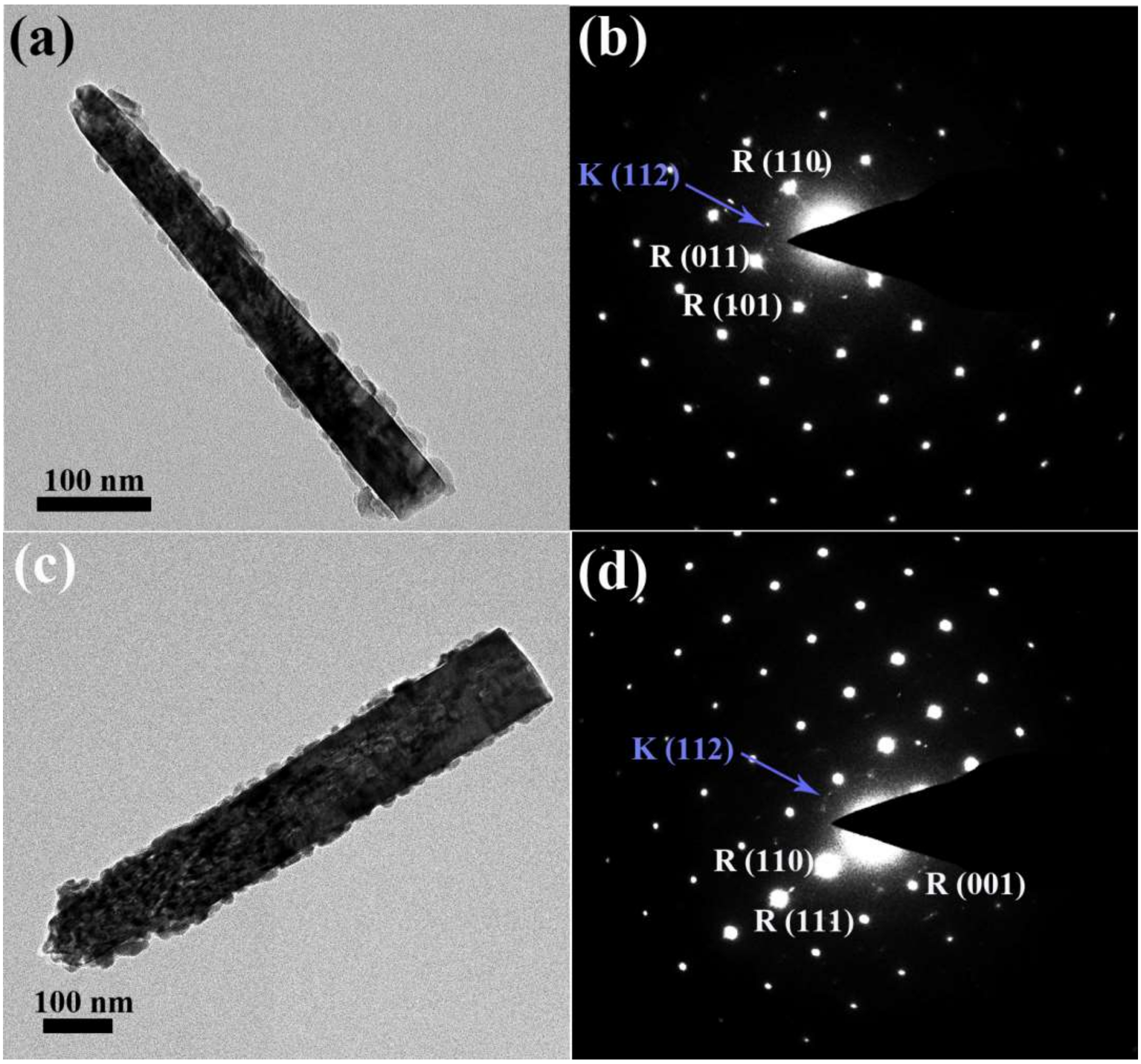

Figure C.5. (a, c) TEM images of two different TNR@CZTS kesterite-decorated rutile nanorods and (b, d) their corresponding SAED patterns (K represents kesterite CZTS phase and R rutile $TiO_2$).

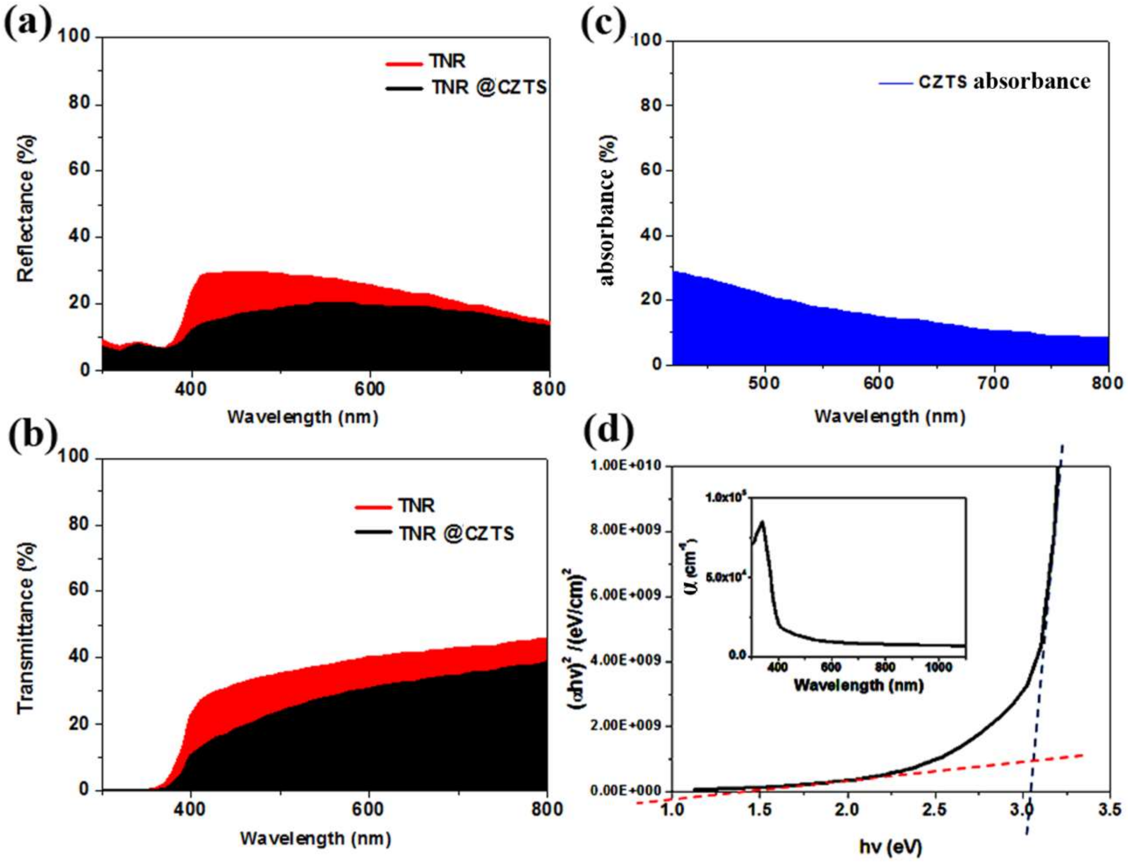

Figure C.6. a) Reflectance and b) transmittance of FTO glass supported TNR@CZTS photoelectrode; c) calculated effective light absorbance of the CZTS nanocrystallites only; d) bandgap estimation of TNR@CZTS photoelectrode; inset shows its light absorption coefficient curve.

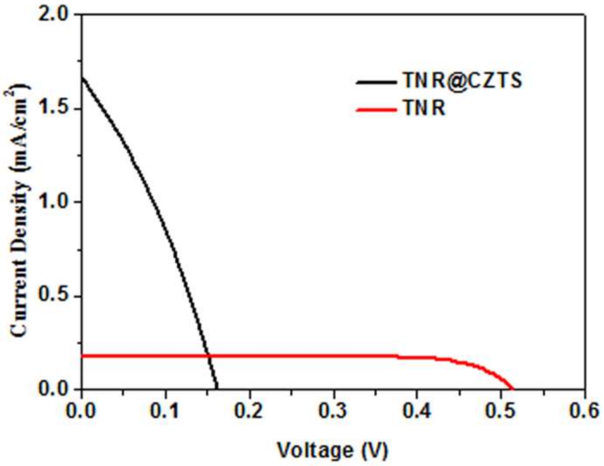

Figure C.7. J-V characteristic curves of devices with TNR and TNR@CZTS photoanodes.

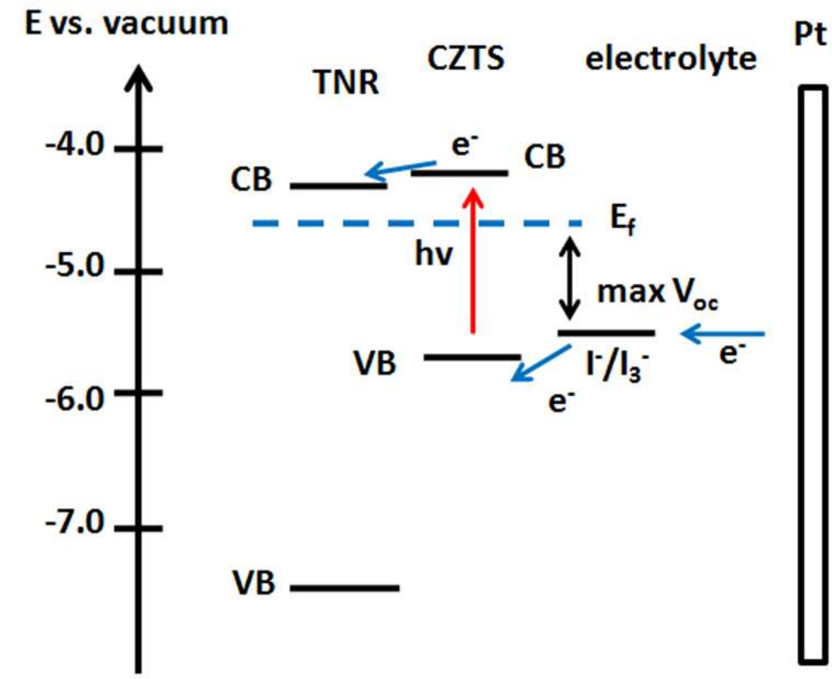

Figure C.8. Energy band diagram of $TiO_2$/CZTS/electrolyte/CE system

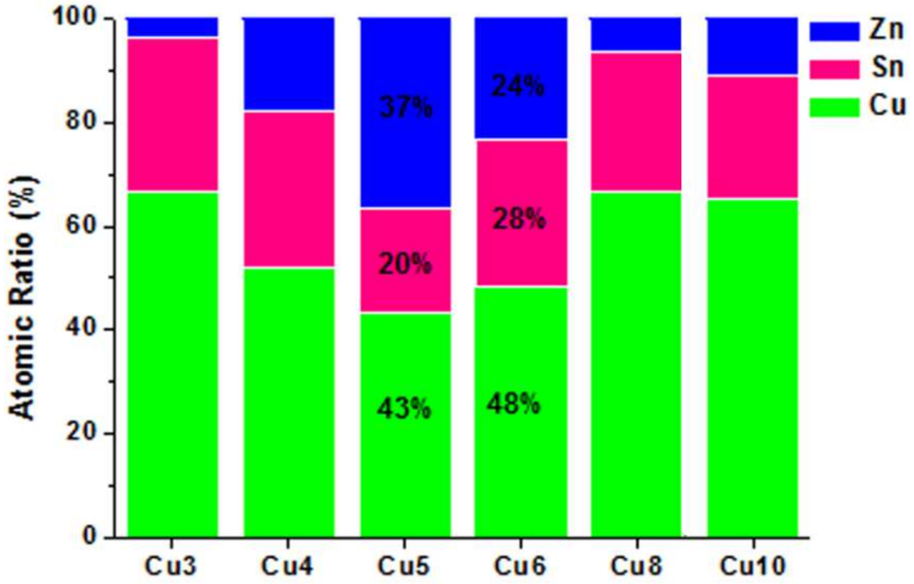

Figure C.9. Metallic element ratio of CZTS with different initial Cu SILAR cycles determined by ICP-OES.

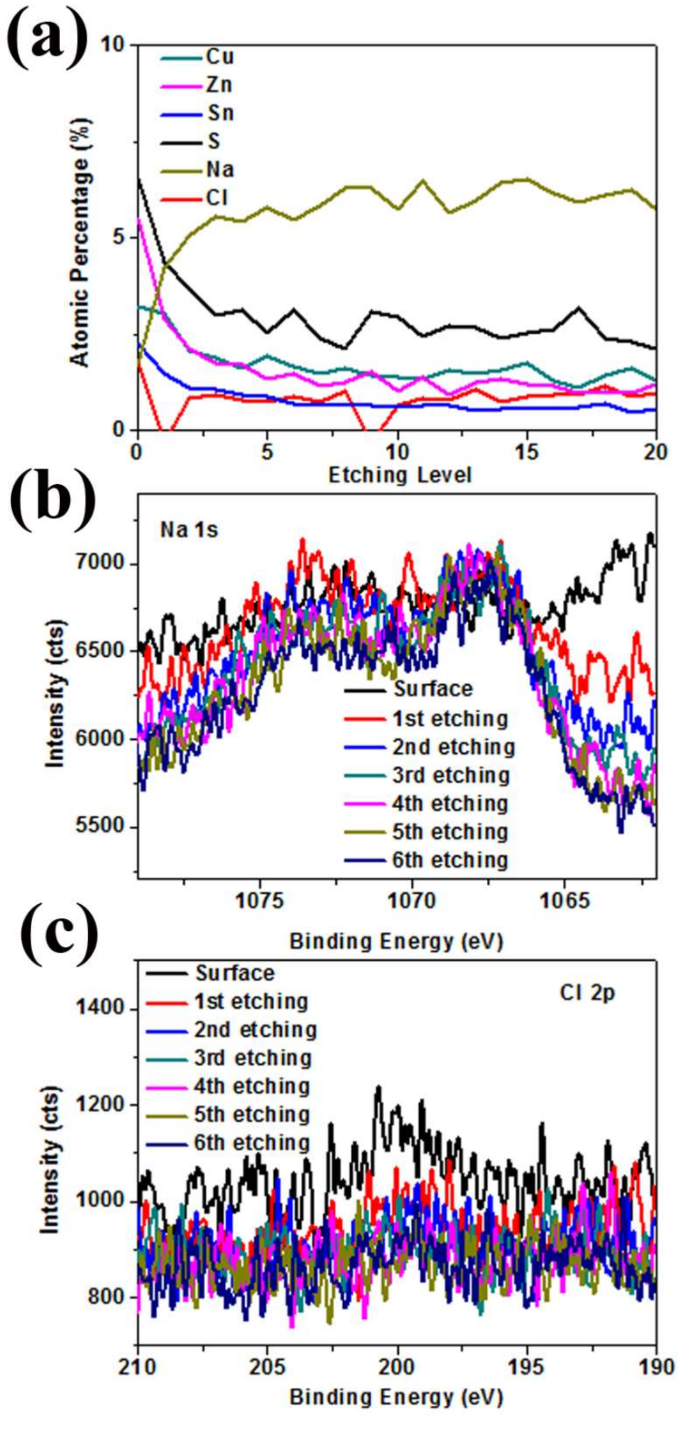

Figure C.10. a) XPS depth profile of Cu5 sample and b) high resolution spectrum depth profile of sodium and c) chlorine.

# APPENDIX D

## SUPPORTING INFORMATION TO CHAPTER 6

Chapter 6 has been published as: Z. Wang, R. Gauvin, and G. P. Demopoulos, *Nanoscale*, 2017, 9 (22), 7650-7665. Appendix D here is the Supporting Information that constitutes for Chapter 6.

Figure D.1 shows the SEM images of TNR synthesized using 0.15M titanium butoxide HCl solution hydrothermally reacting for 2h together with its 3D schematic drawing and photographic image.

Figure D.2 shows the EIS Nyquist plots of TNR 1 – TNR 4 under different bias (0-0.4V) with the plots of fitted $R_{rec}$ and open circuit voltage decay curves.

Figure D.3 shows the XPS depth elemental profiles of CZTS/TNR film annealed at 600 °C for 30 minutes.

Figure D.4 shows the XPS high resolution spectra of copper and zinc of CZTS/TNR films annealed at different temperatures.

Figure D.5 shows the XPS high resolution spectra of a) tin, b) sulfur, c) oxygen and d) titanium of CZTS/TNR films annealed at different temperatures.

Figure D.11 shows the composition dependent device performance chart extracted from J-V and IPCE measurements.

Figure D.12 presents an efficiency contour of CZTS/TNR photoanode based solar cells and the Raman spectra of films with different Cu/Zn ratio.

Figure D.13 presents the SEM secondary electron (SE) image andbackscatter electron (BSE) image of pure $TiO_2$ nanorods and CZTS/TNR on FTO glass.

Figure D.14 presents the SEM images of FIB prepared cross-sectioned CZTS/TNR film.

Figure D.15 presents the EDS maps of the FIB prepared CZTS/TNR cross-sectioned film.

Figure D.16 presents high resolution XPS spectra of double-layer coated CZTS/TNR photoanodes subjected to different duration HCl etching treatment.

Figure D.17 shows the performance of the CZTS/TNR based solar cell with different layers of precursor coating.

Figure D.21 shows the schematic depiction of the TNR-CdS-CZTS solid state device structure.

Figure D.22 shows the dark current and the EIS Nyquist plots of different devices, and the light absorption of CZTS-CdS and CZTS films after deducting the contribution of TNR.

## D.1 Annealing time effect

The effect of annealing time is shown in Figure D.6a. The CZTS/TNR photoanode annealed for 30 min gave the best overall photovoltaic performance. The device with shorter photoanode annealing time (5 min) has a similar $J_{sc}$ value but a relatively lower $V_{oc}$, and both $J_{sc}$ and $V_{oc}$ decrease when the annealing time is extended to 60 or 120 min. The IPCE results in Figure D.6b match the trend of $J_{sc}$ variation. Raman characterization of the four films performed at 514 nm (Figure D.6c) and 785 nm (Figure D.6d) revealed no detectable differences except in the case of the carbon residual bump at around 1440 $cm^{-1}$ that was only visible with the 5 min annealing condition (Figure D.6c). Apparently a longer reaction time, i.e. 30 min, is necessary to eliminate the carbon residual.

In Figure D.7, XPS high resolution core line spectra were taken and compared to probe the effect of annealing time on the CZTS electronic properties of the 600 °C annealed films. Similar to the temperature effect, when the time increases from 5 min to 30 min and over, a noticeable Cu 2p peak shift towards the lower binding energy position is shown in Figure D.5a and D.5b. We assume this to be due to longer annealing time inducing more complete copper-involved reaction. But the case of Zn 2p core line spectra is different. As we can see in Figure D.7c and D.7d, there is no Zn 2p peak shift for the films annealed for different times. Hence it is deduced that the zinc surface reaction is completed after only five minutes thermal treatment at 600 °C.

## D.2 Comparison of XPS Spectra of CZTS/TNR Films with Binary Standards

As an advanced surface analysis method, XPS is extremely sensitive to the element chemical state change by showing a peak shift. In fact, merely relying on the peak binding energy from the database or the literature to determine the chemical/bonding state of elements can be confusing as the peak shift is really insignificant in most cases, experimental conditions and equipment calibration can make a great difference. Therefore, we used various standards for XPS spectra comparison to investigate the chemical reactions and possible formation/occurrence of secondary phases. All standards were purchased from Sigma-Aldrich including $SnO_2$ (99.9%), SnS (99.99%), ZnS (99.99%), CuS (99.99%) and $Cu_2S$ (99.99%) except for the $SnS_2$ that was prepared in our lab and verified by EDS, XRD and XPS.

Figure D.8 shows the results of the XPS comparative analysis of the standards. From Figure D.8a we can notice the different binding energy of O-Sn and O-Ti oxygen core line spectra. It is evident that after 600 °C annealing the additional “bump” appearing to the right of the O-Ti peak can be attributed to the $SnO_2$ impurity. As for Sn 3d core line spectra in Figure D.8b, the Sn 3d peak position is almost the same for annealed CZTS/TNR, $SnO_2$ and $SnS_2$, but quite different from SnS. In fact, SnS is very unstable and easy to be oxidized on the surface. Here we consider this SnS “standard” has a thin oxide layer on the surface showing a $Sn^{4+}$ state, while the real $Sn^{2+}$ core line 3d peaks centered at the lower binding energy as being reported elsewhere[1]. This difference confirmed the oxidation state of tin in the obtained CZTS is $Sn^{4+}$, but still it is difficult to distinguish between Sn-O bond and Sn-S bond at this stage. In Figure D.8c, we can see the Zn 2p peak of ZnS is at the same position of the 350 °C annealed CZTS film while a shift can be noticed after 600 °C annealing, indicating a chemical bonding state change of Zn after high temperature annealing. Hence we conclude from the observed difference of Zn bonding state in CZTS and ZnS that the film is free of the ZnS impurity. Similarly, the results in Figure D.8d show the CZTS films to exhibit different peak position in comparison to CuS and $Cu_2S$ standards suggesting the absence of copper sulfides as impurities. The peak shift between the two CZTS films annealed at 350 °C and 600 °C indicates a more complete reaction happening at higher temperature.

S 2p core line spectra with standards are shown in Figure D.9. It is interesting to see that the binding energy of S 2p peak for each sulfide is different from the others even they all should be $S^{2-}$. This observation can be a valuable reference in distinguishing CZTS from other binary secondary phases by performing S core line XPS spectroscopy.

## D.3 Surface Oxidation Impurities

Surface oxidation is found to depend on applied annealing time. Figure D.10a provides the S 2p core line spectra of the CZTS/TNR films annealed for different times. A dash line at ~168 $cm^{-1}$ indicates the binding energy of sulfate or oxidized sulfur[2], where a distinguishable bump shows up after 30 min annealing and becomes more significant for the 120 min annealed CZTS. For O 1s spectra there is no apparent difference among these four samples as shown in Figure D.10b, the additional "shoulder" peak exists in all conditions, which is strengthened when prolonging the annealing time. We attribute this "shoulder" to $SnO_2$ impurity phase (Figure D.8a). Quantitative analysis was done by plotting the elemental fraction according to its ratio to titanium and shown in Figure D.10c, where we see a gradually enhanced oxygen level when the time being prolonged to over 30 min. This can be prescribed as annealing time-induced surface oxidation. In contrast, a significant decrease of carbon content is observed from 5 to 30 min annealing time, which is due to complete decomposition of carbon complex, similar with what we observed in the 514 nm Raman spectrum of 5 min annealed sample in Figure D.6c. Figure D.10d depicts the fraction of Cu, Zn, Sn and S as a function of annealing time, where we observe Sn content to increase and S level to decrease as annealing time is prolonged from 5 min to 30 min. Afterwards the Sn keeps increasing but much more slowly while the S levels off. Therefore, 30 min is deemed the right annealing time in lowering the carbon residual content and avoiding significant loss of sulfur, tin oxide impurity formation or damage on FTO substrate. With reference to the latter, we should mention that after annealing for 2 h have we found the FTO resistance to increase by 2-3 times but not after annealing for 30 min. Hence, to avoid FTO substrate damage while maximizing the CZTS crystallinity benefit, annealing at 600 °C should be limited to 30 min.

## D.4 Band Alignment of CZTS and Rutile $TiO_2$

X-ray photoelectron spectroscopy (XPS) was used to determine the band offsets in the two phase composite using a well-established method[3]. In this method the energy difference between a core line (CL) and the valence band maximum (VBM) is first measured for the individual components of the composite in isolation. The sample preparation of the CZTS and rutile $TiO_2$ pure samples for the band alignment study is straight forward. Rutile $TiO_2$ was prepared by placing an air assisted pre-annealed TNR in the furnace and annealed at the same Sn/S existed condition for CZTS synthesis at 600 °C for 30 minutes, and hence we consider this TNR is the same as the one coated by CZTS. To guarantee the exact same condition to reproduce pure CZTS, we directly spin-coated the precursor solution on FTO glass following the same procedure as we did for CZTS/TNR, and then the film was annealed as well. The valence and core line spectra of the CZTS and TNR are shown in Figure D.18 and Figure D.19. Cu and Ti are selected for the core-line spectra characterization. Zn was also verified and the band-alignment result is very similar to the Cu core-line based calculation.

Then by measuring the difference between the CLs in the composite material, the band alignment and energy offset can be determined according to the equation below:

$$\Delta E_{VBM} = (E_{CL}^{CZTS} - E_{VBM}^{CZTS}) - (E_{CL}^{TNR} - E_{VBM}^{TNR}) - \Delta E_{CL}$$

This methodology is commonly applied to determine the band offsets in film substrate, here from Figure D.18, we obtained the valence band maximum (VBM) position $E_{VBM}^{CZTS} = 0.4$ eV, $E_{VBM}^{TNR} = 2.63$ eV in reference to its Fermi energy level, and from Figure D.19 the $E_{CL}^{CZTS}$ and $E_{CL}^{TNR}$ core line energy value from Cu $2p_{3/2}$ and Ti $2p_{3/2}$ are obtained to be 932.08 eV and 458.58 eV, respectively. $\Delta E_{CL}$ represents the energy difference of Cu (CZTS) and Ti (TNR) core line, which is calculated to be 472.71 eV in Figure D.20. Therefore, the calculated offset of valence band maximum $\Delta E_{VBM}$ is 3.02 eV. The bandgaps of both CZTS and TNR are measured by light absorbance, which are further used to determine the conduction band minimum offset as shown in Figure 6.13 in Chapter 6. For all spectra displayed, C 1s 285 eV was used for charge correction.

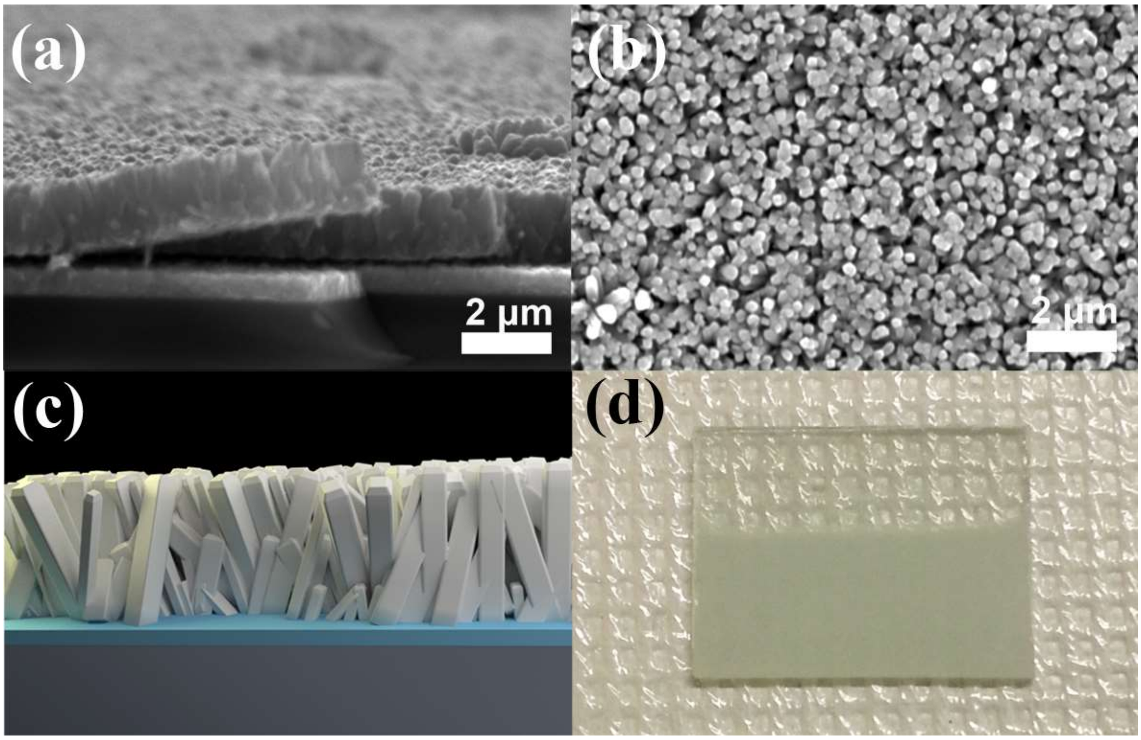

Figure D.1. SEM images of a) cross-section and b) top view of TNR synthesized using 0.15M titanium butoxide HCl solution hydrothermally reacting for 2h; c) 3D schematic drawing of the TNR cross section; d) photograph of an as-prepared TNR film on FTO glass.

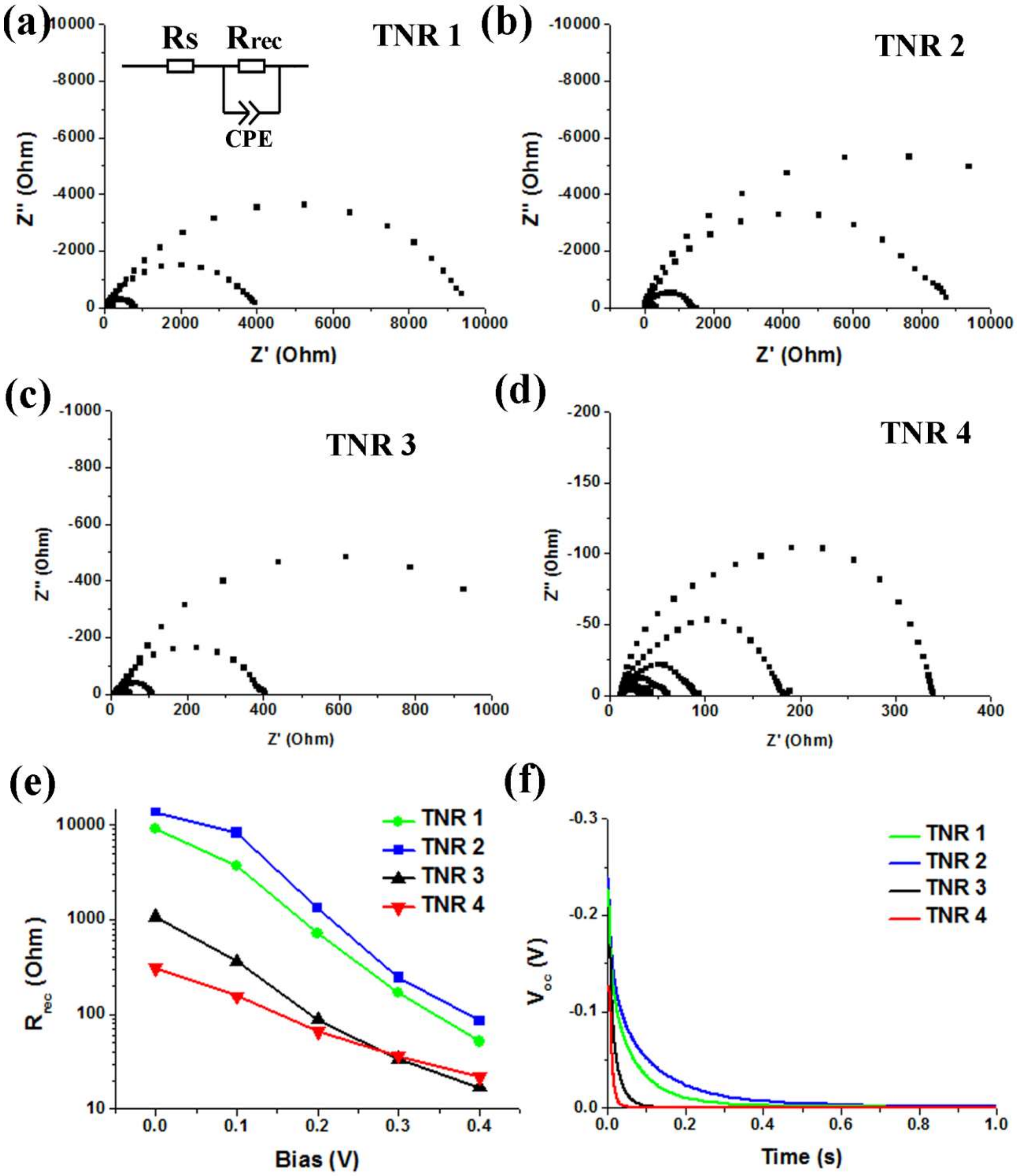

Figure D.2 a-d) EIS Nyquist plots of TNR 1 – TNR 4 under different bias (0-0.4V); inset in a) shows the equivalent circuit; e) the plots of fitted $R_{rec}$ and f) open circuit voltage decay curves.

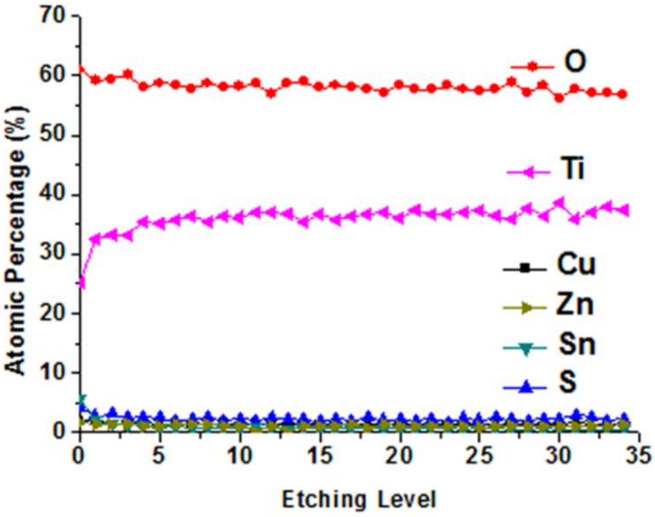

Figure D.3. XPS depth elemental profiles of CZTS/TNR film annealed at 600 °C for 30 minutes.

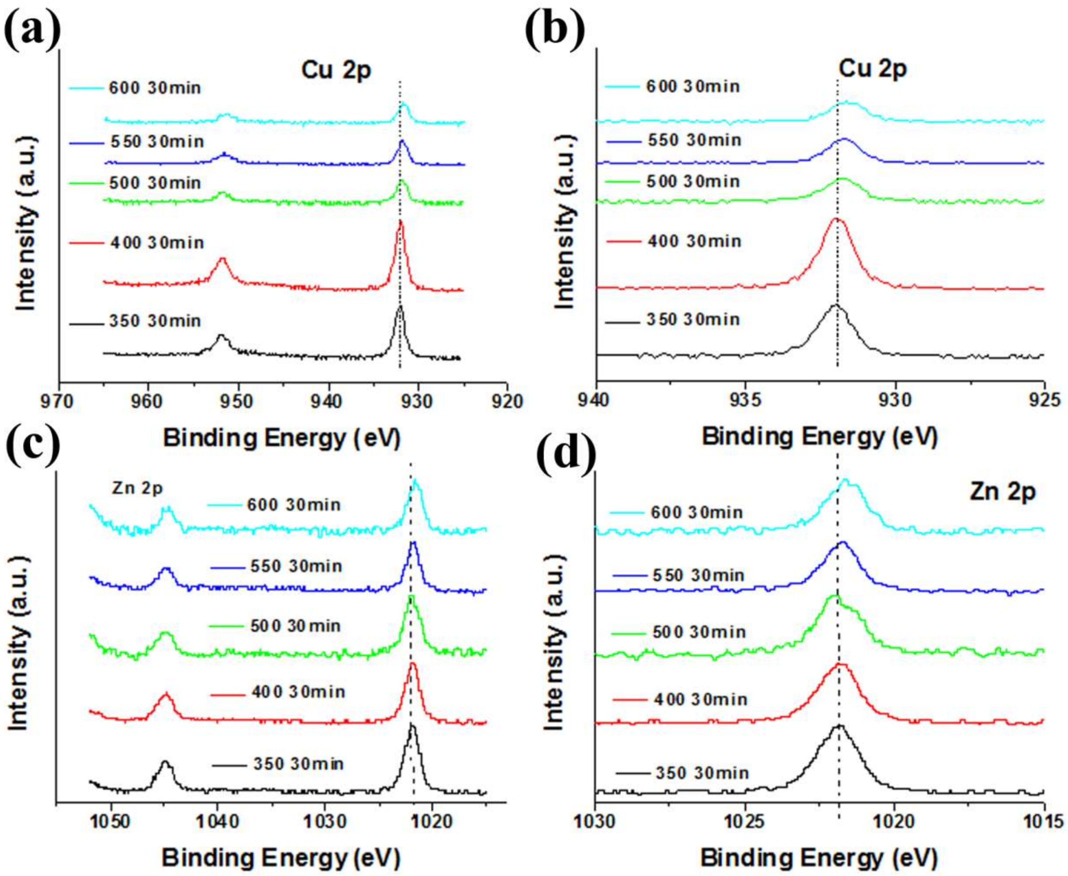

Figure D.4. XPS high resolution spectra of a, b) copper and c, d) zinc of CZTS/TNR films annealed at different temperatures.

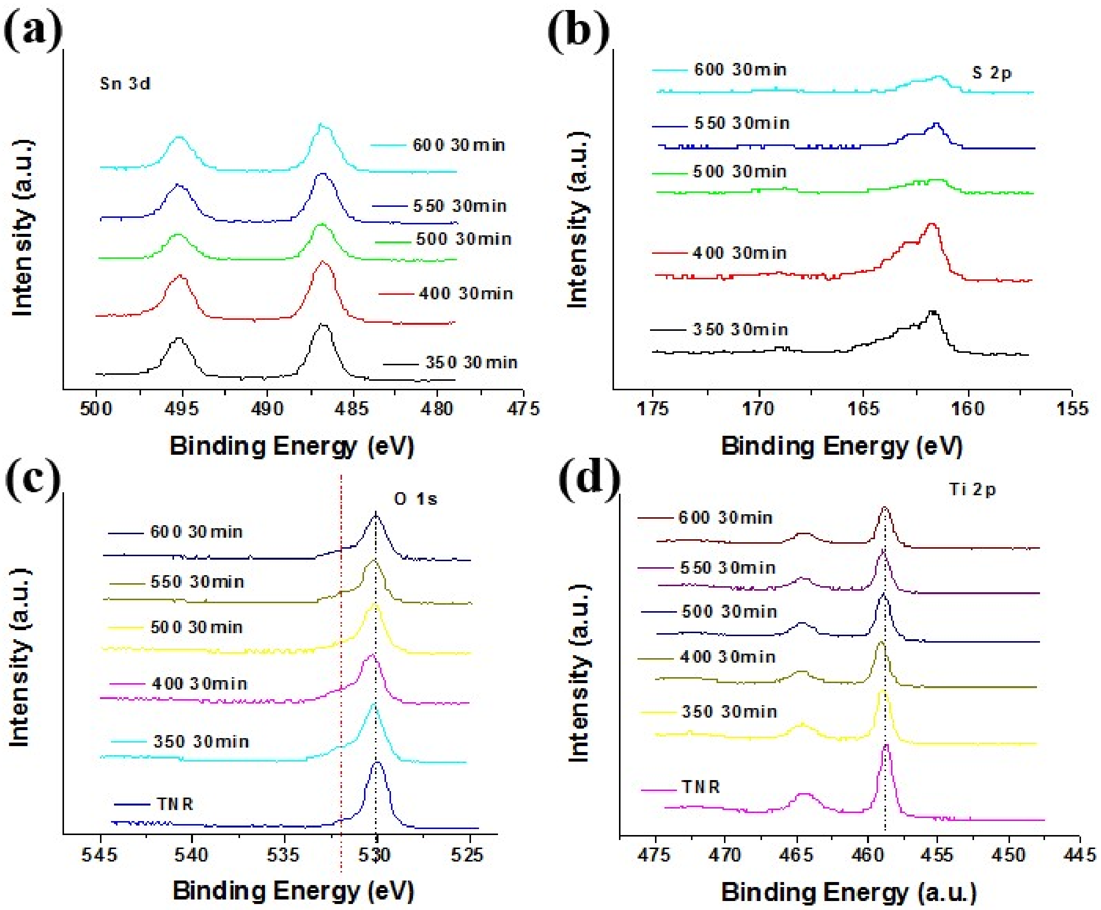

Figure D.5. XPS high resolution spectra of a) tin, b) sulfur, c) oxygen and d) titanium of CZTS/TNR films annealed at different temperatures.

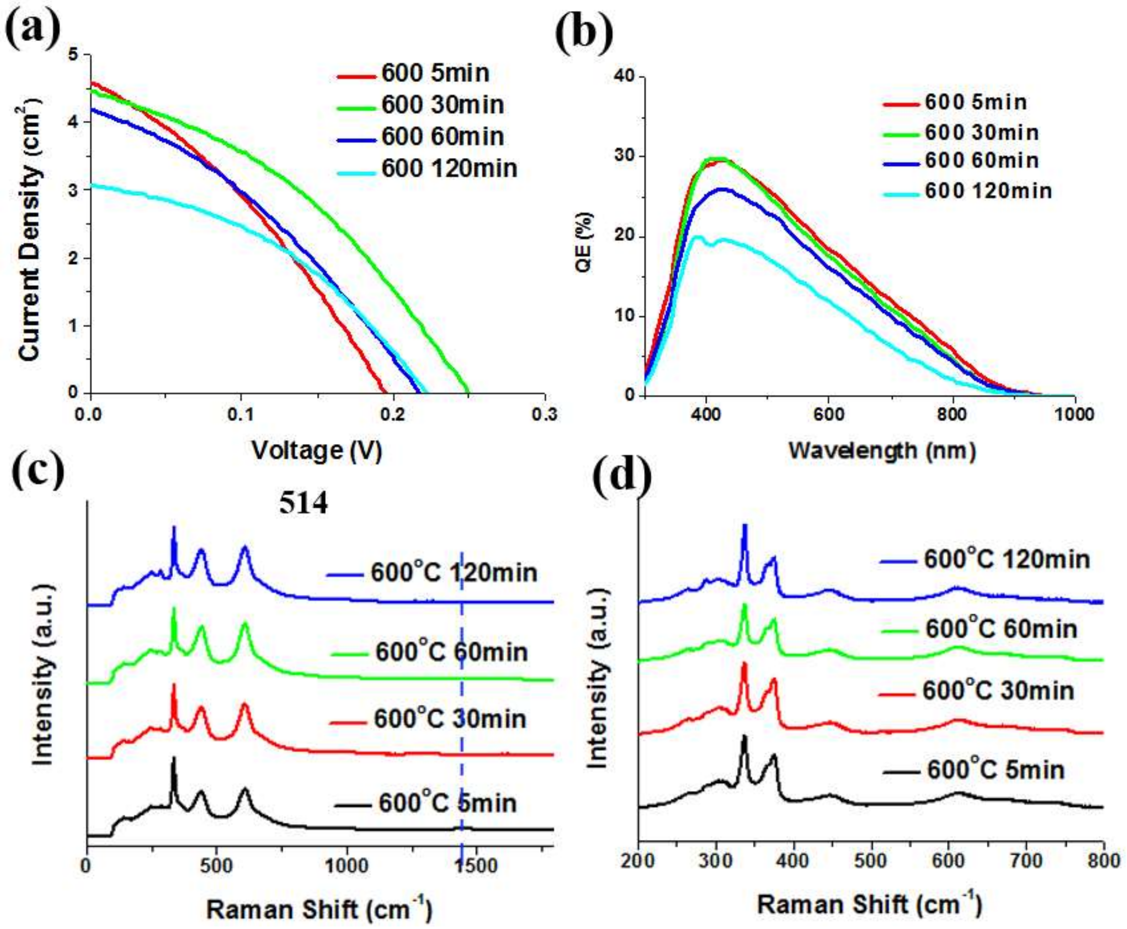

Figure D.6. Effect of annealing time on CZTS/TNR photoanodes: a) solar cell J-V characteristics; b) IPCE; c) Raman spectra at 514 nm laser; and d) 785 nm laser excitation conditions. Annealing done at 600 °C.

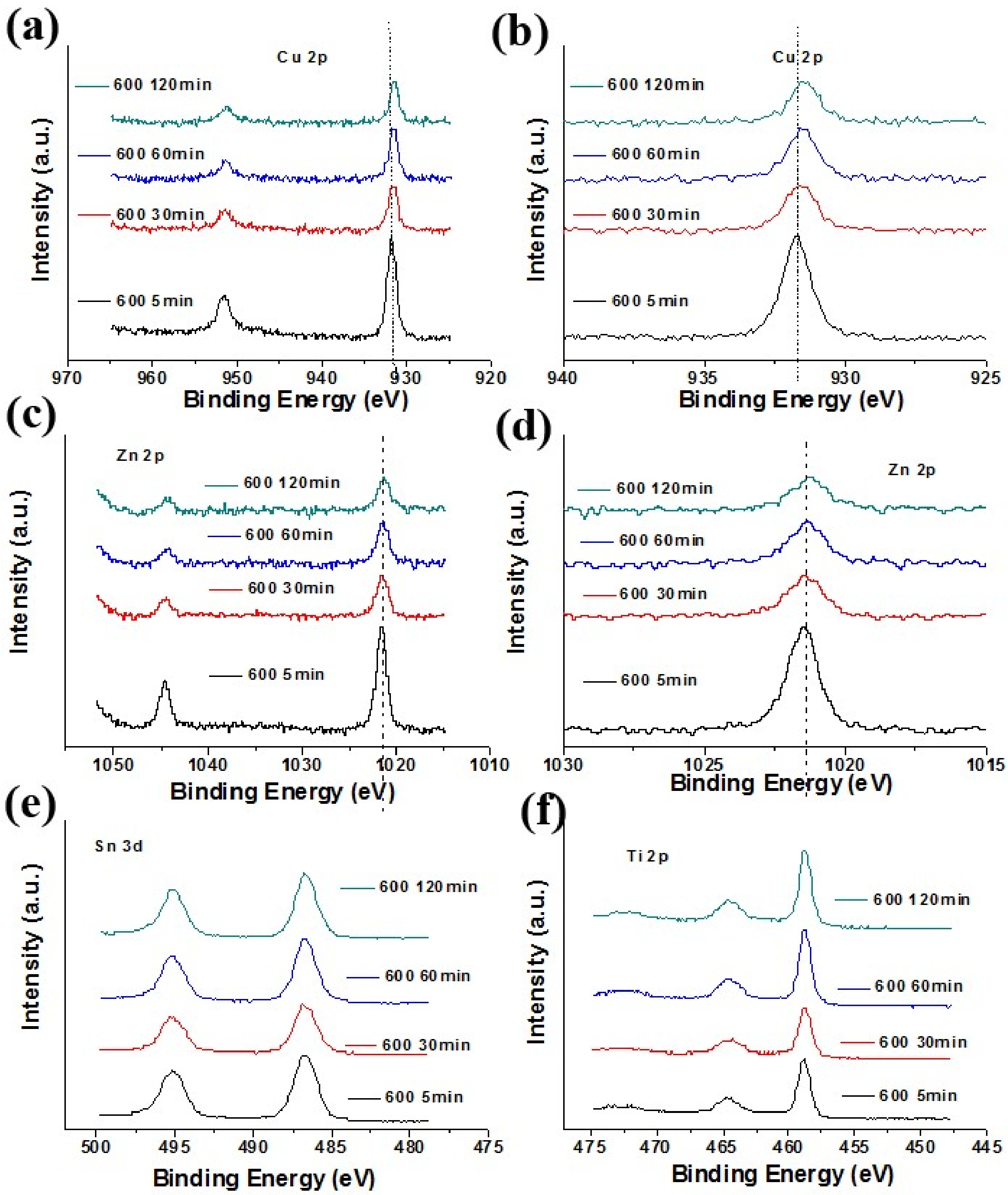

Figure D.7. XPS high resolution spectra of a, b) copper, c, d) zinc, e) tin and f) titanium of CZTS/TNR films annealed at 600 °C for different times.

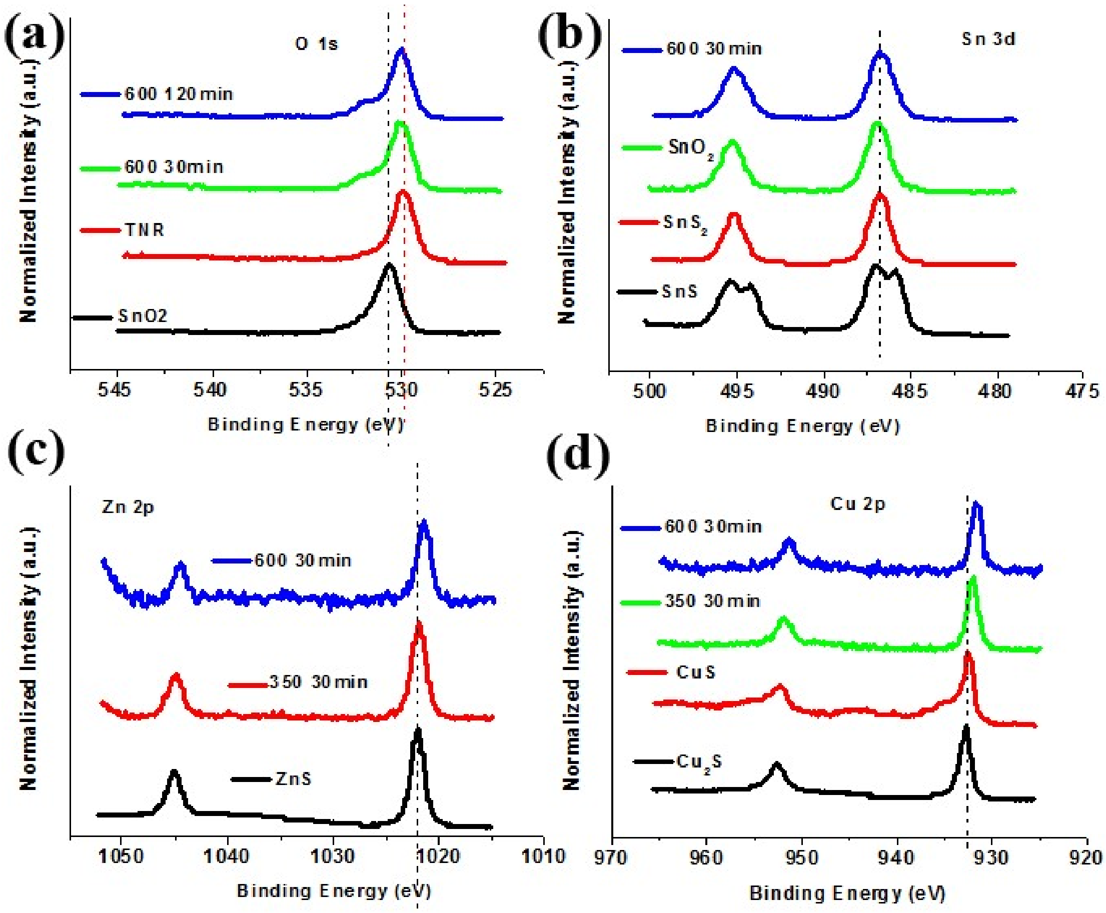

Figure D.8. XPS high resolution spectra of a) oxygen, b) tin, c) zinc and d) copper in 600 °C annealed CZTS/TNR films compared to spectra of commercially available binary standards.

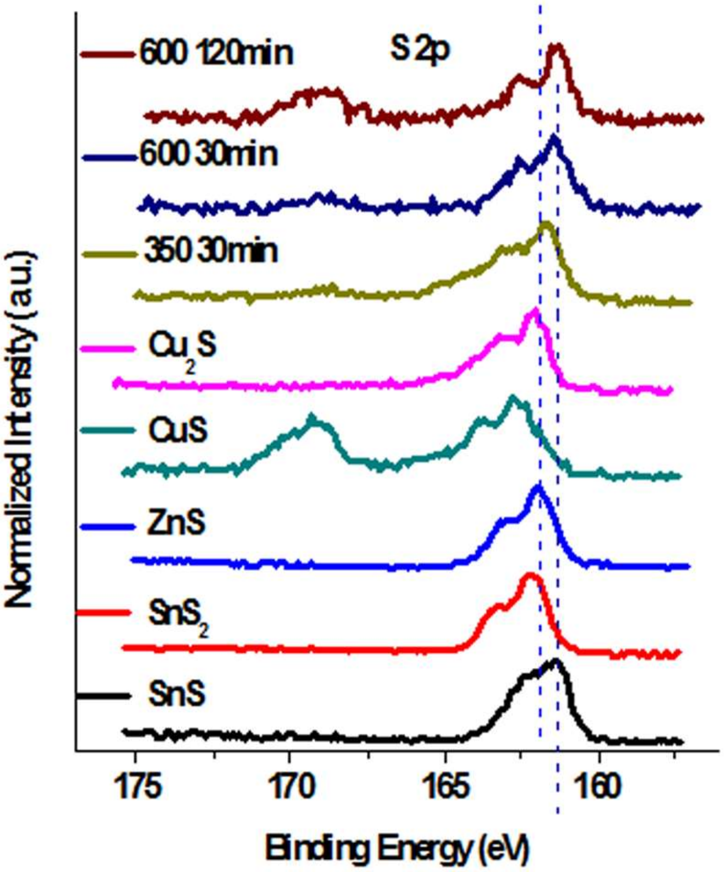

Figure D.9. XPS high resolution S 2p spectra of as-prepared CZTS compared to commercially available binary sulfides.

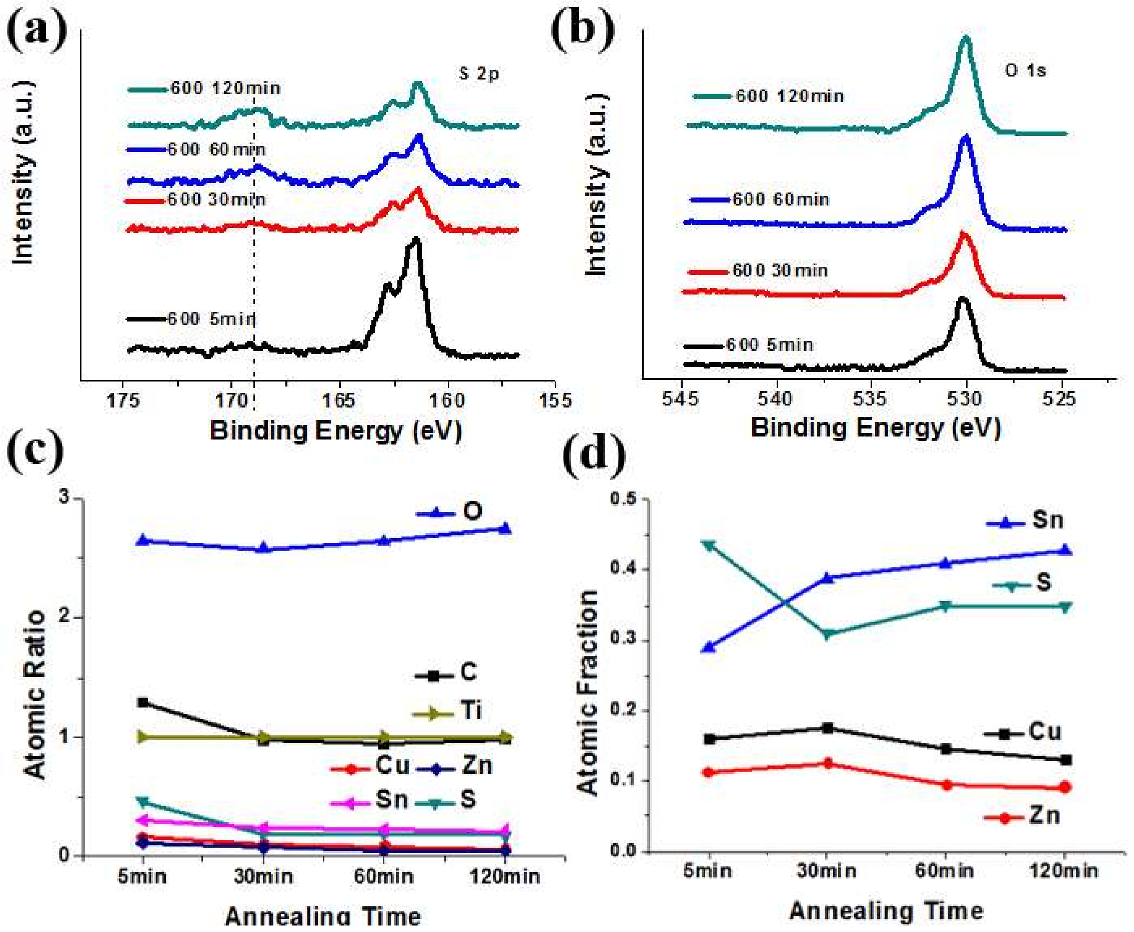

Figure D.10. XPS high resolution spectra of a) sulfur and b) oxygen of the CZTS/TNR film annealed at 600 °C for different times. Quantitative analysis of the CZTS/TNR films: a) annealing time dependent ratio of all the other elements to titanium and b) annealing time dependent CZTS composition change.

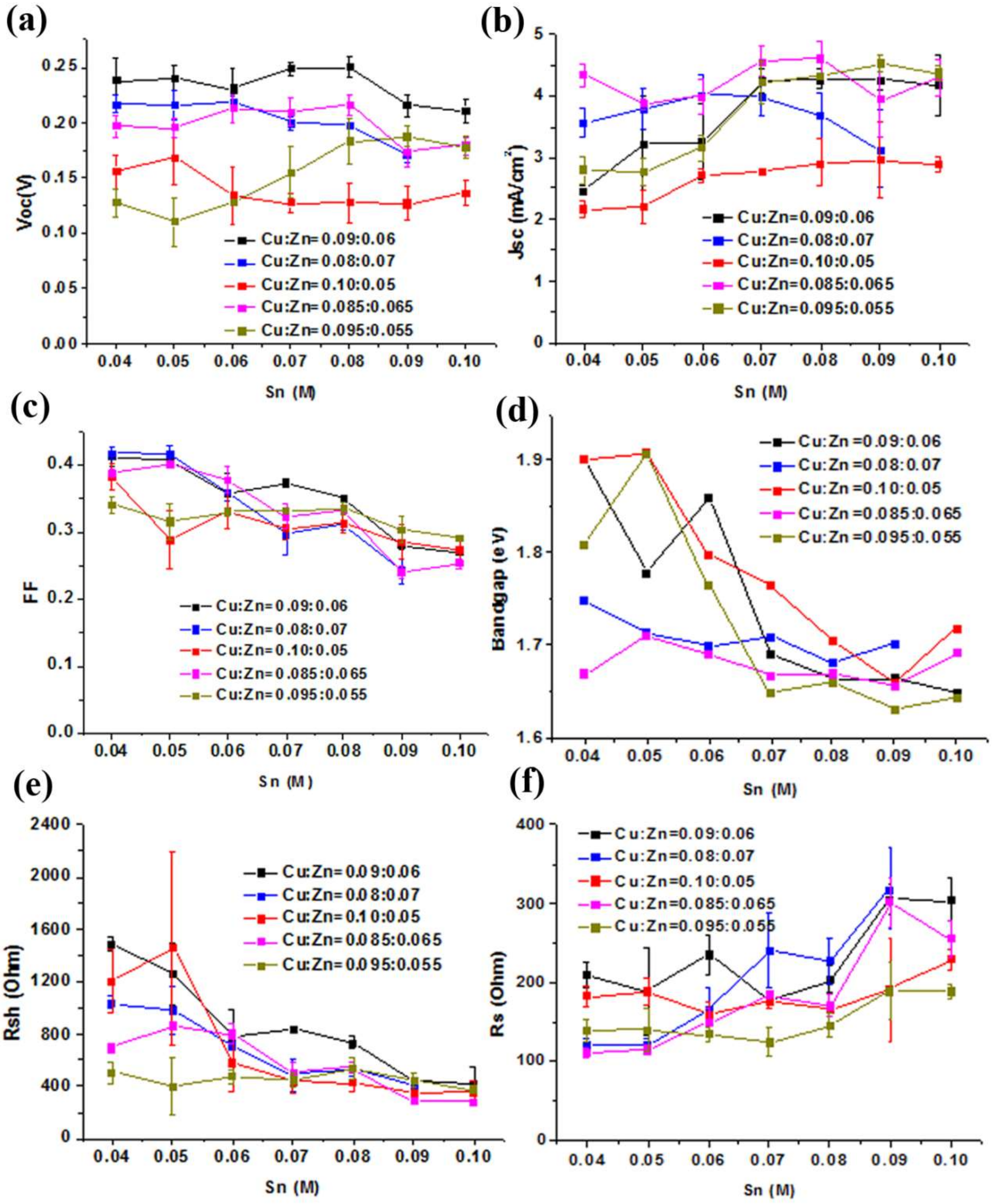

Figure D.11. Composition dependent device performance chart extracted from J-V and IPCE measurements: a) open-circuit voltage; b) short-circuit current density; c) fill factor; d) bandgap; e) shunt resistance and f) series resistance.

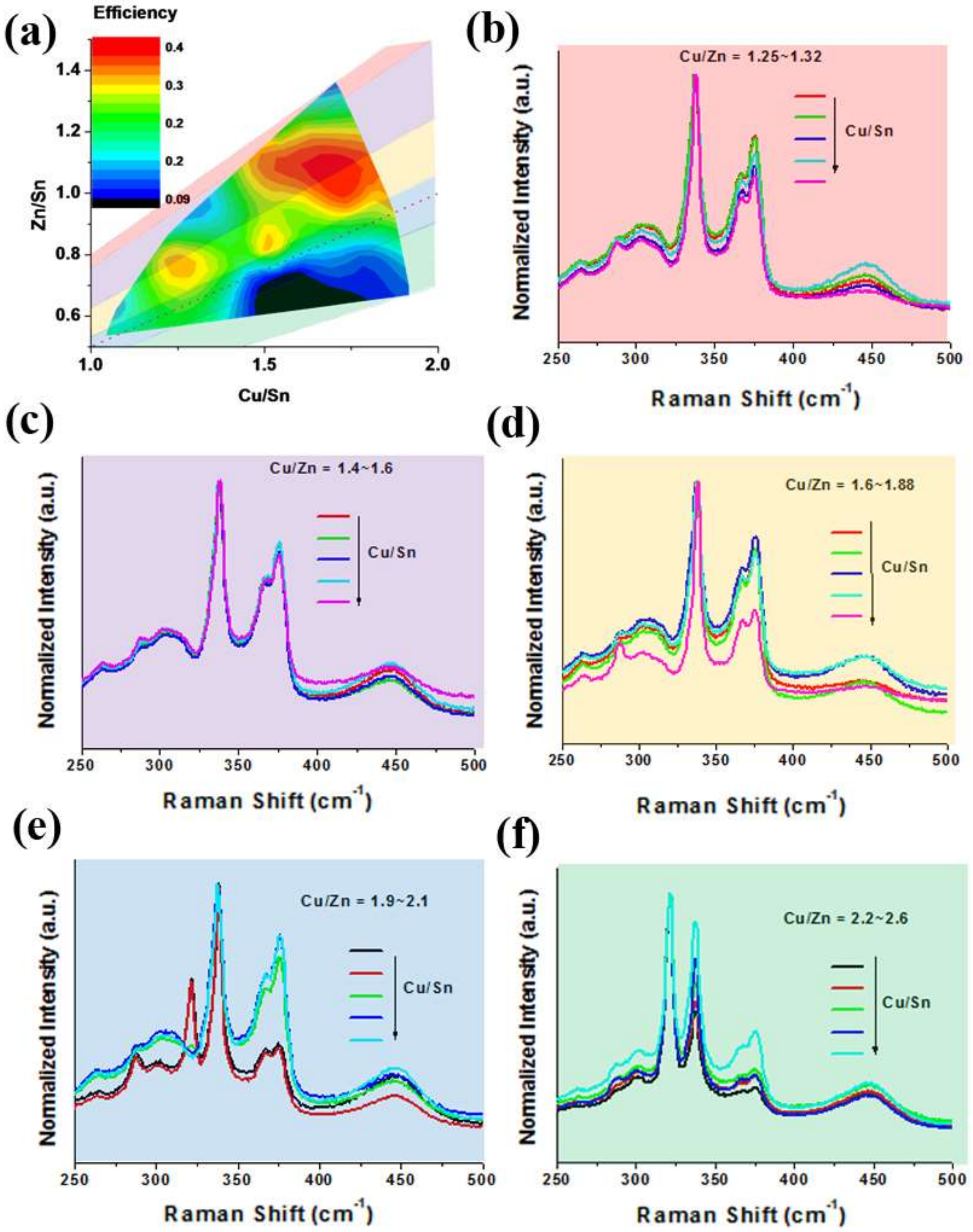

Figure D.12. a) Efficiency contour of CZTS/TNR photoanode based solar cells and the Raman spectra of films with Cu/Zn ratio of b) 1.25~1.32, c) 1.4~1.6, d) 1.6~1.88, e) 1.9~2.1 and f) 2.2~2.6.

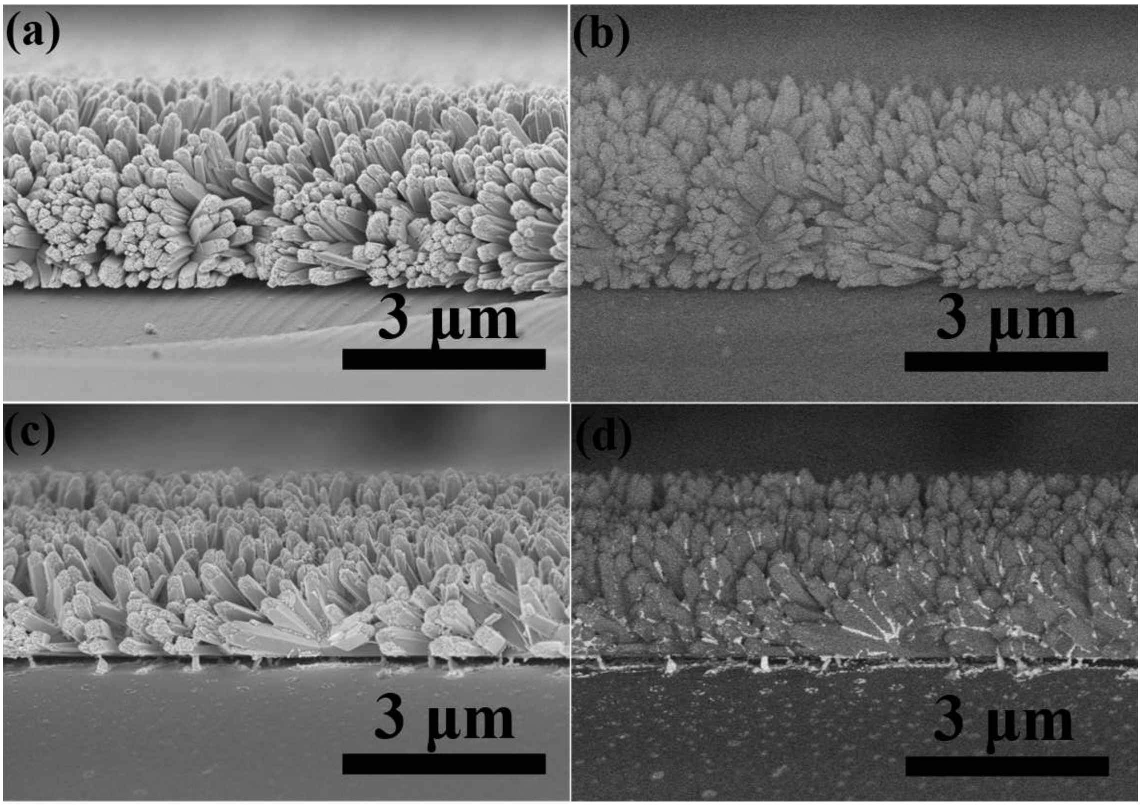

Figure D.13. a) The SEM secondary electron (SE) image and b) backscatter electron (BSE) image of pure $TiO_2$ nanorods on FTO glass; c) the SE image and d) BSE image of CZTS/TNR on FTO glass.

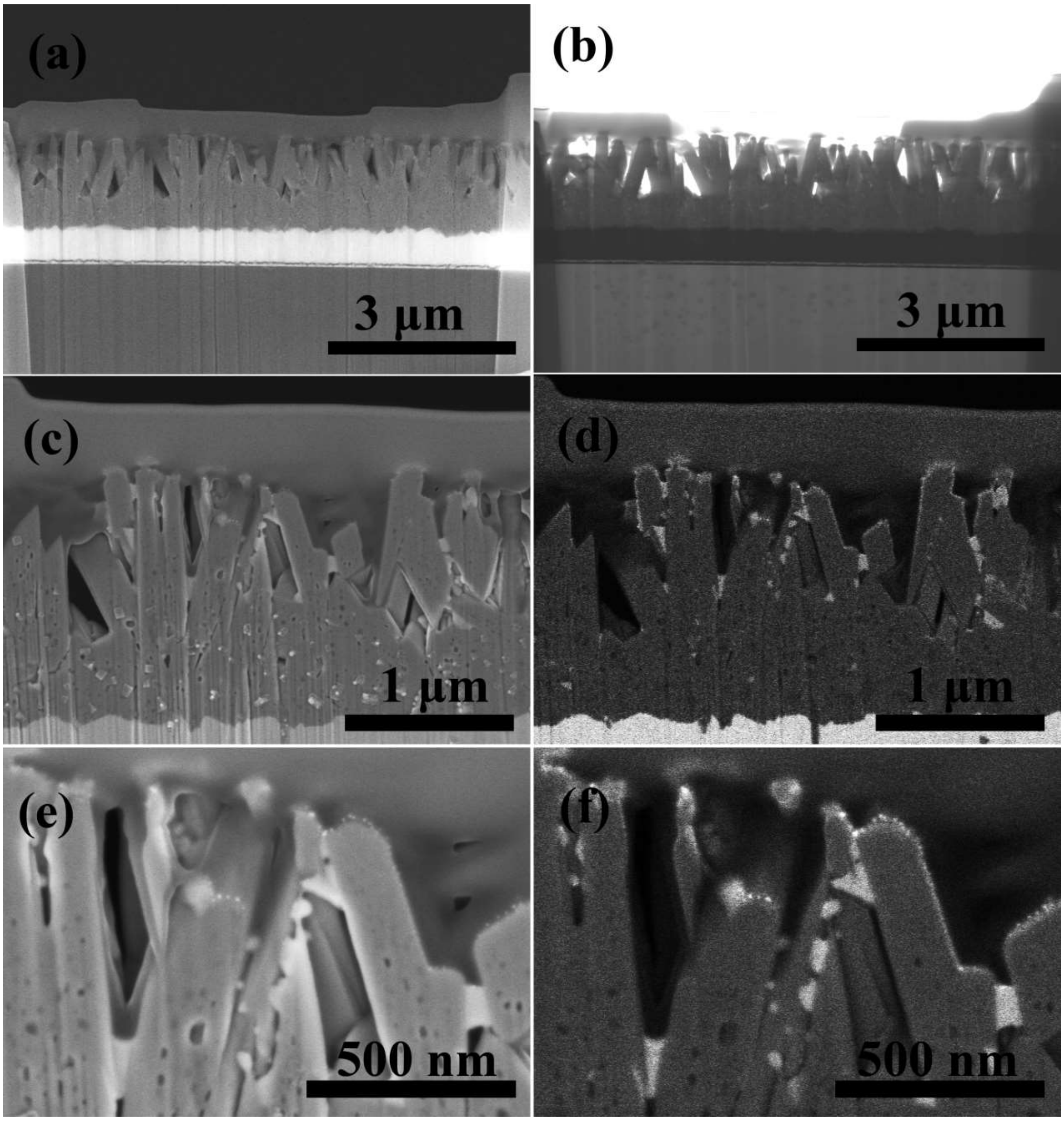

Figure D.14. a) Dark field and b) bright field electron microscope images of a cross-sectioned CZTS/TNR film; c,e) secondary electron (SE) and d,f) backscatter electron (BSE) images of the cross-sectioned CZTS/TNR film.

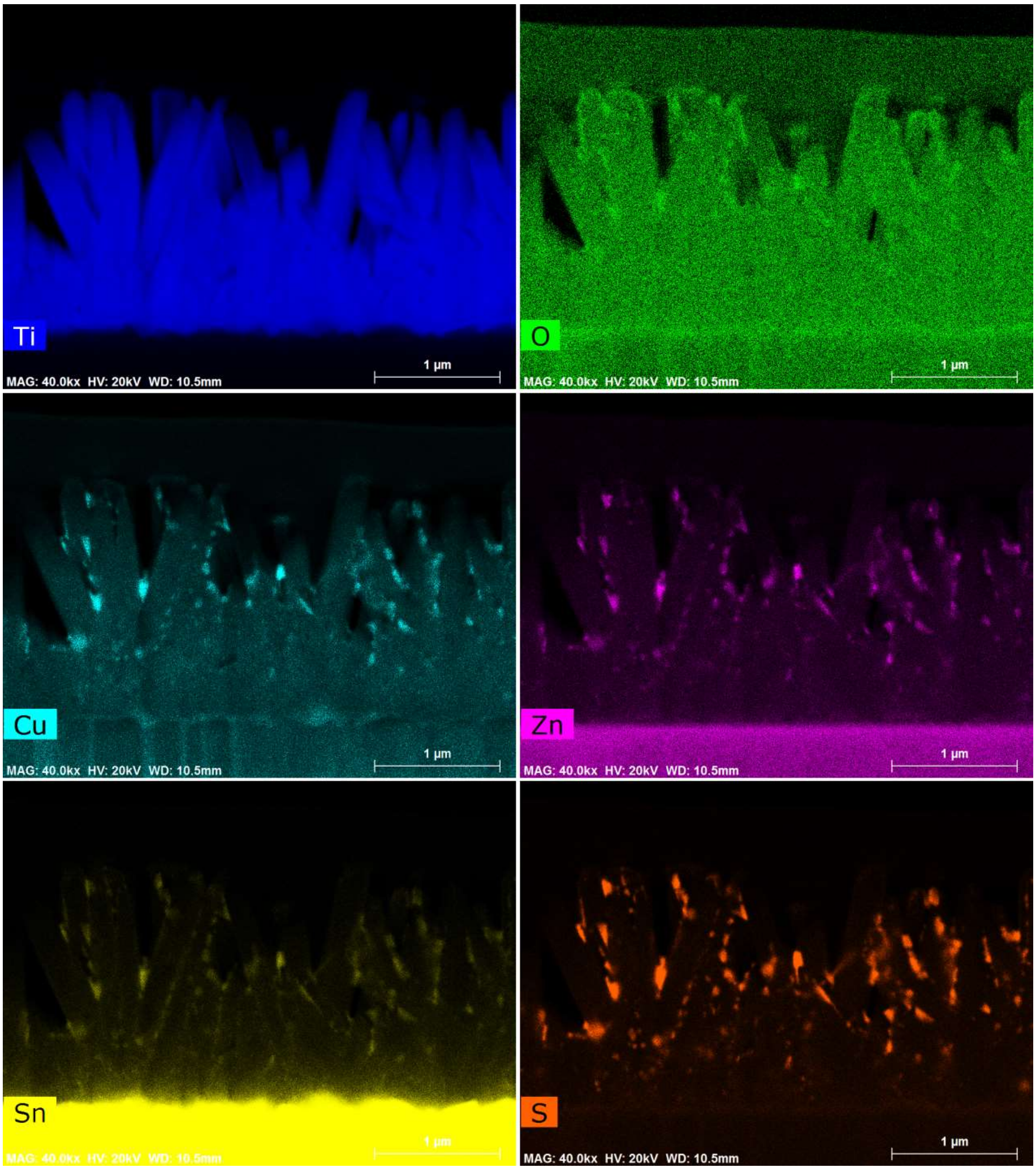

Figure D.15. EDS maps of the FIB prepared CZTS/TNR cross-sectioned film.

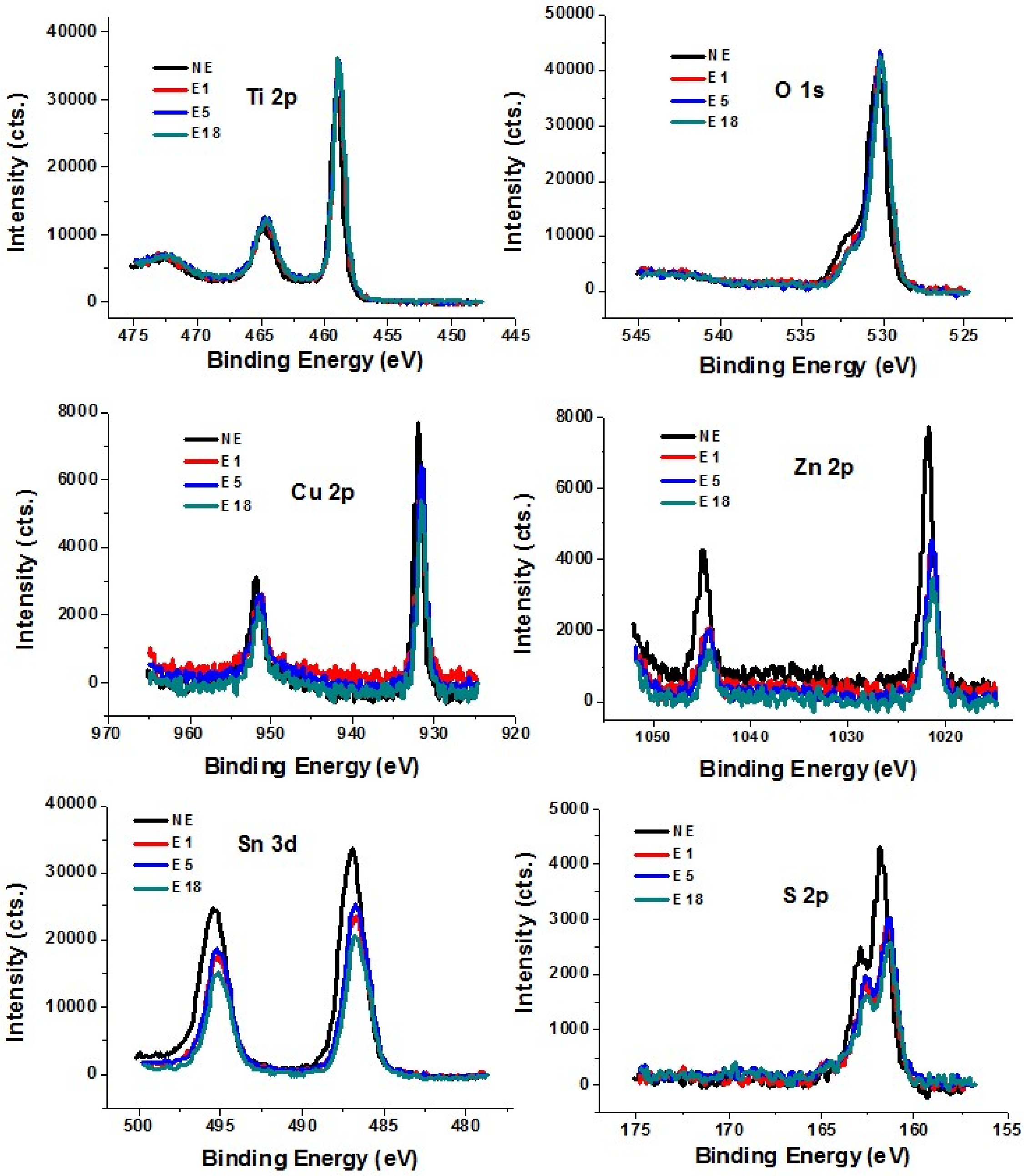

Figure D.16. High resolution XPS spectra of double-layer coated CZTS/TNR photoanodes subjected to different duration HCl etching treatment.

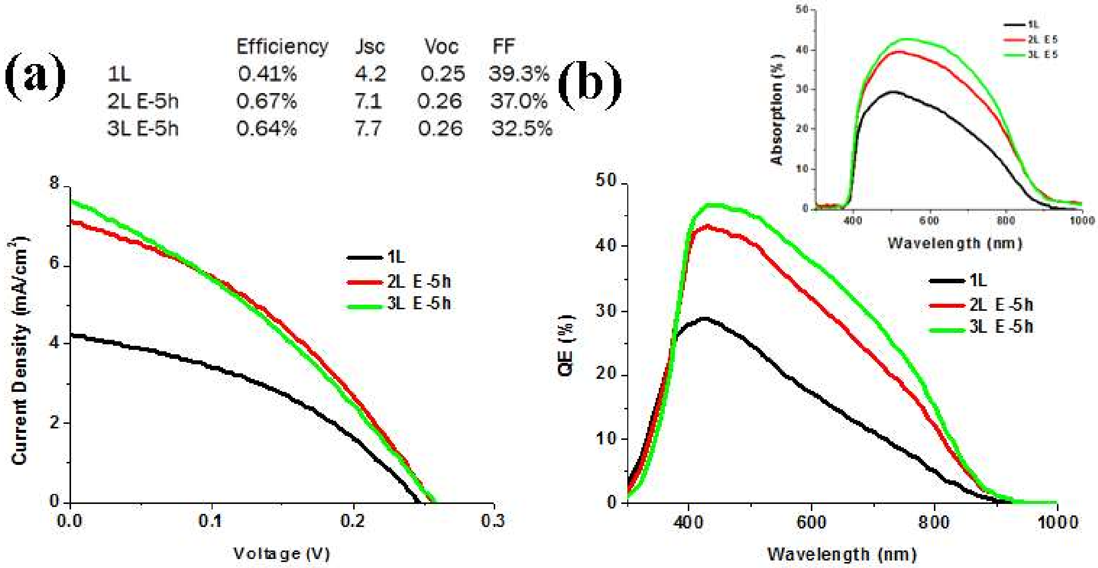

Figure D.17. Performance of the CZTS/TNR based solar cell with different layers of precursor coating.

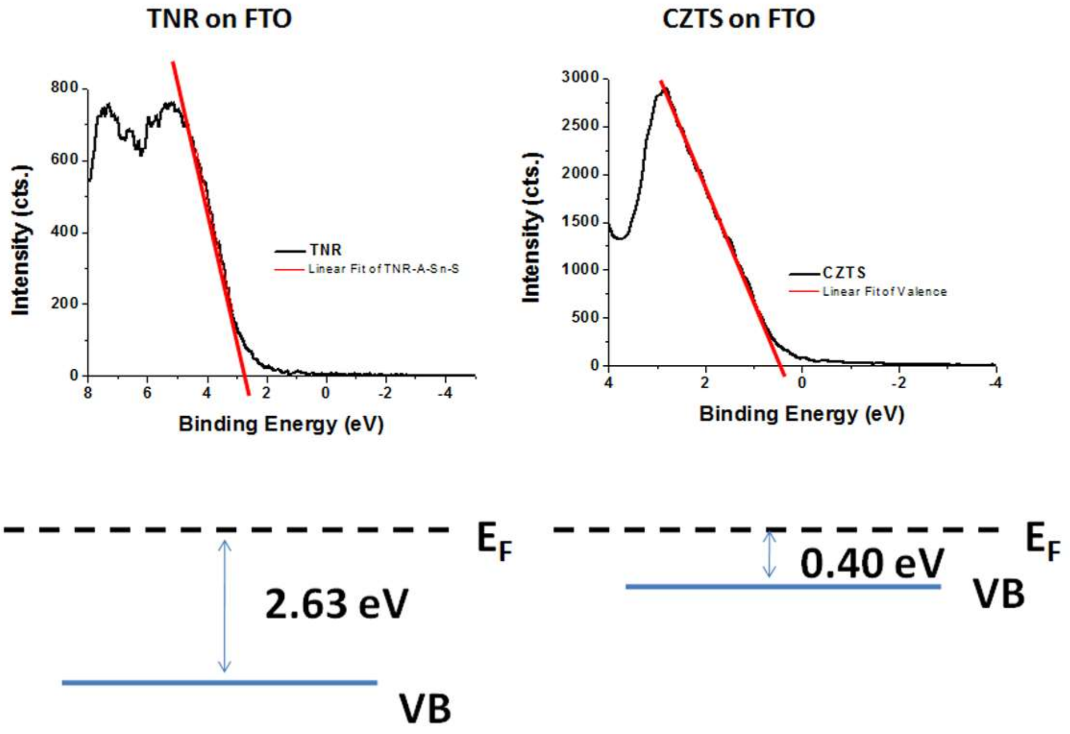

Figure D.18. Valence spectra of pure TiO2 nanorods and CZTS on FTO glass and the extracted valence band position.

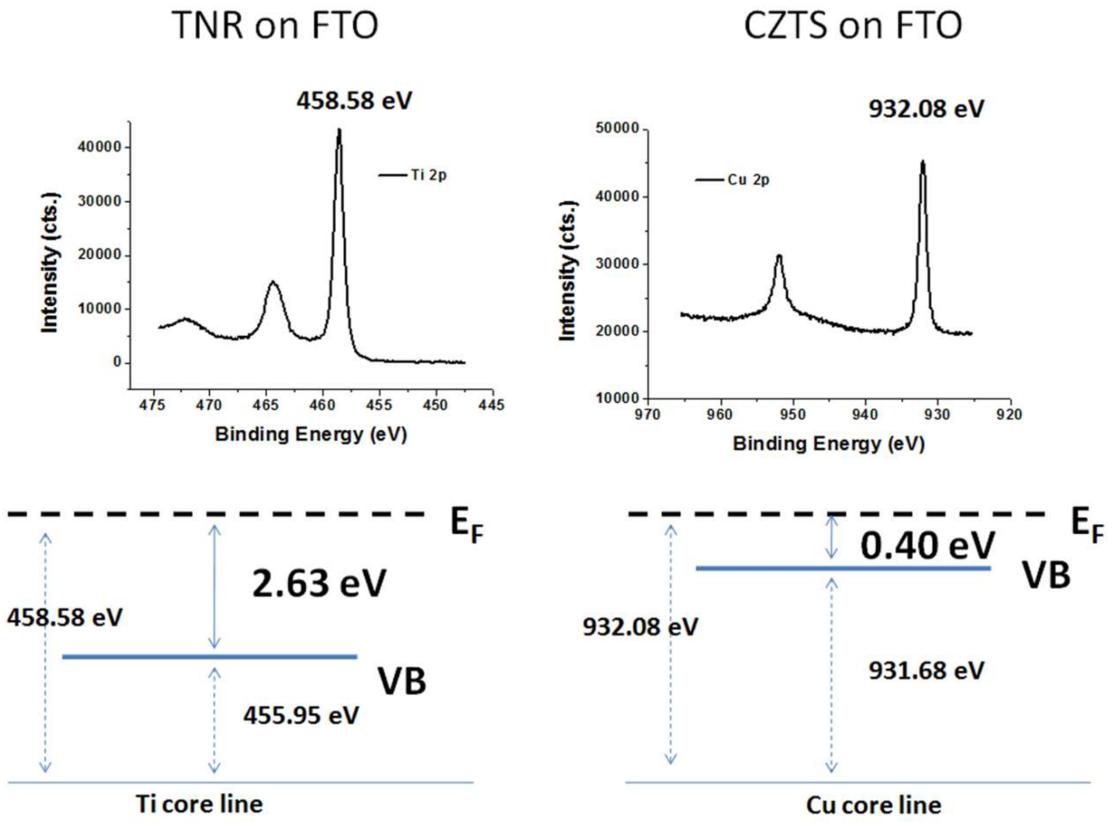

Figure D.19. Ti and Cu core line spectra from XPS and the extracted core line position.

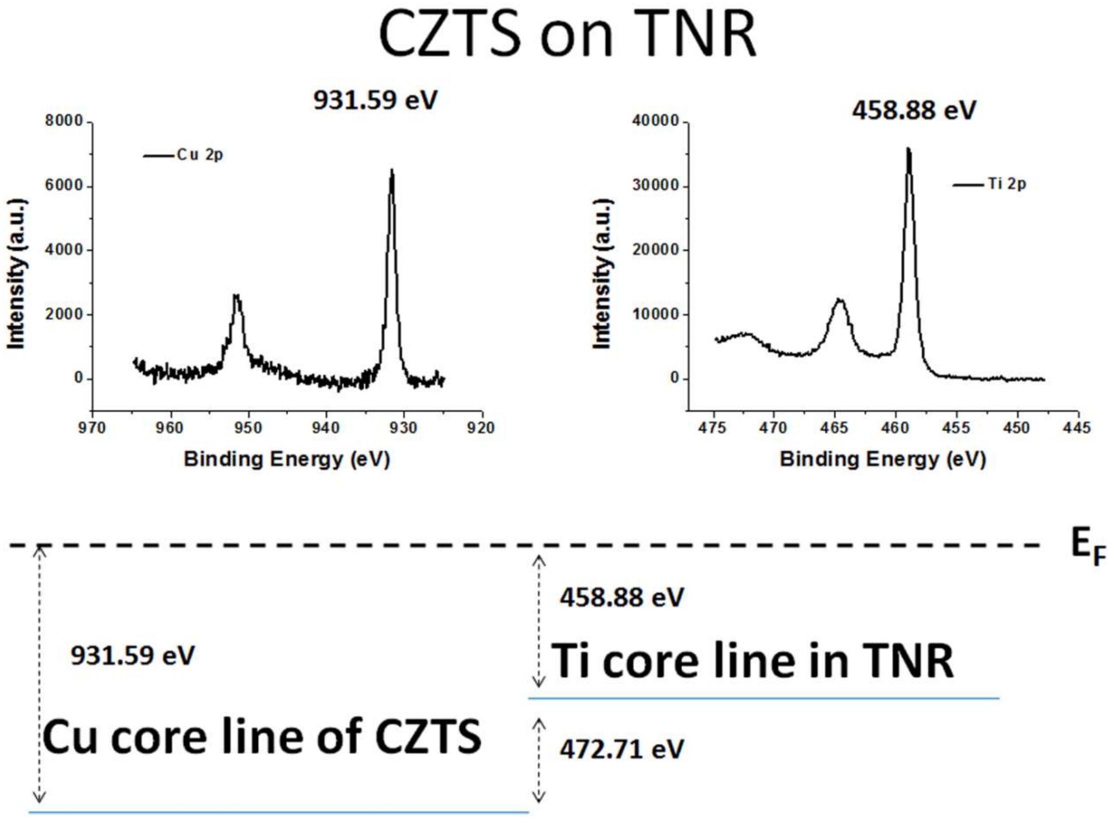

Figure D.20. Cu 2p and Ti 2p core line spectra of CZTS/TNR composite and the determined core line offset.

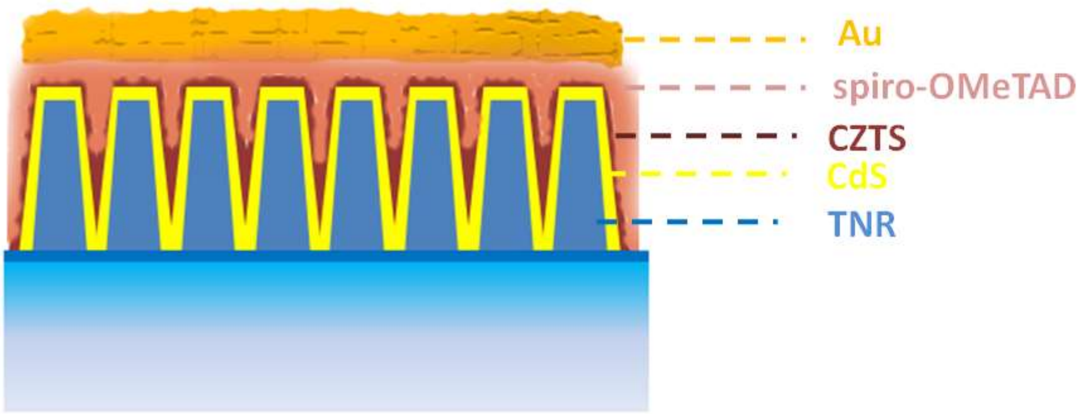

Figure D.21. Schematic depiction of the TNR-CdS-CZTS solid state device structure.

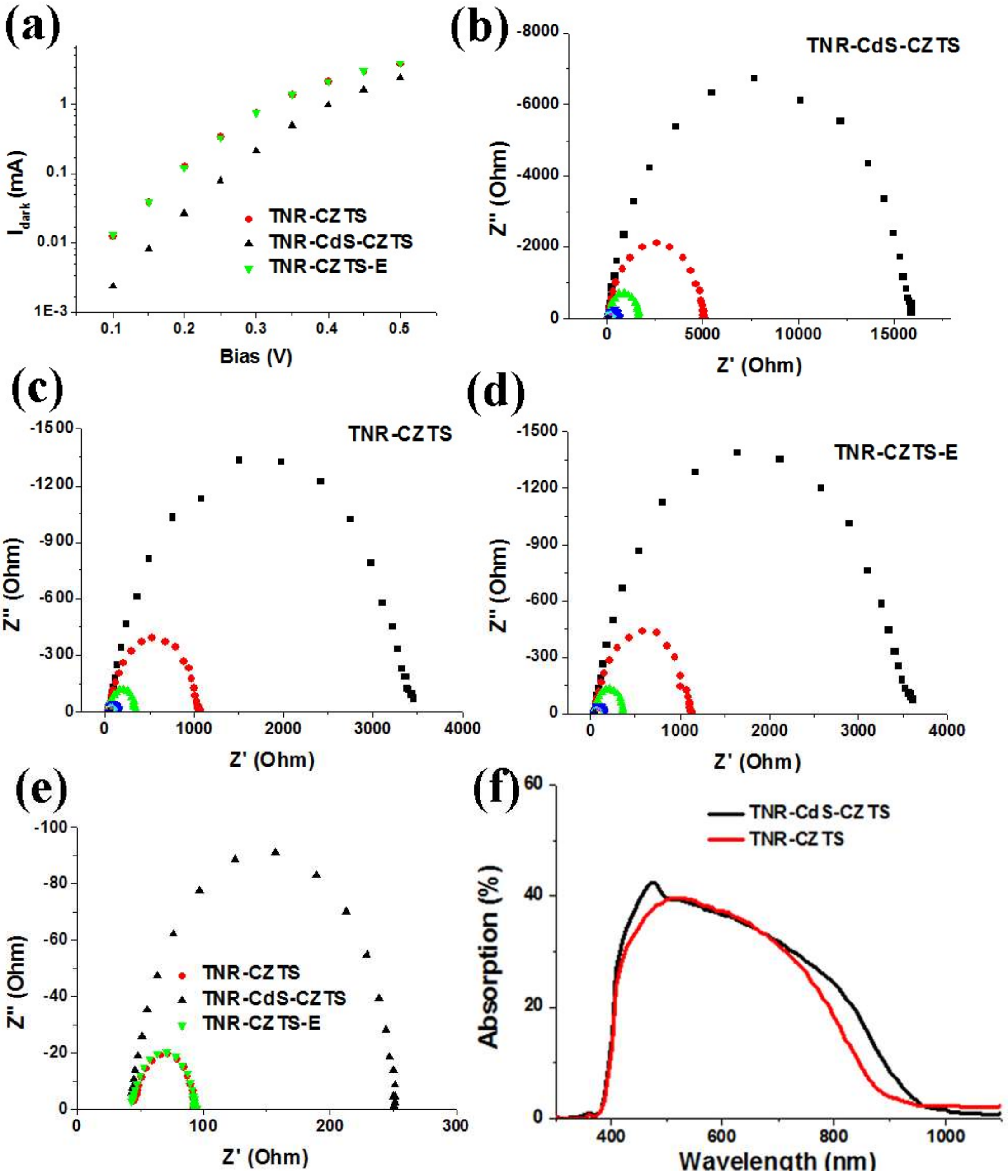

Figure D.22. a) Dark current of different devices; and the EIS Nyquist plots of b) TNR-CdS-CZTS, c) TNR-CZTS, and d) TNR-CZTS-E device under reverse bias from 0.1V to 0.5V; e) comparison of EIS Nyquist plots of all three devices under 0.3V bias; and f) light absorption of CZTS-CdS and CZTS films after deducting the contribution of TNR.

## D.5 References:

1. Whittles, T. J.; Burton, L. A.; Skelton, J. M.; Walsh, A.; Veal, T. D.; Dhanak, V. R., Band Alignments, Valence Bands, and Core Levels in the Tin Sulfides SnS, $SnS_2$, and $Sn_2S_3$: Experiment and Theory. *Chemistry of Materials* **2016,** *28* (11), 3718-3726.

2. Choi, Y. C.; Lee, D. U.; Noh, J. H.; Kim, E. K.; Seok, S. I., Highly Improved $Sb_2S_3$ Sensitized-Inorganic–Organic Heterojunction Solar Cells and Quantification of Traps by Deep-Level Transient Spectroscopy. *Advanced Functional Materials* **2014,** *24* (23), 3587-3592.

3. Scanlon, D. O.; Dunnill, C. W.; Buckeridge, J.; Shevlin, S. A.; Logsdail, A. J.; Woodley, S. M.; Catlow, C. R. A.; Powell, M. J.; Palgrave, R. G.; Parkin, I. P.; Watson, G. W.; Keal, T. W.; Sherwood, P.; Walsh, A.; Sokol, A. A., Band Alignment of Rutile and Anatase $TiO_2$. *Nature Materials* **2013,** *12* (9), 798-801.